This is to certify that the

dissertation entitled

CONTINUOUS PROCESSING OF
UNIDIRECTIONAL PREPREG

presented by

Shridhar R. Iyer

has been accepted towards fulfillment
of the requirements for

Ph.D. degree in Chemical Engineering

Lawrence T. Drzal
Major professor

Date October 23, 1990

CONTINUOUS PROCESSING OF UNIDIRECTIONAL PREPREG

by

Shridhar R. Iyer

A DISSERTATION

Submitted to
Michigan State University
in partial fulfillment of the requirements
for the degree of

DOCTOR OF PHILOSOPHY

Department of Chemical Engineering
1990

ABSTRACT

CONTINUOUS PROCESSING OF UNIDIRECTIONAL PREPREG

By

Shridhar R. Iyer

The use of thermoplastic composites has been limited by the lack of reliable techniques to make prepreg tapes of consistent quality. The intractability of thermoplastic matrices leads to problems such as the manufacture of stiff and boardy tape, solution or carrier devolatilization leading to the formation of voids with its attendant loss in mechanical properties and high resin content. Dry powder impregnation methods offer a clean inexpensive solution to this problem. The objectives of this investigation were to explore the viability of dry powder processes and to study the fundamental physical phenomena associated with the manufacture of powder-impregnated thermoplastic composites.

A novel powder prepregging process suitable for the manufacture of high quality powder-impregnated tapes was successfully developed as a result of this investigation. The important components of the process are an acoustic spreader to spread narrow fiber tows to expose individual filaments, an acoustic aerosolizer which delivers a controlled concentration of fine particles to the spread fiber tow and a heater where the particles are sintered on the fibers. It is shown that the powder-prepregging process can achieve fine control over both fiber-matrix composition in the prepreg tape and intimate wetting between individual fibers and the thermoplastic

matrix. The coalescence of polymer particles on fibers is a sequential process which is comprised of heat transfer to the impregnated tow, interparticle sintering, formation of a polymer film and its subsequent retraction to form droplets on the fibers. The consolidation of powder-impregnated tapes under heat and pressure to form void-free parts is also discussed. Consolidation cycles are shown to be simple and require the use of temperatures above the softening or melting point of the polymer, and optimum pressure which depends on fiber volume fraction in the composite and a contact time that allows for intimate wetting between interfaces and interdiffusion of polymer chains across the interface.

ACKNOWLEDGEMENT

My sincere appreciation goes to Dr. L. T. Drzal for his guidance, support and encouragement throughout the duration of the project. It has been a pleasure to work with him and I have learned a great deal during my stay at Michigan State University.

I wish to thank all members of the "Composites Group" past and present - Raj Agrawal, Javad Kalantar, Tesh Rao, Craig Chmielewski, Jim Dounis, Brent Larson and many others for their assistance and friendship and for making my sojourn here a pleasant one. In addition, I wish to thank Mike Rich and Madhu Madhukar for their help in the project. My thanks are also due to Dr. K. Jayaraman for his technical assistance in the development of the process.

I wish to acknowledge the excellent fabrication skills of Tom Palazzolo, Jim Muns and Tom Hudson of the Physics Machine Shop; and Dan Shakespear and Frank Palazzolo for their role in the automation of the process.

I am grateful to the other members of my committee - Dr. J. V. Beck, Dr. B. W. Wilkinson, Dr. Selim Yalvac and Dr. J. L. Dye for many discussions and for the time that they dedicated to this dissertation.

I thank my parents for their continual support and encouragement throughout my educational career.

Finally, I thank my wife Rupa for her love and support in enabling me to complete this work and for enduring my long irregular work hours over the years.

Table of Contents

1. **Introduction** 1
2. **Background** 7
   - 2.1 Slurry Processing 7
   - 2.2 Solution Processing 8
   - 2.3 Melt Impregnation 10
   - 2.4 Film Stacking 10
   - 2.5 Fiber Co-mingling 11
   - 2.6 Dry Powder Impregnation 11
   - 2.7 Process Design 15
3. **Theory** 18
   - 3.1 Tape Manufacture 18
     - 3.1.1 *Spreading* 20
     - 3.1.2 *Impregnation* 20
     - 3.1.3 *Coalescence* 25
   - 3.2 Consolidation 39
4. **Proposed Process** 44
   - 4.1 Fiber Motion 45
   - 4.2 Aerosolizer 45
   - 4.3 Spreader 54
   - 4.4 Heater 58
   - 4.5 Process Description 58
   - 4.6 Automation 60
     - 4.6.1 *Fiber Motion* 60
     - 4.6.2 *Oven Temperature* 64
     - 4.6.3 *Data Acquisition* 66
   - 4.7 Ancillary Equipment 66
5. **Material Characterization** 69
   - 5.1 Particle Size Analysis 71
   - 5.2 Differential Scanning Calorimetry 74
   - 5.3 Viscosity 84
   - 5.4 Summary of Properties 89
6. **Tape Manufacture** 90
   - 6.1 Fluidized Bed Behavior of Cohesive Powders 90
     - 6.1.1 *Experimental* 91
     - 6.1.2 *Fluidized Bed Behavior* 95
   - 6.2 Pulsed Gas Flow 109

6.3 Aerosolization 111
6.3.1 *Determination of Natural Frequency* 111
6.3.2 *Aerosolizer Behavior at the Natural Frequency* 115
6.3.3 *Future Improvements* 119
6.3.4 *Discussion - Aerosolizer Performance* 120
6.4 Spreading 121
6.4.1 *Discussion - Spreader Performance* 124
6.5 Coalescence 124
6.5.1 *Heat Transfer* 128
6.5.2 *Interparticle Sintering and Coalescence* 132
6.5.3 *Droplet Formation* 133
6.5.4 *Spreading of Polymer Droplets on Fibers* 140
6.5.5 *Discussion of Coalescence Phenomena* 141
6.6 Process 143
6.6.1 *Discussion - Process Performance* 151
7. **Consolidation** 154
7.1 Experimental 154
7.2 Optimum Cycles for Void-Free Consolidation 158
7.3 Intimate Contact and Autohesion 164
7.4 Crystallinity 165
7.5 Fracture Toughness and Failure Mode 166
7.6 Discussion of Consolidation Experiments 171
8. **Unified Approach** 173
8.1 Fiber Motion 173
8.2 Spreader 173
8.3 Aerosolizer 174
8.4 Heater 174
9. **Conclusions And Future Work** 176
Appendix A : Engineering Drawings 182
Appendix B : Automation 203
Appendix C : Contact Angle Program 237
Bibliography 244

LIST OF FIGURES

Figure 1. Slurry processing [8].

Figure 2. Melt impregnation process [18].

Figure 3. Electrostatic fluidized bed process [18].

Figure 4. Recirculating powder deposition chamber.

Figure 5. Design of powder prepregging process.

Figure 6. Flowchart for the manufacture of thermoplastic composites.

Figure 7. Coalescence in the heater.

Figure 8. Heat transfer to the impregnated tow.

Figure 9. Sintering between adjacent equal-sized spherical particles (initial radius = a).

Figure 10. Spreading of a liquid on a planar surface.

Figure 11. Unduloidal droplet on a cylindrical fiber.

Figure 12. Non-symmetric perturbation of an axisymmetric droplet.

Figure 13. Transition from axisymmetry to non-symmetry for a droplet on a cylindrical fiber.

Figure 14. Consolidation of powder-impregnated tapes.

Figure 15. Fiber motion in the powder prepregging process.

Figure 16. Aerosolizer.

Figure 17. Momentum balance inside the aerosolizer.

Figure 18. Spreader.

Figure 19. Fiber spreading operation.

Figure 20. Schematic of powder prepregging process.

Figure 21. Data acquisition and control of powder prepregging process.

Figure 22. Temperature control of oven.

Figure 23. Hot stage for coalescence experiments.

Figure 24. Consolidation mold.

Figure 25. Experimental investigation.

Figure 26. Plot of length vs breadth for each particle.

Figure 27. SEM photograph of polyamide particles.

Figure 28. Particle size distribution of Orgasol 2001 Ex D Nat.

Figure 29. DSC thermogram of as-received polyamide.

Figure 30. Estimation of relative crystallinity of polyamide.
Figure 31. DSC thermogram of polyamide quenched in liquid nitrogen.
Figure 32. Viscosity-temperature plot of polyamide at a shear rate of 0.1 sec^{-1}.
Figure 33. Distributor pressure drop as a function of gas velocity.
Figure 34. Particle size distributions of the fine, medium and coarse powders.
Figure 35. Bed pressure drop vs velocity, fine powder.
Figure 36. Bed pressure drop vs time, fine powder.
Figure 37. Fluidized bed profiles.
Figure 38. Bed pressure drop vs velocity, medium powder.
Figure 39. Bed pressure drop vs time, medium powder.
Figure 40. Bed height vs velocity, medium and coarse powders.
Figure 41. Bed pressure drop vs velocity, coarse powder.
Figure 42. Bed pressure drop vs time, coarse powder.
Figure 43. Effect of gas pulsing.
Figure 44. Experimental scheme to determine natural frequency of aerosolizer.
Figure 45. Weight of particles collected in filter vs frequency.
Figure 46. Sound pressure level vs time, two hour experiment.
Figure 47. SPL and particle concentration vs time.
Figure 48. SEM photographs of coalescence in the heater - (a) and (b) show heat transfer to the impregnated tow, the particles initially adhering to the fiber surface. (c) shows interparticle sintering and coalescence into a film, droplet formation. (d) shows the formation of droplets and (e) the formation of axisymmetric thermodynamically droplets at long times.
Figure 49. Cross section of prepreg tapes of different widths. Bar at bottom right represents 50 microns.
Figure 50. SEM photograph of a polyamide particle showing the presence of nodules.
Figure 51. Plot of K vs L for the polyamide droplets on carbon fibers. The solid line is the prediction by the model [45] for $\theta = 23°$.
Figure 52. Residual error for different contact angles.
Figure 53. Histogram of droplet sizes.
Figure 54. Axisymmetric droplets on a fiber at equilibrium, $S < S_c$.
Figure 55. SEM photographs of prepreg tapes. (a) 90.9% V_f, (b) 77.5% V_f, (c)70.2% V_f, and (d) 33.2% V_f.
Figure 56. Prepreg tapes of different widths. Bar at bottom right represents 1 cm.
Figure 57. Turning angles, fiber tow over spreader.
Figure 58. Consolidation cycle, specimen 2.
Figure 59. ENF test, loading pins and specimen geometry.
Figure 60. Operating curve for optimum consolidation of polyamide-AS4 composites.
Figure 61. Optical micrographs of polyamide-AS4 composites. (a) Specimen 3, and (b) specimen 7.
Figure 62. Mode II fracture energy vs fiber volume fraction, polyamide-AS4.
Figure 63. SEM photographs of fractured specimens. (a) and (b) specimen 15, (c) and (d) specimen 9.
Figure 64. Mode II fracture energy vs void fraction, $V_f = 70\%$.

LIST OF TABLES

Table I. High performance polymers.
Table II. Behavior of cohesive powders.
Table III. Definitions of mean diameters.
Table IV. Specific heats of polyamide.
Table V. Crystallinity of polyamide.
Table VI. Material properties.
Table VII. Properties of powders.
Table VIII. Sound pressure.
Table IX. Spreading experiments - constant amplitude, varying frequency.
Table X. Spreading experiments - constant frequency, varying amplitude.
Table XI. Coalescence experiments.
Table XII. Calculated heating times for clusters of different sizes.
Table XIII. Predictions of sintering times for selected thermoplastics.
Table XIV. Prepregging experiments - identical conditions.
Table XV. Prepregging experiments - different conditions.
Table XVI. Prepreg tape widths.
Table XVII. Consolidation and ONVFA experiments.
Table XVIII. Unified approach - powder prepregging process.

Chapter 1

INTRODUCTION

A composite material can be defined as a material system consisting of two or more physically distinct and mechanically separable components one of which has distinctly superior properties. The dispersion of the different components in a composite material can usually be controlled to achieve optimum properties, which in many cases, are superior to that of the individual components [1]. Composite materials may be broadly classified as fibrous composites (which consist of fibers in a matrix), laminated composites (which consist of layers of various materials) and particulate composites (which consist of particles in a matrix). The discussion in this investigation will be restricted to fibrous composites, specifically to the manufacture of unidirectional prepreg tapes and their subsequent consolidation to form void-free composite parts.

Unidirectional prepreg tapes are precursors of composites composed of fibers aligned in one direction and embedded in an unconsolidated polymer matrix. The fibers themselves can be of various types, the most prominent among them being glass, carbon and Kevlar fibers. Fiber diameters usually vary from 5 to 15 microns, e.g., Magnamite AS4 Graphite fibers made by Hercules have a diameter of 8 microns. All polymers are potential candidates for matrix materials but limitations such as processability and desired end use properties dictate the final choice. Polymer matrices can be either thermoset or thermoplastic in nature.

The finished composite part is formed by consolidating unidirectional prepreg tapes which have been stacked in a predetermined sequence of orientations, e.g., 0°, 45°, 90° as specified by the end application. The physical phenomena which occur during consolidation are different for thermoset and thermoplastic materials. Thermosets undergo a chemical reaction with curing during consolidation to their final crosslinked form. Curing is the process of polymerization of the resin to form a crosslinked network between fibers in the composite part. Curing is accomplished by the application of heat and/or pressure during processes such as vacuum bagging, autoclave molding, hot press molding etc. Thermoplastic matrices are usually in their final polymerized form and the consolidation step primarily ensures that the polymer interfaces within and between adjacent prepreg tapes fuse into each other to form a homogeneous part. If a solvent or liquid carrier is used in the prepregging step, then devolatilization is carried out prior to actual consolidation to prevent volatiles from being trapped within the composite part.

Thermoset matrices such as epoxy resins are widely used in the composites industry. Their advantages include low shrinkage, excellent adhesion, good chemical resistance and easy processability [1]. Prepreg tapes are made by pulling a fiber tow (fiber bundle wound on a spool, available commercially in numbers ranging from 30 fibers/tow to 250,000 fibers/tow) through a heated pot containing liquid matrix and then through a die. The fibers are individually coated with the matrix and aligned in one direction. This process is called hot melt impregnation. Since the resin is partially cured during the impregnation step, the tape is said to be B-staged. Thermoset tapes have a limited shelf life and are stored at low temperatures to prevent unwanted additional curing. Among the drawbacks of these resins are the tendency to degrade at high temperatures (usually above 175°C), low resin strength and fracture toughness and a high degree of brittleness.

Thermoplastic matrices offer many advantages [2,3] over thermosetting resins. These include short molding cycle time, infinite shelf life of prepreg, capability of fusion bonding, recyclability and repairability, reduced storage and handling problems, increased moisture resistance and better fracture toughness. However, their use has been limited by the lack of good processing techniques to make flexible prepreg tapes. The general intractability of these matrices due to their high viscosity gives rise to a host of problems such as the manufacture of stiff and boardy tape, solution devolatilization leading to the formation of voids with its attendant loss in mechanical properties and prepreg tapes with high resin content.

The desire for improved properties of matrix materials led to the quest for polymers with improved toughness and strain capability along with good chemical resistance, stiffness, strength and the ability to withstand high temperatures. Many high temperature resins (a high temperature resin has the ability to retain its mechanical properties for thousands of hours at 232°C, hundreds of hours at 316°C, and/or minutes at 538°C [4]) were developed. Most of these failed to be incorporated into composite materials for advanced structural applications primarily due to their poor processability. Hergenrother and Johnston [4] proposed the following requirements for an ideal high temperature polymeric system to be used as a composite matrix : easy prepreg preparation, good shelf life, acceptable tack (stickiness) and drape (shape relaxation), acceptable quality control procedures, low processing temperature and pressure, no volatile evolution, dense void-free matrix, good mechanical performance over the desired temperature range, time, and environmental conditions, acceptable repairability and cost-effectiveness. No available matrix conforms to all these properties and hence the choice of a matrix usually represents a compromise.

High temperature polymers have highly stable structural units in the polymer chain such as aromatic rings and/or heterocyclic rings [5]. These units absorb thermal energy and contain a minimum number of oxidizable hydrogen atoms, thus lending thermo-oxidative stability to the resin matrix. Also, they degrade at a very slow rate at elevated temperatures into thermally stable residues which retain structural integrity. The structural units, which lend thermal stability to the matrix also serve to make processing of these polymers, most of which are thermoplastic, extremely difficult. They are not easily soluble and they melt or soften at very high temperatures. Their viscosities are very high, usually of the order of 1000 to 10,000 Pa.s. Table I lists the properties of some popular high temperature polymers which are being investigated for advanced structural applications.

The primary objective of this investigation was to explore the possibility of developing a viable technique to prepreg reinforcing fibers with thermoplastic matrices to form flexible prepreg tapes. The basic premise can be summarized as follows :

If polymers can be synthesized and/or pulverized to sufficiently fine powders (of the order of 1-20 microns) and suspended in a fluidizing medium inside a chamber, then fiber tows can be passed through this chamber so that the fine polymer particles would impact and adhere to the fibers. This impregnated fiber tow can be subsequently heated to sinter the particles without consolidation and thereby form flexible prepreg tapes.

Such a process would be solvent-free and offer complete control over the final configuration of the prepreg tapes, i.e., fiber-matrix volume fractions, prepreg tape width and hence flexibility. The secondary objective was to couple this process with a fundamental investigation into the different aspects of powder adhesion, coalescence and the consolidation of the prepreg tapes to form void- free parts.

TABLE I. HIGH PERFORMANCE POLYMERS [6]

Polymer/Source	Type of Polymer†	T_g (T_m), °C	Processing T, °C
Polyetherether Ketone (PEEK) ICI	SCT	143 (343)	360-400
Polyether Ketone (PEK) BASF	SCT	165 (365)	400-450
Poly (EKEKK) BASF	SCT	173 (370)	420-450
Polyimide (LaRC-TPI) Mitsui Toatsui	APT	250 (325)	350
Polyether Sulfone (HTA) ICI	AT	260	400-450
Polyetherimide (Ultem) GE	AT	21	350-400
Polyetherimide (P-IP) Mitsui Toatsui	SCT	270 (380)	380-420
Polyimide (PMR-15) Hysol	ATS	320	315
Polyimide 2080 Lensing	APT	280	350
Polyimide (Matramide 9725) Ciba-Geigy	APT	265	350

† AT : Amorphous Thermoplastic
APT : Amorphous Pseudothermoplastic
SCT : Semi-crystalline Thermoplastic
ATS : Amorphous Thermoset
T_g : Glass transition temperature
T_m : Melting temperature

The chapters in this thesis are arranged as follows :

(1) Chapter 2 reviews existing techniques for the manufacture of thermoplastic composites and provides the rationale for the development of a new dry powder process from fundamental principles.

(2) Chapter 3 discusses the different unit operations which are integral to a dry powder prepregging process as well as the theory underlying prepreg tape consolidation into a composite part.

(3) Chapter 4 discusses the configuration and operation of the components of the proposed process.

(4) Chapter 5, 6 and 7 describe the experimental and theoretical investigation into the manufacture of void-free thermoplastic composite parts from its precursor materials, namely thermoplastic powders and reinforcing fibers using this process. Chapter 5 describes the characterization of the properties of the fiber and the matrix, chapter 6 discusses tape manufacture and chapter 7 describes the consolidation of these tapes to form composite parts.

(5) Chapter 8 is attempts to provide guidelines for the manufacture of thermoplastic composites from any fiber-matrix precursor.

(5) Chapter 9 enumerates the conclusions that can be drawn as a result of this investigation and makes suggestions for future work.

The appendices include engineering drawings of the different equipment, the electrical diagrams and the computer program implemented for the automation of the process, and a finite difference program used to calculate contact angles from drop dimensions on fibers.

Chapter 2

BACKGROUND

Different methods have been employed in the past to make thermoplastic pre-impregnated tapes. This chapter enumerates and discusses the salient features of each of these methods and develops the reasoning for the choice of dry powder impregnation as a technique ideally suited for the manufacture of flexible prepreg tapes.

2.1 Slurry Processing :

In this technique, the polymer powder is suspended in a liquid carrier and this slurry is used to infiltrate the fiber tow. The process is shown in Figure 1. The fiber tow/tows are passed through a roving guide and past a spray nozzle (which sprays a gas such as air) optionally used to spread the fibers to a limited extent. It passes through the impregnation tank containing the polymer in suspension and fitted with several impregnation pins. The impregnated tow is dried in a drying chamber and then passes through a preheater and die before being wound on a takeup spool.

Taylor [7] outlined a slurry process whereby the particles are suspended in water thickened with a material such as polyethylene oxide to increase the viscosity to 40-300 Pa.s at 25°C, e.g., 0.5 weight % polyethylene oxide and 0.5 weight % hydroxyethyl cellulose are mixed in water for 15 hours to produce an aqueous solution with a viscosity of 0.4 Pa.s at 25°C. 162 g of polysulfone powder less than 177 microns in size is added to 800 g of solution and a carbon fiber cloth

impregnated with this solution. The cloth is then dried at 100°C and heated to 350°C to fuse the polysulfone around the fibers. O'Connor [8], in a very thorough discussion in a patent, pointed out potential problems which include finding the right concentration of slurry, maintaining the optimum concentration in the resin tank and accumulation of excess resin at the die entrance (where the impregnated tow is consolidated into a tape or flat sheet). The minimum void content in the slurry-processed tapes were about 2-4%. Dyksterhouse et al. [9] impregnated fibers in an impregnation bath filled with a polymer binder in which the polymer particles are uniformly suspended. The gelled binder has plastic flow characteristics and shear-thinning behavior. As an example, a PEEK-carbon fiber composite was made by impregnating G30-500 carbon fibers in a gelled impregnation bath having a viscosity of 81 Pa.s. In addition to the problems pointed out by O'Connor [8], slurry processes require a time-consuming drying step prior to consolidation to ensure that there is no remaining liquid that can lead to voids in the final composite. Also, the consolidation step has to ensure that fibers are completely wetted by polymer.

2.2 Solution Processing :

Thermoplastic particles are dissolved in a solvent and the fiber tow is impregnated with the resulting low viscosity solution [10]. The solvent must be completely removed to eliminate void generation during composite consolidation. Methylene chloride and N-methyl pyrrolidone are widely used as solvents but complete removal of solvent after impregnation is often a difficult time- consuming step. Turton et al. [10] dried the prepreg tapes (carbon fibers impregnated with poly (phenyleneoxy) polyphenylenesulfonyl) for 16 hours at 120°C to remove methylene chloride before consolidating them into a part. Polysulfone, polyphenyl sulfone and polyether sulfone are some of the thermoplastics which have been solution-impregnated. A major limitation is that some polymers are not soluble in solvents

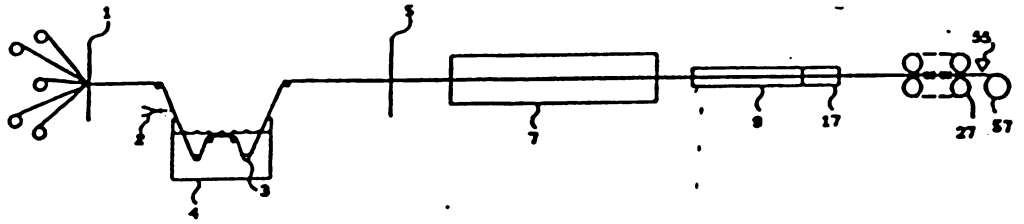

Figure 1. Slurry processing [8].

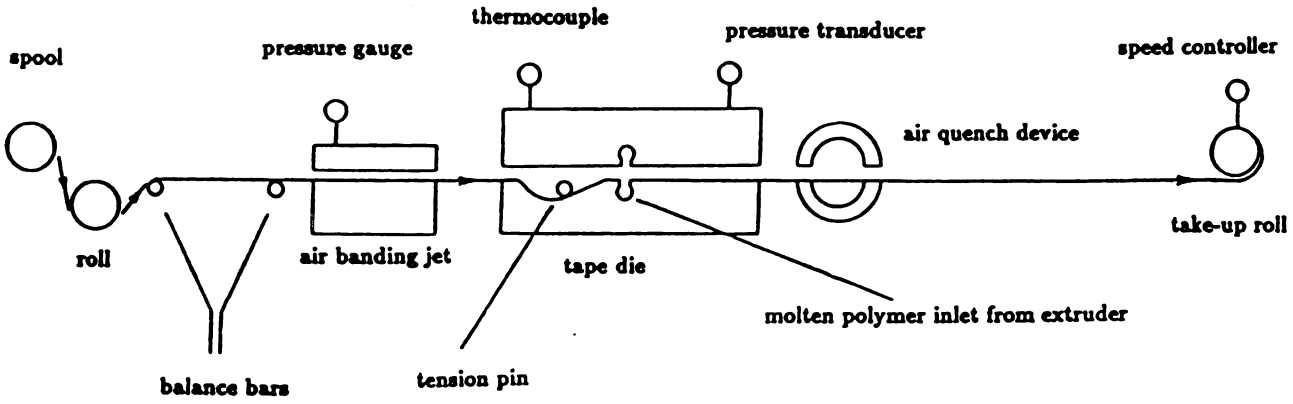

Figure 2. Melt impregnation process [18].

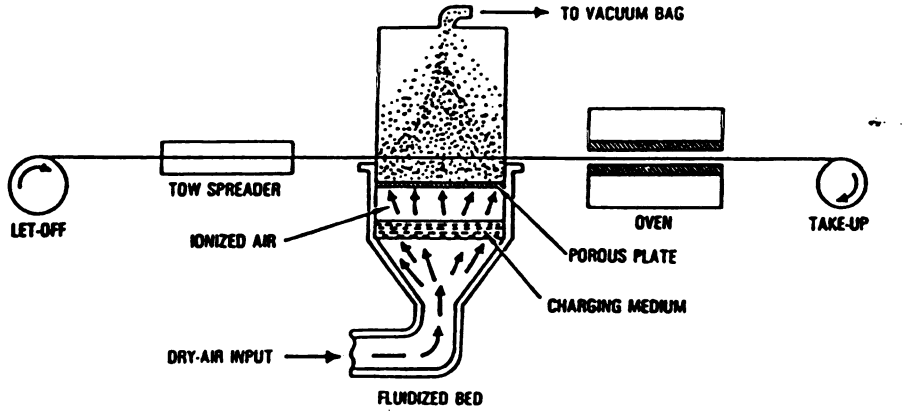

Figure 3. Electrostatic fluidized bed process [18].

but the solubility of those polymers used in the process also indicates that they will be prone to solvent attack. The use of toxic corrosive solvents such as methylene chloride which have to be recovered and recycled is another factor which detracts from its appeal.

2.3 Melt Impregnation :

In this method, prepreg tapes are produced by the impregnation of fiber tows with molten polymer. A sketch of this technique is shown in Figure 2. Two approaches have been used to accomplish this - (a) A crosshead extruder feeds molten polymer into a die through which the rovings pass [11], and, (b) the fibers pass through a molten resin bath fitted with impregnation pins to increase the permeability of the polymer into the tow. The impregnation pins can be heated to decrease viscosity locally to further improve the impregnation process [12]. In either case, the forces exerted on the fibers e.g. from the die pressure for the crosshead extruder are extremely high and may cause fiber damage. Chung [13] estimates die pressures in excess of 1450 psi are required for a Newtonian fluid with a viscosity of 10 Poise. The resulting prepreg usually lacks tack (stickiness or the ability of the prepreg tapes to retain their position after they have been laid up for consolidation) and drape (flexibility). The tapes have to be spot welded in position before consolidation.

2.4 Film Stacking :

Film stacking is a process where layers of fiber reinforcement either in the form of unidirectional tows or woven fabrics are stacked with thermoplastic sheets and consolidated under pressure for long times. Lind et al. [14] made a 50% fiber volume fraction composite by interleaving 60 micron thick polycarbonate film with unidirectional carbon fibers. Film stacking is widely used with low viscosity matrix

materials due to the relative ease of manufacture. Disadvantages include high resin content, the uneconomic (labor- intensive) nature of the process and difficulty in impregnating the fiber tow (high pressure forces the fibers together) with high viscosity matrix material.

2.5 Fiber Co-mingling :

In the fiber co-mingling process, thermoplastic matrix is spun into a fine yarn and co-mingled with the reinforcing fiber tow to produce a co-mingled hybrid yarn [15]. These hybrid yarns can be consolidated to form composite parts. An advantage of this technique is the drapeability of the hybrid yarn while the high cost involved in producing thermoplastic yarn and weaving it with the reinforcing fibers is an obvious disadvantage. Clemans et al. [15] spun thermoplastic yarn from high temperature polymers such as PEEK and PPS and comingled them with carbon fibers to produce hybrid yarn with fiber volume fractions of upto 61%. A consolidation step is needed to ensure that the thermoplastic fibers melt and wet the reinforcing fibers intimately to ensure good adhesion between the two components.

2.6 Dry Powder Impregnation :

Dry thermoplastic powder can be used to produce a prepreg. The powder is introduced into a fiber tow which is processed by heating to sinter the powder particles onto the fibers. This technique was first employed by Price [16] who passed glass roving through a bed (either fluidized or loosely packed) of thermoplastic powder. Polypropylene particles with an average diameter of 250 microns were used. The particles stick to the fibers due to natural electrostatic attraction. The tow is then heated and passed through a die to produce an impregnated tow. The impregnation is macroscopic, i.e. the particles coat clusters of fibers rather than individual fibers. Thus, the process is targetted mainly at producing short-fiber reinforced

thermoplastics. Ganga [17], fluidized polyamide particles less than 20 microns in size in a fluidization chamber, impregnated glass rovings and then covered this with an outer sheath of a second material of lower melting point than the impregnated particles. The second sheath is extruded onto the tow. The process offers little or no control over fiber-matrix volume fractions during the impregnation step. The possibility of motion of particles within the sheath during handling leads to higher standard deviations in particle pickup than intended by the manufacturer.

Muzzy et al. [18] demonstrated the ability to manufacture powder prepreg by passing a spread tow through an electrostatic fluidized bed of PEEK powder (50 microns average particle size). The process is shown in Figure 3. The fiber tow passes through a spreader and then through an electrostatic fluidized bed of polymer particles around 10-250 microns in size. The electrostatic fluidized bed is based on the principle of conventional fluidization except for one difference - it has charging electrodes located under the distributor to charge the fluidizing gas which in turn charges the particles. It has been primarily used for powders with average particle sizes greater than 30 microns. In this size range, fluidization can be accomplished by conventional means. The imposed electrostatics ensures that the particles adhere to the fibers and is necessary due to the large particle sizes used in the process i.e. the particles do not inherently have sufficient charge in them to be attracted to the fiber surface. An electrostatic fluidized bed has to solve the problem of agglomeration and channeling faced by conventional techniques before it is applied successfully to the fluidization of lower particle sizes. The impregnated tow then passes through a heater where the particles are sintered on the fibers. The residence time in the oven is directly proportional to the flexibility of the prepreg. This is because of capillarity between fibers which causes the polymer to bond adjacent fibers together and hence reduce flexibility. Muzzy et al. used temperatures in excess of 600°C (PEEK has a melting point of 343°C) in the heater for short times to sinter the particles and ensure

flexibility. The possibility of thermal degradation of the matrix increases at temperatures so far above the melting point.

Allen et al. [19] impregnated the fibers in a recirculating powder deposition chamber with annular walls to aid in powder recovery. The recirculating powder deposition chamber is a unit which merits more serious consideration in the particle sizes of interest used in this investigation. The chamber is shown in Figure 4 and includes powder recovery in its basic design. It consists of a screw feed which drops particles from the top of the chamber. This "shower" of particles impacts the fibers and falls down to the base where an exhaust fan recirculates the powder through a tube to the top of the chamber. Baffles at the sidewalls with a slight vacuum in between trap any particles that escape from the tow entry and exit slots and recirculate them through gaps at the base into the chamber. The humidity of the environment, material balances in the chamber to decide feed rates, pressure drop in the recirculating tubes to prevent clogging and the cohesive nature of fine powders all serve to make this a complex operation which works satisfactorily if conditions are at their optimum. The particle concentration in the chamber is in excess of 10,000 mg/m^3 and good control over this variable is difficult. The response time of this system to instabilities is of the order of minutes after a change is implemented. Baucom et al. [20] used the process to impregnate carbon fibers with PEEK and LaRC-TPI particles 7-19 microns in size. A resin control monitor which measures weight fraction matrix in the prepreg tape is mounted before the takeup drum. This measurement is used in a feedback loop to control the speed of the takeup drum to account for instabilities in the powder deposition chamber and ensure consistent particle pickup by the fiber tow. Standard deviations of around 4 weight % fiber are reported within each prepregging run. The powder processes by both Muzzy et al. [18] and Allen et al. [19] were developed concurrently with this investigation.

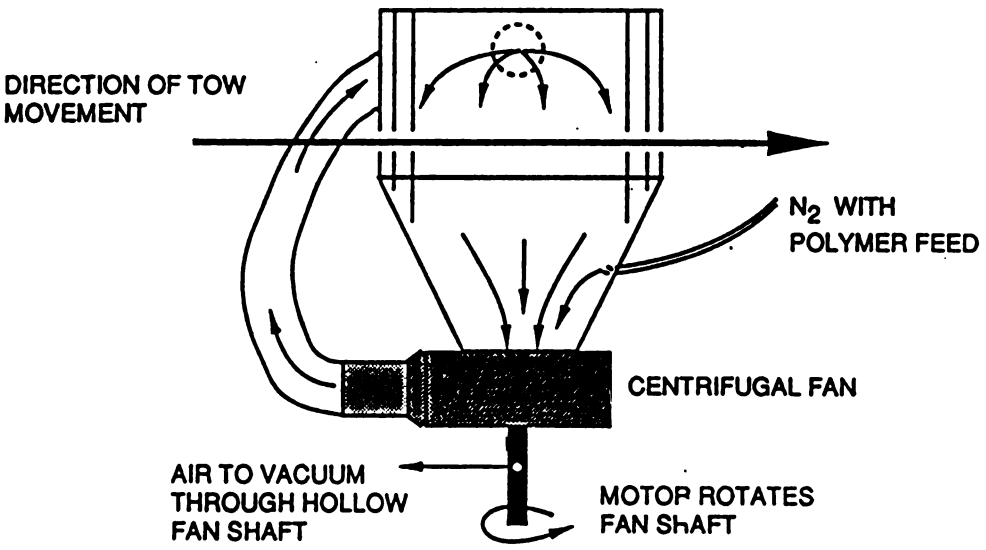

Figure 4. Recirculating powder deposition chamber.

2.7 Process Design :

The above review of the different thermoplastic processing techniques leads to the conclusion that dry powder processes offer several advantages for the manufacture of thermoplastic prepreg tapes. An ideal dry powder process would have the following advantages over other processes :

(i) It would be independent of matrix viscosity. Most high performance thermoplastic matrices are highly viscous (10^4 to 10^5 Poise) above their softening point (amorphous) or melting temperature (semi-crystalline). A good dry powder process would circumvent this problem by coating fibers individually with fine particles so that flow occurs over very short distances of the order of microns instead of millimeters as in a process such as melt impregnation.

(ii) It would avoid the use of solvents or water which have to be removed during the latter stages of the processing cycle. Incomplete removal may produce voids which have a deleterious effect on the mechanical properties of the composite. Binders must also be avoided since they can alter the matrix or fiber-matrix adhesive properties.

(iii) It would avoid introducing any secondary material processing operations such as fiber spinning which may increase the cost of the final product.

(iv) It would yield prepreg tapes that are completely wetted by the polymer and are almost as flexible as unimpregnated fiber tows.

These advantages can be realized through the design of a dry powder process which possesses the following features :

(i) The average particle size of the material used should be approximately of the order of the dimensions of the fiber for optimum impregnation. Impregnation of individual fibers becomes more difficult with larger particle size resulting in an uneven coating and/or a resin-rich composite. The level of precise control over fiber-matrix volume fractions that can be achieved decreases with increasing particle

size. Polymer flow has to occur over larger distances on the fiber surface as particle size is increased.

(ii) The fiber tow should be spread out to a sufficient width so that each fiber in the tow is uniformly coated with particles.

(iii) The concentration of powder particles in the "impregnation chamber" where the particles meet the fibers should be constant and controllable at all times. This facilitates the manufacture of high quality prepreg tapes in a wide range of volume fractions.

(iv) The mechanism of adhering the particles to the fibers should be controllable and well-understood.

(v) The resulting prepreg tape should be flexible so that complex parts can be formed easily by consolidation.

As a result of this analysis, a powder prepregging process (Figure 5) which incorporates these components was designed in this thesis. The fiber tow is unwound from a fiber spool and passes through a device (spreader) which spreads the collimated fiber tow (or tows) to any desired width. A pretreatment tank may be used to modify the fiber surface to provide better adhesion with the thermoplastic matrix or to apply a binder on the fibers. The spread tow enters the impregnation chamber where it meets a controlled concentration of particles. At this position, the means of adhering the particles to the fibers is either electrostatic attraction or through the use of a binder on the fiber surface. The impregnated tow passes through a heater where the particles are "fixed" on the fiber surface with the help of thermal energy. The resulting flexible tape is then wound on a takeup drum.

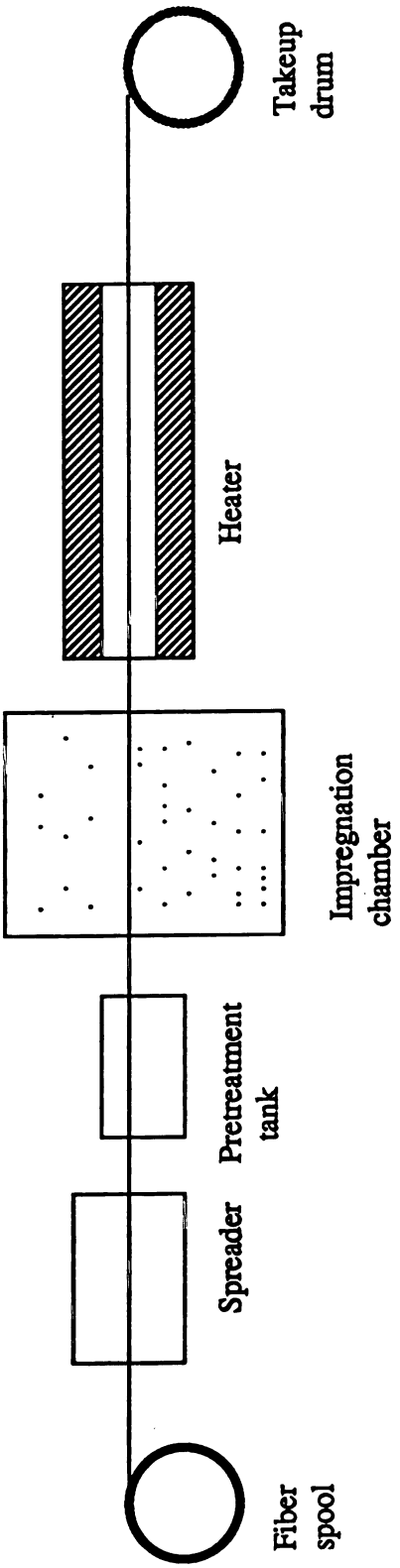

Figure 5. Design of powder prepregging process.

Chapter 3

THEORY

There has been no coherent investigation into the manufacture of thermoplastic composites using dry powder impregnation techniques. This investigation has been undertaken to elucidate the underlying physical principles governing the manufacture of a composite part from its precursor materials, namely thermoplastic powders and reinforcing fibers. The flowchart (Figure 6) lists the important components in the manufacturing process. The two basic steps are : (1) tape manufacture which involves the spreading of the fiber tow, the impregnation of the spread tow with thermoplastic particles and particle coalescence on the fibers to form a flexible prepreg tape, and (2) consolidation which involves the layup of prepreg tapes in a mold followed by the application of heat and pressure to form void-free composites.

3.1 Tape Manufacture :

Tape manufacture by powder prepregging processes involves the following steps : (1) spreading of the fiber tow so that individual fibers are exposed, (2) impregnation of the spread fiber tow by a controlled concentration of fine particles, and (3) coalescence of the particles on the fibers to form a prepreg tape.

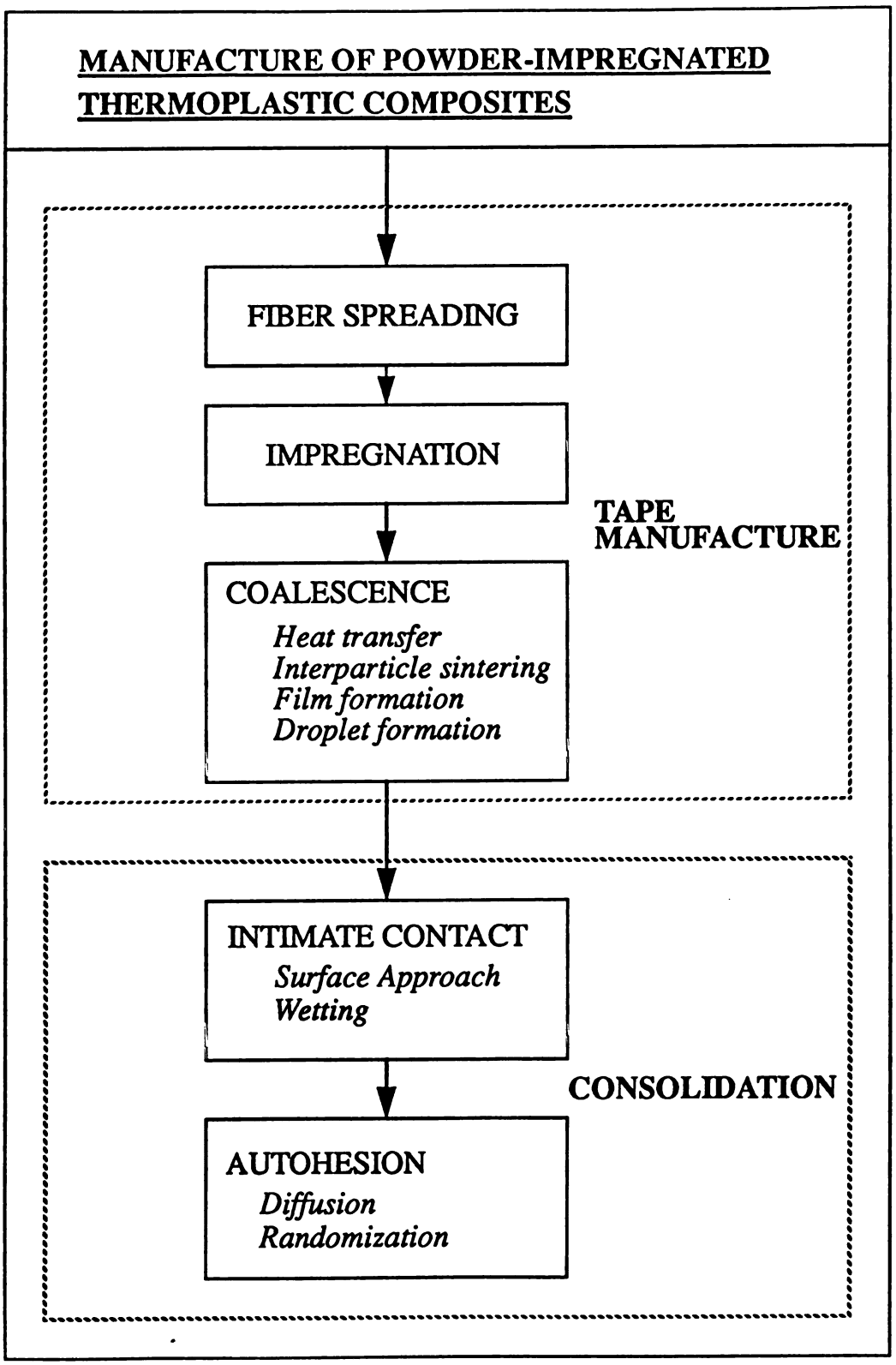

Figure 6. Flowchart for the manufacture of thermoplastic composites.

3.1.1 *Spreading* :

The function of the spreader is to ensure that the fiber tow is spread to a width large enough to expose individual fibers so that powder impregnation occurs throughout the fiber tow. The principle of operation of most spreaders is to use a jet of air directed at the fibers which forces them to spread apart due to the resulting drag. Baucom and Marchello [20] describe a typical spreader in which the tow of fibers enters at the throat of a flat expansion region. Air is drawn in from the tow exit slot and flows out into a vacuum manifold through holes in the side walls of the chamber. The tow spread angle is a function of the tow tension and the pressure drop between the chamber and the surrounding medium. A maximum width of only 1.87 cm was achieved for a 3000 fiber tow (8 microns/fiber, a tow spread to expose monofilaments is 2.4 cm wide). Problems with directed air methods include the drawing of loose fibers through the holes along the side walls, fiber breakage during sudden system shutdown and the narrow spreading width that can be attained by such a system without damage to the fibers.

3.1.2 *Impregnation* :

The impregnation chamber should be designed such that it delivers a controlled concentration of particles to the fibers at all times. This is essential in order to manufacture prepreg tapes of any desired fiber/matrix volume fraction with a minimum standard deviation. The degree of control that can be achieved over the impregnation process increases with decreasing particle size as discussed in Section 2.7 in the previous chapter.

Interparticle forces which act between adjacent particles are significant for fine powders less than 30 microns in size. Van der Waal's forces act over a distance of 100 Angstroms and interparticle distances in a packed bed at the point of contact are of the order of 5 Angstroms [21]. Powder particles also tend to acquire charge by

frictional or sliding contact through a process known as contact electrification or triboelectrification [22]. The work function or the minimum energy required to remove an electron from the surface of a particle to infinity increases with decreasing particle size. Hence fine particles tend to charge negatively. If there is a broad particle size distribution, there may be a change in particle charge with decreasing particle size. Polymer particles also tend to charge easily and retain a charge for long times because they have high values of electrical resistivity and low electrical permittivity. Charge pickup by particles increases with decreasing particle size due to the increased surface-to-volume ratio. All of these effects combine to make fluidization of fine powders a complex phenomenon.

A fundamental understanding of particle impregnation requires the measurement of particle charge and interparticle cohesive forces to characterize the behavior of the powder both in the chamber and its interaction with the reinforcing fibers. Masui et al. [23] outline a technique to measure powder charge. A suction-type Faraday cage is used with an electrometer to measure the charge-to- mass ratio for any powder. Interparticle cohesive forces can be gaged by measuring characteristic angles such as the angle of repose and tilting angle [24]. A simpler way is to measure the Hausner ratio [25] which is the ratio of the loosely packed (or aerated) density to tapped density of a powder (ρ_{bv}/ρ_{blp}). This ratio increases as interparticle forces become larger because such forces prevent particles from flowing smoothly thereby resulting in a more open structure for a cohesive powder. An approximate rule of thumb is that the Hausner ratio is 1 for a powder with negligible interparticle forces and greater than 1.5 for highly cohesive powders.

External means of electrostatic enhancement of particle charge is usually not required for fine particles because the triboelectric effect is sufficiently large to cause strong adhesion of the particles to fiber surfaces on contact. Typically, the particles are carried to the fibers by the gas stream. Inertial forces make the particles impact

the fibers instead of following the gas streamlines around the fibers. Adhesion of particles to the fibers on impact is initially due to electrostatic charging but is followed by van der Waal's forces between the fibers and the particles which also contribute to the adhesion.

Inertial effects are significant for particles greater than 1 micron in size [26]. The collection efficiency of an isolated fiber, η_0 is a function of an inertia parameter ψ -

$$\psi = \frac{D_p^2 u \rho_p}{18 \mu D_f} \qquad [1]$$

The collection efficiency of a single fiber, η_e when other fibers are nearby is given by

$$\eta_e = \eta_0 \, [1 + \beta(1 - \varepsilon_f)] \qquad [2]$$

Here, ε_f is the void fraction of the fiber bed and the parameter β is between 5 and 20 when inertial effects predominate. Baucom and Marchello [20] derive a relationship for the particle pickup by a tow and show that the resin- to-tow weight ratio is directly proportional to the resin cloud density, the collision cross section and the average collection efficiency of each fiber and inversely proportional to the tow velocity. Their analysis ignores the fact that particles charge differently depending on their electrical resistivities and permittivities and the relative humidity of the surrounding medium. A transfer of charge to the particles by external means such as an electrostatic generator will enhance the particle collection efficiency.

An obvious method to convey the particles to the fibers is by fluidization and entrainment. In conventional fluidization, the particles start to fluidize at a gas velocity (minimum fluidization velocity) at which the buoyant force overcomes

gravitational forces caused by the weight of the powder. However, interparticle forces and tribocharging serve to make fluidization difficult for fine powders. Geldart [27] proposed that fine powders fall into 2 categories - Type A powders fluidize homogeneously at the minimum fluidization velocity and expand considerably before bubbling commences. Type C powders are extremely cohesive and difficult to fluidize and do not have a distinct minimum fluidization velocity. Geldart et al. [25,28] observed that the fluidization of Type C powders leads to the formation of cracks and channels in the fluidized bed. This results in bed expansion without the true formation of bubbles. Rietema [29] argued that the border between Type A and Type C powders depends on particle size, particle density, viscosity of the fluidizing gas and interparticle cohesive forces as characterized by a cohesion constant. Geldart et al. [30] included relative humidity of the fluidizing gas as an additional variable.

Dry et al. [31] extended the above classification to include a transitional group AC which is characterized by the absence of a distinct minimum fluidization velocity and the absence of a contraction of the bed when bubbles first pass through. Chaouki et al. [32] discovered that fine aerogel powders agglomerate to form clusters at superficial velocities greater than 4 cm/sec. These larger particles retain their integrity and fluidize homogeneously. They found that these powders form a subset of Type C. They proposed a new group, C', which includes particles which pack very loosely (extremely low bulk densities, 0.066 gm/cm^3 in their experiments) and form clusters. Properties of the bed can be predicted from the sizes of these agglomerated particles. A summary of major observations for the behavior of cohesive powders in fluidized beds of different diameters is given in Table II. The bed diameters ranged from 5 to 64 cm and only cursory analyses of bed behavior was presented in all these papers. This study attempted to gain some insight into the behavior of fine polymer powders during fluidization and thereby design an impregnation chamber where particle concentrations can be precisely controlled.

TABLE II. BEHAVIOR OF COHESIVE POWDERS

Investigators	Bed diameter (cm)	Observations
Geldart et al. [30]	15.2	No clear minimum fluidization velocity; cracking and channeling without sustained bubble formation; cohesiveness increases by decreasing particle size and or increasing relative humidity (Type C, Alumina, 5-12 μm)
Geldart et al. [28]	15.2	Few bubbles; cracks, sloping and vertical channels; decreasing particle size causes vertical channels to predominate (properties of Type C powders listed in Table 2).
Dry et al. [31]	5, 14, 64	No clear minimum fluidization velocity; anomalous fluidization, *i.e.* spread in pressure drop-velocity curves; bubbles present (Type AC, iron oxide/carbon mixtures, 12-30 μm).
Chaouki et al. [6]	5, 10	Fine particles agglomerate to form clusters at higher velocities and homogeneous fluidization results; at low velocities, channeling occurs (Type C', bulk density of 0.066 g/cm^3).

3.1.3 *Coalescence* :

The fiber tow enters the heater after the impregnation step. The sequence of events which occur in the heater (Figure 7) are : the heating up of fibers and the particles; interparticle sintering between adjacent particles until a film forms on the fiber surface; and, finally, the formation of a stable configuration of axisymmetric or non-symmetric droplets. Development of a process control model therefore requires consideration of heat transfer, sintering and film and droplet forming mechanisms.

3.1.3 (a) *Heat transfer* :

The temperature of the powder-impregnated fiber tow is raised by convection and radiation to a value greater than the melting or softening point of the polymer particles. The physical situation is shown in Figure 8. Individual impregnated fibers or clusters of impregnated fibers pass through the heater as a flat porous sheet. The first step in the development of the processing model is to establish upper and lower bounds for the time to reach a temperature at which subsequent events begin to occur. The Biot number measures the significance of internal (heat conduction within the solid) to external (heat convection to the surface of the solid) heat transfer resistances is given by

$$Bi = \frac{hL}{k_s} \qquad [3a]$$

where

h = heat transfer coefficient which includes contributions from convection and radiation

k_s = thermal conductivity of the solid

$L = V_s/S$ = volume of body/surface area.

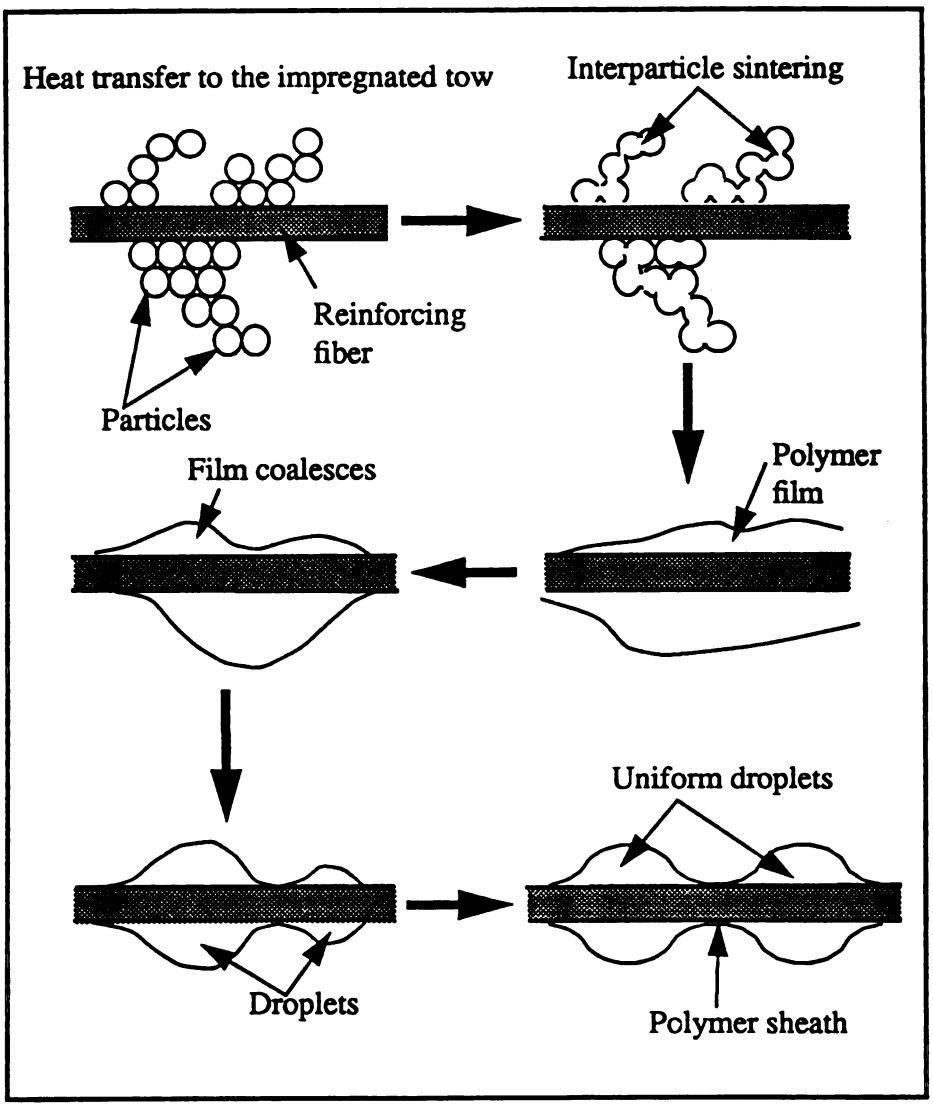

Figure 7. Coalescence in the heater.

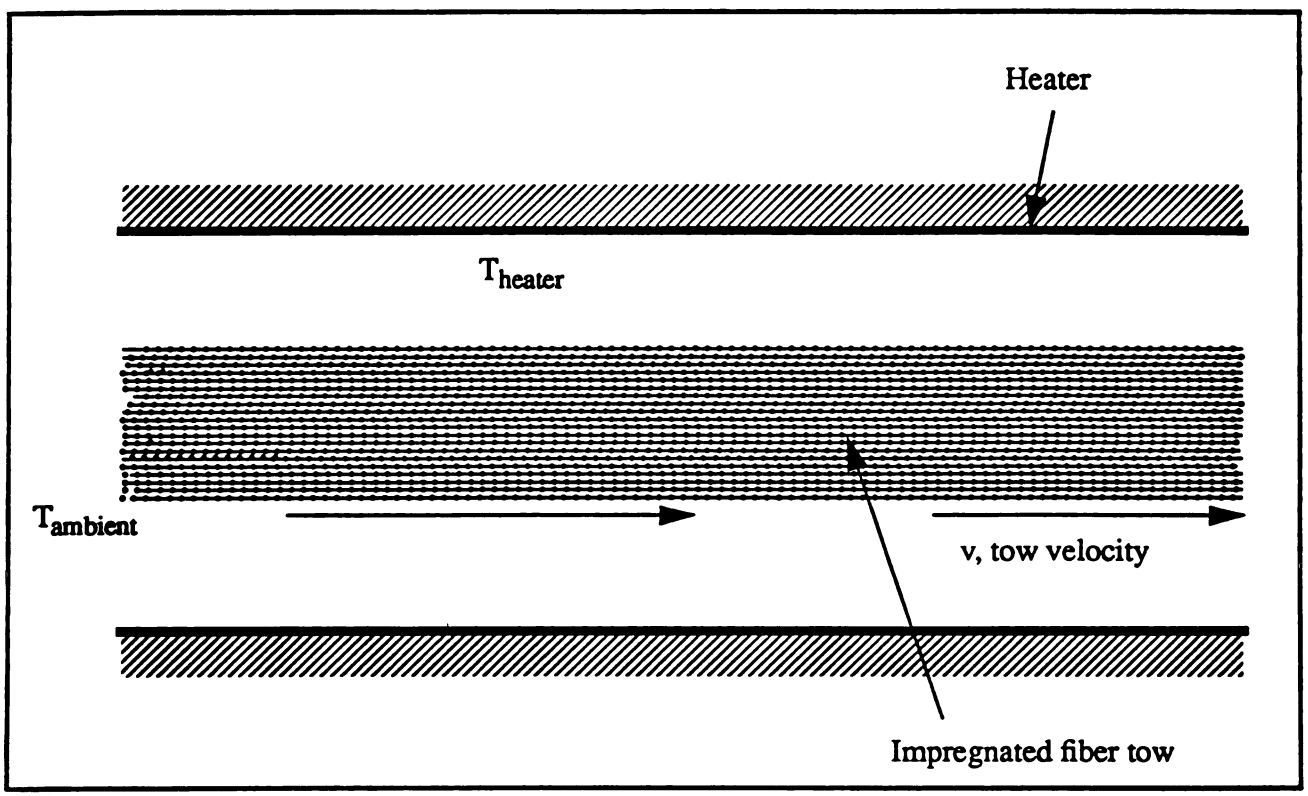

Figure 8. Heat transfer to the impregnated tow.

Bi is extremely low (less than 0.1) for a typical spread fiber tow impregnated with polymer particles. This implies that external heat transfer resistances are rate-controlling and hence a lumped model would serve as an adequate representation of the physical situation. For a lumped system of mass m, specific heat C_p, surface area A, heat transfer coefficient (which includes contributions from convection and radiation) h, the time t required to raise its temperature from T_a (ambient temperature) to T when the temperature of the heater is T_h is given by

$$t = \frac{mC_p}{hA} \ln\left(\frac{T_h - T_a}{T_h - T}\right) \qquad [3b]$$

Lower and upper bounds can be calculated by considering an isolated particle in a convective medium and a large-diameter cluster of coated fibers respectively.

3.1.3 (b) *Interparticle sintering* :

Adjacent particles begin to sinter, i.e., a neck forms between neighboring particles and grows till the particles coalesce into one. The phenomenon of interparticle sintering was first studied by Frenkel [33]. He considered the sintering of two identical amorphous spherical particles (Figure 9). The work required for a change in shape is equated to a decrease in surface energy. Viscous flow dissipation accounts for the work done during coalescence.

$$\frac{x^2}{r} = \frac{3}{2}\left(\frac{\gamma}{\mu}\right)t \qquad [4]$$

where

x = radius of the interparticle bridge

r = radius of the particle

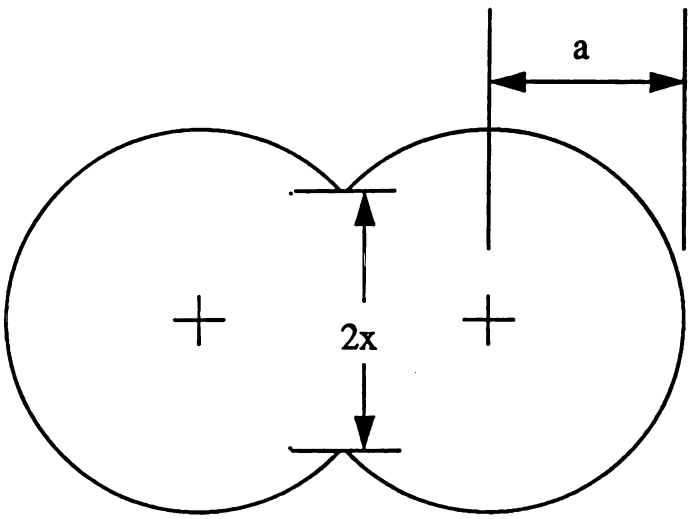

Figure 9. Sintering between adjacent equal-sized spherical particles (initial radius = a)

γ = polymer melt surface tension

μ = polymer viscosity

t = sintering time

In Frenkel's model, it is assumed that dimensional changes occur in the radii of the two amorphous spherical particles during sintering. The analysis is restricted to the early stages where r is approximately equal to the initial radius of the particles. Kuczynski et al. [34] studied the sintering of polymethyl methacrylate spheres and proposed that the sintering process is non- Newtonian, being pseudoplastic at lower and dilatant at higher temperatures. Experiments were conducted in an oven and the sintering process stopped from time to time for microscopic observation thereby increasing the probability for experimental error. Rosenzweig and Narkis [35] developed a precise experimental technique whereby two pre-sintered equal-sized spheres are introduced into a hot stage and observed in situ under a microscope. They observed contradictions to Frenkel's model i.e. a rounded contour in the neck region between the two particles (Frenkel assumed a sharp profile as shown in Figure 9) and no dimensional changes in the two spheres during sintering indicating that flow occurs only in the neck region as opposed to the entire volume. Nevertheless, the overall behavior predicted by Frenkel was confirmed. A plot of x versus t gives a straight line with a slope of 1/2. In a subsequent paper [36], Rosenzweig et al. further demonstrate the applicability of Frenkel's model by calculating activation energies for viscosity from sintering data and comparing it favorably to rheological measurements. Siegman et al. [37] studied the sintering of amorphous and semi-crystalline materials and found that semi- crystalline materials sintered faster than that predicted by Frenkel. The increased surface energy of polyethylene was attributed to its developed internal morphology (nodular and/or fibrillar, less than 1 micron in size) which accelerated the sintering process. In summary, Frenkel's theory, though not exact, provides good estimates of sintering times for amorphous

materials and upper bounds for semi-crystalline materials, with the actual sintering times being dependent on the internal morphology of the particles. Interparticle sintering rates are controlled primarily by viscosity and particle size.

3.1.3 (c) *Film and Droplet Formation* :

Interparticle sintering leads to the formation of a film which breaks up to form droplets on the fiber. These droplets are of varying shape and symmetry with respect to the fiber axis. The shape of these droplets changes with time to an equilibrium configuration which can be axisymmetric or non-symmetric depending on droplet volume and the influence of gravitational forces [38,39]. In the case of a spread fiber tow in which the impregnated fibers are in intermittent contact with each other, capillary forces between adjacent fibers may make film formation thermodynamically favorable. The final configuration depends on interfiber distances and droplet sizes in addition to surface tension forces.

The transition from a polymer film on the fiber surface to droplets is driven by the finite wetting abilities of most thermoplastics. Many investigations have been made on the spreading of spherical drops on planar surfaces. Van Oene [40] modified the momentum equations for a liquid film on a planar surface to account for spreading of polymer droplets and arrived at a result whereby spreading rate is proportional to $\gamma \, \mathrm{Cos}(\theta)/(r \, \mu)$ where θ is the contact angle between the polymer droplet and the solid surface (see Figure 10). The spreading rate depends on the droplet mass (proportional to $1/(\mathrm{mass})^{1/3}$) which explains why small drops take very short times to spread to their equilibrium configurations. The rate of capillary penetration is shown to be proportional to $\gamma \, \mathrm{Cos}(\theta)/\mu$.

Consider the situation shown in Figure 10. For a liquid film to cover an area dA of the solid surface, the driving force is the reduction in surface energy as a result of the spreading (assuming the liquid film to have the same surface area as the

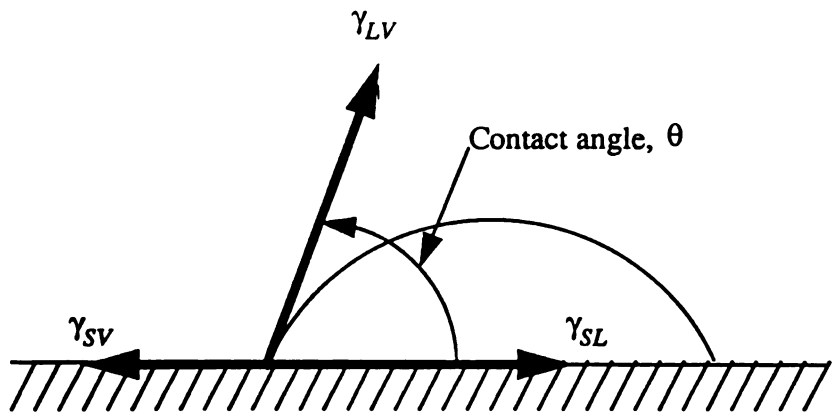

Figure 10. Spreading of a liquid on a planar surface.

surface area of the solid it covers), we have

$$\gamma_{SV}\, dA \geq (\gamma_{SL} + \gamma)\, dA \qquad [5a]$$

The spreading coefficient, S of any liquid on a planar solid is defined by

$$S = \gamma_{SV} - \gamma_{SL} - \gamma \qquad [5b]$$

where γ_{SV} and γ_{SL} are the interfacial energies between solid/air and solid/liquid and γ is the liquid/air interfacial tension. The units of interfacial energy are ergs/cm^2 or dynes/cm.

$S < 0$ corresponds to partial wetting. The liquid does not spread to a film but forms a droplet. The equilibrium contact angle, θ, that the droplet makes with the solid surface is given by Young's equation

$$\gamma_{SV} = \gamma_{SL} + \gamma\, Cos(\theta) \qquad [6]$$

$S > 0$ implies complete wetting and the droplet spreads out to form a film on the surface. The film is stabilized by attractive forces like van der Waal's interactions between the solid surface and the liquid and its thickness, e is given by -

$$e = a\left[\frac{3\gamma}{2S}\right]^{1/2} \qquad [7]$$

Here, a is a molecular size proportional to the Hamaker constant, A, which is a measure of van der Waal's forces

$$\gamma\, a^2 = \frac{A}{6\pi} \qquad [8]$$

London dispersion forces account for almost all of the van der Waal attraction except between highly polar materials [41]. London dispersion interactive energy V_A between spherical particles of radius r separated in vacuum by a shortest distance, H, H << r is given by

$$V_A = -\left[\frac{A\,r}{12H}\right] \qquad [9]$$

Brochard et al. [42,43] studied the spreading of liquid drops on thin cylinders on a microscopic level. In the case of a cylindrical fiber, for S > 0, the interfacial area between the liquid and the solid is less than the surface area of the film due to the larger diameter of the concentric film (the surface area dA in equation (5a) is no longer the same on both sides). Hence, a larger value of the spreading coefficient, S_c is required to achieve complete wetting and form a liquid film on the fiber surface. Brochard argues that in most cases, the film thicknesses are small compared to the radius of the cylinders. Therefore curvature can be neglected in the calculation of the equilibrium film thickness for a cylindrical fiber and equation (7) can be used with reasonable accuracy. S_c is given by

$$S_c = \frac{3}{2}\gamma\left[\frac{a}{b}\right]^{2/3} \qquad [10a]$$

Brochard gives numerical estimates for the molecular size, a, for carbon and Kevlar fibers.

$$\text{Carbon fiber : } S_c/\gamma \approx 0.01,\ D_f/2a \approx 10^3,\ a \approx 0.004\ \mu \qquad [10b]$$

$$\text{Kevlar fiber : } S_c/\gamma \approx 0.005,\ D_f/2a \approx 10^4,\ a \approx 0.0006\ \mu$$

A comparison of the magnitude of a for carbon and Kevlar fibers indicates that van der Waal's forces between the polymer film and the fiber surface will be larger for carbon fibers. This attraction leads to a thicker film as it tends to retard the spreading of the film. The thickness of the film is usually of the order of 100-300°A.

If the droplet is not much thicker than the fiber, then the critical spreading coefficient is S_c^*,

$$S_c^* = S_c\ (1 - D_f/R) \qquad [11]$$

where R is the droplet radius.

In practice, if the spreading coefficient is greater than the critical value, the droplet flows out from both ends to form the film. If there are two droplets separated by a finite distance, then the film serves to drain the smaller droplet into the larger one due to pressure differences as predicted by the Laplace equation.

$$\Delta P = \gamma\ (1/R_1 + 1/R_2) \qquad [12]$$

where ΔP is the droplet pressure, R_1 and R_2 the principal radii of curvature at a point on the surface of the droplet.

The pressure in the film is smaller than the pressure in the droplet, the thickness being stabilized by attractive forces between the fiber and the film. At $S = S_c$, the pressure is 0. On the other hand, if S is less than the critical value, a precursor film forms on either end of the droplet but adjacent droplets will be stable since the film does not extend along the fiber. The length of the precursor film is proportional to the difference between S and the critical value for $S < S_c$. Film formation is unstable as the pressure in the film is larger than the pressure in the droplet.

The contact angles between a cylindrical filament and a liquid can be calculated from drop dimensions that are accurately measured under a microscope by using a method outlined by Carroll [44] and Yamaki et al. [45]. This macroscopic analysis [44] which is based on the Laplace equation applies to axisymmetric droplets. Figure 11 shows an unduloidal droplet on a fiber at equilibrium. R_1 is the radius of curvature at a point of the curve $y = f(x)$ which is rotated around the axis to obtain the Figure of revolution. R_1 is given by the analytical relation [46]

$$R_1 = -\left[\frac{[1+(dy/dx)^2]^{3/2}}{d^2y/dx^2}\right] \qquad [13]$$

R_2 is in the plane perpendicular to the paper and for Figures of revolution, it is obtained by projecting the normal to the axis of revolution

$$R_2 = y/\mathrm{Cos}(\beta) = y\mathrm{Sec}(\beta) = y(1 + \mathrm{Tan}^2(\beta)) = y[1 + (dy/dx)^2]^{1/2} \qquad [14]$$

Substituting equations (13) and (14) in (12), we have

$$\frac{d^2y}{dx^2} = -\frac{\Delta P}{\gamma}\left[1 + \left[\frac{dy}{dx}\right]^2\right]^{3/2} + \frac{1}{y}\left[1 + \left[\frac{dy}{dx}\right]^2\right] \qquad [15]$$

The boundary conditions are

(1) $x = 0$, $y = D_f$

(2) $x = 0$, $dy/dx = \tan(\theta)$

(3) $x = L/2$, $dy/dx = 0$

These three conditions can be used in a finite difference program (Appendix C) to iterate for θ given the two dimensions l and k for a droplet.

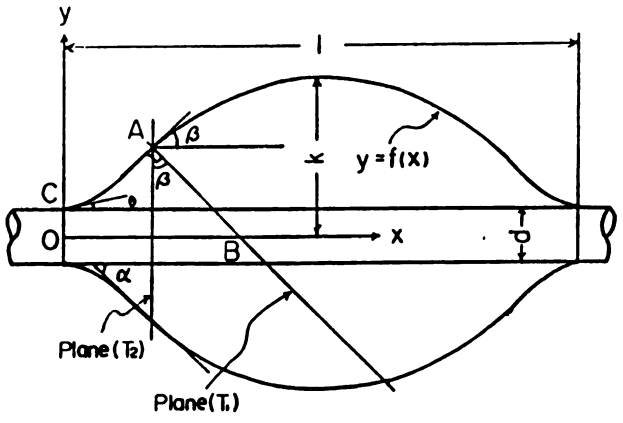

Figure 11. Unduloidal droplet on a cylindrical fiber.

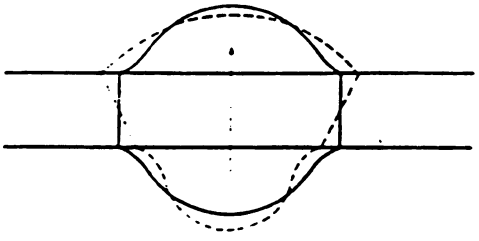

Figure 12. Non-symmetric perturbation of an axisymmetric droplet.

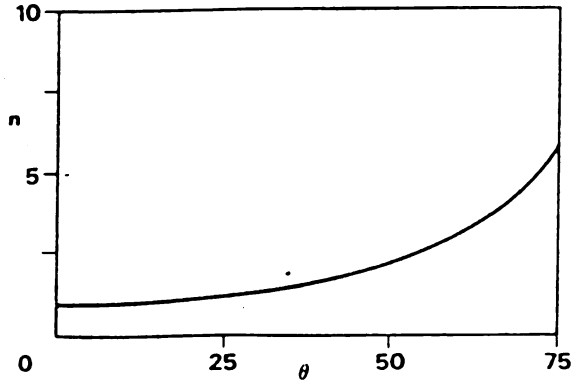

Figure 13. Transition from axisymmetry to non-symmetry for a droplet on a cylindrical fiber.

The above analysis applies only to axisymmetric droplets. Carroll [38] discusses the formation of unsymmetric droplets. The transition between axisymmetry and non-symmetry occurs if the contact angle increases for a given droplet volume or the volume decreases below a threshold value for a given contact angle. Consider a axisymmetric perturbation of the drop from its equilibrium conformation. If the drop volume is kept constant, the effect is to increase one curvature, R_1^{-1}, while decreasing R_2^{-1}. From the Laplace equation we have

$$\delta(\Delta P) = \frac{2\gamma}{D_f} (\delta R_{n1}^{-1} + \delta R_{n2}^{-1}) \qquad [17]$$

where R_{n1} and R_{n2} are $2R_1/D_f$ and $2R_2/D_f$ respectively.

R_{n1} and R_{n2} at $x = l/2$ can be written in terms of θ and n (where $n = 2k/D_f$) as follows [44]

$$\frac{1}{R_{n1}} = \frac{(n^2 - 2n\text{Cos}(\theta) + 1)}{(n(n^2 - 1))} \qquad [18a]$$

$$\frac{1}{R_{n2}} = \frac{1}{n} \qquad [18b]$$

If at $x = L/2$, the perturbation causes a change δx_2 in the drop median radius ($x_2 > 0$), then

$$\delta R_{n1}^{-1} \approx -\left[\frac{d(R_{n1}^{-1})}{dn}\right]\delta n \qquad [19a]$$

$$\delta R_{n2}^{-1} \approx -\left[\frac{d(R_{n2}^{-1})}{dn}\right]\delta n \qquad [19b]$$

Substituting equations (18) and (19) in (17), we have

$$\delta(\Delta P) = \frac{2\gamma}{D_f}\left[\frac{n^4 - 4n^3\text{Cos}(\theta) + 4n^2 - 1}{n^2(n^2 - 1)^2 - (1/n^2)}\right] \qquad [20]$$

Here, if $\delta(\Delta P) < 0$, then change in pressure is negative and the resulting conformation is axisymmetric. But if $\delta(\Delta P) > 0$, then if the perturbation is non-symmetric, there will be a flow of liquid from the upper to the lower part of the drop due to a pressure gradient (Figure 12) resulting in a non-symmetric droplet. Hence the transition is at $\delta(\Delta P) = 0$. Equation (20) can be solved to give

$$2n^3\text{Cos}(\theta) - 3n^2 + 1 = 0 \qquad [21]$$

where $n = k/D_f$.

Figure 13 shows a plot of n vs θ. In the region above the curve, we have axisymmetry while the region below the curve corresponds to non-symmetric droplets.

Both the above analyses (contact angle measurement and droplet transition) hold good only in the case of negligible gravity. The effect of gravity for a droplet can be assessed by considering the basic Bernoulli equation [47] and eliminating the kinetic energy term, we have

$$\Delta P_g = (\rho)gh \qquad [22]$$

where ρ is the liquid density, g the acceleration due to gravity and h the distance between any two points. The largest value of h is 2k. Hence a comparison of ΔP, the Laplace pressure in the droplet, with ΔP_g is sufficient to determine the significance of gravity in the spreading process.

3.2. **Consolidation** :

The powder-impregnated prepreg tapes have to be consolidated under heat and pressure to form void-free composite parts. The physics of the consolidation process is shown in Figure 14. If the impregnation of particles in the fiber tow is uniform,

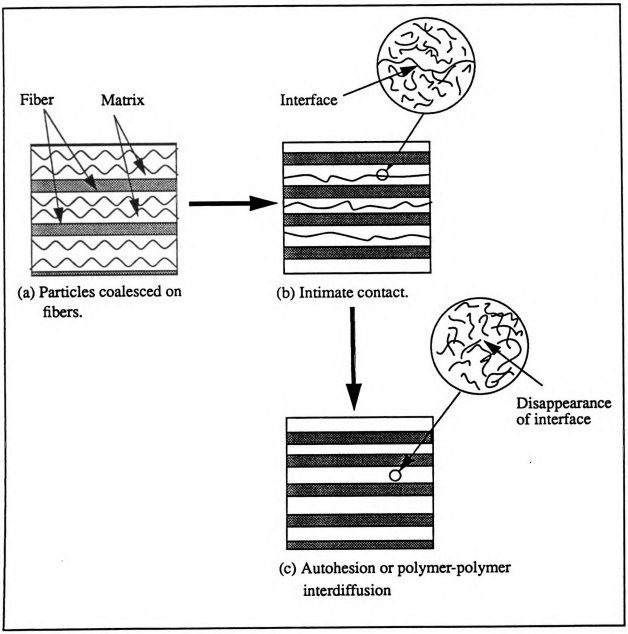

Figure 14. Consolidation of powder-impregnated tapes.

this leads to the formation of uniform-sized droplets and a polymer sheath on the fibers. In such a case, the phenomenon of consolidation broadly involves two steps :- (i) Intimate contact at the polymer-polymer interface at numerous sites across the composite. Consolidation is usually performed at temperatures higher than the melt temperature for semi-crystalline or the softening point for amorphous thermoplastic polymers. Physical deformation at the polymer-polymer interface is required to achieve intimate contact. (ii) Autohesion or the interdiffusion of polymer chains across the interface so as to cause its disappearance.

Wool et al. [48-51] describe healing at the interface for amorphous thermoplastic polymers as a five step process : (i) surface rearrangement of the polymer chains before contact (i.e. chain ends diffuse back into the bulk with time after the creation of a freshly fractured surface), (ii) surface approach (contact of different surfaces to form an interface), wetting (contact at the microscopic level), (iii) diffusion (movement of polymer chains across the interface), and (iv) randomization (disappearance of the interface so that it is no longer distinguishable from the bulk). The interfacial bond strength is the sum of two components, wetting and diffusion. The wetting component (strength associated with wetting between the two surfaces) is constant once complete wetting is achieved at the interface and is primarily due to van der Waal's forces. The diffusion component (strength associated with interdiffusion of polymer chains across the interface) increases with contact time after wetting is achieved until it reaches a plateau when the diffusion process is complete. At this point, the interfacial bond strength is as high as that of the virgin polymer. For an amorphous polymer, the mechanical energy required to separate the two interfaces is a function of contact time, temperature, pressure and molecular weight of the polymer chains at the interface. With the help of reptation theory [52], Wool et al. arrived at relations for the time dependence of mode I fracture energy (G_{Ic}) and stress intensity factor (K_{Ic}).

$$G_{Ic} \approx t^{1/2} \quad [23]$$

$$K_{Ic} \approx t^{1/4} \quad [24]$$

These equations are valid only if free chain ends are available at the interface e.g. for freshly fractured surfaces. The fracture energy at constant contact time decreases with increasing surface rearrangement time. Two modes of fracture are possible : chain scission is favored at low temperature, fast testing rate and high molecular weight; and chain pullout favored at high temperature, low deformation rate and low molecular weight. The fracture toughness of an amorphous polymer increases with pressure until a saturation pressure is reached beyond which there is no further improvement. A high consolidation pressure promotes faster wetting but decreases the volume available for segmental motion of the polymer molecules thereby reducing the diffusion coefficient and slowing down the diffusion process. An increase in temperature accelerates the wetting process while decreasing the saturation pressure needed for complete wetting.

In contrast to pure polymers, healing at incompatible crystallizable interfaces (polyethylene /polypropylene (PE/PP)) was studied by Wool et al. [51] who found that the nucleation of PP spherulites coupled with flow of PE across the interface followed by its subsequent crystallization produced strong mechanical interlocking (fibrils of PE attached to PP spherulites) up to a depth of several microns and increased the interfacial strength. The events occuring at a compatible crystallizable interface of a semi-crystalline polymer are diffusion, homogenous crystallization and mechanical interlocking to a lesser degree.

Healing in thermoplastic composites is complicated by the fact that the fibers act like a spring and absorb a part of the applied load. Therefore a specimen with a high fiber content requires a higher consolidation pressure than a specimen with lower fiber content for optimum consolidation. Howes et al. [53] studied the healing

phenomenon in a thermoplastic composite (polysulfone /graphite fiber) by performing double cantilever beam toughness tests to evaluate Mode I fracture toughness on rehealed specimens. The results were inconclusive because of an inconsistent interface i.e. fiber breakage, excess resin at the interface after initial fracture and possibly changing molecular weight distribution at the interface due to chain fracture. Lee et al. [54] measured bond strength between two crossply APC-2 laminates (two flat 0.016" diameter surfaces) and found that the degree of autohesion was roughly proportional to $t^{1/4}$. They did not see any effect of processing pressure on bond strength probably because of instantaneous wetting at the interface. Manson et al. [55] noted that processing pressure did not affect the toughness values significantly. Lee et al. [54] and Manson et al. [55] reported that fracture toughness values decrease with increasing crystallinity for PEEK/graphite fiber composites.

In summary, the design of optimum consolidation cycles for powder-impregnated thermoplastic composites involves the selection of time, temperature, pressure and cooling rates (for semi-crystalline materials). Another variable which affects consolidation cycles is the volume fraction of matrix in the composite. The saturation pressure increases with decreasing matrix volume fraction (time and temperature constant) due to the ability of the fibers to store elastic energy during consolidation.

Chapter 4

PROPOSED PROCESS

The preceding chapters discussed the rationale for the design of the process and the fundamental physical phenomena underlying the process. This chapter describes the design of each of the components constructed to perform the unit operations identified in Figure 6 (page 19). They are -

(1) The fiber motion system which performs two functions - (a) It conveys the fiber tow from the fiber spool to the takeup drum. (b) Rotary and lateral motion of the takeup drum so that the prepreg tape can be wound across the entire width of the drum.

(2) The spreader which spreads the collimated fiber tow into its individual filaments.

(3) The aerosolizer which disperses the particles in the gaseous medium and delivers a controlled concentration of particles to the spread fiber tow.

(4) The heater in which the particles sinter and coalesce on the fibers to form a flexible prepreg tape.

(5) The automation scheme which monitors the performance of the different components and controls the entire process.

The design of two related pieces of equipment, the heated stage used to study the fundamental phenomena associated with coalescence and the mold used to consolidate the tapes into a part are also discussed. The engineering drawings of all the equipment described in this chapter are attached in Appendix A.

4.1 Fiber Motion :

A schematic of the fiber motion system is shown in Figure 15. The fiber spool is mounted on a shaft which is mounted on a block at each end. The bearing blocks are fitted with precision ball bearings to enable the shaft and consequently the fiber tow to be rotated with a minimum amount of tension. The fiber tow passes through a guide ring and is pulled from the spool by a pair of nip rollers (NR1). All the nip rollers are fabricated with stainless steel case-hardened shafts for the bottom roller, smooth aluminum shafts for the top roller and are mounted on precision ball bearings so that the shafts rotate with minimum friction on their axes. The top rollers can be adjusted to maintain any desired gap between the two rollers. A second pair of nip rollers (NR2) is mounted downstream and connected by a chain drive to ensure that they operate at identical speed. A third pair of nip rollers (NR3) is mounted before the takeup drum. This arrangement ensures that the fiber tow is devoid of any tension between NR1 and NR3. Nip rollers 1 and 3 are driven by precision d.c. motors while a gear system with chains links 1 and 2 and drives them both synchronously.

The takeup drum is mounted similar to the fiber spool on a shaft. It is powered by a d.c. motor to enable it to rotate on its own axis. The mounted drum is placed on a table which can be moved laterally by a linear motion system. The prepreg tape is wound on the drum as the drum rasters in a direction perpendicular to the rotary motion. This ensures that the tape is wound across the entire drum. Limit switches make the drum change direction as the tape reaches either end.

4.2 Aerosolizer :

Preliminary experiments were done on the fluidized bed behavior of cohesive powders [56]. These experiments led to the conclusion that enhancement to conventional fluidization is necessary for good controllable fluidization and

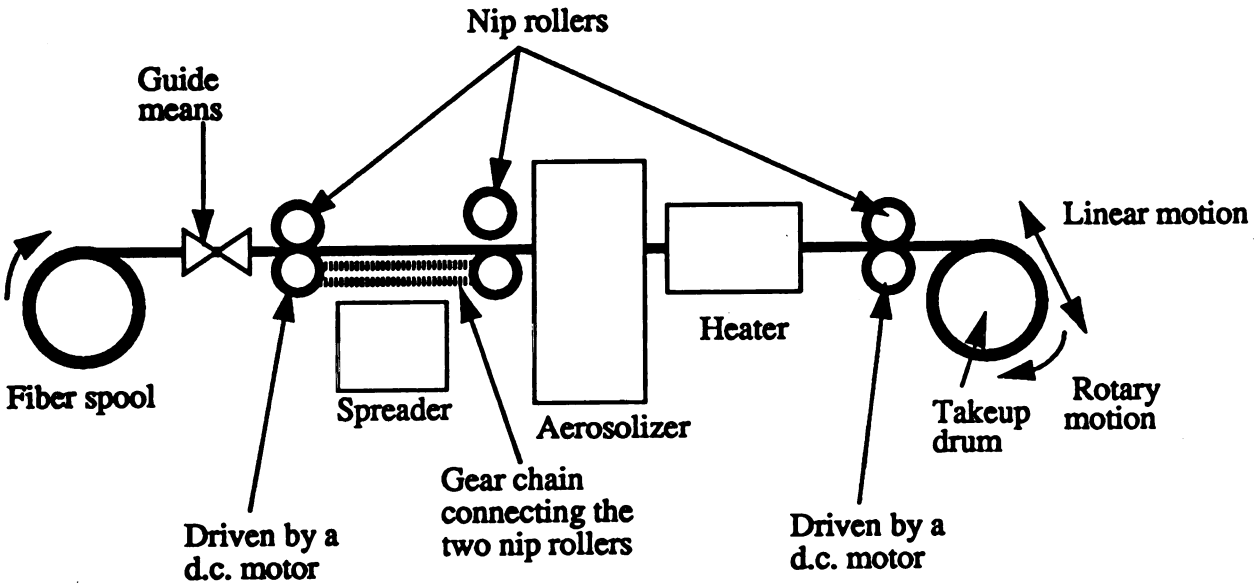

Figure 15. Fiber motion in the powder-prepregging process.

entrainment of cohesive polymer powders. Enhancements include the addition of fluidization promoters such as fumed silica, some form of pulsed energy e.g. pulsed gas flow (low frequency less than 1 Hz), acoustics (1-20,000 Hz) and ultrasonics (greater than 20,000 Hz); and electrostatics. The addition of fluidization promoters is undesirable because it would lead to the presence of impurities in the final part that could detract from its mechanical performance. Gas flow pulsing with the help of a solenoid valve did not improve the quality of fluidization significantly compared with that of a conventional bed (Section 6.2). This led to the selection of the acoustic aerosolizer as a reliable system for the controlled entrainment of polymer particles [57].

The principle of operation of the aerosolizer is that the acoustic energy generated by an audio speaker prevents agglomeration and aids in fluidizing and entraining the cohesive particles within and out of the fluidizing chamber. The aerosolizer is packed with particles at the base of a column on a rubber diaphragm. The speaker is operated at a predetermined frequency and amplitude. The acoustic energy is absorbed by the vibrating diaphragm which in turn imparts this energy to the particles. Standing waves are set up between two diaphragms placed at either end of the chamber. This system consisting of the diaphragms, the chamber including the slits which allow the fiber tow to pass through and the weight of the powder resonates with a natural frequency. At this frequency, the aerosolization of particles attains a concentration which remains constant with time if the amplitude of the sound wave is kept constant.

A sketch of the aerosolizer is shown in Figure 16. It consists of a speaker box over which a cylindrical plexiglass column is mounted. Vibrating rubber diaphragms are placed on a lip between the column and the speaker box and at the top of the column. There is a gas inlet near the base of the column. Two slits at either side of the column provide entry and exit means for the spread fiber tow. The

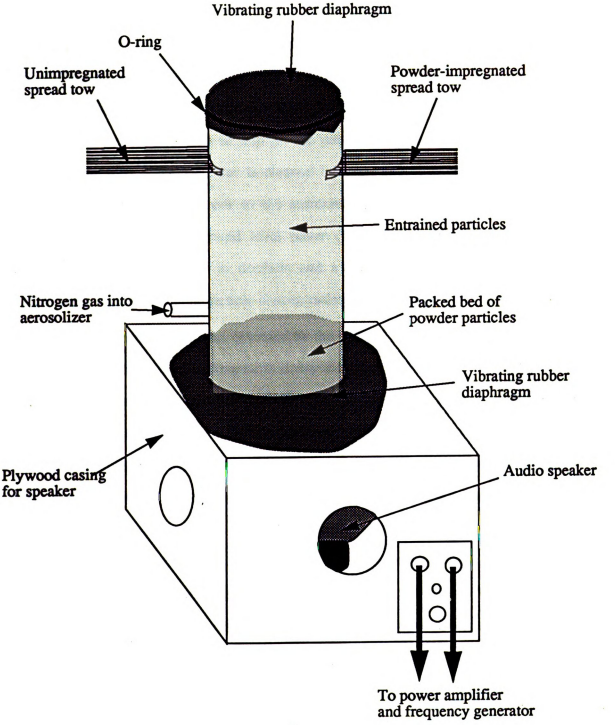

Figure 16. Aerosolizer.

inside walls are covered by smooth Aluminum foil to reduce particle caking on the walls. The speaker is powered by an audio amplifier connected to a frequency generator. The column with its vibrating diaphragms is enclosed in a rectangular plexiglass housing. The housing has two slits corresponding to the entry and exit means for the fiber tow. The back wall of the housing is fitted with an air filter and an exhaust fan (not shown) to trap all the particles which escape from the column through the slits. The air filter is cleaned between experiments. This arrangement eliminates particle entrainment to the surrounding environment. The chamber has two sensing devices - a sound level meter (Type 2231, Bruel and Kjaer) which measures acoustic pressure in decibels and a Realtime Aerosol Monitor (RAM-S, MIE Inc.) which measures particle concentrations in the range 0-200 mg/m^3.

The aerosolizer is best operated at the natural frequency of the system. The choice of materials for diaphragms is dictated by their stiffnesses. The magnitude of acoustic energy that is transferred to the powder particles decreases with increasing stiffness. The tension with which the diaphragms are stretched over the two ends of the chamber and the weight of the powder packed on top of the lower diaphragm are experimental variables which change the compliance for a given material. As shown in Figure 16, a gas stream is introduced into the chamber at a level greater than the height of the packed bed. This helps in the entrainment process by providing an additional steady buoyant force for entrained particles which are thrown up into the upper regions of the chamber from the packed bed by acoustic energy.

A simple momentum balance around a control volume is shown in Figure 17. This analysis serves to highlight some of the phenomena which occur in the aerosolization of particles. If T_{yx} is the shear stress and u is the average velocity ($u = u(x,y)$), then

$$C\,\rho_p u\frac{du}{dx} = -\frac{dT_{yx}}{dy} - \rho_p gC + F \qquad [25]$$

where

F = buoyant force, the sum of the acoustic force and any upward gas flow

ρ_p = the particle density

C = volume concentration (m^3 of particles/m^3 of total volume), C = C(x).

Bagnold [58] considers the flow of powders in two regimes, the grain-inertia region which corresponds to high shear rates and where interparticle interactions dominate and the macro-viscous region which corresponds to lower shear rates and where the viscosity of the fluid plays a significant role.

$$\text{Grain–inertia region : } T_{xy} \alpha \left[\frac{du}{dy}\right]^2 \qquad [26]$$

$$\text{Macro–viscous region : } T_{xy} \alpha \left[\frac{du}{dy}\right] \qquad [27]$$

Savage [59] also arrived at similar results for the grain-inertia region. Johnson et al. [60] theorized that interactions between colliding particles can be of two kinds - frictional contacts which are characterized by long contact times and collisional-translational contacts characterized by short contact times. Though they considered a dense flow of solid particles, these phenomena, especially inelastic collisions of short contact times also occur in aerosols of low particle concentrations.

When particles in a medium are exposed to sound waves, they experience hydrodynamic sound pressure [61]. If the radius of a particle is small compared to the wavelength, λ, of sound, the pressure F_M on an isolated spherical particle due to standing waves is

$$F_M = \frac{5}{3} \lambda \pi^2 \rho_g r_p^3 U_0^2 \sin\left[\frac{4\pi x}{\lambda}\right] \qquad [28]$$

where

ρ_g = density of gas

r_p = radius of particle

U_0 = amplitude of vibration of the particle relative to the medium

x = distance of the particle from the nearest node.

As entrainment of particles by the oscillating medium increases, the sound pressure decreases in proportion and becomes zero for complete entrainment. In an aerosol, the sound waves undergo scattering, absorption and diffraction. The scattering of sound by aerosols is negligibly small and is usually neglected. The absorption of sound depends on particle concentration and on the extent to which the particles follow the vibration of the sound waves i.e. resonance. The attenuation of sound pressure due to the presence of aerosol particles is proportional to the absorption coefficient of sound waves by the aerosol. Other mechanisms for sound absorption include viscous loss and the irreversible heat transfer between the particle and the gas which causes an increase in entropy with a subsequent decrease in free energy.

Another issue which comes up in the operation of the aerosolizer is the agglomeration of particles in acoustic sound fields [61]. In an acoustic field, different particles oscillate at different amplitudes due to the competition between acoustic and gravitational forces. Small particles tend to oscillate along with the sound wave while larger particles remain relatively stationary. This leads to the collection of small particles by the larger particles to form agglomerates. This phenomenon increases in magnitude with sound intensity and is called the mechanism of orthokinetic interaction. A sonic agglomeration constant, b, is defined such that

$$b \propto I^{1/2} \qquad [29]$$

where I is the sound intensity which is the average rate of flow of energy through a unit area normal to the direction of wave propagation. In real terms, the intensity level is usually expressed in decibels and is the same as the sound pressure

$$IL = 10 \log\frac{I}{I_0} = 20 \log\frac{P_e}{P_0} \qquad [30]$$

where

I_0 = reference intensity, usually 10^{-12} watt/m^2

P_e = effective or root mean square pressure = $P/\sqrt{2}$}

P_0 = reference pressure, usually .00002 N/m^2 which corresponds to a pressure barely audible to the human ear at a frequency of 1000 Hz.

$I = P_e^2/(\rho_0 c)$, c is the velocity of sound in a medium of density ρ_0.

(The intensity level IL is known as the sound pressure level SPL, a reference pressure of 0.00002 N/m^2 is commonly used for computing sound pressure levels in air.)

The sound intensity in the aerosolizer is proportional to the amplitude of the sound wave fed to the speakers at the natural frequency of the chamber. Hence the aerosolizer operates best within a narrow range of amplitudes where b is low. At very high amplitudes, the polydispersity in particle size causes a variation in particle oscillations thereby leading to the agglomeration of small particles to larger ones. The oscillation of particles with the acoustic field also generates multiple collisions with the reinforcing fibers which pass through the aerosolizer. This increases the probability of each particle being carried away by the fibers compared to a conventional entrainment system where particle paths are either Brownian or follow the profiles dictated by the flow of gas.

A rigorous analysis to predict concentration profiles within the aerosolizer must take all of the above phenomena into account. The instantaneous velocity at any point is the sum of the average velocity, u and the fluctuating component due to the sinusoidal nature of sound waves. Equation (25) assumes that the particles and the gas medium behave as a continuum. This may be adequate as a first approximation but subsequent refinements should incorporate the discrete nature of the particles and the medium. The bulk of the shear stresses T_{yx} are generated by interparticle collisions which are treated by several workers [57-59]. The two buoyant forces, gas flow and acoustic force have to be taken into account in the governing equations. The acoustic force depends on many factors such as diaphragm tension which includes the weight of the packed bed, the geometry of the chamber, the operation of the chamber at its natural frequency and the sound absorption characteristics of the aerosol which cause attenuation of the acoustic force along the length of the chamber. Concentration profiles and sound pressure profiles measured within the chamber during each experiment will aid in the development of this theory.

4.3 Spreader :

The conventional technique for spreading currently used in the composites industry is elucidated in Section 3.1.1. This investigation attempted to design a spreader which would spread fiber tows to a width large enough that individual filaments are exposed. The design chosen for spreading is an extension of the principle of operation of the aerosolizer [63] where a pulsating flow of energy provided by a vibrating speaker cone is used to separate the collimated fiber tow to its individual filaments. The speaker vibrates at a constant predetermined frequency and amplitude. The acoustic energy enables the fiber tow to spread to any desired width. The acoustic pressure generated by the speaker in the region above the

spreader is transferred to the filaments in the fiber tow. This energy forces them to spread apart. For a particular fiber tow, there is a narrow range of frequencies at which the efficiency of spreading is the maximum. This range is centered around the natural frequency at which the fibers absorb the most energy. The spreading width is a function of tow tension in the region over the spreader and the amplitude of the sound wave once the right frequency is selected. The spreading width increases with increasing amplitude (frequency and tension constant) to a plateau beyond which there is no appreciable increase. The spreading width increases with decreasing tension to a point beyond which there is too much slack which causes uncontrollable fiber motion and oscillations resulting in fiber damage. A spreading device based on acoustics was also used by Hall [64] to spread internally wound spools (which are unwound from the inside and have no tension in the tow).

A sketch of the spreader is shown in Figure 18. It consists of a speaker mounted in a housing and driven by a frequency generator and power amplifier. Adjacent to the speaker are mounted several highly polished shafts. The shafts are held in place by means of an aluminum block fitted with precision bearings. A fiber tow of narrow width containing 3000 filaments enters the spreader and is spread to a width sufficient to expose individual filaments. The function of the shafts is to hold the tow in its spread form (due to friction) as it is being conveyed forward. The bearings enable the shafts to rotate along with the fibers whenever there is excessive friction between the fibers and the shafts. Alternatively, the shafts can be driven by a motor so that they rotate synchronously with the same velocity as the fiber tow.

A schematic of the spreading operation is shown in Figure 19. The fiber tow of narrow width is unwound from the spool by a pair of nip rollers. Both externally and internally wound spools can be used with this process. The fiber tow is held at a constant level of slack between this pair of nip rollers and a second pair of nip rollers mounted between the first pair and the takeup drum. This arrangement ensures that

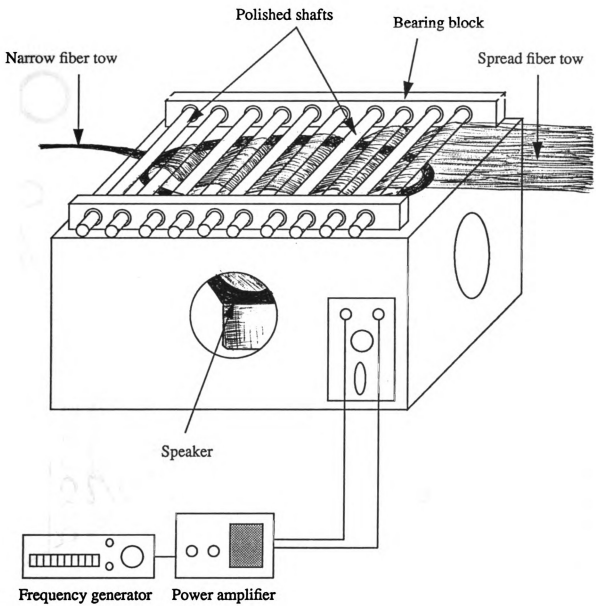

Figure 18. Spreader

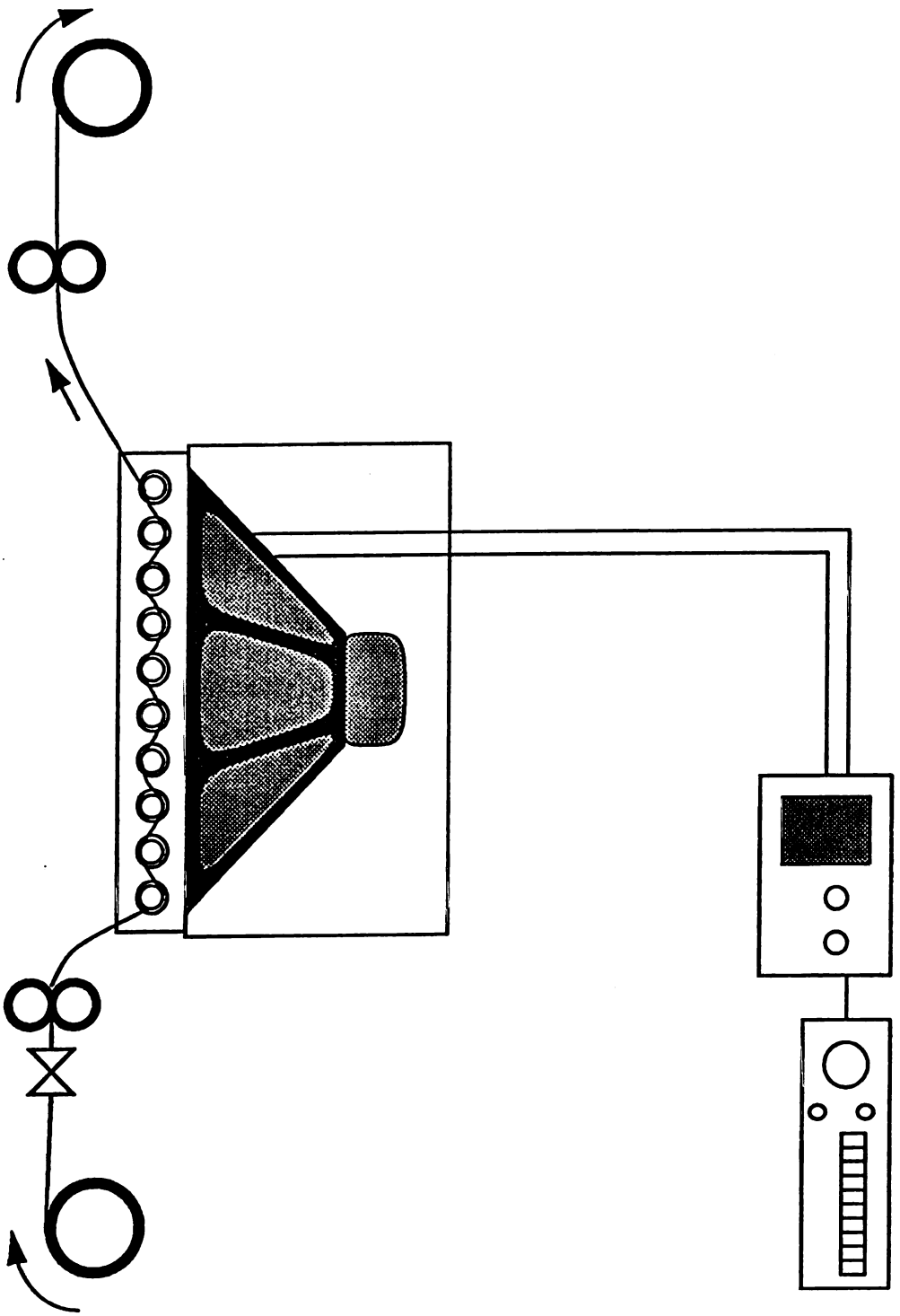

Figure 19. Fiber spreading operation.

the tow is held at the desired level of slack over the spreader regardless of the level of tension of the tow in the fiber spool. Alternatively the speed of the takeup drum can be regulated to maintain a constant level of slack in the fiber tow as it passes over the spreader.

4.4 Heater :

The function of the heater is to ensure that the particles which are electrostatically attracted to the fibers in the aerosolizer sinter, coalesce and adhere to the fibers so that there is no loss of matrix during subsequent processing operations. The heater currently used in the process is a natural convection oven (VWR 1300, 750 Watts) capable of heating to a maximum temperature of 250°C. Slits have been machined at the front and back faces of the oven for the impregnated fibers to pass through.

4.5 Process Description :

A schematic of the entire powder prepregging process is shown in Figure 20. A fiber tow 2 is unwound from a spool 1. The tow 2 passes through a guide ring 3 and between nip rollers 4a before passing over the spreader 6. The spreader uses an audio speaker to separate the tow into its individual filaments. Nip rollers 4a and 4c maintain a constant level of tension in the spread tow 5 in the region above the spreader. The spread tow passes through an aerosolizer 9 which coats the fibers in the tow with a controlled concentration of particles. The impregnated tow 12 then enters an heater 14 which sinters the particles on the fibers. The resulting prepreg tape is wound on a takeup drum 15.

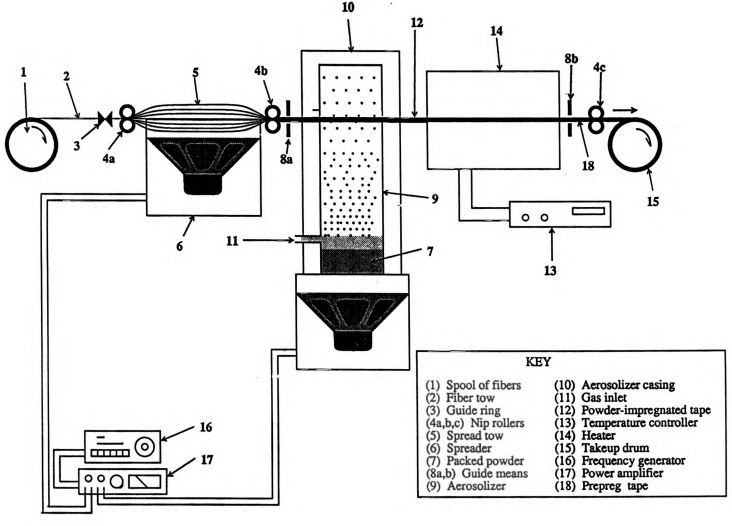

Figure 20. Schematic of powder prepregging process

4.6 **Automation** :

The automation scheme for the powder-prepregging process is shown in Figure 21. It consists of a Hewlett-Packard personal computer QS/16S with an interface card (Data Translation DT2811-PGH), a controller box (Composite Line Controller or CLC) and various sensors monitoring the process. Each of the tasks performed by the control system is described conceptually in this section. The specifications of the various components, the control program and the wiring diagrams are enclosed in Appendix B. The tasks performed by the control system are - (1) Fiber motion which includes speeds of the nip rollers, a slack controller which controls the speed of the takeup drum depending on tow tension between the third nip roller and the takeup drum and the linear motion of the takeup drum; (2) control of oven temperature; and (3) data acquisition within the process.

4.6.1 *Fiber motion* :

The speeds of the nip rollers are maintained at any desired speed by the computer. An optical slotted disk is mounted on the drive shaft of nip rollers 4a and 4c (Figure 20). A photosensor placed around the disk keeps track of the number of slots that pass through in a given time period. This signal is fed to a pulse counter in CLC which holds this information in 3 data registers as a 12- bit number. The computer program accesses these data registers through the interface card, decides the next control strategy and sends a command to the motor controller within the CLC in the form of a 12-bit number (0-4095). The motor controller pulses full power to the motors driving the rollers for a time period proportional to this number e.g. if the number is 1200, the motor is on for 1200/4095 of one period (1/9.1 seconds). Both the nip rollers 1 and 2 are powered by a 20 V d.c. power supply. Both the input and output signals for this control loop use the digital input/output channels in the interface card.

[ ]

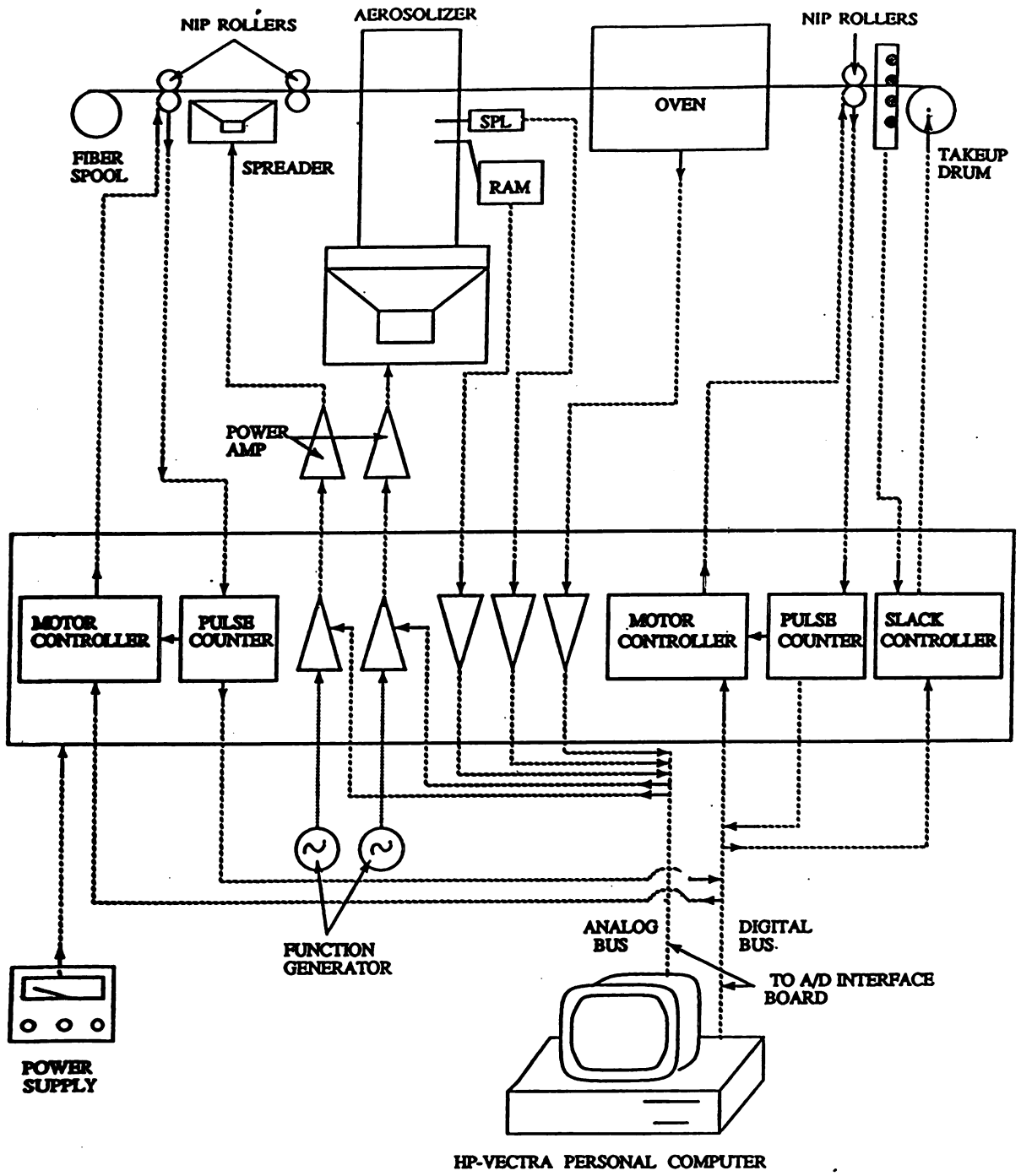

Figure 21. Data acquisition and control of powder prepregging process.

The control scheme used by the program to maintain the speeds at their set points is a PID algorithm (proportional-integral-derivative control). The ideal PID controller equation is [65]

$$p(t) = \bar{p} + K_c \left[e(t) + \frac{1}{\tau_I} \int_0^t e(t')dt' + \tau_D \frac{de}{dt} \right] \qquad [31]$$

where

$p(t)$ = controller output

$\bar{p}$ = bias value

K_c = controller gain (proportional constant)

$e(t) = U_{set} - U$ = set point - measured value

τ_I = integral constant

τ_D = derivative constant

The use of this equation for computer control entails its conversion to digital form by the use of the following approximations

$$\text{Trapezoidal rule : } \int_0^t e(t')dt' = \sum_{k=1}^{k=n} \frac{(e_k + e_{k-1})}{2} \qquad [32]$$

$$\text{Backward Difference : } \frac{de}{dt} = \frac{(e_n - e_{n-1})}{\Delta t} \qquad [33]$$

where Δt is the time step.

Substituting equations (31) and (32) in (30)

$$p_n = \bar{p} + K_c \left[e_n + \frac{\Delta t}{2\tau_I} \left[e_k + \frac{e_{k-1}}{2} \right] + \frac{\tau_D}{\Delta t} (e_n - e_{n-1}) \right] \qquad [34]$$

Writing a similar equation for p_{n-1} and subtracting the two, we have

$$\Delta p_n = K_c\left[(e_n - e_{n-1}) + \frac{\Delta t}{\tau_I}\left[\frac{e_n + e_{n-1}}{2}\right] + \frac{\tau_D}{\Delta t}(e_n - 2e_{n-1} + e_{n-2})\right] \qquad [35]$$

This is called the velocity form of the PID controller and is the primary equation used for motor control in the process. The main advantage of this equation over (33) is that the summation term does not have to be computed. This avoids the problem of reset windup which occurs when the error summation term grows to a very large value and exaggerates the fluctuations of the controlled variable about the set point.

If the motors are controlled directly by a d.c. power supply, fluctuations in the power supply cause a fluctuation in motor speed and synchronous control of multiple motors is extremely difficult. Feedback control by a PID controller such as the one described above theoretically allows speed regulation to any desired set point. The role of K_c is to accelerate the system response while τ_I eliminates the error and τ_D reduces the oscillations of the controlled variable about the set point. Increasing the value of K_c increases the system response and reduces the offset. Above a certain value, the response becomes oscillatory and unstable. The addition of τ_I eliminates offset but makes the system oscillatory. Reducing τ_I makes the system sluggish in its response to any fluctuation about the set point. The derivative constant, τ_D, reduces oscillation and increases response time but above a certain value, the response becomes oscillatory. If there is system noise or instantaneous fluctuations in the measured speeds, then local derivatives will fluctuate wildly and result in an unstable system. Optimization of the three constants is required for the synchronous control of speeds by digital computer control.

The takeup drum is driven by a d.c. motor which is powered by a 20 V power supply. The drum rotates at a constant base speed throughout each experiment except when slack is present. A slack sensor is mounted between nip roller 4c and the drum. The optical sensor detects slack whenever the tape falls below a certain height. This switches a transistor in the CLC which accelerates the speed of the takeup drum by boosting its power supply till the slack is no longer present. This assembly is mounted on a table which tracks linearly thereby facilitating the takeup of prepreg tape across the entire width of the drum. The table is fastened to a linear actuator tube which is powered by a 90 V d.c. motor which runs on a 25 % duty cycle. The computer resets the value of a bit in a data register (0 or 1) in the CLC to turn the motor off or on in accordance with this duty cycle. Limit switches mounted at either end of the travel reverse polarity of the voltage supplied to the motor causing the table to change direction.

4.6.2 *Oven Temperature* :

The oven is maintained at a desired set point temperature during each experiment. The oven temperature is measured by a K-type thermocouple which converts temperature to a millivolt reading in differential output. A converter changes this differential signal into a single-ended output which is fed to an analog channel in the interface card. This voltage is read by the control program which converts it to temperature. The program changes the status of a bit in a data register (0 or 1) in the CLC to turn the oven on or off depending on the deviation of the temperature from its set point. The control scheme utilizes proportional control and is shown in Figure 22 as a conceptual plot between temperature and % ON time.

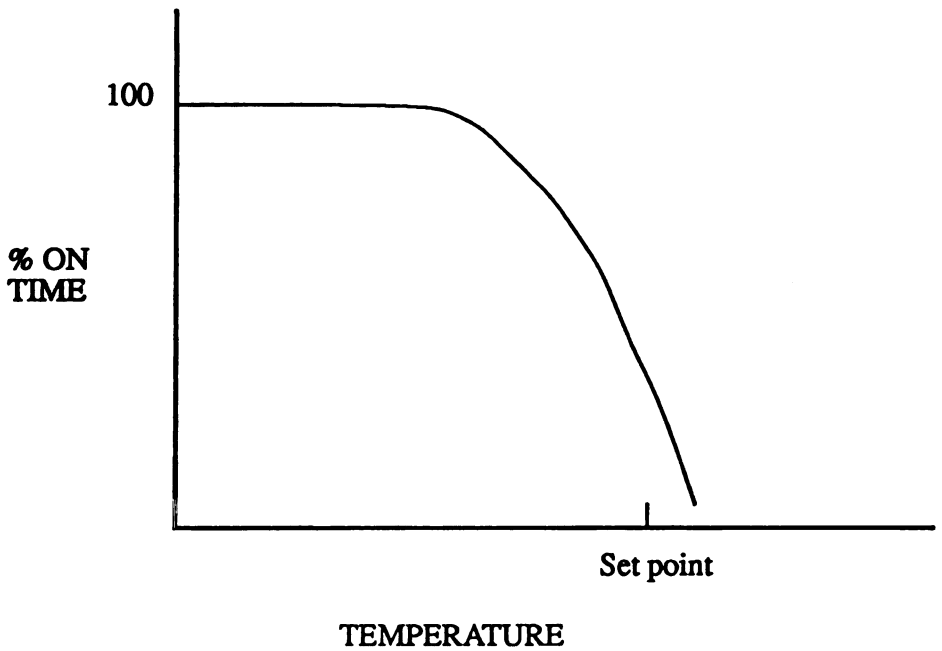

Figure 22. Temperature control of oven.

4.6.3 *Data Acquisition* :

Other signals which are acquired by the computer at the present time include the sound level in decibels and the particle concentration in mg/m^3 inside the aerosolizer. Both signals are analog voltages which are acquired by analog channels in the interface card at any frequency set within the control program.

4.7 Ancillary Equipment :

A heated stage was designed to simulate the phenomena which occur in the heater under an optical microscope. An exploded sketch of the stage is shown in Figure 23. It is a double-walled chamber, the outer wall fabricated out of Teflon and the inner wall made from aluminum. The side walls of the inner chamber are fitted with two firerod heaters (500 Watts, Watlow) controlled by a temperature controller (Omega, CN310 KC). Slits are machined into the chamber to facilitate insertion of the samples from the sides. The samples consist of a stiff aluminum frame with the fibers laid across the center and glued to the sides as shown in Figure 23. The top and bottom panels of the stage have a rectangular hole in the center where a 22 mm cover slip is inserted to permit observation under the microscope.

A consolidation mold was fabricated to consolidate the prepreg tapes manufactured by the process into composite specimens. The open-ended mold is shown in Figure 24. The male and female parts are machined to a close tolerance and are kept in position by means of two locater pins on either side of the mold cavity. Prepreg tapes are laid up in the mold and consolidated to form specimens which are tested for their mechanical properties.

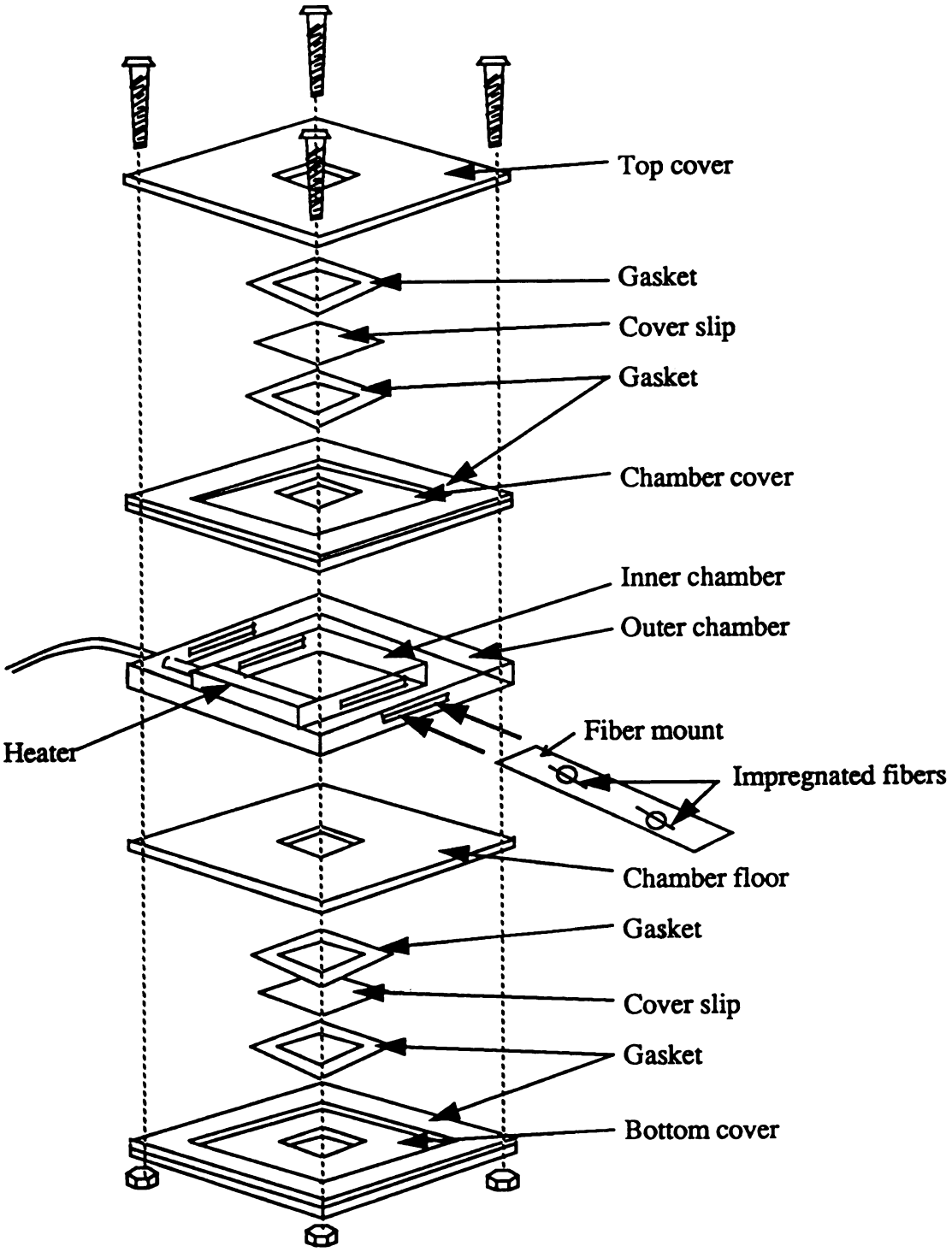

Figure 23. Hot stage for coalescence experiments.

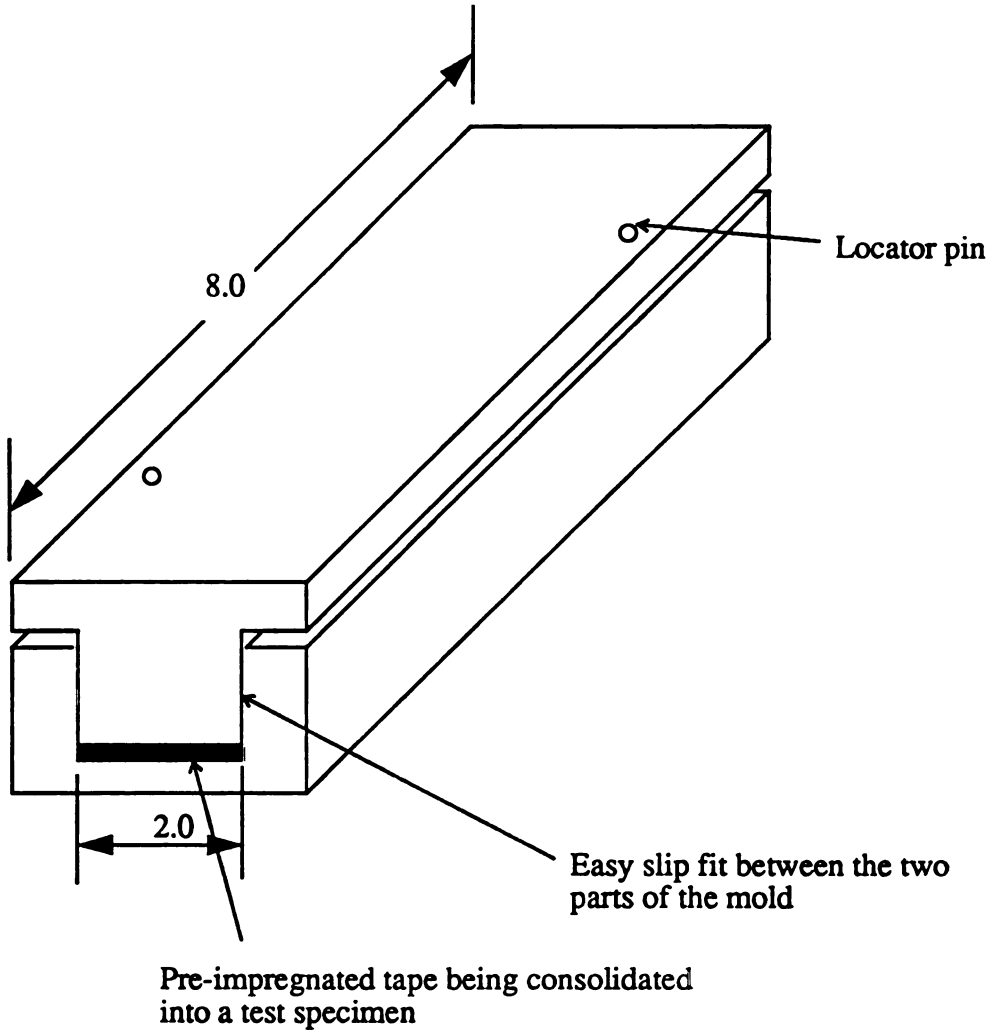

Figure 24. Consolidation mold (All dimensions in inches).

Chapter 5

MATERIAL CHARACTERIZATION

An investigation encompassing the entire manufacturing process was undertaken to gain an understanding of dry powder impregnation processes. A flowchart which summarizes the different thrusts of the investigation is shown in Figure 25. They are - (1) Characterization of the different properties of the thermoplastic matrix and the reinforcing fiber. (2) Tape manufacture which includes a study of the powder prepregging process and its different unit operations i.e. spreading, impregnation and coalescence. (3) Consolidation of the prepreg tapes to form a void-free part. This chapter describes material characterization while subsequent chapters discuss tape manufacture, consolidation and an unified approach for the manufacture of thermoplastic composites.

The fiber and the matrix need to be characterized for their properties in order to optimize processing. These properties include particle size, fiber diameter, charge-to-mass ratio of the particles, electrical conductivity of the fiber, interparticle cohesive forces, matrix viscosity, crystallinity, transition temperatures, fiber-matrix thermal properties and surface energies.

A model fiber-matrix system was used throughout the investigation. The thermoplastic matrix chosen for this study is a polyamide called "Orgasol" manufactured by ATOCHEM, Inc. This material was chosen because of its

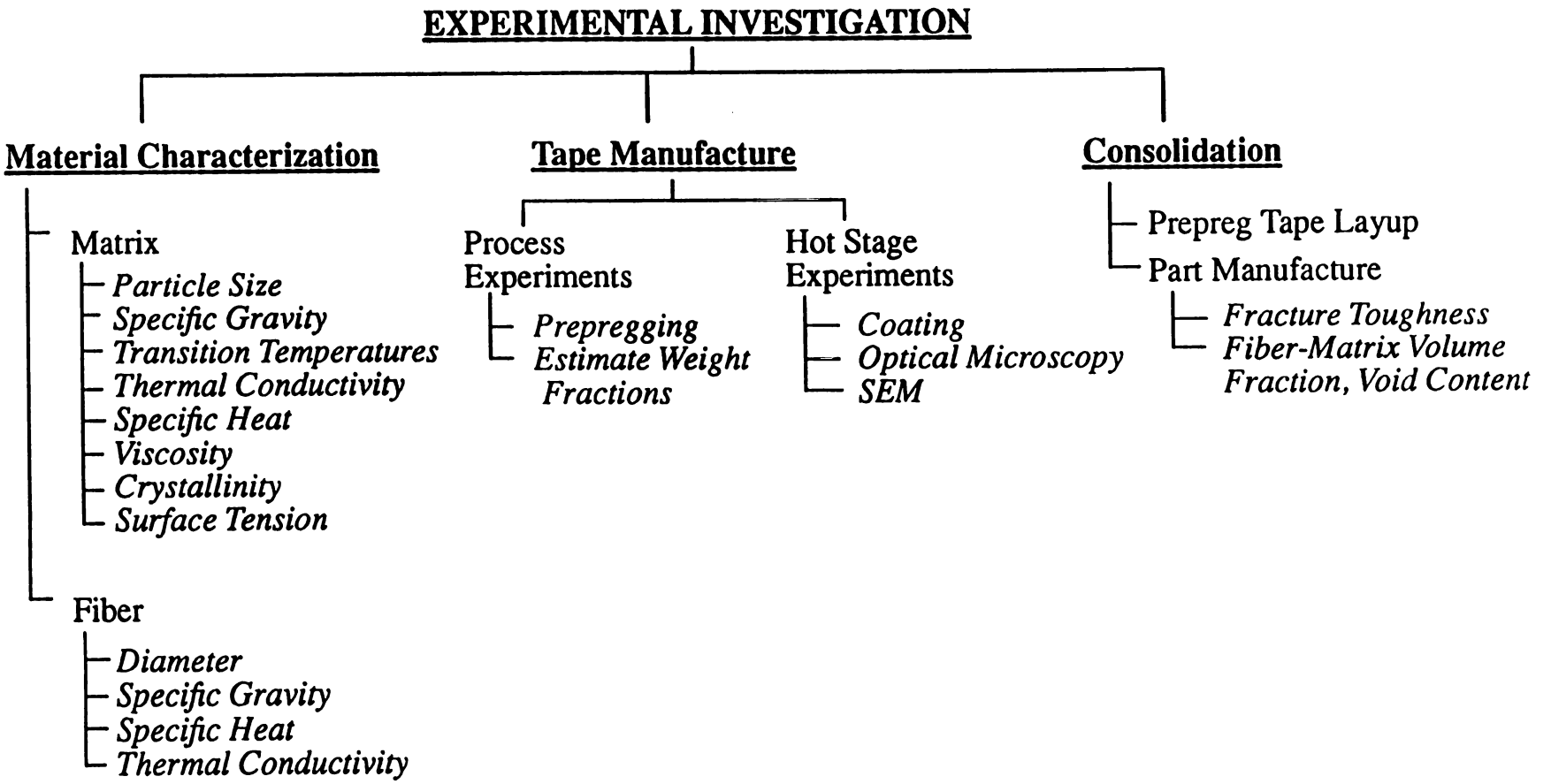

Model Materials : *Polyamide 12 (Orgasol, ATOCHEM, Inc.), Carbon Fibers (AS4-3K, Hercules Corporation)*

Figure 25. Experimental and theoretical investigation.

availabi

Carbon

Hercule

5.1 Pa

determi

The pr

beaker

was th

dispers

particl

was m

consis

the po

compa

accord

where

ϕ_p =

V_p =

R =

ϕ_1 =

ϕ_2 =

availability in the size range of interest - 1 to 30 microns in diameter. Unsized Carbon fibers in fiber tows of 3000 fibers each with the designation AS4-3K made by Hercules, Inc. were used as the reinforcement.

5.1 **Particle Size Analysis** :

The particle sizes of the different powders used in the project were determined using an image analysis technique (Joyce-Loebl Magiscan Version 2A). The procedure used involved suspending particles in a beaker filled with acetone. The beaker was stirred vigorously to break up clumps of powder. A dilute suspension was then deposited on a slide and the acetone allowed to evaporate. This left a dispersion of unagglomerated particles on the slide which was protected from dust particles with the help of a cover slip. The particle size distribution of each powder was measured by image analysis from a population of 500-600 particles which consisted of five different samples taken from various locations in the powder bin.

The choice of a liquid carrier such as acetone in the above technique raises the possibility of swelling of the particles by the acetone. This can be gaged by comparing solubility parameters δ and calculating an interaction parameter χ according to the equation [66] -

$$\chi = \beta_1 + \left[\frac{V_1}{RT}\right](\delta_1 - \delta_2)^2 \qquad [36]$$

where

β_1 = Lattice constant, usually 0.35 ± 0.1

V_1 = Molar volume of solvent, $cm^3/gmole$

R = Gas constant = 1.9872 cal/gmol K

δ_1 = Solubility parameter of solvent, $(cal/cm^3)^{1/2}$

δ_2 = Solubility parameter of polymer, $(cal/cm^3)^{1/2}$

T = Temperature, K

δ for nylon which is a polyamide is 13.6 $(cal/cm^3)^{1/2}$ while that for acetone is 10.0. χ for this system is 1.96. A value of χ greater than 0.5 implies that the polymer-solvent pair is immiscible and there is no swelling of the polymer. Hence acetone was chosen as a liquid carrier for the image analysis experiments.

Image analysis involves the digitization of an image and its subsequent quantification and classification [67]. It consists of five steps - (1) *Image capture* involves the digitization of the image. The image is stored as digital information by dividing it into a square or rectangular grid of elements called pixels each of which can have 64 (6-bit) or 256 (8-bit) intensity levels (grey scales). (2) *Segmentation* is the separation of the regions of interest by thresholding, edge finding and/or region-growing. These operations result in the distinct separation of the object from the background e.g. the powder particle from the slide background. (3) *Object detection* is a data reduction step which reduces the storage requirements of each image. Each object is stored either as run-length encoding (the object start point and length along the raster-scanning horizontal lines) or as boundary chain encoding which stores the coordinates of the boundary. The latter technique reduces the storage requirements for each image as compared with run-length encoding. (4) *Measurement* is the quantitation of the encoded image in terms of dimensions of interest i.e. lengths and areas. (5) *Analysis of the measurements* to arrive at meaningful information such as particle size distributions.

The measurements on the Orgasol 2001 sample were done on 488 particles. The length (the longest dimension), breadth (perpendicular to the length) and detected area were measured for each particle. A plot of length vs breadth of each particle is shown for the entire sample in Figure 26. The plot results in a linear correlation between the two dimensions with a slope close to 1. This implies that the particles are approximately spherical which can also be ascertained from the scanning

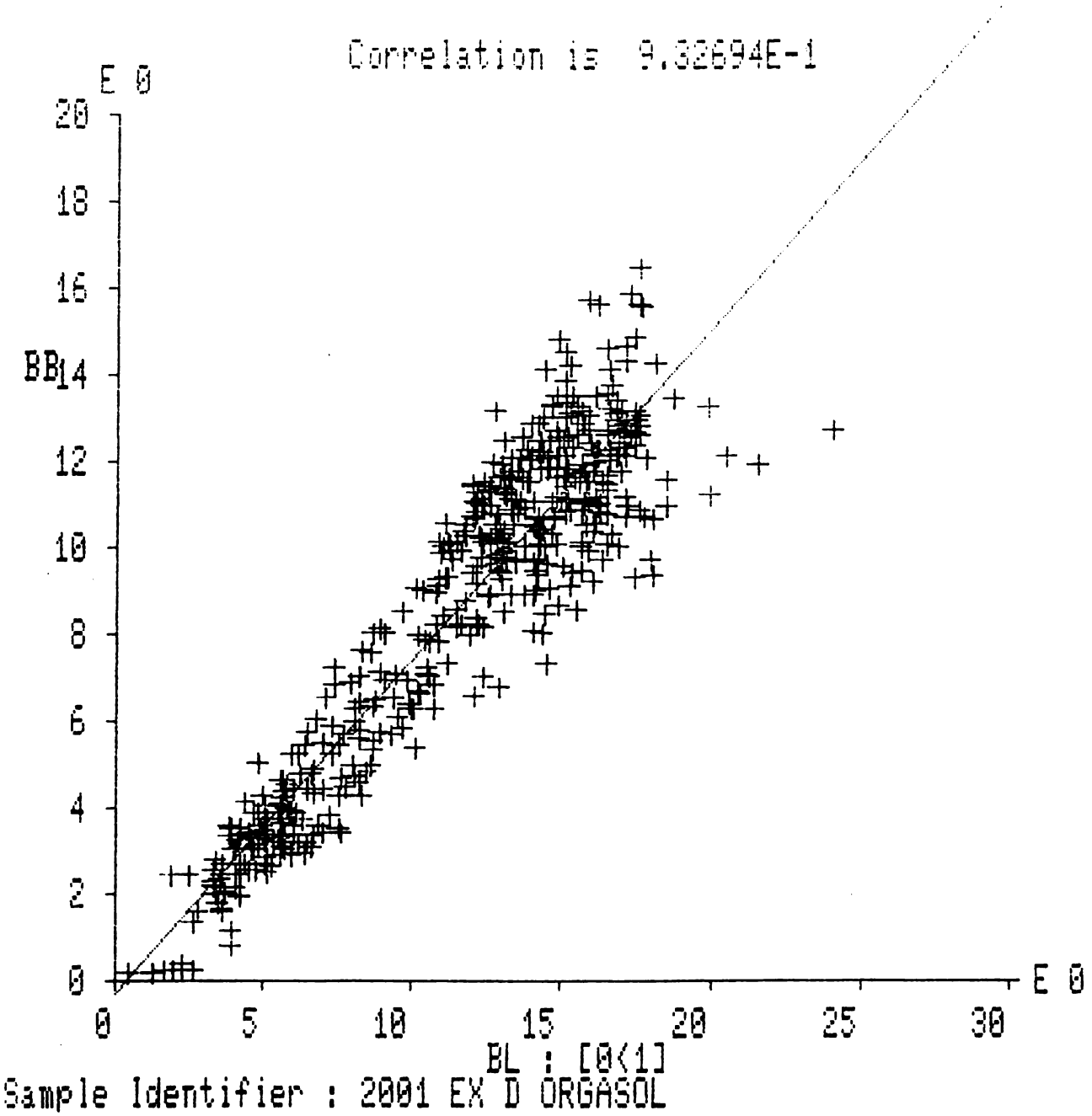

Figure 26. Plot of length vs breadth of each particle.

electron micrograph shown in Figure 27. The particle diameters were therefore calculated from the detected area of each particle by the formula

$$D_p = \left[\frac{4\,A}{\pi}\right]^{1/2} \qquad [37]$$

where

D_p = diameter of particle

A = detected area

The mean diameter of a sample can be represented in different ways as tabulated in Table III [68]. The linear diameter of the Orgasol 2001 Ex D Nat powder was calculated to be 9.16 ± 3.96 microns from equation (37). A histogram of particle diameters as a function of frequency (number of particles in each size range) is shown in Figure 28.

5.2 **Differential Scanning Calorimetry** :

Differential scanning calorimetry was used to estimate transition temperatures, specific heats and crystallinity of the polyamide. The differential scanning calorimeter (DSC) measures temperature and heat flow associated with material transitions and provides qualitative and quantitative information on both endothermic and exothermic processes. A sample pan containing the material and an empty reference pan are placed in the DSC cell. The cell is heated or cooled through a temperature profile. The temperature is monitored by thermocouples placed beneath the cell. A heater maintains the temperature in the cell according to the profile whenever there is an instability e.g. exothermic crystallization, endothermic change of phase etc. This power is recorded as a peak which can be integrated to calculate the total energy transferred to or from the sample. A DuPont DSC 910 with a ramping

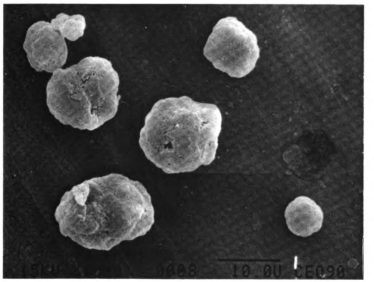

Figure 27. SEM photograph of polyamide particles.

TABLE III. DEFINITIONS OF MEAN DIAMETERS.

Order $(p+q)$	p	q	*Name of* $\bar{D}$ *symbol*	*Where used*		*Other symbols*	*Alternative nomenclature*	
1	0	1	**Linear**	$\bar{D}_l$	Comparison, evaporation	$\bar{d}_{10}$	$x_{NL} = \frac{\Sigma\, dL}{\Sigma\, dN} = \frac{\Sigma x\, dN}{\Sigma\, dN}$	**Number, length mean diameter**
2	0	2	**Surface**	$\bar{D}_s$	Absorption	$\bar{d}_{20}$	$x_{NS} = \frac{\Sigma\, dS}{\Sigma\, dN} = \frac{\Sigma x^2\, dN}{\Sigma\, dN}$	**Number, surface mean diameter**
3	0	3	**Volume, mass**	$\bar{D}_v, \bar{D}_m$	Comparison, hydrology atomizing	$\bar{d}_{30}$	$x_{NV} = \frac{\Sigma\, dV}{\Sigma\, dN}^{1/3} = \frac{\Sigma x^3\, dN}{\Sigma\, dN}^{1/3}$	**Number, volume mean diameter**
3	1	2	**Surface-diameter**	$\bar{D}_{s-D}$	Absorption	$\bar{d}_{21}$	$x_{LS} = \frac{\Sigma\, dS}{\Sigma\, dL} = \frac{\Sigma x^2\, dN}{\Sigma x\, dN}$	**Length, surface mean diameter**
4	1	3	**Volume-diameter**	$\bar{D}_{v-D}$	Evaporation, molecular diffusion	$\bar{d}_{31}$	$x_{LV} = \frac{\Sigma\, dV}{\Sigma\, dL}^{1/3} = \frac{\Sigma x^3\, dN}{\Sigma x\, dN}^{1/3}$	**Length, volume mean diameter**
5	2	3	**Sauter**	$\bar{D}_{Saut}$	Efficiency studies	$\bar{d}_{32}$	$x_{SV} = \frac{\Sigma\, dV}{\Sigma\, dS} = \frac{\Sigma x^3\, dN}{\Sigma x^2\, dN}$	**Surface, volume mean diameter**
7	3	4	**DeBroukere**	$\bar{D}_{DeB}$	Combustion, equilibrium	$\bar{d}_{43}$	$x_{VM} = \frac{\Sigma\, dM}{\Sigma\, dV} = \frac{\Sigma x^4\, dN}{\Sigma x^3\, dN}$	**Volume, moment mean diameter**
							$x_{WM} = \frac{\Sigma\, dM}{\Sigma\, dW} = \frac{\Sigma x\, dW}{\Sigma\, dW} = \frac{\Sigma x^4}{\Sigma x^3}\frac{dN}{dN}$	**Weight, moment mean diameter**

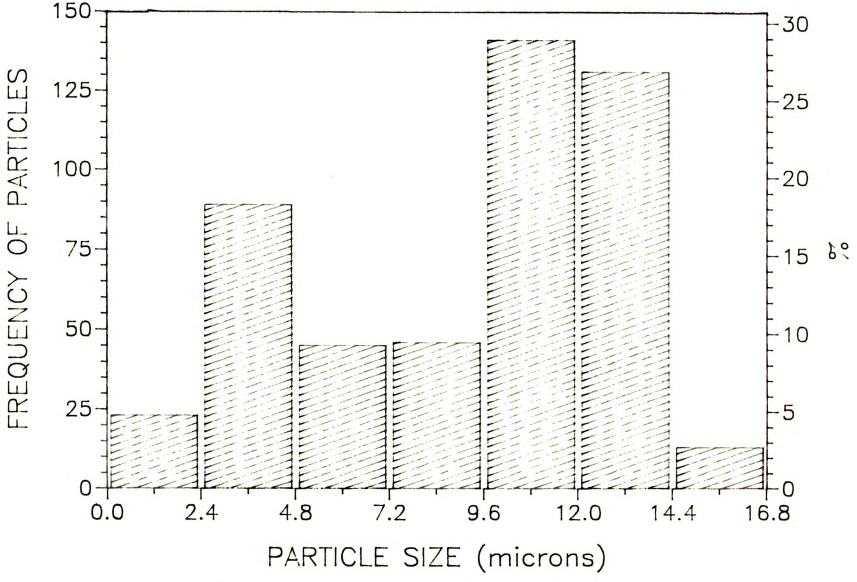

Figure 28. Particle size distribution of Orgasol 2001 Ex D Nat.

rate of 5-10°C/min was used for all the experiments.

A typical scan of the as-received material in the DuPont DSC 910 is shown in Figure 29. The thermogram shows a melting transition with an onset of 171°C. The glass transition temperature which is reported to be 42°C [69] for polyamide-12 could not be identified in the DSC runs. The endothermic heat of fusion was calculated by peak integration to be approximately 100 Joules/gm for the as-received powder.

The *specific heats* were estimated by the following procedure -

(1) Perform a baseline run with two empty pans in both the sample and reference holders.

(2) Repeat with sample pan filled with powder.

(3) Subtract baseline run from sample run.

(4) Calculate specific heat by the formula [70] -

$$C_p = \frac{60\ E}{H_r}\left[\frac{Y}{m}\right] \qquad [38]$$

where

E = Cell constant, dimensionless (1.1577 for the DSC 910)

H_r = Heating rate in °C/min

Y = Absolute value of heat flow in mW after subtraction

m = Weight of the sample in mg

C_p = Specific heat, J/gm°C

The measured values which are listed in Table IV showed a wide degree of experimental scatter. They ranged from 0.58 ± 0.15 at 40°C to 0.81 ± 0.16 cal/gm/°C at 140°C (average of 5 runs) prior to melting.

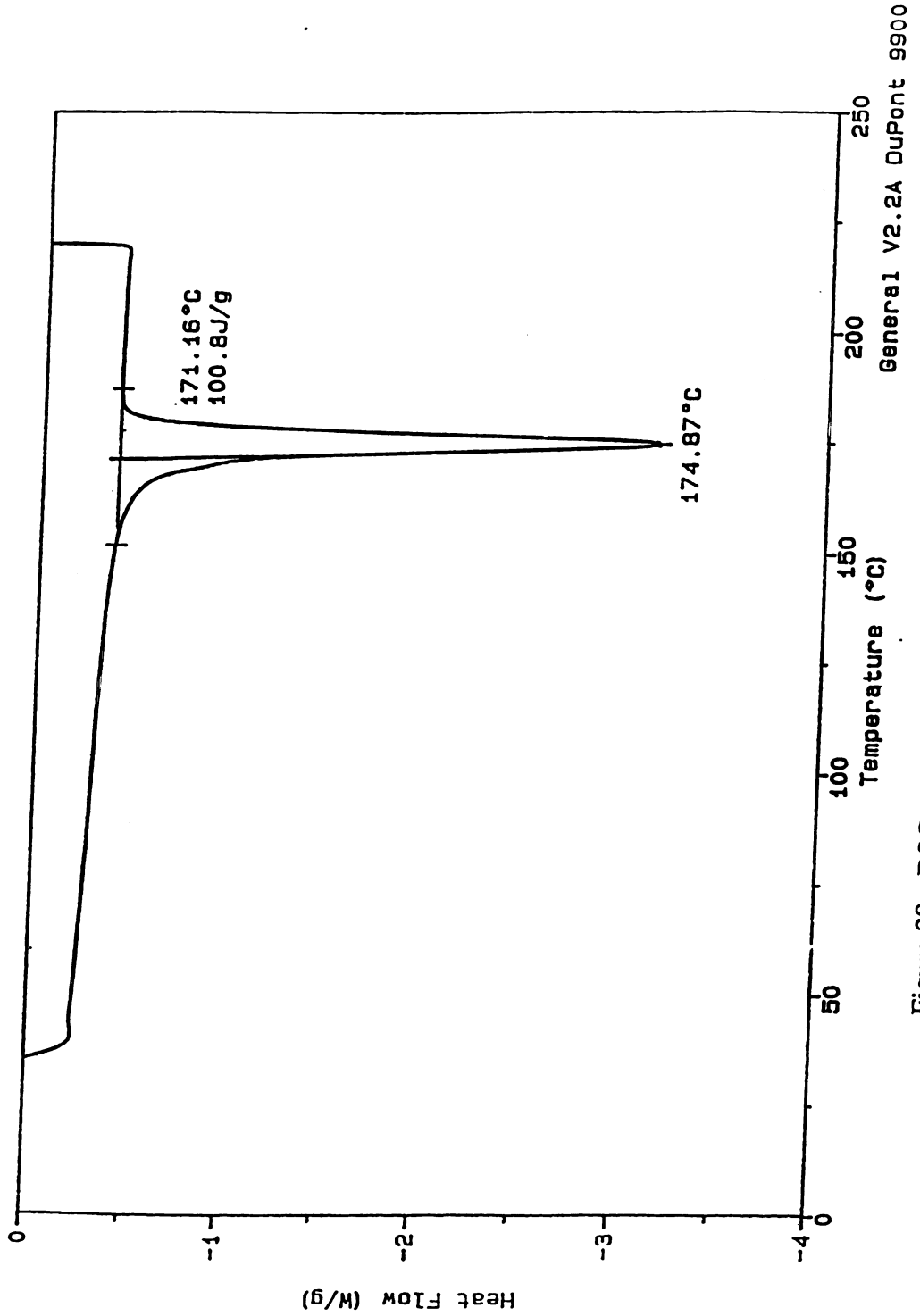

Figure 29. DSC thermogram of as-received polyamide.

TABLE IV. SPECIFIC HEATS OF POLYAMIDE

Temperature, °C	C_p, cal/gm/°C
40	0.58 ± 0.15
60	0.63 ± 0.16
80	0.68 ± 0.17
100	0.71 ± 0.17
120	0.76 ± 0.17
140	0.81 ± 0.16

DSC is the most widely used instrument for the measurement of degree of crystallinity in polymers. The weight-fraction degree of crystallinity, $w_{c,h}$, can be defined [71] as

$$w_{c,h} = \frac{\Delta H_{fT}}{\Delta H_{f,cT}} \qquad [39]$$

where

ΔH_{fT} = Measured heat of fusion referred to temperature T

$\Delta H_{f,cT}$ = Heat of fusion of the 100% crystalline polymer determined at T

The degree of crystallinity of the polyamide could not be estimated due to lack of reliable values for the heat of crystallinity of 100% crystalline polyamide. However, the endothermic heats associated with melting were computed for different samples in an attempt to gage relative crystallinity. All the baselines for integration were constructed as follows - (1) Plot heat flow (J/gm) and the first derivative i.e. the heat flux (J/gm/°C) as a function of temperature in the same graph. (2) Determine the temperatures at which the first derivative changes prior to the melting transition and falls back to a constant value after the melting transition. (3) Draw a baseline for integration between these two points. This procedure is illustrated in

Figure 30.

The relative crystallinities of the polyamide subjected to different thermal histories i.e. annealing at a constant temperature (165°C) for 2 hours, quenching with liquid nitrogen and different cooling cycles from 1°C/min to 20°C/min were estimated by the above procedure. Programmed heating experiments performed in the DSC show that the endothermic heat of melting of the neat resin does not change significantly for the different processing conditions. Table V lists the endothermic heats calculated from the integration of peak areas for all the runs. The average endothermic heat calculated from the 15 runs is 50.8 ± 2.9 J/gm. The quenched samples and the ones cooled at 20°C/min were the only ones which showed an exotherm associated with crystallization of the amorphous portion of the polyamide in addition to the melting endotherm (Figure 31).

TABLE V. CRYSTALLINITY OF POLYAMIDE

No	Thermal History	Endothermic Heat (J/gm)
1	1°C/min cool	54.7
2	1°C/min cool	52
3	2°C/min cool	51.5
4	5°C/min cool	49.9
5	5°C/min cool	49.9
6	5°C/min cool	48.9
7	5°C/min cool	50.1
8	5°C/min cool	49.6
9	Ambient cool (5-10°C/min)	50
10	Ambient cool (5-10°C/min)	49.3
11	Ambient cool (5-10°C/min)	46.7
12	Ambient cool (5-10°C/min)	50.3
13	Cooling water (20°C/min)	45.7
14	Quenched sample	55.7
15	Quenched sample	55.6
16	Anneal at 165°C (2 hrs)	52.9

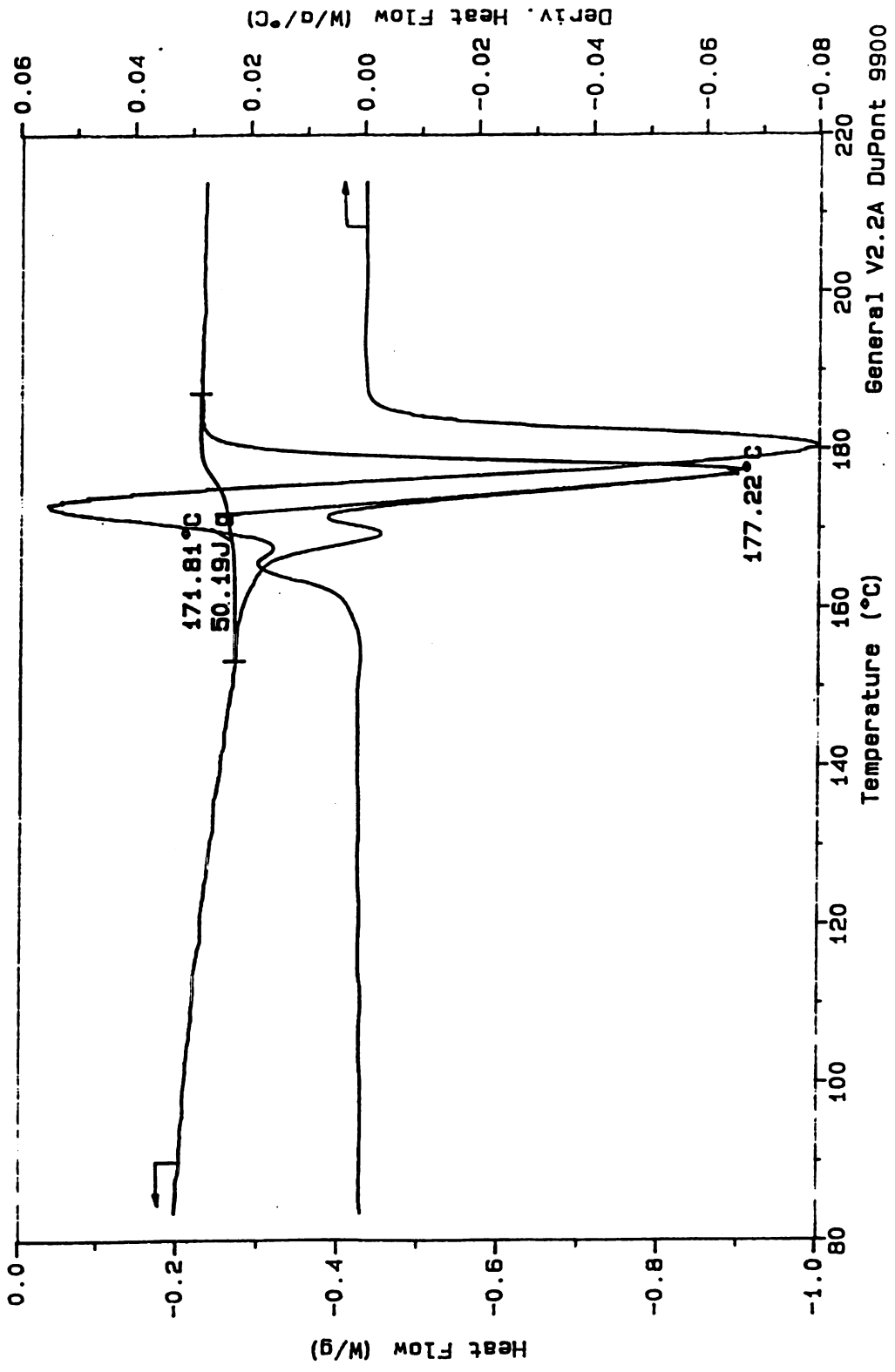

Figure 30. Estimation of relative crystallinity of polyamide.

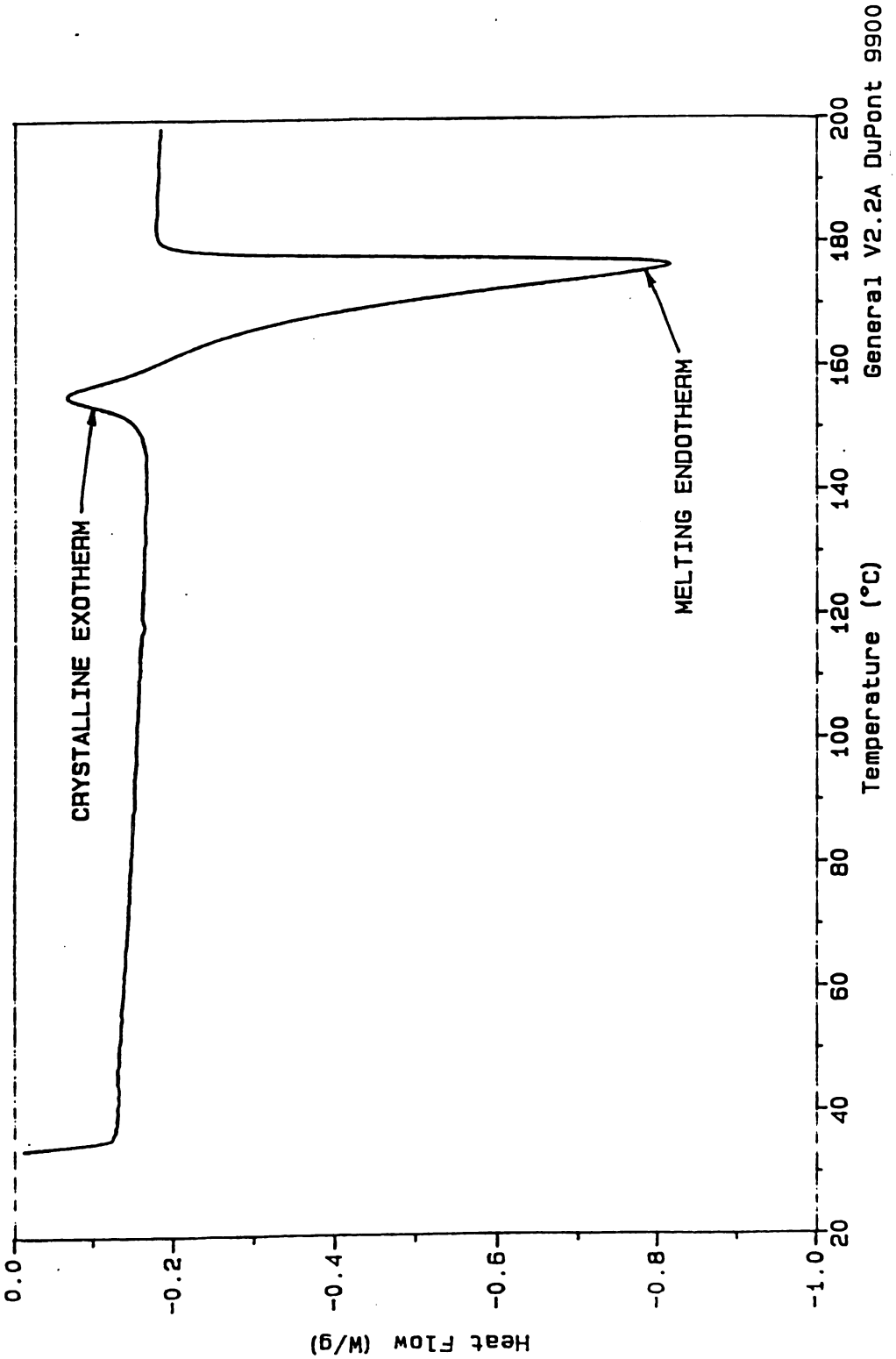

Figure 31. DSC thermogram of polyamide quenched in liquid nitrogen.

One feature that the DSC runs bring out is that the as-received powder shows a single endothermic peak while all samples which have a thermal history i.e. heated beyond the melting point at least once show two endothermic peaks adjacent to each other (Figure 30). Though the reason for this is not clear, it is postulated that the existence of different crystalline states for polyamides [72] may be a contributing factor. It can also be seen that the as-received powder has a much higher level of crystallinity than any of the samples which were subjected to different thermal cycles.

5.3 **Viscosity** :

The objective of this exercise was to generate a master curve in order to be able to predict viscosities at any value of shear rate and temperature. Viscosity was estimated by performing steady shear experiments in a parallel plate rheometer (RMS800 Rheometrics Mechanical Spectrometer) and a mastercurve generated for shear rates 0.1-100 sec^{-1} for a temperature range from 180°C to 220°C. Parallel plate or cone and plate experiments can be conducted to measure viscosities. A parallel plate configuration was chosen because of the availability of disposable plates since it is very difficult to dissolve and hence clean the polyamide off the plates (the solvent recommended by ATOCHEM Inc. is m-cresol at 50°C). The torque transducer of the instrument has a range of 2-2000 gm cm. The lower end of this range is the one of interest in this set of experiments. 50 mm diameter parallel plates were used (25 mm plates are also available) as lower shear rates are attainable with the larger diameter. The lowest attainable shear rate with this dimension (50 mm) is 0.1 sec^{-1}. The experiments were done in the range 0.1-100 sec^{-1} at different temperatures between 185-220°C. The material showed signs of degradation at temperatures above 240°C. The zero shear viscosity could not be predicted because the lower limit of 2 gm cm of the torque transducer precluded experiments at shear

rates below 0.1 sec^{-1}.

Two types of experiments were carried out -

1. Steady shear experiments were done in which the temperature is kept constant and the shear rate is varied from 0.1 to 100 sec^{-1}. Five readings were taken per decade (tenfold increase in shear rate) and 30 seconds allowed for the instrument to reach equilibrium before each reading. Two readings were taken, one each in the clockwise and counter clockwise directions and an average was computed.
2. A strain sweep was done at 1 rad/sec and 215°C to determine the region over which G′ and G″ remain constant with strain rate. It was intended that dynamic experiments be performed at this strain rate.

Dynamic Experiments :

The strain sweep experiments revealed that the torque values are above 2 gm cm (the sensitivity of the instrument) only after a strain rate of 30 % or higher. The G′ and G″ values also did not stay constant over this range of strain rates. Hence it was not possible to determine the linear region over which dynamic experiments could be performed. This led to the conclusion that steady shear experiments were the only possibility for this project.

Steady Shear Experiments :

25 mm parallel plates were initially used for the experiments. Torque readings of 2 gm cm or higher were achieved only at shear rates of 10 sec^{-1} or more. The minimum measurable shear rate was lowered to 0.1 sec^{-1} by using 50 mm parallel plates. For a particular shear rate, the torque required to keep the upper plate stationary against the movement of the lower plate and the polymer melt decreased with increasing temperatures.

The problems encountered during the experiments were - (1) Extrusion of the sample occured at high shear rates. The centrifugal forces at high shear rates (or high angular frequencies) caused the melt to squeeze out from the sides. This is unavoidable and the upper limit of the shear rate for each experiment was determined by monitoring the experiment and terminating it when extrusion occured. (2) The presence of bubbles in the melt can reduce the measured torque. This problem was countered by letting the sample equilibrate on the bottom plate at the desired temperature before bringing the two plates together to the desired gap width. This procedure eliminated the presence of bubbles most of the time. Another option tried out was to extrude the sample (and hence the bubbles) at very high shear rates, decrease the gap width to account for the decreased volume and then conduct the experiment. (3) Non-isothermal experiments. There was a variation of 0.2-0.6°C in the temperatures measured in any particular experiment. This problem was solved by treating each viscosity-shear rate measurement as a discrete point, conducting many experiments and grouping together all points ± 0.1°C to obtain an isothermal run. This scheme also served as a check on the accuracy of different runs conducted at the same temperature.

Data reduction was done as follows [73] -

(1) Classify data from different experiments into isothermal sets ± 0.1°C.

(2) Calculate shear stress, τ, which is the product of the viscosity and shear rate at each point.

(3) Calculate a reduced shear stress, τ_r, at a reference temperature of (197.3°C).

$$\tau_r = \tau \frac{T_0 d_0}{T d} \qquad [40]$$

where

T_0 = reference temperature in K (197.3+273)

d_0/d = ratio of reference to actual density (1 for most polymers in the region of

interest).

(4) Plot $\log(\tau)$ vs $\log(\dot{\gamma})$ where $\dot{\gamma}$ is the shear rate for each temperature.

(5) Fit a straight line using least squares for each isothermal set of data.

(6) Calculate a_T based on the amount of shifting needed to move each of the isothermal lines to a reference temperature (197.3°C).

(7) Plot $\log(a_T)$ vs $\log(1000/T)$ and fit a line to this plot.

(8) Determine the reduced shear rate-viscosity master curve.

The prediction of viscosity at any temperature and shear rate from the above mastercurve consists of the following steps :

(1) Calculate a_T for the particular temperature

$$\log(a_T) = 2.664031(1000/T) - 5.680173$$

(2) Calculate τ_r

$$\log(\tau_r) = 0.9813163\log(\dot{\gamma}) + 2.702483$$

(3) Calculate reduced viscosity, μ_r

$$\mu_r = \tau_r/\dot{\gamma}$$

(4) Calculate actual viscosity, μ

$$\mu = a_T \mu_r \left[\frac{T}{T_0}\right]$$

A viscosity-temperature plot is shown in Figure 32 along with the relevant equations for the shift factor, a_T and the reduced shear stress, τ_r (reduced shear stress in dyne/cm^2 reduced to a reference temperature of 197.3°C). In the equations, T is given in Kelvin and $\dot{\gamma}$, the shear rate in sec^{-1}. The zero shear viscosity is not reported since none of the curves of viscosity vs shear rate at constant temperature reached a plateau for shear rates greater than 0.1 sec^{-1}.

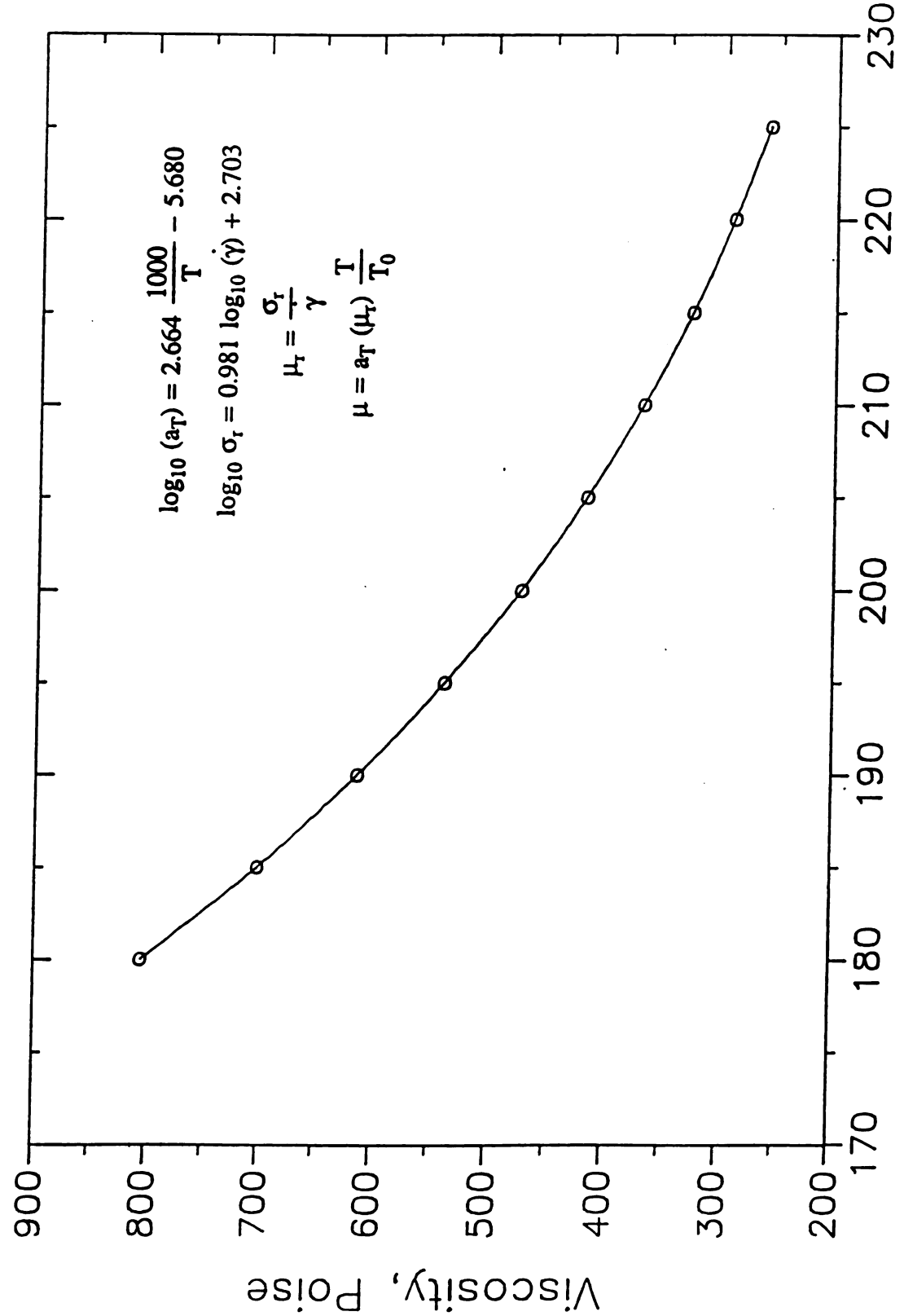

Figure 32. Viscosity-temperature plot of polyamide at a shear rate of 0.1 sec^{-1}.

5.4 Summary of Properties :

In addition to the above measured properties, other relevant values were taken from the data sheets provided by the manufacturers and from references. The material properties of the polyamide and the carbon fibers are tabulated in Table VI.

TABLE VI. MATERIAL PROPERTIES OF POLYAMIDE AND CARBON FIBERS

Property	Value
Polyamide :	
Particle size, microns	9.2 ± 4
Specific gravity	1.02 [a]
Apparent density (loose), gm/cm^3	0.20-0.35 [a]
Apparent density (compact), gm/cm^3	0.35-0.50 [a]
Melt temperature, °C	175
Specific heat, cal/gm/°C	
@ 40°C	0.58 ± 0.15
@ 140°C	0.81 ± 0.16
Thermal Conductivity, W/m/°C	0.22-0.31 [b]
Viscosity, Pa·s	
(0.1 sec^{-1}, 197.3°C)	52.6
Surface tension, dyne/cm	0.30 [c]
Carbon Fibers :	
Diameter, microns	8.0 [d]
Specific gravity	1.80 d
Specific heat, cal/gm/°C	
@ 75°C	0.22 [d]
@ 175°C	0.27 [d]
Thermal conductivity, W/m/°C (parallel to fiber axis)	5.73 [e]

a Manufacturer's literature (ATOCHEM, Inc.)
b Reference 43
c Reference 44
d Manufacturer's literature (Hercules Corporation)
e Reference 45

Chapter 6

TAPE MANUFACTURE

This chapter describes the experimental and theoretical analyses of the different unit operations involved in the manufacture of prepreg tapes. The topics discussed in this chapter are -

(1) The behavior of fine polymer powders in a conventional fluidized bed and in an aerosolizer.

(2) The operation of spreading and the performance of the spreader in separating fiber tows into their individual filaments.

(3) The coalescence operation which includes all the physical phenomena which occur in the heater.

(4) An evaluation of the entire process and its efficacy in manufacturing flexible prepreg tapes of controlled resin content.

6.1 **Fluidized Bed Behavior of Cohesive Polymer Powders** :

Section 3.1.2 discussed the classification of fine powders below 30 microns broadly into Type AC and Type C powders. A fluidization column was built to investigate the behavior of these powders the results of which are presented in this section.

6.1.1 *Experimental* :

All experiments were conducted in a 5 cm i.d., 200 cm tall glass column. Pressure taps were mounted at various points so that the pressure drops across the distributor and the bed could be measured. The fluidizing medium was Argon, dried of moisture by passing through a bed of silica gel. The static bed height used for all the experiments was about 60-65 cm. The distributor used for the study was a fritted glass disc sandwiched between two pieces of Whatman No 5 filter paper. The pressure drop developed across the distributor as a function of gas velocity is shown in Figure 33.

The powders studied were all of the same kind - a polyamide (Orgasol 2002 D Nat series, specific gravity 1.02-1.03, manufactured by Atochem Inc.). The particle size distributions of the three powders, fine, medium and coarse are shown in Figure 34. The properties of the fine, medium and coarse powders are shown in Table VII. The particle sizing was done on a Joyce-Loebl Image Analyzer (Magiscan Version 2A). The particle diameters shown in Figure 34 are the Sauter diameters which are defined in Table III (page 75). Sauter diameters can be measured by sieving techniques which are commonly used for particle size characterization. They are a popular form of particle size representation in the fluidization literature and are used in this section to facilitate comparisons with prior work.

All experiments were performed as follows :

(1) The bed was aerated at approximately 9 cm/s for 1-2 minutes. This was done to get rid of all cracks and channels which may have developed during the previous experiment.

(2) The gas flow was then shut off and the bed allowed to contract and settle down.

(3) The gas valve was reopened to the desired velocity of the experiment as indicated by a flowmeter.

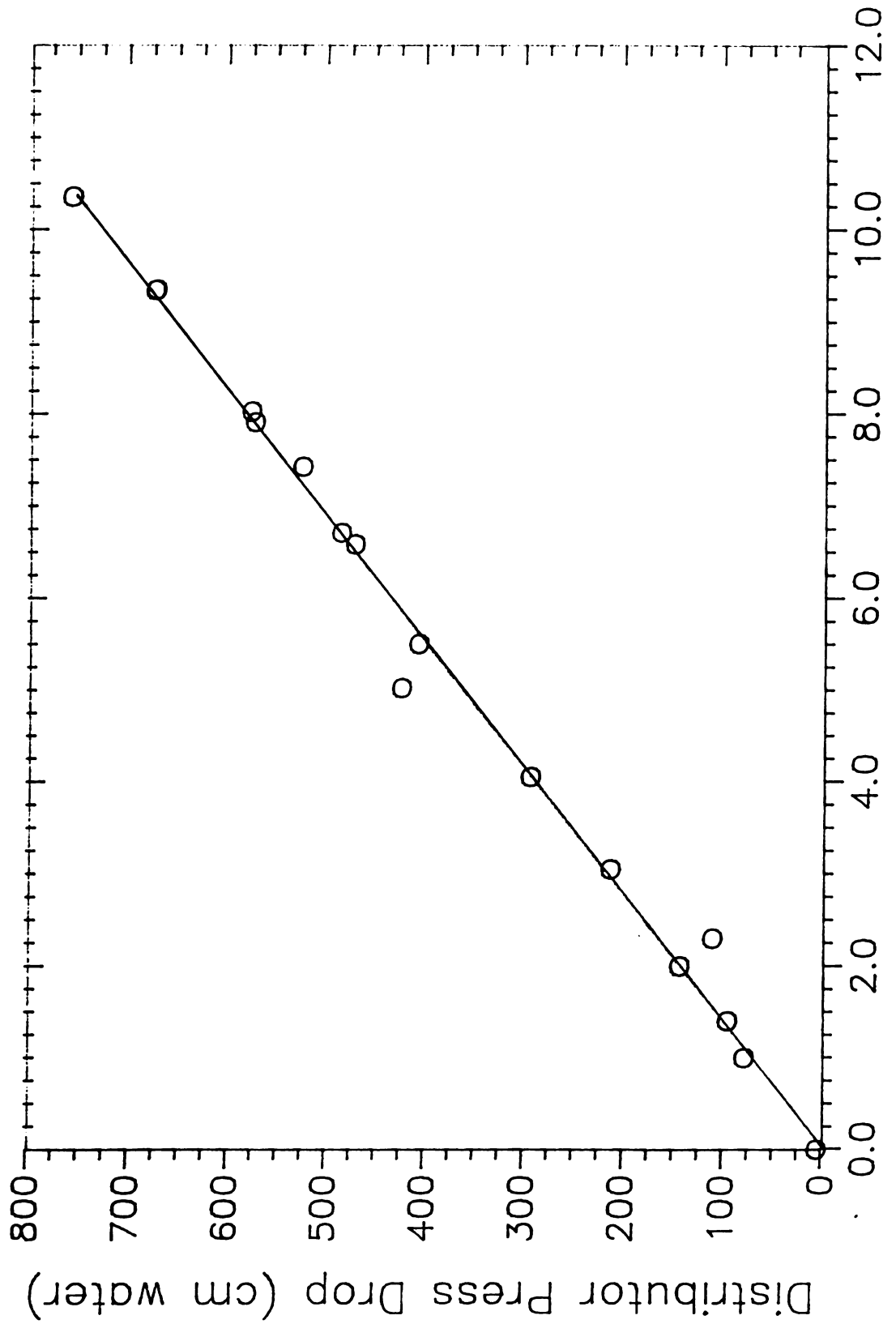

Figure 33. Distributor pressure drop as a function of gas velocity.

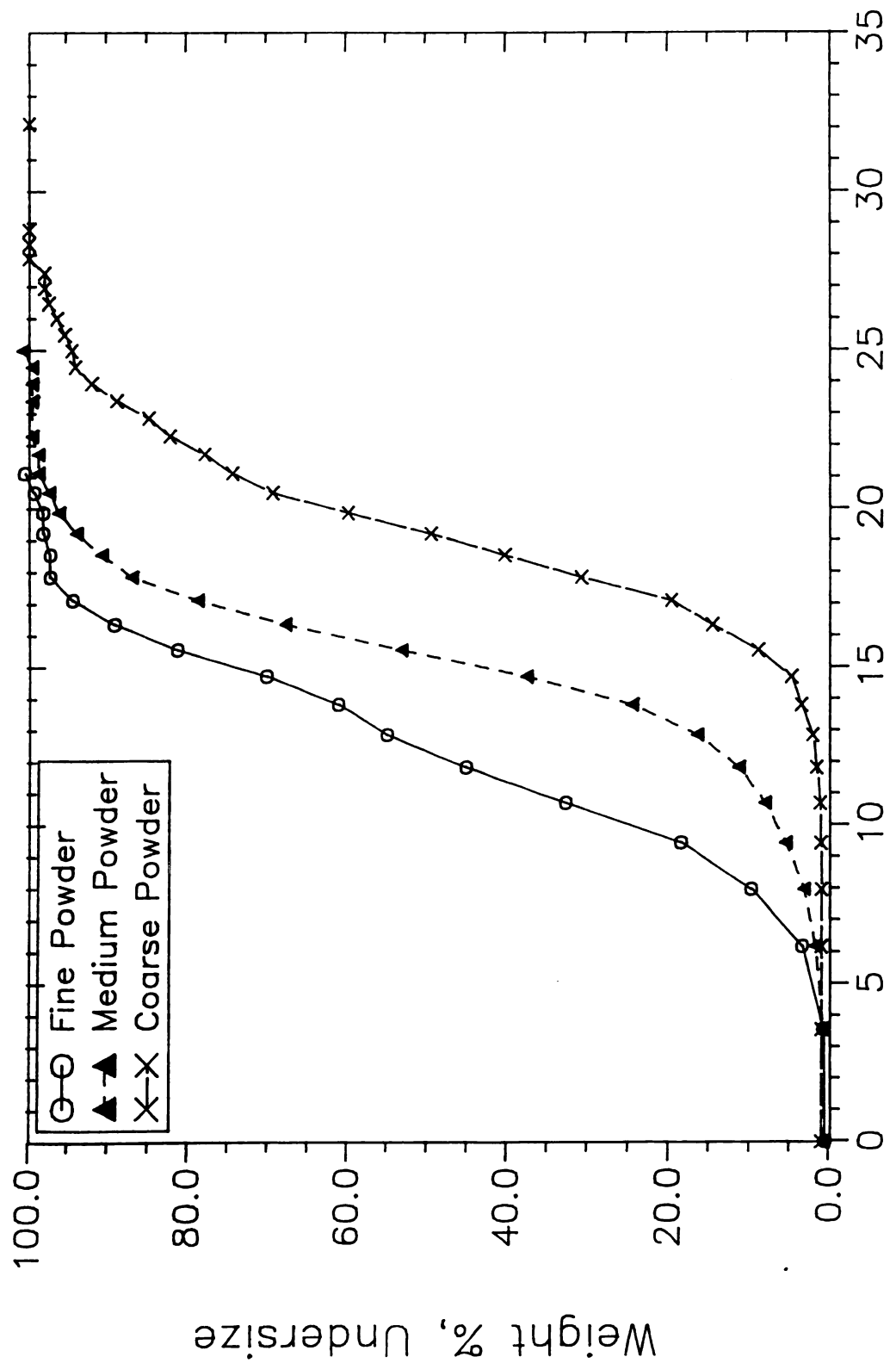

Figure 34. Particle size distributions of the fine, medium and coarse powders.

TABLE VII. PROPERTIES OF POWDERS†

Powder	Specific gravity	d_p (microns)	r/d_{pm}	Type of Powder
This work :				
Fine Polyamide	1.02	12.2	0.28	C
Medium Polyamide	1.02	14.9	0.15	AC
Coarse Polyamide	1.02	19.4	0.16	AC
Geldart et al. [25] :				
FRF20	2.43	12	0.55	C
FRF40	2.43	10	0.5	C
FRF85	2.43	5	0.47	C
Corvic/M	1.637	30	0.8	C
Corvic/U	1.637	26	0.65	C
α320–N	3.97	30	0.09	AC
α360	3.97	24	0.14	AC

† $r = (d_{84\%} - d_{16\%})/2$
$d_{16\%}$, $d_{84\%}$ = Particle sizes below which there are 16 and 84 weight % particles respectively
d_p = average particle size (Sauter diameter)
d_{pm} = median particle size (based on weight)

The bed pressure drop measurements shown in Figures 35, 36, 38, 39, 41 and 42 were all taken 11 minutes after the experiments were begun to allow the pressure drop to stabilize to a constant value. The values have been normalized with the weight of the powder packed into the bed divided by the cross sectional area (i.e. the hydrodynamic pressure drop).

6.1.2 *Fluidized Bed Behavior* :

Fine Powder :

All attempts to sustain the fine powder in a fluidized state for long periods of time resulted in failure. The formation of cracks of different orientations, lengths and tortuosities is observed at velocities less than 3.6 cm/sec. The bed is therefore in an expanded state, though there is no actual fluidization per se. The presence of cracks results in the development of a sizeable pressure drop across the bed as shown in Figure 35. The reproducibility of these measurements is poor because each experiment produces a fresh set of cracks, with their "density", inclinations and tortuosities determining the pressure drop.

At higher velocities, the bed initially fluidizes but cracks and vertical channels are seen to form. These vertical channels extend across the entire bed with time resulting in defluidization of the bed. Most of the cracks which are present drain into these vertical channels. This sequence of initial fluidization with crack formation, followed by vertical channeling eventually leading to defluidization is observed at all velocities higher than 3.6 cm/s. The time span of the initial fluidization roughly increases with an increase in velocity eg. 5 minutes at 8.9 cm/s as opposed to 1.5 minutes at 4.24 cm/s. Figure 36 shows that the bed pressure drop decreases with increasing velocity due to increased gas bypassing through vertical channels. It also shows the variation of bed pressure drop with time at constant velocities. As can be seen, the reproducibility of bed pressure drop is suspect. The primary reason for this is the presence of cracks as was noted earlier.

A profile of such a bed is shown in Figure 37a. Cracks are the predominant means for the transport of gas across the bed at low velocities (less than 3.6 cm/s). The vertical channels shown form only at higher velocities.

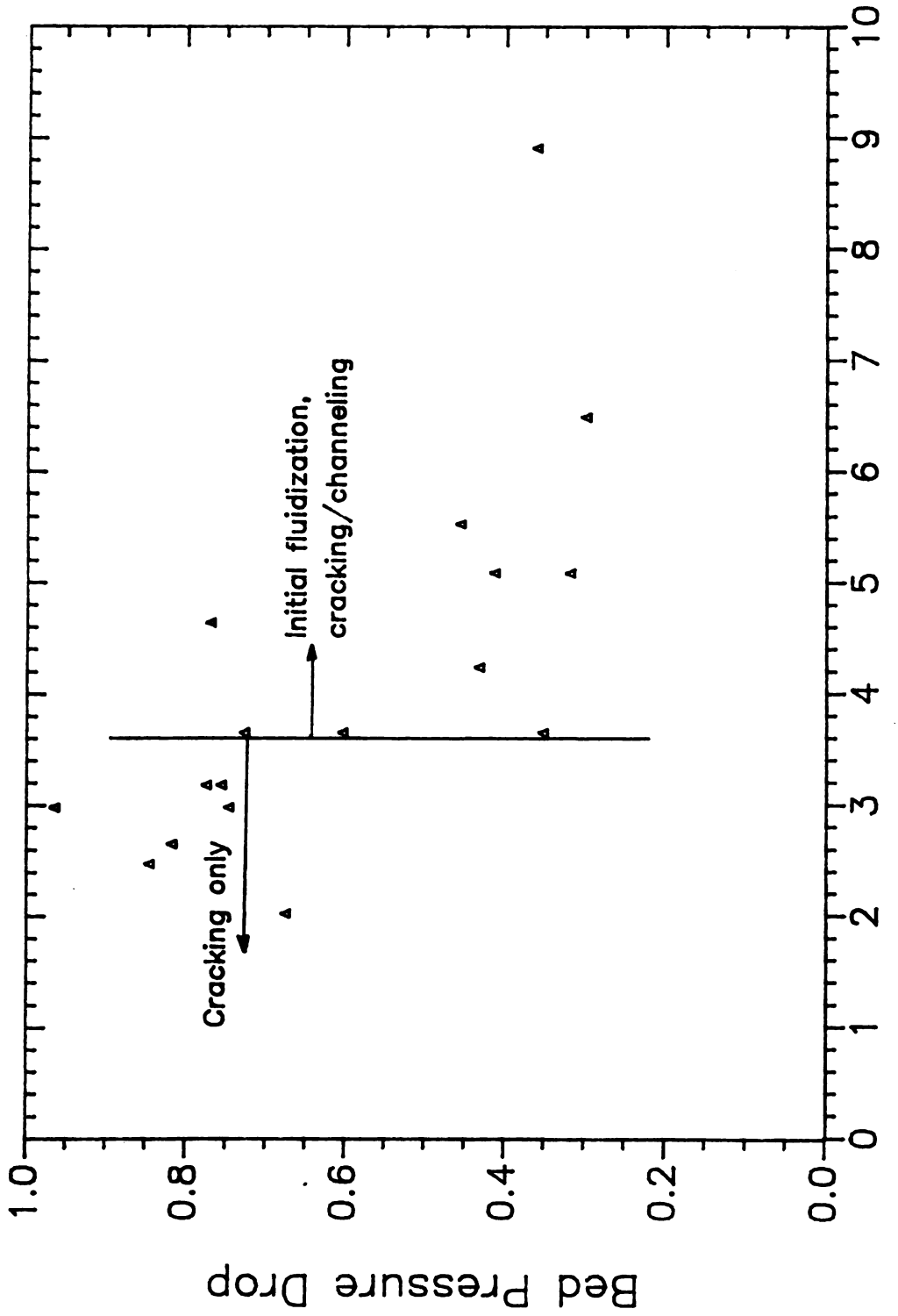

Figure 35. Bed pressure drop vs velocity, fine powder.

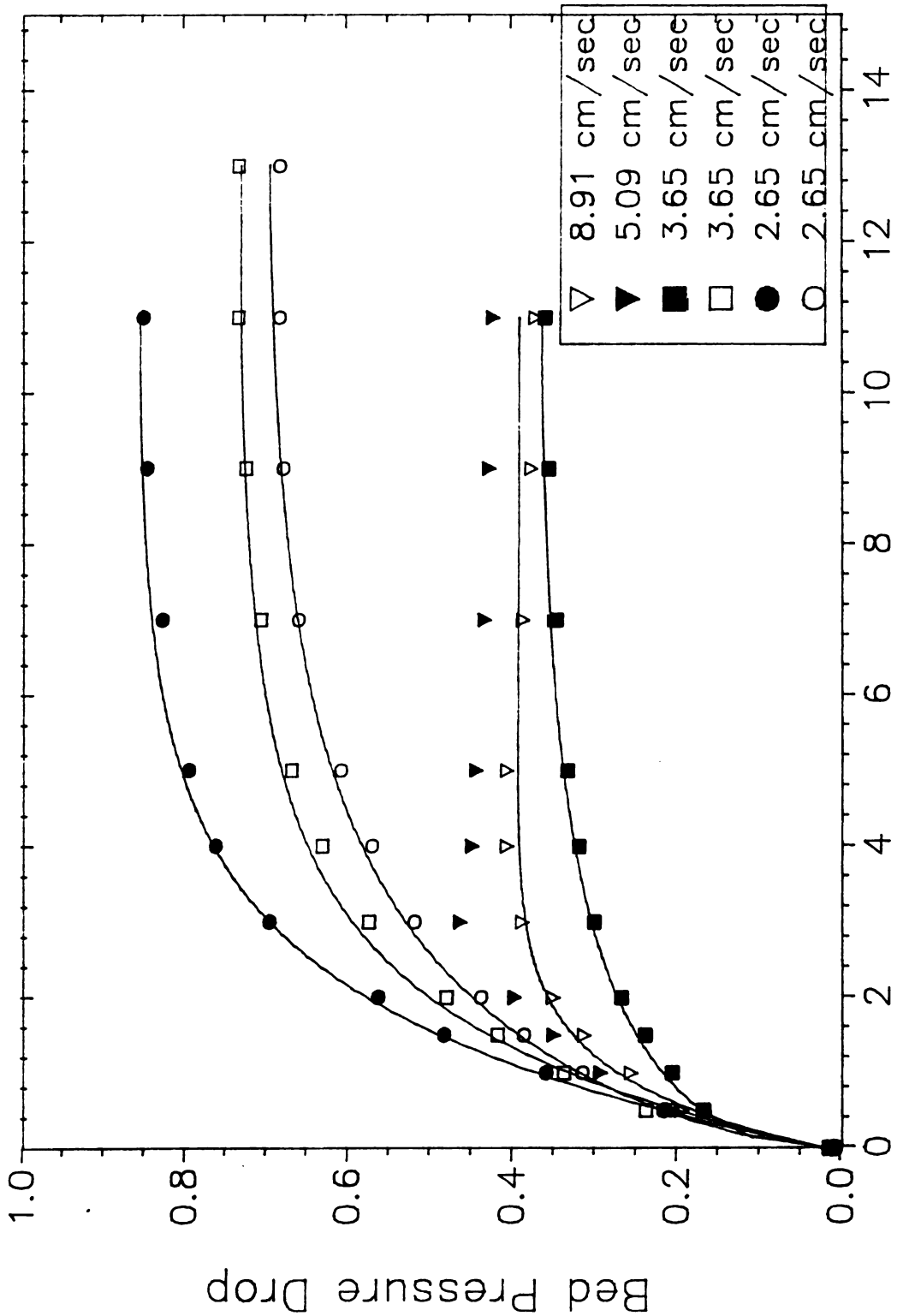

Figure 36. Bed pressure drop vs time, fine powder.

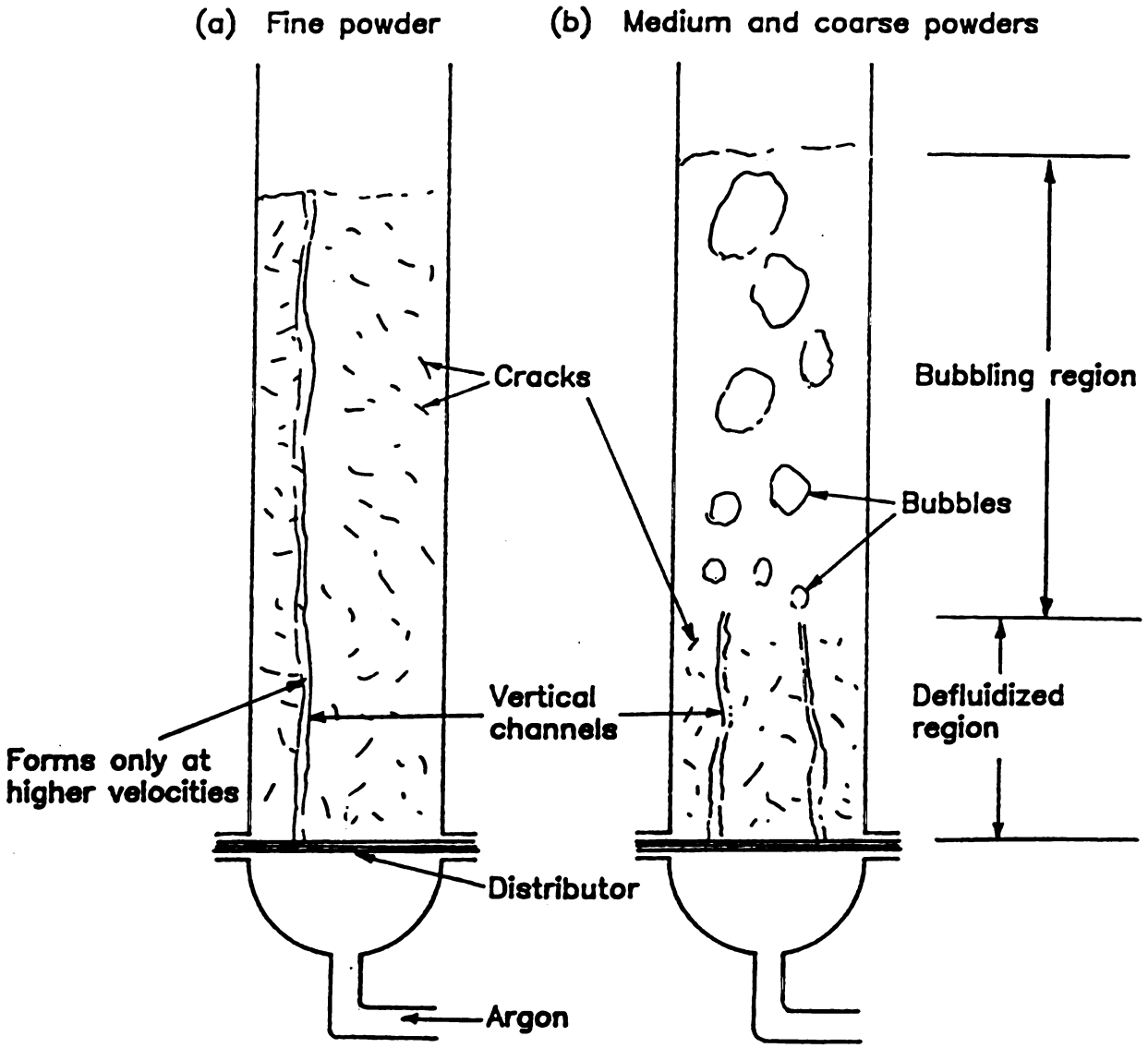

Figure 37. Fluidized bed profiles.

Medium Powder :

The fluidization behavior of the medium powder is different from that of the fine powder though the difference in particle size is less than 3 microns. A profile of a typical fluidized bed observed in this case is shown in Figure 37b. There is a defluidized region near the distributor where only cracks and channels form and there is no true fluidization. Above the defluidized region, bubbles start forming which increase in size as they proceed towards the top of the bed. These bubbles keep disrupting the cracks and channels as they form thus maintaining the bed in a fluidized state. Hence bubbles lend a measure of stability to the fluidized bed.

At velocities less than 4.6 cm/s, the bed initially fluidizes with a profile as described above. But the defluidized region grows with time, eventually traversing the entire length of the bed. The only point in Figure 38 which shows an unusually high pressure drop ratio (0.65 at a velocity of 3.65 cm/s) defluidized at 13 minutes dropping down to a pressure drop of 0.37. In most cases, a vertical channel was seen to form alongside the wall.

At velocities greater than 4.6 cm/s, the bed remained in a fluidized state indefinitely. The scatter in the data is caused by variations in the depth of the defluidized region. This trend is more noticeable at lower velocities. At higher velocities i.e. greater than 6 cm/s, the defluidized region is so small that the scatter in the data is greatly reduced. Also, at lower velocities, one sees a slightly higher pressure drop. It is postulated that the defluidized region develops a higher pressure drop than an equivalent length of the bubbling region. The ability of the cracks/channels to generate a sizeable pressure drop was amply demonstrated in the fine powder experiments. Figure 39 shows the variation of the bed pressure drop with time at constant gas velocity. It is obvious from this Figure that the bed fluidizes initially at all velocities. The cohesive forces overcome the buoyant forces exerted by the gas at lower velocities thus resulting in defluidization of the bed. At

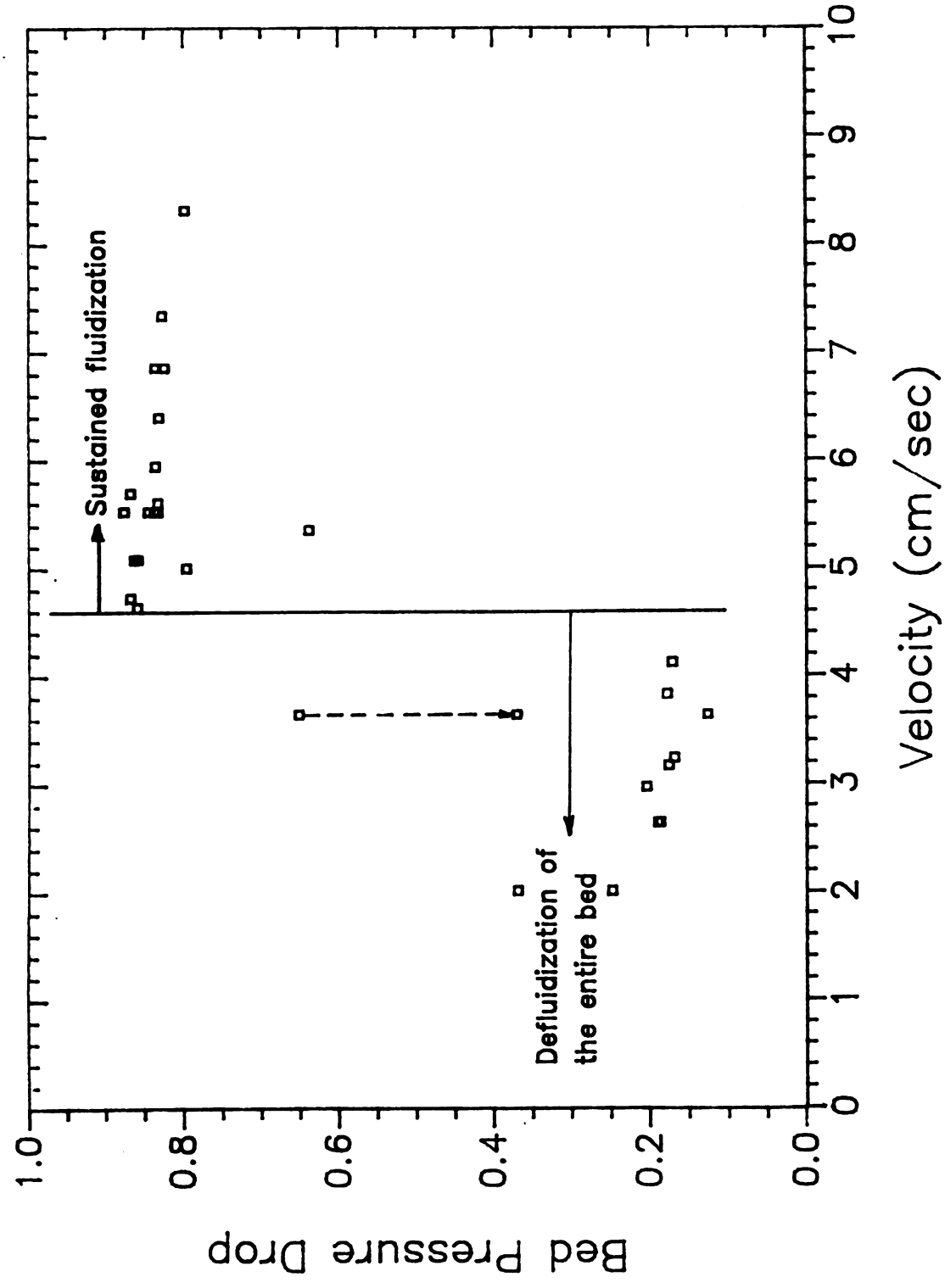

Figure 38. Bed pressure drop vs velocity, medium powder.

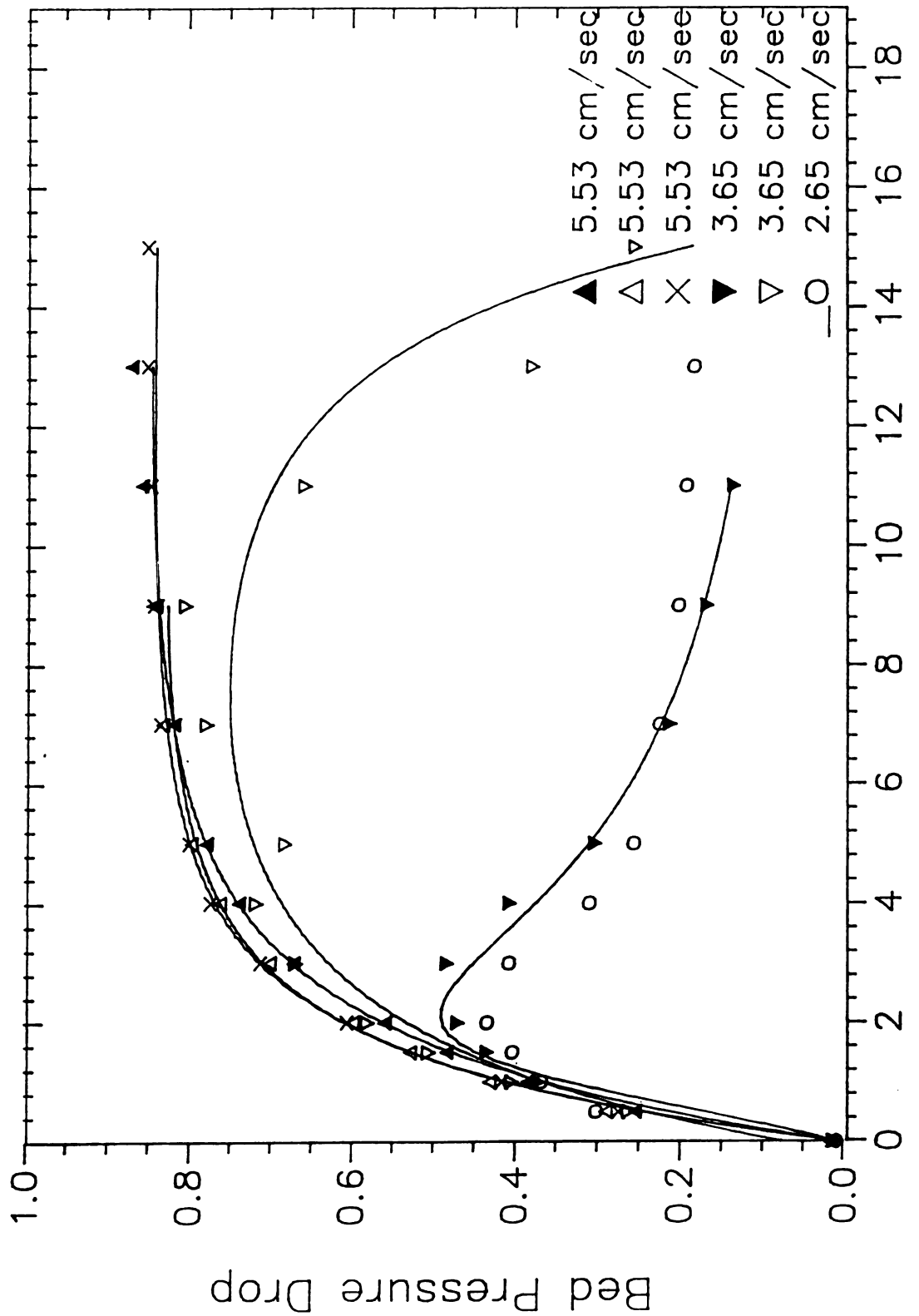

Figure 39. Bed pressure drop vs time, medium powder.

higher velocities, bubbles keep the bed in an agitated state and the depth of the defluidized region is small. Hence we see a plateau in the measured bed pressure drop.

It can be seen from Figure 40 that bed expansion of the medium powder is very high, reaching a maximum of 2.23 (bed height/static bed height) at a velocity of 8.32 cm/s. A variation in the height of the fluidized bed of less than 5 % was observed during the course of most experiments. This can be attributed to the periodic bursting of bubbles at the top of the bed. Each time this occurs, there is an instantaneous drop in bed height.

Coarse Powder :

The coarse powder shows an ability to remain fluidized at velocities greater than 3.2 cm/s. The scatter in the data is quite widespread between 3.2 to 5.5 cm/s (Figure 41). This is primarily due to the large fluctuations in the depth of the defluidized region. The bed fluidizes to attain a certain bed height. The defluidized region then starts rising, sometimes reaching upto 60 - 70 % of the total bed height. The bed does not sustain this growth indefinitely and the cracks/channels break up to reduce the size of the defluidized region. This constant "tussle" between the interparticle cohesive forces which tend to build a defluidized zone and the hydrodynamic forces which give rise to bubbling leads to fluctuations in the observed bed pressure drop and bed height. As the gas velocity increases, the defluidized region decreases in size and at velocities greater than 5.5 cm/s, it is less than 5-7 cms tall, thus leading to a more reproducible pressure drop. Figure 42 reflects the stability of pressure drop measurements at higher velocities compared to that at lower velocities at which the bed tends to defluidize.

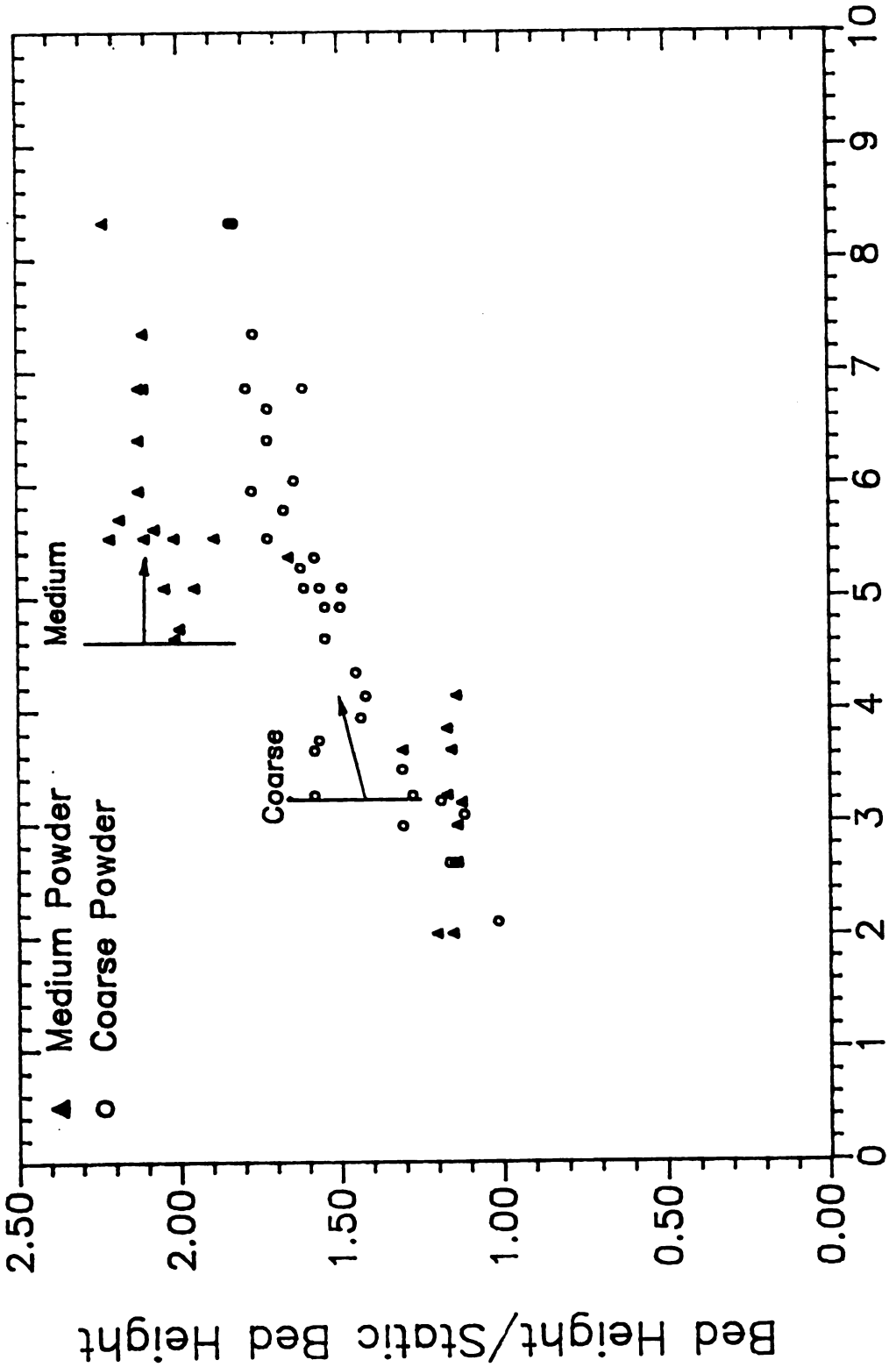

Figure 40. Bed height vs velocity, medium and coarse powders.

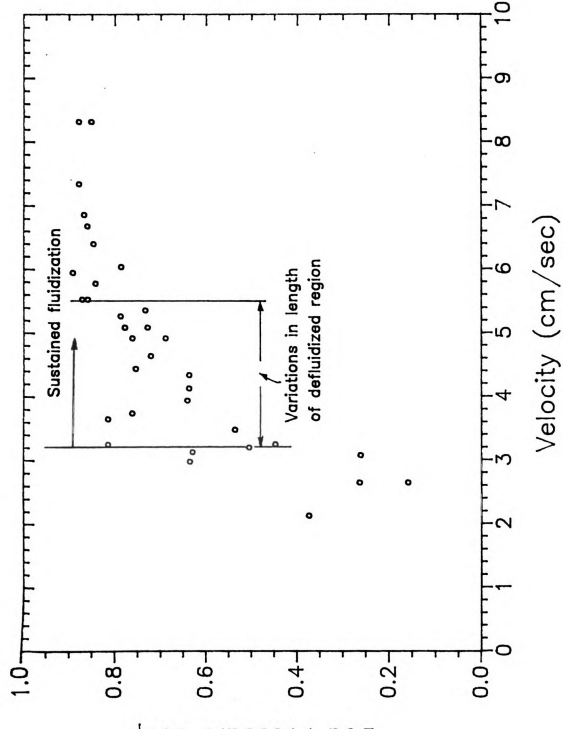

Figure 41. Bed pressure drop vs velocity, coarse powder.

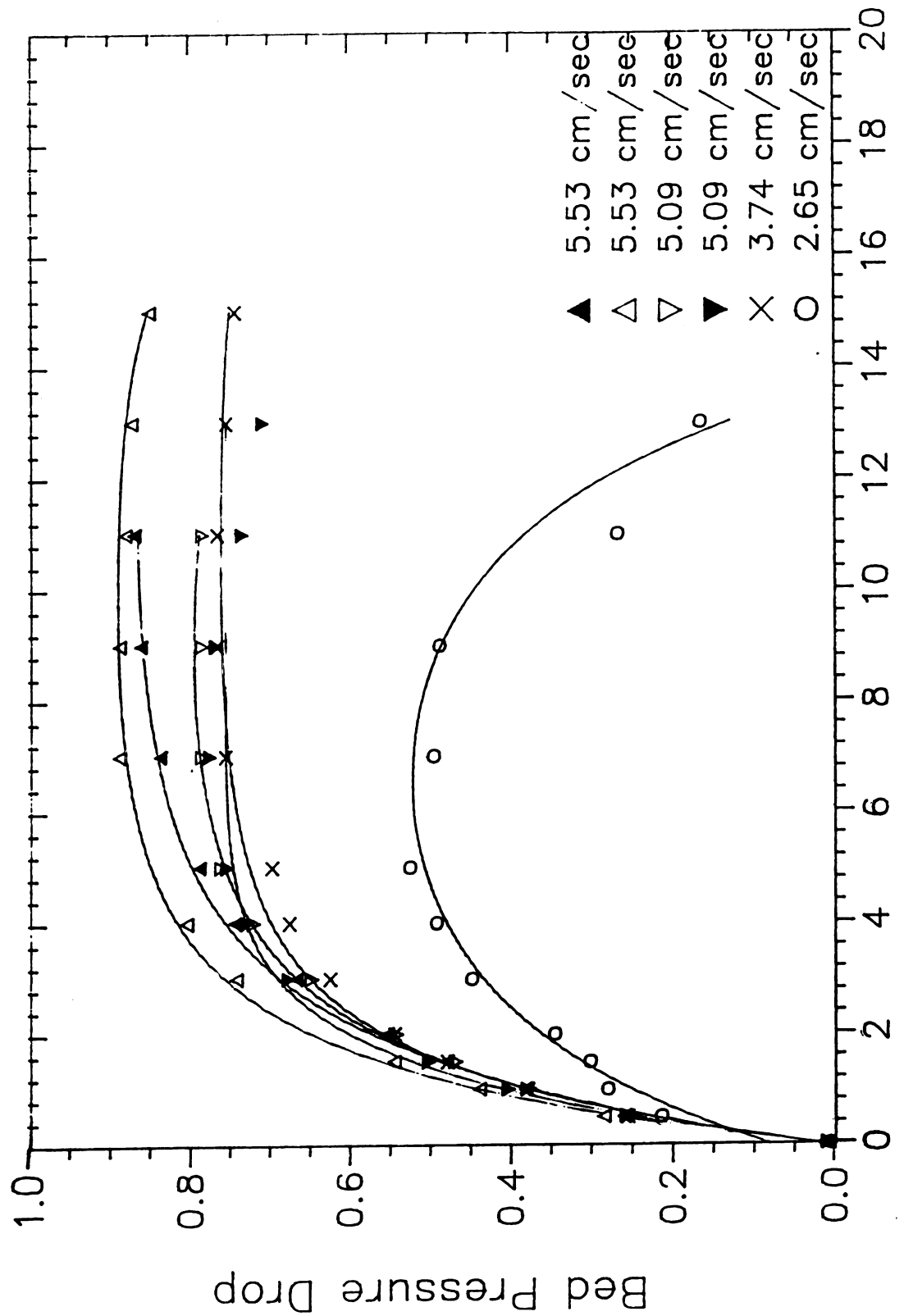

Figure 42. Bed pressure drop vs time, coarse powder.

Differences in bed behavior :

Bed expansion of medium and coarse powders at different velocities is shown in Figure 40. It is evident that medium powders expand more than coarse powders. It appears that for beds of particles with sustained fluidization, bed expansion increases with decreasing particle size. This is in keeping with the findings of Geldart and Wong [25]. They report that bed expansion increases as particle size goes down for Types A and AC powders.

An inspection of Figures 38 and 41 reveal that the highest pressure drop attained by the coarse powder is 0.89. At velocities greater than 5.5 cm/s, the bed routinely achieves pressure drops of 0.86-0.87. The medium powder peaks at 0.88 and achieves average pressure drops of 0.83 at high velocities. There is a decrease of 4-5 % in the pressure drop between the coarse and medium powders. Geldart et al. [30] also noticed this decrease in pressure drop as the particles become more cohesive.

The reason for the high pressure drops seen at velocities where the defluidized region contributes to the total pressure drop was enunciated in the section on medium powders. The coarse powder does not show such behavior. This is the result of crack formation in the defluidized region which is more stable and intricate as powders decrease in particle size. Hence the defluidized region develops a larger pressure drop for a more cohesive (in this case a smaller- sized) powder. It must be noted that in the bubbling region, particle mixing is too vigorous to allow any cracks to form.

This investigation emphasizes the transitional nature of the change from Type C to Type A as argued by Dry et al. [31]. Attempts to fluidize the fine powder result in crack and channel formation, with hardly any bubbling. This is characteristic of Type C behavior as outlined by Geldart [25]. The medium powder fluidizes at 4.6 cm/s with the help of bubbles. There is no homogeneous fluidization preceding the

bubbling phase and pressure drops attained are less than 1. Crack formation here is stronger than for the coarse powder which fluidizes at 3.2 cm/s and achieves higher pressure drops than the medium powder. Both the medium and coarse powders diplay Type AC behavior. It is likely that increasing the particle size will cause a gradual transition into Type A behavior characterized by bed pressure drops close to 1 and weaker interparticle forces which allow for homogeneous fluidization initially before bubbling sets in.

Effect of Relative Spread of the Particle Size Distribution :

The width of the particle size distribution can be characterized by the ratio r/d_{pm} where r is the spread and d_{pm} the median particle size. It can be seen from Table VII that the fine powder has a fairly wide particle size distribution while the medium and coarse powders have a narrow distribution. Figure 32 shows that the medium powder has a size distribution which lies in between the fine and coarse powders. Therefore, bed behavior for the medium powder should be transitional with respect to the behavior of the other two powders. This concurs with the observations made in this investigation. A large relative spread of a powder might serve to accentuate the transitional nature of bed behavior i.e. the presence of fines leads to channeling and cracking (a defluidized region) while the presence of larger particle sizes results in a larger bubbling region. The precise effects of the relative spread i.e. differences in bed behavior for different samples of a material with the same mean particle size and different values for the relative spread remain to be characterized. Geldart et al. [25] fluidized different powders with r/d_{pm} ranging from 0.47 to 0.8 and 0.09 to 0.14 and found that the powders evinced Type C and Type AC behavior respectively (listed in Table VII).

Influence of Bed Diameter :

Dry et al. [31] found that the dense phase voidage and dense phase velocity (of transitional Type AC and Type A powders) do not show an equipment dependence in going from the 5 cm unit to the 14 cm unit. The 64 cm unit however yielded different values as the gas from the multi-orifice distributor (porous distributor for the smaller units) had difficulty penetrating the dense phase at velocities less than 40 cm/sec. Dry et al. [76] observed that bubble velocities in fluidized beds of Type A powders show an axial dependence in larger-diameter beds (64 cm) which is not seen in narrow beds (5 cm). In narrow-diameter beds, the dimensions of the bubbles approach the column diameter especially near the top of the bed. A perusal of Table II (Section 3.1.2) shows that the general nature of bed behavior observed by different investigators is in line with the findings of this paper. The formation of cracks and channels alongside the wall in addition to those inside the bed suggests that gas bypassing through cracks and channels is likely to diminish as the bed diameter is increased. The bed structure of a cohesive powder in the defluidized region is likely to be preserved better in a narrow fluidized bed due to the presence of wall forces. This suggests that bed diameter could be a variable which influences the transition between different types of behavior for the same powder. But the extent of the change in bed behavior as one progresses to larger-diameter beds has not been investigated.

Discussion - Conventional Fluidization of Cohesive Powders :

True Type C powders are very difficult to fluidize. They tend to form cracks at lower velocities and cracks/channels at higher velocities thereby precluding any actual fluidization. Bed pressure drop measurements are irreproducible due to the randomness involved in crack and channel formation. As powders increase in particle size, they begin to undergo a gradual transition in bed behavior. Bubbles start

forming which lend stability to the fluidized bed and lead to sustained fluidization. There is no distinct minimum fluidization velocity. This can be characterized as Type AC behavior. The bed structure of Type AC powders in narrow fluidized beds consists of a defluidized region near the distributor where cracks/channels form and a bubbling region where bubbles ensure that the particles remain in a fluidized state. Reproducibility of bed pressure drop measurements depends on the variations in the length and the structure of the defluidized region. In general, a large defluidized zone with a varying density of cracks, of different inclinations and tortuosities implies that there will be more scatter in the data. Bed expansion for such powders increases as particle size goes down. Additional work needs to be done to characterize the influence of bed diameter and width of the particle size distribution on the bed behavior of cohesive powders.

6.2 **Pulsed Gas Flow** :

A solenoid valve with a relay timer was installed before the gas distributor to pulse the gas flow to the column. Figure 43 shows a plot of the bed pressure drop as a function of elapsed time for different pulsing speeds for a Type C polyamide powder.

For the open cycle (no pulsing), the bed initially fluidizes but the formation of cracks/channels across the entire bed with time results in defluidization of the entire bed. When the gas flow is pulsed, it leads to the breakup of channels between pulses i.e. when the gas valve is closed in each cycle, the solids start settling and disrupt the channels. The bed therefore remains fluidized for a longer period of time. The bed pressure drop is a function of the pulsing cycle. The pulsing cycles investigated (0-60 sec open/closed) revealed that the bed pressure drop increases with the time that the valve is kept open. There is a gradual decrease in bed pressure drop with elapsed time as the disruption of channels in the closed phase does not keep pace with the

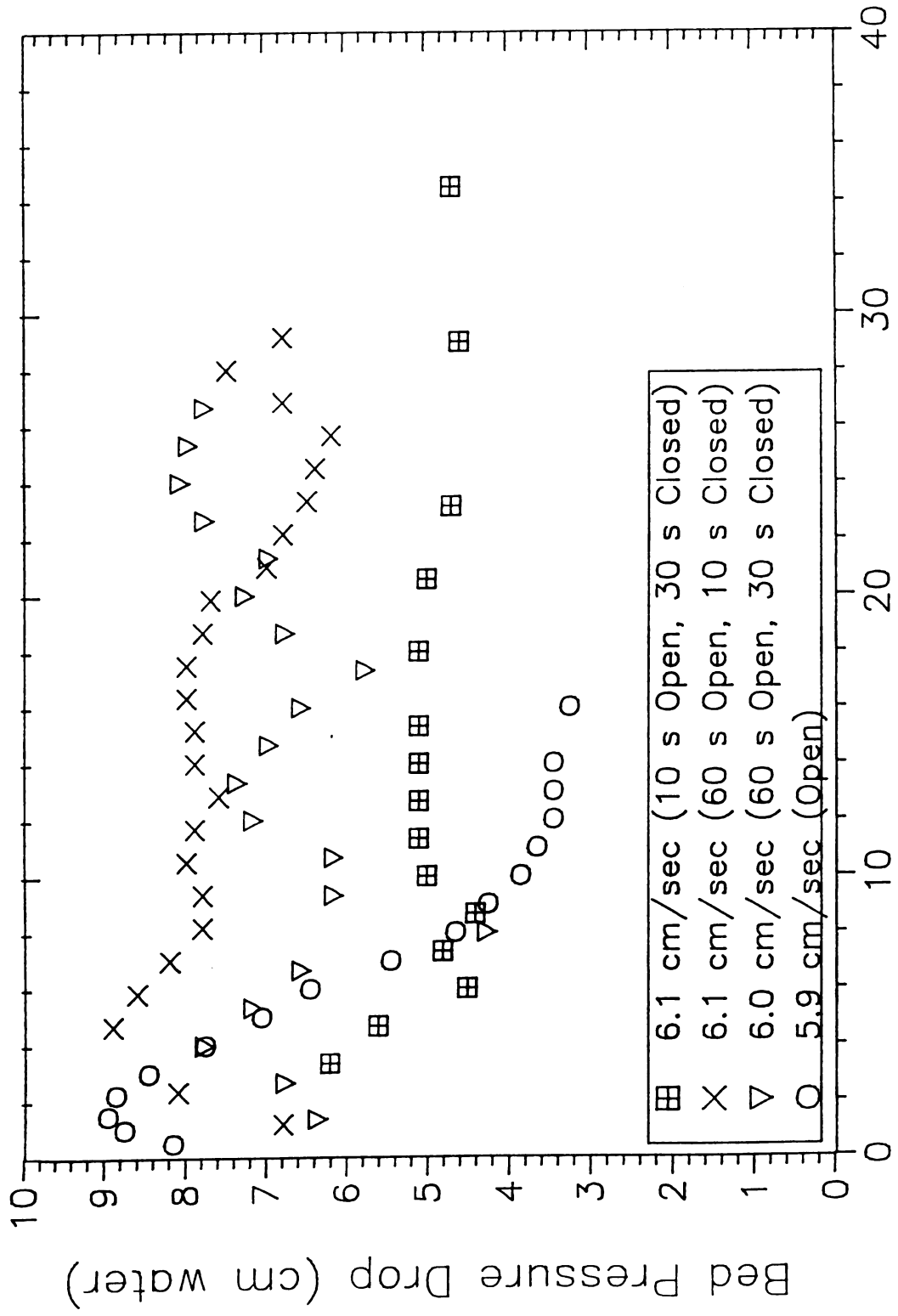

Figure 43. Effect of gas pulsing.

formation and growth in the open phase unless the former is so large that it causes defluidization in each cycle.

Gas pulsing does not have an appreciable effect on the quality of fluidization. The inherent problems of cracks/channels in the fluidized bed and lack of control of bed parameters still persist for gas pulsed fluidized beds. Pulsing only delays the onset of defluidization for a Type C powder. The cylical behavior of the pulsed fluidized bed is unacceptable for an impregnation chamber in a powder-prepregging process since this would lead to non-uniform pickup of particles by the fiber tow. This led to the conclusion that other options which work at higher frequencies such as acoustics and ultrasonics should be considered in the design of an optimum fluidization chamber.

6.3 **Aerosolization** ‡ :

6.3.1 *Determination of Natural Frequency* :

The design and operation of the aerosolizer are described in Section 4.2. A 3 inch internal diameter aerosolizer chamber with a 6.5 inch diameter speaker was initially used to explore its performance. The first step is to determine the resonant frequency of the chamber. The scheme used in these experiments is shown in Figure 44. The entrained particles from the aerosolizer were trapped in a disposable filter for a constant duration of time (30 minutes) and weighed to determine the entrainment rate of powder during each experiment. The amplitude, height of the packed bed and the gas velocities were kept constant while the frequency was varied from run to run. A plot of such an experiment is shown in Figure 45. The natural frequency of the system was determined to be approximately 34 Hz for the

‡ All the aerosolizer experiments discussed in this chapter were done with the polyamide powder (Orgasol 2001, 9.16 ± 3.96 microns diameter) unless otherwise noted.

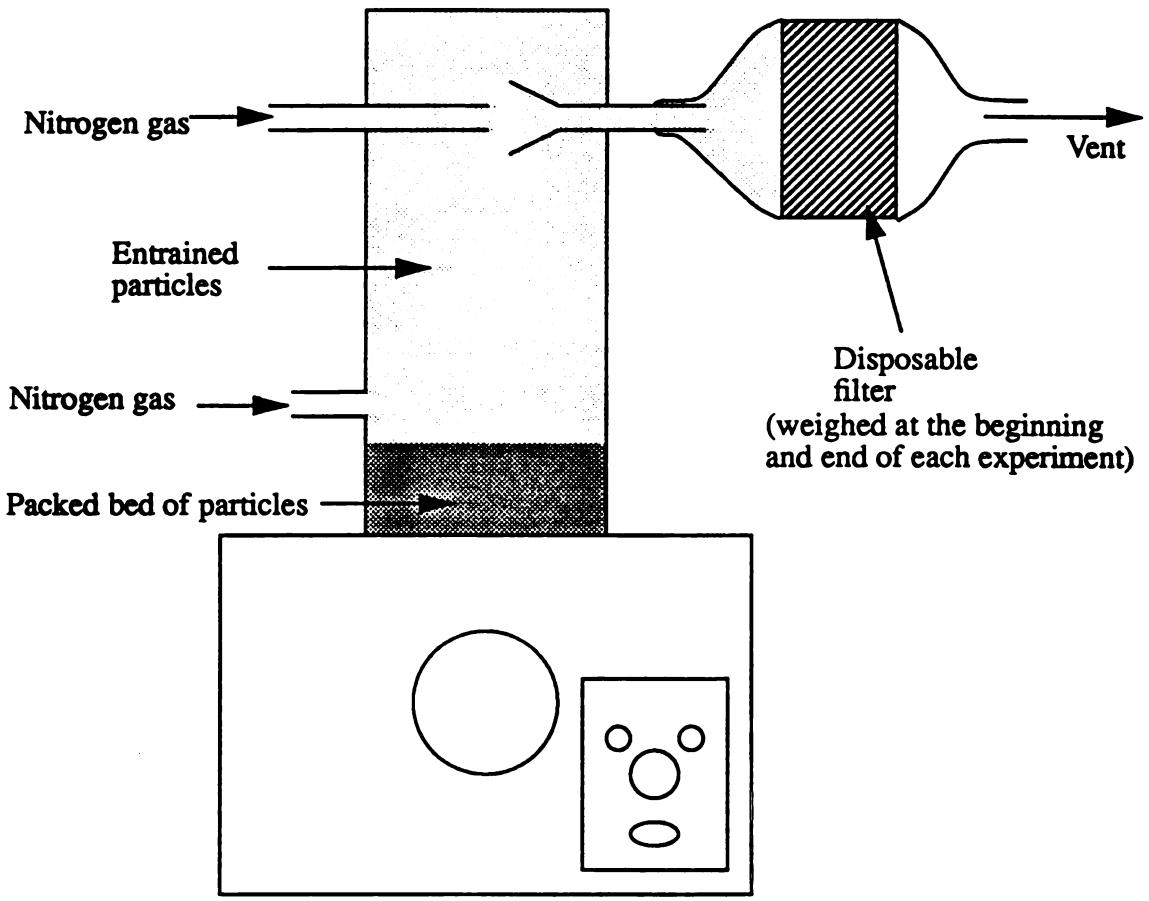

Figure 44. Experimental scheme to determine natural frequency of aerosolizer.

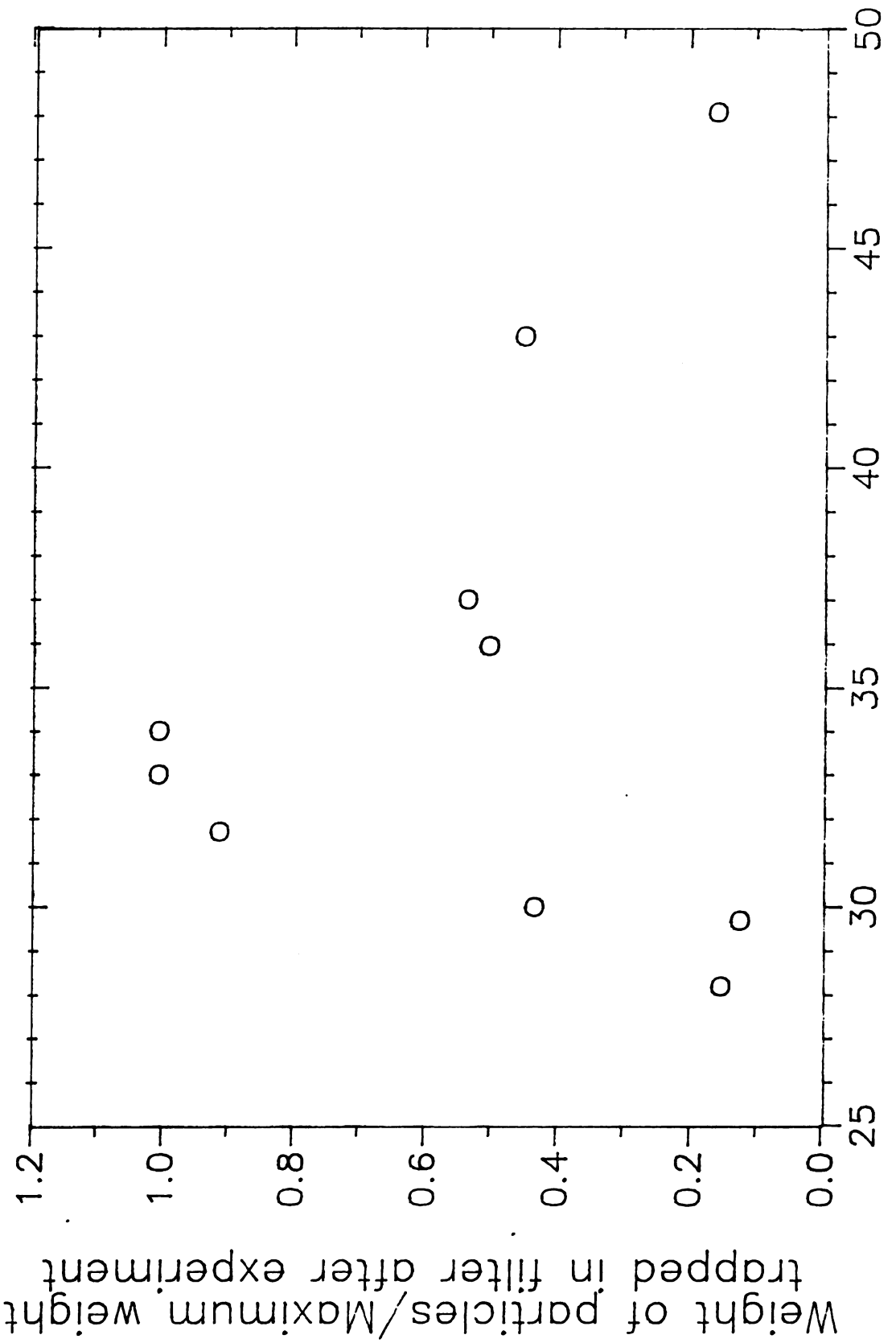

Figure 45. Weight of particles collected in filter vs frequency.

2002 Fine Orgasol powder, the height of the packed bed approximately 4 cm for all the experiments and the amplitude at 15 V peak- to-peak. The particle pickup is the maximum at the resonant frequency of the system if the other variables i.e. gas velocity, amplitude of the sound wave and the height of the packed bed are kept constant.

Reproducibility of these experiments was poor because of the following reasons - (1) Caking on the walls. The walls of the plexiglass chamber get caked with particles which absorb sound and reduce the weight of the packed bed. This causes a deviation from resonance with time and thereby reduces particle entrainment. (2) Pressure drop across the disposable filter increases with particle buildup which adversely affects the weight of powder trapped in it with time. (3) Environmental factors such as relative humidity adversely affect interparticle cohesive forces and may influence the particle pickup by the filter. Hence there is a marginal gain if any in determining the natural frequency by rigorous experimentation as opposed to a frequency sweep to pinpoint the value at which the diaphragms oscillate with the maximum amplitude. Resonance can be visually detected since the diaphragms vibrate with the maximum amplitude at this frequency. A sound level meter can also be used during the frequency sweep to aid in pinpointing the resonant frequency (maximum sound pressure). This method was subsequently used throughout the investigation to determine natural frequencies at the start of each experiment. The natural frequency of the scaled up system (8.2 inches internal diameter, 15 inches length, 15 inch speaker) with 200-300 gms of the 10 micron polyamide powder (2001 Orgasol) was determined to be approximately 11-13 Hz.

6.3.2 *Aerosolizer Behavior at the Natural Frequency* :

As outlined in Section 4.2, a SPL meter and a RAM unit (Realtime Aerosol Monitor) were installed online in the scaled up aerosolizer chamber. The RAM unit monitors particle concentrations ($mg/m^{3)}$ inside the chamber. The sampling takes place with a copper tube which conveys the particles to an optical detection unit outside the chamber. But the inherently high particle charge on the fine polyamide particles was a constant source of contamination in the optical assembly which drifted from zero with time during each experiment. Zeroing problems at the end of each experiment were also encountered due to particles sticking to the optical detection unit.

The sound pressure was monitored inside the chamber at a height of 10 inches from the lower vibrating diaphragm. For a system at its resonant frequency, the sound pressure is proportional to the amplitude of the sound wave. Figure 46 shows a typical plot of sound pressure vs time for a two hour run at the resonant frequency of the system. The sound pressure decreased by around 1 db for a typical one hour run. The decrease in sound pressure for various runs is listed in Table VIII. The probable reasons for this decrease are caking on the walls and the decrease in weight of the powder on the diaphragm with a consequent deviation in resonant frequency. Two runs were conducted with the RAM-S unit online before it malfunctioned due to zeroing and contamination problems. Figure 47 shows a plot of sound pressure and particle concentration during an experiment. It shows that particle concentration follows the same trends as the sound pressure which is to be expected because sound pressure is the buoyant force which causes the upward motion of the particles. Nitrogen gas was piped to the chamber at a height above the packed bed. The gas flow helped in providing an additional buoyant force to the entrained particles and

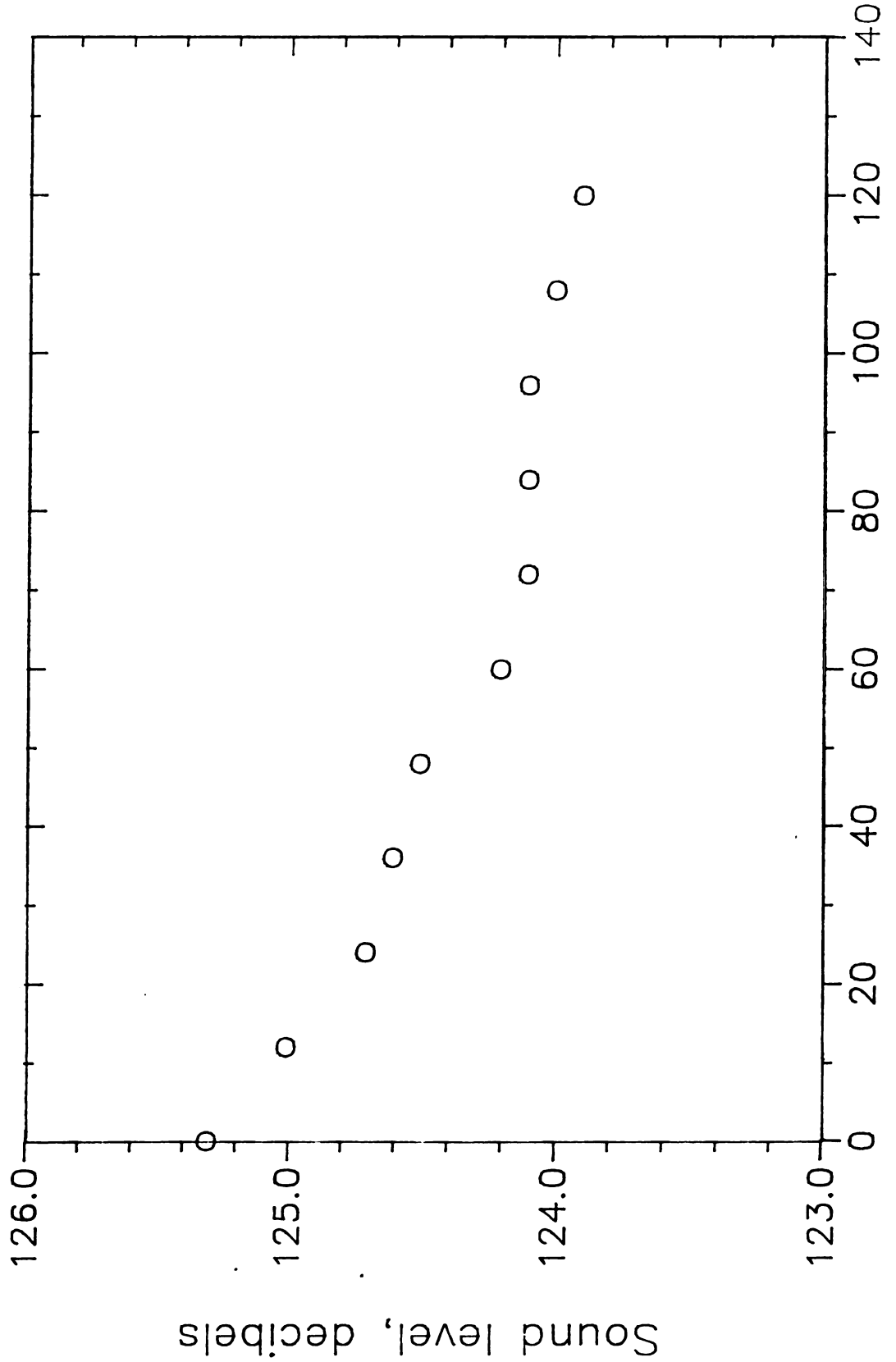

Figure 46. Sound pressure level vs time, two hour experiment.

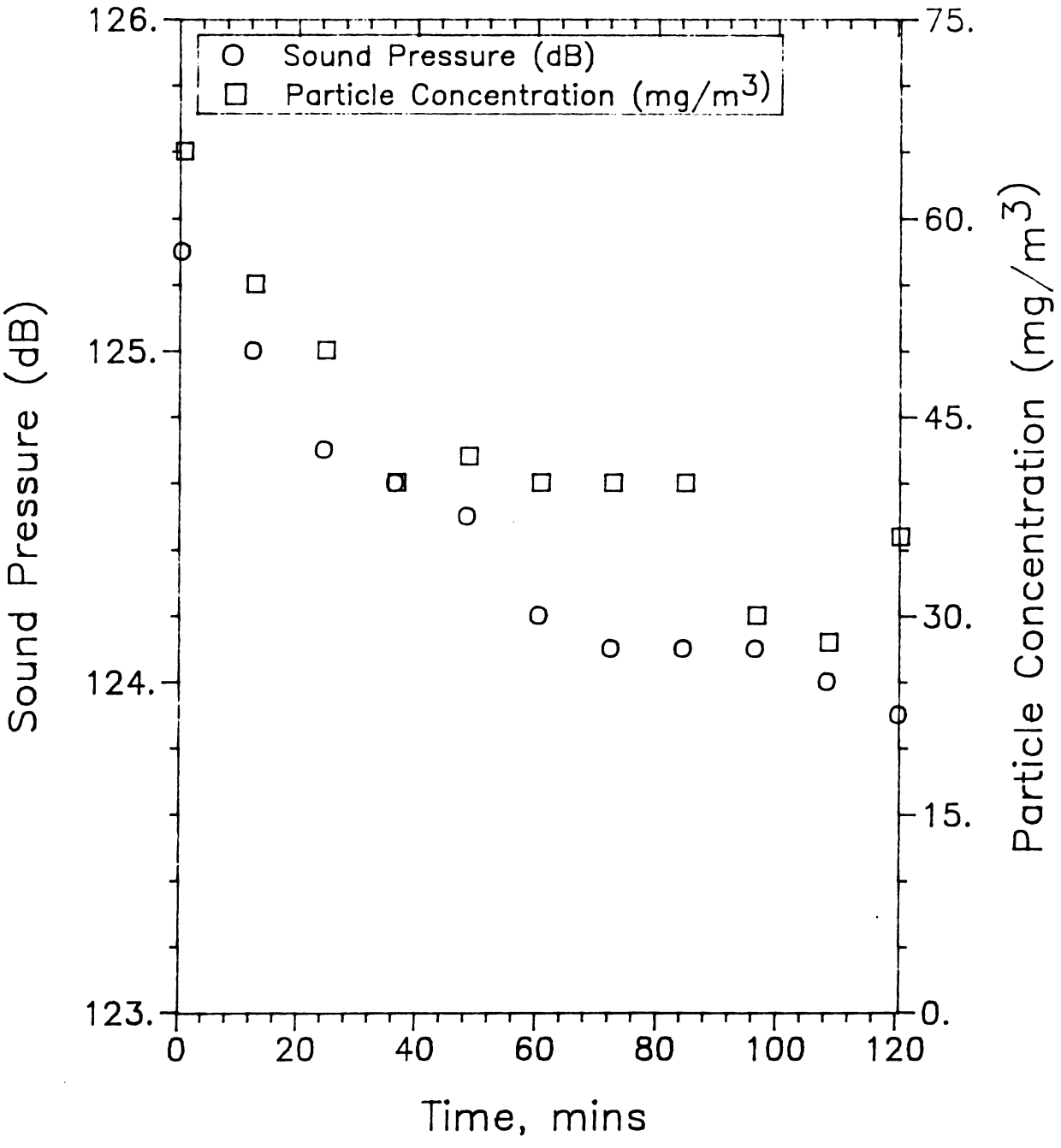

Figure 47. SPL and particle concentration vs time.

maintaining a steady concentration of particles in the chamber. The experimental evidence for this principle is presented in Section 5.2.5.

TABLE VIII. SOUND PRESSURE

No	Duration of Experiment, mins	Sound Pressure Level, db		
		Maximum	Minimum	Difference
1	60	126.3	124.8	1.5
2	60	124.8	123.8	1.0
3	60	124.3	123.5	0.8
4	60	123.9	123.2	0.7
5	61	126	125.3	0.7
6	80	125.1	122.6	2.5
7	86	123.1	122.2	0.8
8	83	122.4	121.6	0.8
9	57	125.7	124.4	1.3
10	62	125.7	124.2	1.5

The aerosolization of 5 micron polyamide particles in the small aerosolizer (3 inch i.d.) was investigated. Agglomeration of the particles was observed at high amplitudes, the agglomerated clusters reaching sizes of 2-3 cms for the higher amplitudes (greater than 15 V peak-to-peak). This decreased the particle concentrations in the chamber to zero since the agglomerates fell down to the lower diaphragm due to gravity and grew larger in the packed bed. Agglomeration to form such large clusters was not observed during the aerosolization of the 9.2 micron polyamide particles though small agglomerates (1-3 mm in diameter) were noticed occasionally at high sound pressures near 130 db. This implies that sonic agglomeration, in addition to increasing with sound intensity (equation 29, Section 4.2) also increases with decreasing particle size, all other conditions in the aerosolizer being constant. A possible reason for this is that particles oscillate with larger amplitudes at the smaller particle sizes and therefore have a larger probability of

interparticle collisions. Interparticle cohesive forces are also larger for the fine particles thereby increasing the probability of agglomeration on contact. Due to this phenomenon of sonic agglomeration, there is an upper limit for achievable particle concentrations in the aerosolizer chamber. This limit decreases with increasing particle size.

The system discussed in Section 4.2 to eliminate entrainment to the surroundings was very effective in performing this function. Practically no leakage of particles to the surroundings was seen after the casing with the air filter and exhaust was installed. Leakage was gaged by checking for particle deposits on adjacent pieces of equipment. The air filter was vacuumed once in 2-3 runs to ensure that the filter stayed unclogged.

6.3.3 *Future Improvements* :

The following modifications can be made to improve the performance of the aerosolizer -

(1) A deionizer should be installed in the sampling tube between the intake in the aerosolizer and the RAM-S unit to neutralize the charge on the particles before they enter the optical detection assembly in the RAM-S.

(2) An AccuRate Screw Feed should be installed to feed the aerosolizer with particles to replenish the loss of powder during the course of the experiments. A material balance around the chamber to calculate the rate of powder loss can be used to set the required feed rate for each experiment. An alternative scheme is to monitor the height of the packed bed within the aerosolizer and control the feed rate to maintain this height constant.

(3) At present, there is no facility for powder recovery of the particles entrained out of the chamber. This should be incorporated in order to reduce operating costs. A possible design scheme is one in which the powder is recovered and recycled at the

end of each experiment while the powder sump in the chamber is being replenished with a feeder. The system consists of an annular chamber with two or more baffles surrounding the fiber entry and exit slots to the aerosolizer. A slight vacuum is applied to keep the outer chamber at a lower pressure than the surrounding environment. The powder collected in this chamber is emptied back into the aerosolizer at the end of each experiment. This scheme keeps all the operating parameters of the aerosolizer unchanged during each prepregging run.

(4) The chamber walls were covered with stiff aluminum foil to alleviate the problem of caking. A long term solution will involve the application of a conductive coating to rid the surface of static charge. A process that will enable both visual observation of the aerosolizer and the use of photosensors to determine the height of the packed bed as a direct means to control the feed rate of powder into the bed by maintaining the height at a constant level is desirable.

6.3.4 *Discussion - Aerosolizer Performance* :

The aerosolizer works on the simple concept of acoustics providing the buoyant force to lift particles up individually and thereby prevent agglomeration. The two key variables are frequency and amplitude of the sound wave. At resonance, the amplitude should be kept below the range where sonic agglomeration becomes a problem. As shown in the above experiments, the aerosolizer can run for long periods of time at constant particle concentrations if the weight of the powder packed at the bottom of the bed remains constant to the extent that resonance is not affected. Powder recovery can be easily added to the system as suggested in the previous section on future improvements. The system does not need careful supervision because of its inherent stability at the resonant frequency. Even in the case of a fluctuation, response time to changes such as an increase in amplitude of the sound wave is quicker than for the powder deposition chamber [19,20] since

there is no recycling of powder during the experiment. It should also be noted that particle concentrations in an aerosolizer are around 0-200 mg/m^3 while that in a fluidized bed or the powder deposition chamber described in Section 2.6 are orders of magnitude larger i.e. 10000 mg/m^3 or more. This affords better control over the impregnation of particles into the fiber tow. Overall, the aerosolizer is a stable system which can provide a constant concentration of particles for long periods of time if operated at its optimum conditions and with replenishment of the powder in the packed bed.

6.4 Spreading :

A set of 10 spreading runs was performed with the spreading system. The spreading operation is described in Section 4.3 (Figure 19). The fiber tow [2] (width less than 5 mm) was unwound from a spool [1]. It passed through a guide ring [3] and in between nip rollers [4] before entering the spreader [6]. The spreader consisted of a 10 inch speaker [6a] (8 ohm, 100 Watts) mounted in a plywood housing [6g]. The speaker [6a] was operated at different frequencies and amplitudes with the help of a frequency generator [6c] and a power amplifier [6b]. The fiber tow zigzagged over and under highly polished shafts [6e] while being spread by the spreader [6] into its individual filaments [7]. The spread tow was then pulled in between nip rollers [8] and wound on a takeup drum. The speeds of the two nip rollers [4] and [8] were controlled by a computer and monitored 9.1 times every second. This maintained a constant level of fiber tension in the tow as it passed over the spreader. The speed of the takeup drum [9] was controlled manually to take up any slack in the tow between the nip rollers [8] and the takeup drum. The amplitude and frequency of the sound wave entering the speaker were monitored by means of a multimeter (the voltages reported in Tables IX and X are root-mean-square amplitudes i.e. V_{rms} = 0.707 (Amplitude)) and a frequency counter respectively. The

width of the spread tow was measured after the tow passed over the last of the shafts [6d]. The distance travelled by the fiber tow from the fiber spool [1] to the takeup drum [9] was 65 inches. The duration of each of the runs shown in Table IX was 10 minutes. In Tables IX and X, NR (4) and NR (8) refer to nip rollers [4] and [8] respectively. The values shown in parenthesis for motor speeds are the standard deviations of the instantaneous speeds of the nip rollers measured during each run.

Table IX shows the effect of frequency of the sound wave on spreading width provided the amplitude is kept constant. The carbon fibers used in this example have an average diameter of 8 microns, hence a width of 4.8 cm implies that the tow has been spread to expose individual filaments with an average spacing of one fiber diameter in between adjacent fibers. As can be seen, there is a narrow range of frequencies between 32-39 Hz at which the efficiency of spreading is the maximum i.e. the fibers absorb the most acoustic energy causing them to vibrate and the tow to spread to its individual filaments.

A second set of 6 runs were performed with the same version of the process as in the first set. Here the frequency of the sound wave was kept approximately constant at 36.0-36.4 Hz while the amplitude was varied from 4.7 to 11.8 V (Table X). The measured widths show that spreading improves with increasing amplitude to a maximum beyond which there is no further improvement with increase in amplitude. It can be seen above an amplitude of 9.8 V, there is no tangible improvement in the quality of spreading.

In both sets of experiments, the variations in spreading width are caused primarily by instantaneous fluctuations in the level of fiber tension in the tow as it passes over the spreader. At the optimum range of frequencies and amplitudes, the fibers absorb a significant amount of acoustic energy and are able to retain their spread shape in response to these fluctuations. Outside this range, the fibers tend to collapse to a narrow width. Once this happens, they take longer times to spread in

proportion to the deviation of the operating variables of the spreader from their optimum values.

TABLE IX. SPREADING EXPERIMENTS - CONSTANT AMPLITUDE, VARYING FREQUENCY

No	Frequency (Hz)	Amplitude (rms) (V)	Speed of nip rollers (cm/sec)		Width (cm)
			NR (4)	NR (8)	
1	21.1	10.5	3.00 (0.16)	3.00 (0.10)	0.5-4
2	25.3	10.7	3.00 (0.16)	3.00 (0.08)	3-7
3	30.0	10.5	3.00 (0.15)	3.00 (0.11)	4-9
4	32.1-32.4	10.5	3.00 (0.13)	3.00 (0.09)	5-9
5	34.3	10.5	3.00 (0.14)	3.00 (0.09)	5-9
6	36.1	10.6	3.00 (0.14)	3.00 (0.09)	6-9
7	38.3-38.4	10.5	3.00 (0.14)	3.00 (0.09)	5-9
8	40.0	10.5	3.00 (0.15)	3.00 (0.10)	4-7
9	42.2	10.5	3.00 (0.14)	3.00 (0.09)	2-6
10	44.1	10.5	3.00 (0.14)	3.00 (0.09)	0.5-5

TABLE X. SPREADING EXPERIMENTS - CONSTANT FREQUENCY, VARYING AMPLITUDE

No	Frequency (Hz)	Amplitude (rms) (V)	Speed of nip rollers (cm/sec)		Width (cm)
			NR (4)	NR (8)	
1	36.3-36.4	4.7	3.00 (0.15)	3.00 (0.09)	0.5-4
2	36.3	7.6	3.00 (0.14)	3.00 (0.09)	4-7
3	36.3	9.8	3.00 (0.14)	3.00 (0.09)	6-9
4	36.3-36.4	10.1	3.00 (0.13)	3.00 (0.08)	7-9
5	36.1	10.6	3.00 (0.14)	3.00 (0.09)	6-9
6	36.0	11.8	3.00 (0.16)	3.00 (0.09)	7-9

6.4.1 *Discussion - Spreader Performance* :

The spreader designed for this process works very well as compared with existing directed air methods for spreading fiber tows. The fundamental concept on which the spreader is based requires only two variables to be controlled - frequency and amplitude of the sound wave fed to the speaker. The spreading width is limited only by the length of the spreader over which the fiber tow passes and the spreader width under a set of optimum conditions (resonant frequency, amplitude of sound wave greater than a threshold value). System instabilities downstream or sudden system shutdown do not affect the performance of the spreader or cause fiber damage unlike existing systems such as the one described by Baucom et al. [20]. When operating at its optimum settings, the spreader is fairly insensitive to variations in speed.

6.5 Coalescence :

The sintering and coalescence of the polyamide particles on carbon fibers was studied with the help of a specially designed hot stage (Section 4.7, Figure 23) which mounts under an optical microscope. Experiments were performed in the following manner : Fiber frames were made by punching holes through a stiff aluminum sheet. Single fibers were mounted across these holes and glued at the two ends. The fibers were coated with polyamide particles. Each of these frames was placed inside the hot stage which is maintained at the heater temperature for a specified length of time. The coalescence events were observed visually under the microscope. These frames were then mounted on metal stubs with the help of conductive carbon paint and sputter coated with a thin layer of gold for observation under the scanning electron microscope (JEOL 35-CF). Table XI lists a series of experiments on single fibers in which the residence time in the hot stage was varied from less than 5 seconds to 30 minutes. There was a temperature variation of 1-6°C during each experiment due to

thermal instabilities whenever a frame was introduced into the chamber.

TABLE XI. COALESCENCE EXPERIMENTS †

No	Temperature, °C	t, secs	Comments
1	154-160	20	P
2	153-158	20	P, IPS
3	165-173	30	P, IPS
4	≈166	20	P, IPS, FF
5	174-177	4-7	P, IPS, FF, PDF
6	173-177	< 5	P, IPS, PDF, DF
7	173-177	< 5	P, IPS, PDF, DF
8	197-204	5-9	FF, PDF, DF
9	187-193	5-9	FF, PDF, DF
10	188-193	5-9	FF, PDF, DF
11	190-192	< 5	FF, PDF, DF
12	200-208	10	FF, PDF, DF
13	210-215	< 5	IPS, FF, PDF, DF
14	201-205	< 20	FF, PDF, DF
15	201-205	900	DF
16	201-205	900	DF
17	≈200	1500	DF

† P = Particles adhering to fibers
IPS = Interparticle sintering
FF = Film formation
PDF = Preliminary droplet formation from the film
DF = Axisymmetric droplets

Figures 48(a) - 48(e) show the sequence of events that occur in the heater as discussed in Section 3.1.3 and hypothesized in Figure 7. The polyamide particles initially adhere to the fibers (P, in the above table) because the fibers have a higher thermal conductivity than the polyamide. Adjacent particles then start sintering with each other (IPS) as shown in Figure 48(a). Figure 48(b) clearly shows the adhering of particles to the fiber at the base of each particle. The distinction between particles adhering to fibers (P) and interparticle sintering (IPS) was established by rapping

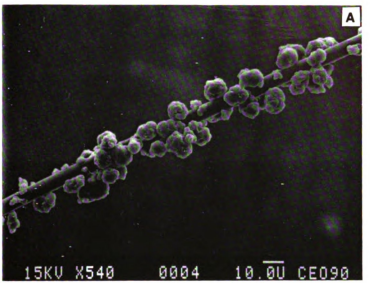

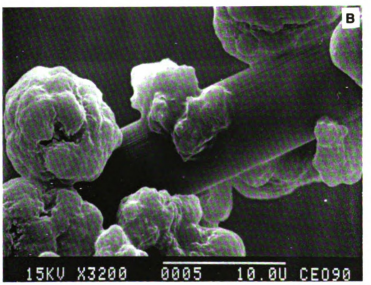

Figure 48. SEM photographs of coalescence in the heater : (a) and (b) show heat transfer to the impregnated tow.

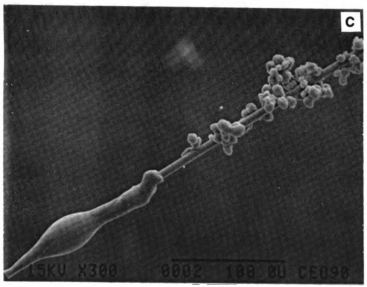

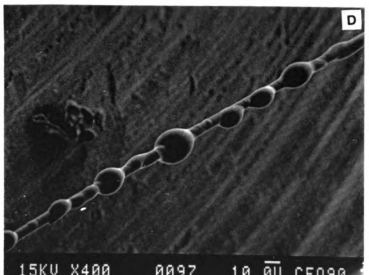

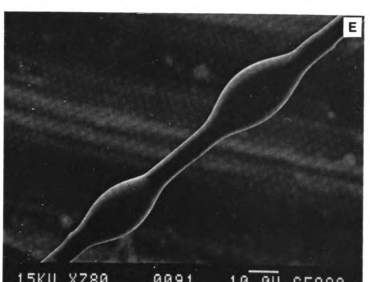

Figure 48. SEM photographs of coalescence in the heater : (c) shows interparticle sintering and coalescence into a film and initial droplet formation. (d) shows the formation of droplets, and (e) the formation of axisymmetric thermodynamically stable droplets at long times.

the fiber mounts after each experiment. Without interparticle sintering between adjacent particles (IPS), only a monolayer of particles is left on the fibers after vibrating the fiber mounts. Interparticle sintering leads to their coalescence to form a film on the fiber surface (FF). The film retracts to form droplets (PDF) which adopt an axisymmetric conformation at long times (DF). Figure 48(c) shows interparticle sintering, film formation and preliminary droplet formation. The initial formation of droplets can be seen in Figure 48(d) while 48(e) shows two axisymmetric droplets on the fiber at long times.

6.5.1 *Heat Transfer* :

The impregnated tows are initially heated to a temperature above the melting point of the polyamide. The heat transfer coefficients in the heater were estimated assuming free-convection heat transfer from horizontal cylinders in gases and liquids [77] -

$$Nu = \frac{hD}{k_g} \approx 0.45 \qquad [41]$$

From this equation, h can be calculated for different cluster diameters. The contribution of radiative heat transfer to h is calculated to be negligible compared with that by convective heat transfer.

In Section 3.1.3, the basic assumption of the lumped model is that external resistances are rate-controlling i.e. the Biot number is less than 0.1. The prepreg tapes made by the process were mounted in acrylic mounts and polished for observation under an optical microscope. It can be seen from Figure 49 that the impregnated fibers show a tendency to cluster in bundles in the heater. Hence it is obvious that the preferred configuration of the prepreg tapes is an array of fiber-matrix clusters, each cluster diameter ranging from that of a single fiber to multiple

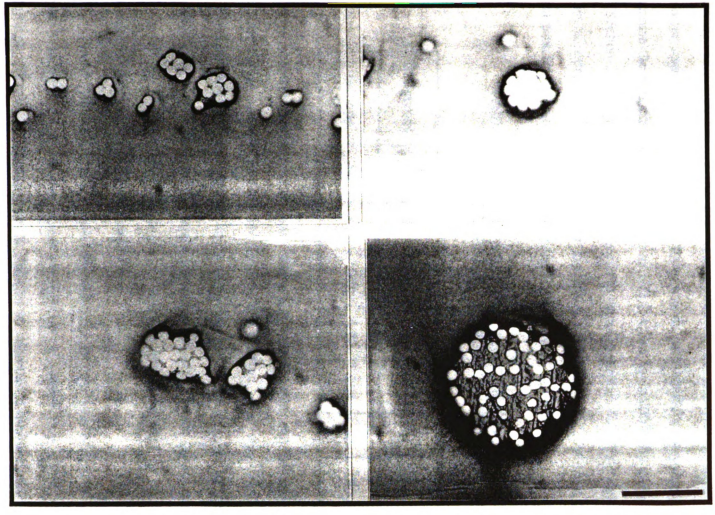

Figure 49. Cross section of prepreg tapes of different widths. Bar at bottom right represents 50 microns

fibers. Assuming a large cluster diameter of 100 microns (most cluster diameters are between 10-50 microns), we can calculate Bi to be approximately 0.0002. Here a value of k_s is calculated by a simple rule of mixtures for a 50 volume % fiber and matrix. This argument clearly proves that convective resistances dominate the heat transfer step. In such a case, heating times can be calculated for the prepreg tapes to increase the temperature from ambient to 180 C when T_h is 200°C by using equation 3 (Section 3.1.3). Table XII summarizes the calculated times for clusters of different sizes to raise their temperature from ambient (21°C) to 180°C. The time taken for heat transfer increases with increasing cluster diameter.

TABLE XII. ESTIMATED HEATING TIMES FOR POLYAMIDE-AS4 PREPREG TAPES

D, microns	1250	500	300	100	50	20	10
t, seconds	166	30.4	10.9	1.22	.304	.05	.012

A lower bound for the time taken for heat transfer can be estimated by considering an isolated particle in a convective medium. For very small spheres, convection tends to approach pure conduction through a stagnant layer adjacent to the surface [77] and Nusselt number approaches a value of 1. If the heater temperature T_h is 200°C, the time required for a 10 micron particle to heat up to 180°C is calculated (equation 1) to be 1 millisecond.

From Table XI, it can be seen that the heat transfer step occurs in much less than 5 seconds whenever the heater temperature is greater than 171°C (onset of melting). The exact heating time is difficult to ascertain experimentally since the particle temperature cannot be measured directly but must be assessed by observing the progress in physical phenomena resulting from changes in particle shapes.

Convection currents occur when the frame is introduced into the chamber and temperature gradients within the hot stage increase the heating time to a value larger than the predicted times. This analysis however leads to the conclusion that for the polyamide, heat transfer to the impregnated tow for this process occurs in less than 5 seconds.

6.5.2 *Interparticle Sintering and Film Formation* :

The sintering of adjacent particles on the fiber surface leads to the formation of a polymer film. Frenkel's theory which leads to equation (4) (Section 3.1.3) predicts that interparticle sintering rates are influenced by viscosity, polymer surface tension and particle size. Surface tension of most polymers lies between 20-50 dynes/cm whereas viscosity can vary by orders of magnitude. Hence interparticle sintering times (defined to be the time when the interparticle bridge is equal to the particle diameter) are primarily influenced by viscosity and particle size. Table XIII lists predictions of sintering times for some engineering thermoplastics of interest in structural applications. The surface tension in all the cases is assumed to be 30 dynes/cm. As can be seen, an increase in particle diameter and/or viscosity would serve to increase sintering times.

TABLE XIII. PREDICTIONS OF SINTERING TIMES FOR SELECTED THERMOPLASTICS BY FRENKEL'S THEORY [a]

Polymer	PA	PEEK	PPS	PEI	PS
Processing Temp, °C	215	390	315	350	350
Viscosity of Melt, Pa·s	33	3500	2500	2000	2000
t_s, sec					
10 microns	< 0.004	< 0.39	< 0.30	0.22	0.22
100 microns	< 0.04	< 3.90	< 3.0	2.22	2.22
250 microns	<0.18	< 9.72	< 6.94	5.56	5.56

(a) PA = Polyamide
PEEK = Polyetherether ketone
PPS = Polyphenylene sulfide
PEI = Polyetherimide
PS = Polysulfone

In the coalescence experiments with polyamide, interparticle sintering is an instantaneous step which cannot be visually detected at temperatures above the melting point. A perusal of runs 5-17 in Table XI shows that it was not possible to halt the coalescence process at the sintering step even for times much less than 5 seconds. This is in line with predictions by Frenkel's theory of sintering times of less than a millisecond. However, at temperatures lower than 171°C, it was possible to "freeze" the sintering step as seen in runs 2 and 3. This is because the viscosity of the material is extremely high below the melting point. Adherence of adjacent particles to each other is probably caused by the interdiffusion of polymer chains across the interparticle interfaces because of limited segmental motion available for the polymer chains at temperatures above the glass transition temperature. At the higher temperatures, sintering is predominantly a viscous flow phenomenon, surface tension being the primary driving force for flow across the interparticle neck.

Figure 50 shows an SEM photograph of a polyamide particle at high magnifications. The semicrystalline nature of polyamide as evidenced by the presence of nodules as well as the sharp melting transition observed in the DSC runs suggests that the sintering may be occuring at a rate faster than that predicted by Frenkel's theory.

6.5.3 *Droplet Formation* :

The film which forms after sintering of the polyamide particles retracts back to form droplets almost all of which are axisymmetric around the fiber axis. It can be seen from Table XI (runs 5-17) that at a temperature above the onset of melting, it is difficult to distinguish between the steps leading up to droplet formation. The formation of thermodynamically stable droplets over long times is demonstrated in runs 15-17 and is illustrated in Figure 48(e).

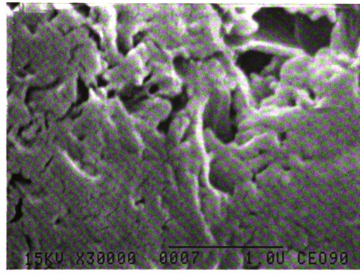

Figure 50. SEM photograph of a polyamide particle showing the presence of nodules.

The dimensions of 87 polyamide droplets on fibers were measured by image analysis (Joyce-Loebl Magiscan 2A). The droplet-on-fiber system was prepared by coating fibers with polyamide particles and inserting them into a heater at 200 C for 30 minutes. The drop length l and drop median diameter 2k were measured for each droplet. The average fiber diameter was calculated by measuring the diameters of a number of single fibers.

The fiber diameter was found to be 7.42 ± 0.20 microns from 19 measurements. The droplet dimensions of one droplet were measured repeatedly to determine the error involved in the measurements. The drop median diameter was found to be 32.7 ± 0.12 microns while the drop length was found to be 53.5 ± 1.1 microns. The length dimension has a larger standard deviation because there is some subjectivity associated with deciding where the droplet meets the fiber. A plot of K (2k/d) vs L (2l/d) is shown in Figure 51.

Section 3.1.3 (c) reviewed the theory by Yamaki et al. [45] to calculate the contact angle of a liquid in equilibrium with a cylindrical fiber. The equations (15, 16) were solved for droplet profiles by using a finite difference algorithm (backward difference) with a Regula-Falsi root-finding subroutine. The finite difference form of equation (15) (page 35) is -

$$\frac{(y_i - 2y_{i-1} + y_{i-2})}{\Delta x^2} = -\frac{\Delta P}{\gamma}\left[1 + \frac{(y_i - y_{i-1})^2}{\Delta x^2}\right]^{3/2} + \frac{1}{y_i}\left[1 + \frac{(y_i - y_{i-1})^2}{\Delta x^2}\right] \qquad [43]$$

The program (listed in Appendix C) predicts droplet dimensions (K as a function of L) for each contact angle. These predictions were compared with the measured dimensions, and the residual sum of squares, $\Sigma(K_{expt} - K_{theory})^2$ calculated for each contact angle. Figure 52 shows a plot of the residual error as a function of the predicted contact angle. From this analysis, the equilibrium contact angle for the polyamide-AS4 system was determined to be 23°. The solid line in Figure 51 is the

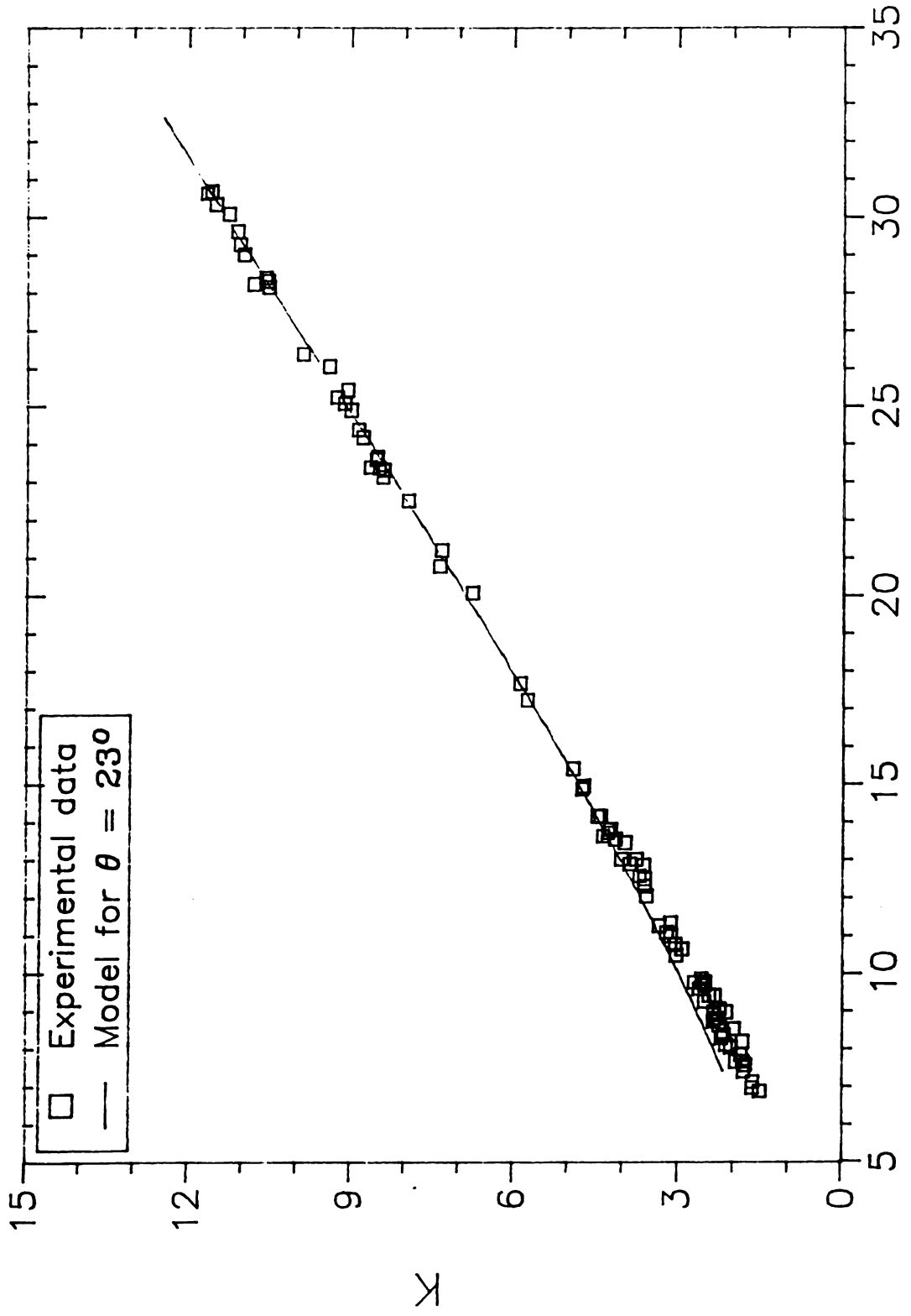

Figure 51. Plot of K vs L for the polyamide droplets on carbon fibers. The solid line is the prediction by the model [45] for $\theta = 23°$.

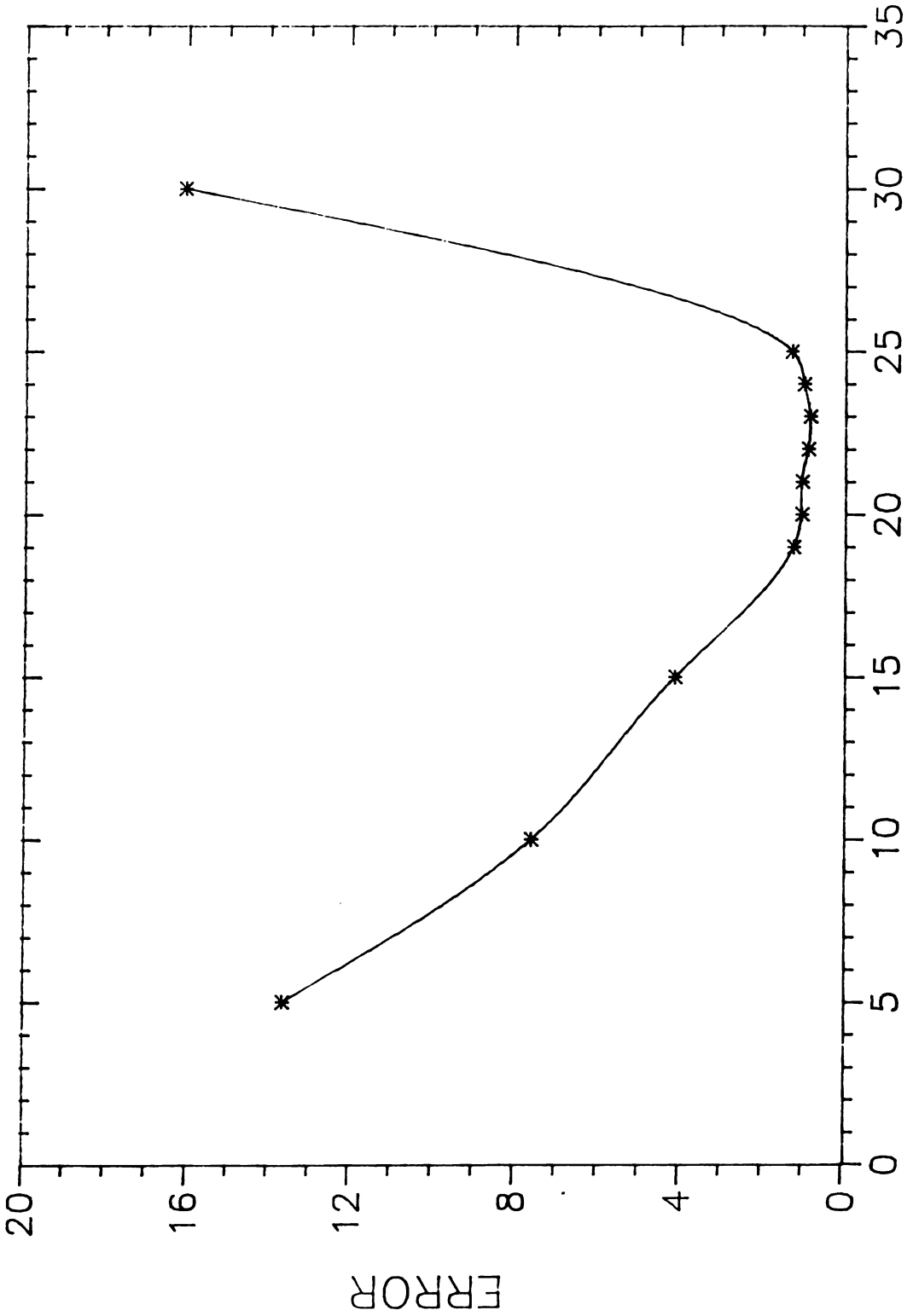

Figure 52. Residual error for different contact angles.

prediction by Yamaki's model for an assumed angle of 23°. The predictions are excellent for values of K greater than 4 but deviate for lower values. The program also predicts excess pressures for different-sized droplets. The pressures approximately range from 12,000 to 60,000 dynes/cm^2 for droplets ranging in size from 46 to 8 microns in median radius respectively.

Yamaki's analysis ignores the influence of gravity. The validity of this assumption can be examined by considering a large droplet -

$$\frac{\Delta P}{\gamma} = 400 \text{ cm}^{-1}$$

ΔP = 12000 dynes/cm^2, assuming a value of 30 dynes/cm for γ.

l = 121 microns, k = 46 microns for a large droplet with an excess pressure of 12000 dynes/cm^2.

From equation (22),

$\Delta P_g = \rho g h$

Here h = 2k

ΔP_g = 9.2 dynes/cm^2 for the above system.

A comparison of the two pressure values ΔP and ΔP_g proves that gravity is indeed negligible for the polyamide-carbon fiber system.

Figure 53 is a histogram showing the size distribution of polyamide droplets on carbon fibers. Carroll [38] investigated the transition between axisymmetry and non-symmetry and arrived at equation (21) which is plotted in Figure 11. Equation (21) can be solved for a contact angle of 23° to give a value of 1.32 for n at which the droplets make a transition to non-symmetry. This implies that the droplets become non-symmetric when k < 9.8 microns. The smallest measured axisymmetric droplet was 10.8 microns in diameter, larger than the dimension calculated by Carroll's theory.

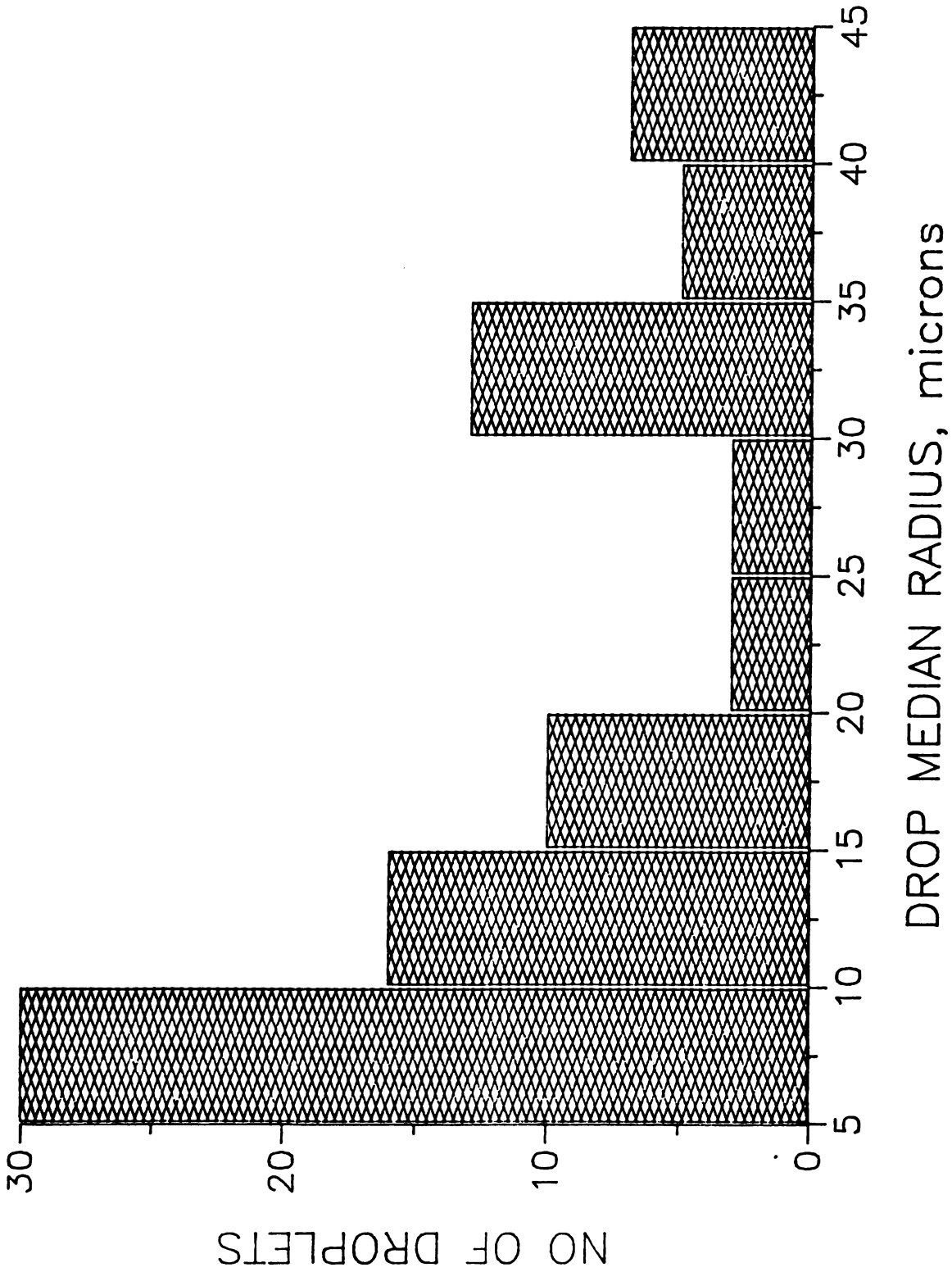

Figure 53. Histogram of droplet sizes.

6.5.4 *Spreading of Polymer Droplets on Fibers* :

Brochard et al. [42,43] state that if the spreading coefficient of the liquid film is greater than the critical spreading coefficient, then a polymer sheath of the order of 100-500°A wets the entire fiber surface at equilibrium. Since coalescence phenomena involve the retraction of a polymer film to form equilibrium droplets, this implies that a sheath would exist right from the beginning, the equilibrium configuration being the formation of equal-sized droplets bridged by a thin polymer film. Small droplets would drain into larger droplets due to Laplace pressure differences and the droplets would meet the film with a contact angle of zero. The critical spreading coefficient for carbon fibers can be calculated from equations 10(a) and 10(b) -

$$S_c = \frac{3}{2}\gamma\left[\frac{a}{b}\right]^{2/3} \qquad [10a]$$

Here, $\gamma = 30$ dynes/cm, $a \simeq 0.004\ \mu$, $b = 8\ \mu$; $S_c = 0.3$.

The equilibrium thickness of a wetting film on carbon fibers can be calculated by equation (7) -

$$e = a\left[\frac{3\gamma}{2S}\right]^{1/2} \qquad [7]$$

For carbon fibers, $a = 0.004\ \mu$, $\gamma = 30$ dynes/cm and $S = S_c = 0.3$, the equilibrium thickness is around 490°A.

But the polyamide droplets make an equilibrium contact angle of 23°. From Young's equation, we have -

$$\gamma_{SO} - \gamma_{SL} = \gamma\,\mathrm{Cos}\theta \qquad [6]$$

We can calculate $\gamma_{SO} - \gamma_{SL}$ to be 27.6 dynes/cm. Hence the spreading coefficient can

be calculated from equation (5b) to be -2.4. A comparison of the spreading coefficient for the polyamide-AS4 system with the critical value indicates that thermodynamics favors the retraction of the film into droplets leaving areas of exposed bare fiber in between them. This prediction is confirmed by experiment as shown in Figure 54. There are many unequal sized droplets sitting adjacent to each other having the same equilibrium contact angle as evidenced by Figure 51. Figure 48(e) also shows the presence of bare fiber surface between two equilibrium droplets.

6.5.5 *Discussion of Coalescence Phenomena* :

From the standpoint of high quality prepreg tapes, uniform impregnation of fibers in the spread tow leads to interparticle sintering and coalescence into an uniform film. The heat transfer rate for a given fiber matrix system depends on the average cluster diameter and the heater temperature. It is advantageous to have good spreading so that individual fibers are exposed thereby reducing the average cluster diameter. Sintering time between adjacent particles is a function of the matrix viscosity and the average particle size of the powder. The time taken for sintering increases with increasing viscosity and particle diameter. Thermodynamic instability forces the film formed by interparticle sintering to break up into droplets depending on the value of the spreading coefficient. A spreading coefficient smaller than the critical value will lead to the exposure of bare fibers while the converse will ensure a polymer sheath 100-500°A thick all along the fiber surface. In the former case, the polymer forms a distinct non-zero contact angle at the three phase contact line. The droplets are either axisymmetric or nonsymmetric depending on the contact angle and their size. As the equilibrium contact angle increases, the droplet-on-fiber system is unsymmetric for larger and larger droplets. This has an adverse effect on the flexibility of the prepreg tapes manufactured by the powder prepregging process. Interfiber distances have to be larger to avoid the bonding of adjacent fibers by the

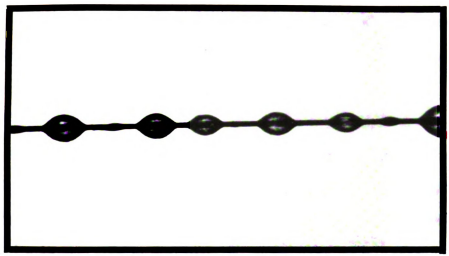

Figure 54. Axisymmetric droplets on a fiber at equilibrium, $S < S_c$.

droplets. The bond strength between droplet and fiber for an unsymmetric droplet is lower than an equivalent symmetric one because of its reduced fiber-droplet interfacial area. Hence the probability of losing a part of the impregnated matrix by attrition during handling is greater for materials which make a large equilibrium contact angle with the fiber. Large contact angles are also detrimental to the quality of prepreg tapes even when there are symmetric droplets because of the following reasons - (1) The fiber-droplet interfacial area decreases with increasing contact angle for the same droplet volume, and (2) the drop median radius increases with increasing contact angle thereby requiring that interfiber distances be greater for the same droplet volumes to avoid contact with adjacent fibers.

6.6 **Process** :

A set of 6 prepregging runs were performed with the powder prepregging process. The carbon fiber tow was unwound from a fiber spool with the help of nip rollers (Figure 20, page 59). The tow was then spread by the spreader which consisted of a 10 inch speaker (8 Ohms, 100 Watts) mounted in a plywood housing. The fiber tow passed over the speaker on top of which were mounted 10 polished steel shafts (3/8 inch diameter) spaced 1 inch apart. The shafts serve to hold the spread tow in position once they are spread by the speaker. The spread tow passed through nip rollers and entered the aerosolizer. The aerosolizer consisted of a plywood speaker box (15 inch speaker, 8 Ohms, 100 Watts) over which a cylindrical plexiglass column (8.2 inch internal diameter, 15 inches in length) was mounted. Vibrating rubber diaphragms were placed on a lip between the column and the speaker box and at the top of the column. The aerosolizer was cleaned and packed with 225 grams of powder at the beginning of the first run. Both the aerosolizer and the spreader were operated at the natural frequency of the respective systems. The natural frequencies were determined as delineated in Section 6.2. The tow was

impregnated with particles in the aerosolizer and then entered a heater (12 inch length) where the particles sintered and coalesced on the fibers. The resulting prepreg tape was wound on a takeup drum. The distance travelled by the fiber tow from the fiber spool to the takeup drum was 65 inches.

Table XIV shows the values of the different variables monitored in the process. The volume fractions were calculated by weighing 28 inch lengths of the prepreg tapes and comparing the weight of an equivalent length of unimpregnated fiber tow. The runs have identical oven temperature, aerosolizer and spreader conditions. Run 1 starts with a clean chamber and the walls get progressively caked with powder to a saturation level beyond which there is no further caking. Consequently, particle pickup was higher in run 1 as compared with the other 5 runs. The gas velocity of run 2 was zero and the volume fraction matrix showed a higher standard deviation than the other 5 runs. This indicates that a gas flow is recommended for optimum particle entrainment. The tow velocities of all the runs were slightly different due to manual speed control of the motors used in the process. Run 6 indicates that the chamber needs to be replenished with powder. Despite these discrepancies, the average volume fraction matrix was 22.5 with a standard deviation of 3.5. The corresponding Figures are 22.4 and 1.5 if the first and last runs are excluded.

Table XV shows a set of 4 prepregging runs all performed at different conditions. The volume fractions attained prove that a judicious combination of aerosolizer conditions and tow velocity can be employed to make a prepreg tape with any desired volume fraction of matrix.

A set of 21 prepregging runs of 15 minutes duration each were done with a preliminary alternative version of the process in which the fiber tow after spreading passed through a separate impregnation chamber which was supplied with entrained particles from the aerosolizer. The aerosolizer (3.15 inch internal diameter, 6.50 inch

TABLE XIV. PREPREGGING EXPERIMENTS- IDENTICAL CONDITIONS

No	Duration (mins)	Aerosolizer		Spreader		Oven Temp (C)	Gas Vel (cc/s)	Tow Speed (cm/s)	Vol Fraction (Standard Deviation)
		Amplitude (rms V)	Freq (Hz)	Amplitude (rms V)	Freq (Hz)				
1	50	5.3-5.4	12.1	11	38.5	215-217	4.34	1.73	27.8 (4.1)
2	47	5.3-5.4	12.1	11	38.5	215-217	0	2.45	23.5 (5.7)
3	35	5.3-5.4	12.1	11	38.5	215-217	5.72	2.24	23.6 (3.1)
4	58	5.3-5.4	12.1	11	38.5	215-217	4.42	2.09	20.5 (3.2)
5	55	5.3-5.4	12.1	11	38.5	215-217	4.42	2.03	22.0 (2.0)
6	55	5.3-5.4	12.1	11	38.5	215-217	4.42	2.23	17.3 (3.4)

TABLE XV. PREPREGGING EXPERIMENTS- DIFFERENT CONDITIONS

No	Duration (mins)	Aerosolizer		Spreader		Oven Temp (C)	Gas Vel (cc/s)	Tow Speed (cm/s)	Vol Fraction (Standard Deviation)
		Amplitude (rms V)	Freq (Hz)	Amplitude (rms V)	Freq (Hz)				
1	60	5.3-5.4	11.6	11	38.5	215-217	4.42	1.94	11.9 (3.9)
2	61	6.6-6.7	11.4	11	38.5	215-217	4.42	4.11	21.3 (3.8)
3	30	7.4-7.5	11.4	11	38.5	215-217	4.42	1.94	42.2 (4.1)
4	40	7.4-7.5	11.8	11	38.5	215-217	4.42	0.90	52.9 (3.2)

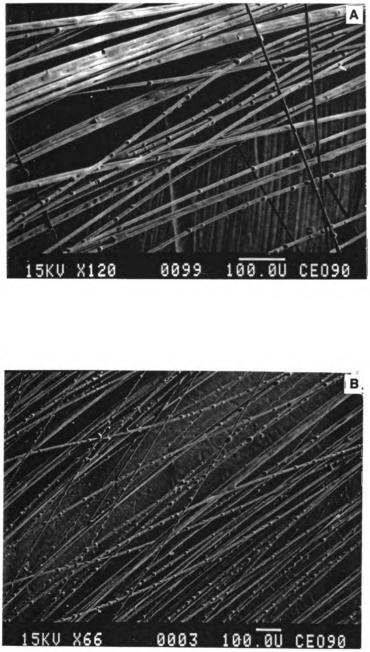

Figure 55. SEM photographs of prepreg tapes : (a) 90.9% V_f, and (b) 77.5% V_f.

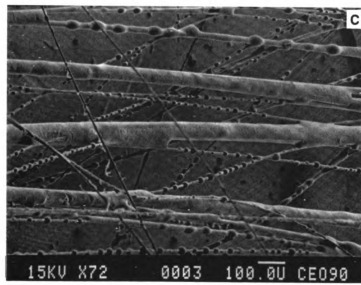

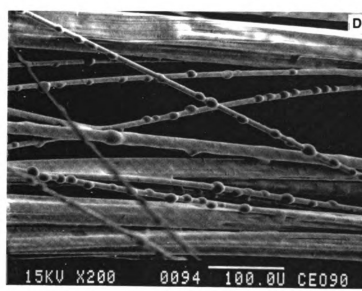

Figure 55. SEM photographs of prepreg tapes : (c) 70.2% V_f, and (d) 33.2% V_f.

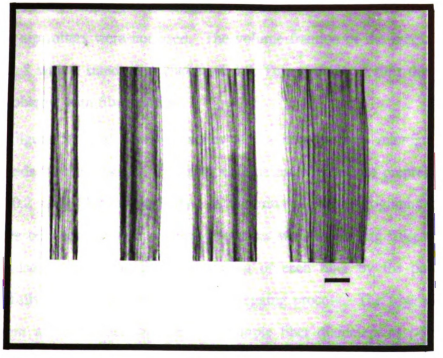

Figure 56. Prepreg tapes of different widths. Bar at bottom right represents 1 cm.

speaker, 8 Ohms, 50 Watts) and the spreader (6.50 inch speaker, 8 Ohms, 50 Watts) were powered by the same frequency generator and amplifier (39 Hz, peak-to-peak amplitude greater than 24 V). The prepregging was done in a semi-continuous mode i.e. the tow was stationary from time to time to give an effective residence time of 2 minutes in the impregnation chamber. The heater was held at 200°C. In this version, nip rollers were not used. The volume fraction of the matrix was computed to be 51.8 with a standard deviation of 3.9. This excludes 4 runs during which there were problems with fiber motion.

Figure 55(a)-(d) shows a series of scanning electron micrographs of prepreg tapes made by the process. The fiber volume fractions of the prepreg tapes are 90.9, 77.5, 70.2 and 33.2 respectively. A perusal of the photographs shows that the distances between adjacent droplets decreases with decreasing fiber volume fraction. It can also be seen that intimate wetting of each fiber by the polymer matrix is successfully realized by the powder prepregging process. The fiber clusters range in size from a single fiber diameter to multiple fiber diameters as pointed out earlier (Figure 49). The efficiency of the spreading step decides the diameter of the fiber clusters in the prepreg tape. Figure 56 shows a photograph of prepreg tapes of different widths. The widest tape made by the process was 6 cm. The wide tapes (greater than 2.5 cm) consisted predominantly of individually coated fibers. Figure 55(b) shows the SEM photograph of such a tape. It should be pointed out that the tape width in the process was the widest immediately following the spreader and decreased gradually all the way to the takeup drum. The width of the fiber tow before it entered the aerosolizer was always maintained at a value greater than 5 cm (a width of 4.8 cm implies that there is one fiber diameter between adjacent fibers). Table XVI shows an average variation in prepreg tape width within selected experiments of 25 %. The primary cause for this variation is the fluctuation in spreading width which is caused by instantaneous fluctuations in speed of the nip

rollers and tow tension.

TABLE XVI. PREPREG TAPE WIDTHS

No	Duration, mins	Tape Width, cm
1	121	13.4 ± 4.2
2	60	21.4 ± 4.3
3	60	19.7 ± 4.1
4	60	16.2 ± 3.3
5	60	11.5 ± 3.6
6	60	12.8 ± 2.9
7	60	14.1 ± 5.2
8	61	13.6 ± 2.6
9	80	20.8 ± 5.1
10	86	18.3 ± 3.0

The process in its present configuration is capable of manufacturing prepreg tapes with any desired volume fraction of fiber and matrix with a standard deviation of 3-4% within each prepregging run. The reasons for the deviation in volume fraction are - (1) aerosolizer performance : caking on the walls and deviations from resonance, (2) spreading : variations in spreading width caused primarily by improper fiber motion, and (3) fiber motion : variations in speed control of the nip rollers and the takeup drum.

The prepreg tapes manufactured by the process possess the qualities of tack and drape as defined in Chapter 1. The surface roughness of the tapes is induced by the undulating contours of loosely bound individually coated fibers. This facilitates the layup procedure during consolidation since the tapes remain in position when stacked one on top of each other due to mechanical interlocking. Tape flexibility is achieved primarily by the excellent spreading of the fiber tow. Post-processing operations such as weaving can be easily accomplished with such a configuration.

6.6.1 *Discussion - Process Performance* :

The fiber motion system is capable of tow speeds from 2-10 cm/s. The speeds of the nip rollers can be controlled at the set point with a minimum standard deviation in instantaneous speeds of 0.1 cm/s. The instantaneous speed is monitored and controlled 9.1 times a second by the computer. Fluctuations are due to the inherent friction in the system i.e. in one rotation of the nip roller, the friction between the bearings and the shafts is different at different locations on the shaft. This fluctuation is periodic in nature and the computer controls the average speed at the set point for each rotation.

The spreader, when operated at its optimum settings performs extremely well in separating collimated fiber tows into their individual filaments. It responds well to fluctuations in speed and tow tension as evidenced by the experiments described in Section 5.2.3. The smooth shafts which are mounted in precision bearings turn along with the fiber tow whenever there is friction. Fiber damage is minimized by this mechanism and by the fact that the turning angles of the fibers are kept as low as possible (Figure 57). Motor stalls and malfunctions in other parts of the system do not cause damage to the fiber tow in the region over the spreader as with directed air methods. Scaleup of the spreader can be accomplished easily to handle any number of tows. The extra surface area needed for spreading is created by powering a series of speakers with an high wattage amplifier.

The aerosolizer is operated in the low particle concentration regime of around 0-200 mg/m^3 for the polyamide powder. Constant particle concentrations in the chamber can be maintained over long periods of time if the particle sump is replenished on a periodic basis. Maximum attainable particle concentrations in the chamber can be increased by increasing the particle size of the powder. Particle pickup by the fiber tow can be increased either by decreasing the tow velocity or increasing the dimensions of the chamber for a particular powder. The increased

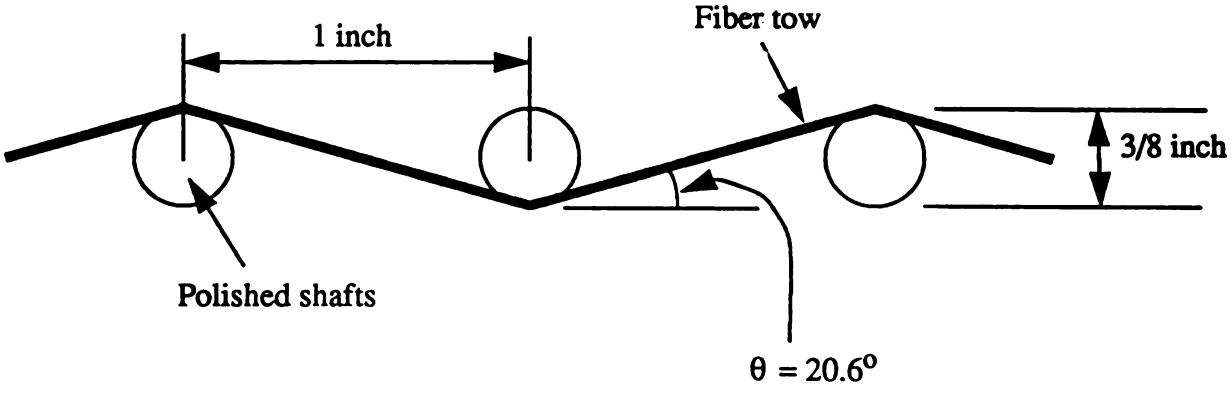

Figure 57. Turning angles, fiber tow over spreader.

charge-to-mass ratio of fine powders results in a natural electrostatic force between the electrically ground carbon fibers and the polymer particles. This obviates the need for additional equipment such as charging electrodes to increase the surface charge on the powder. The oscillatory motion of the particles induces multiple collisions with the fibers and increases the particle collection efficiency. The aerosolizer can be scaled up in a similar manner as the spreader - by installing multiple speakers. An alternative is to design an acoustic horn to cover a larger surface area. The above discussion also considered a different configuration whereby the particle impregnation chamber was maintained separate from the aerosolizer. This is a viable alternative in which case a large impregnation chamber can be maintained at a constant particle concentration with multiple aerosolizers feeding into the chamber all powered by the same amplifier.

Coalescence in the heater is described in detail in Section 6.5. The formation of a film and/or droplets on individual fibers results in the manufacture of flexible tapes which are suitable for post-processing operations such as weaving and filament winding. Intimate wetting between the fiber and the matrix also results in reduced consolidation times since the matrix has to flow over very short distances of the order of microns to seal up local voids rather than millimeter distances in processes such as melt impregnation. Hence the role of viscosity is reduced as a factor in the manufacturing process. Scaleup of the heater is easily accomplished by the construction of a muffle furnace open at both ends to facilitate the entry and exit of the powder- impregnated tow.

Chapter 7

CONSOLIDATION

The objective of this phase of the investigation was to determine optimum consolidation cycles for the manufacture of void-free parts of different fiber- matrix volume fractions. The prepreg tapes made by the process were consolidated into specimens using processing cycles in which the temperature, pressure and time were controlled and monitored. The specimens were then characterized for their fiber-matrix volume fractions, void content and their fracture toughness.

7.1 **Experimental** :

The prepreg tapes were laid up in a two-part mold described in Section 4.7 (Figure 24) and consolidated under heat and pressure in a plate and frame press (Carver Press) to form composite specimens. A typical temperature-pressure profile for a consolidation run is shown in Figure 58. The consolidation procedure was as follows :-

The prepreg tape wound on the takeup drum was cut into 28 or 32 inch lengths and weighed on a Sartorius balance. An approximate fiber-matrix volume fraction was calculated by comparing these weights to the measured weight of an uncoated AS-4 fiber tow. The prepreg tapes were then cut up into 7 or 8 inch lengths. A non- porous Teflon® film was placed in between the two mold faces and the laid up tapes. The mold faces were also sprayed with a mold release agent as a precautionary measure. Platens of a Carver press were heated to the desired

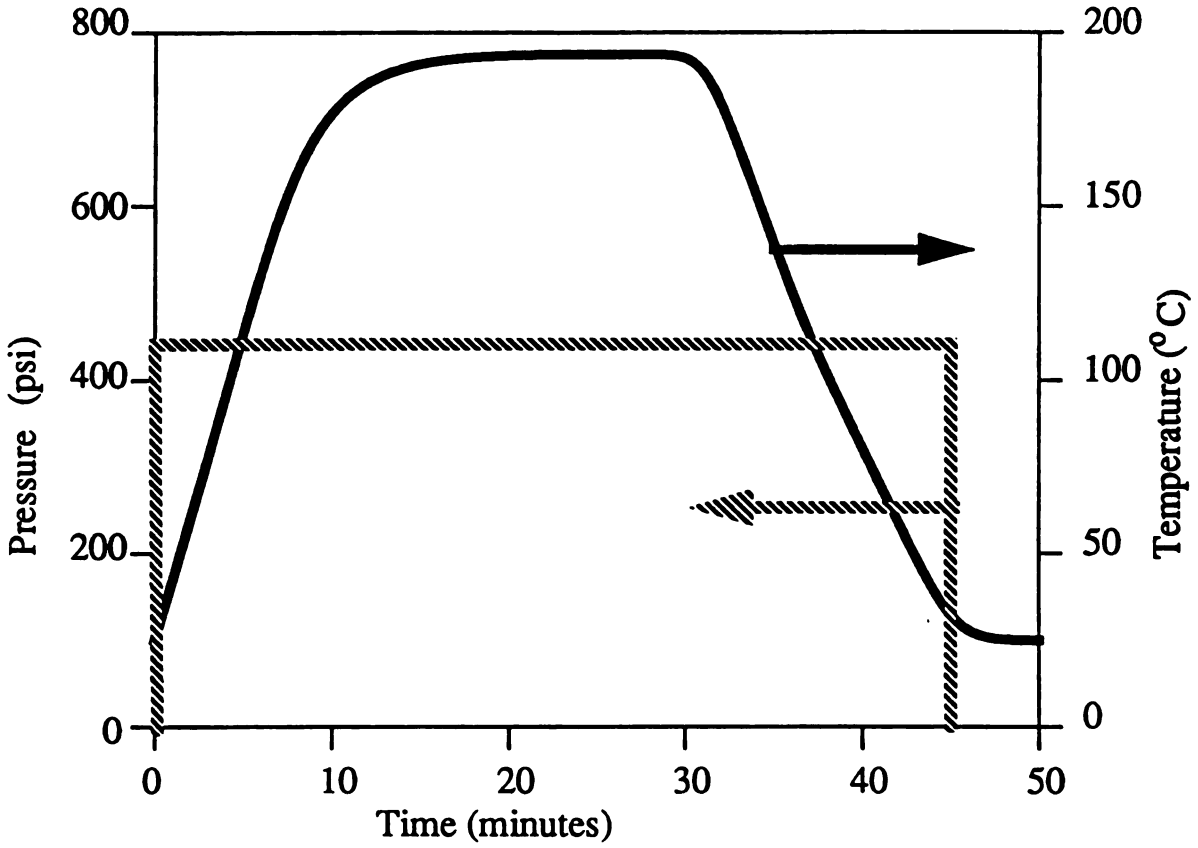

Figure 58. Consolidation cycle, specimen 2.

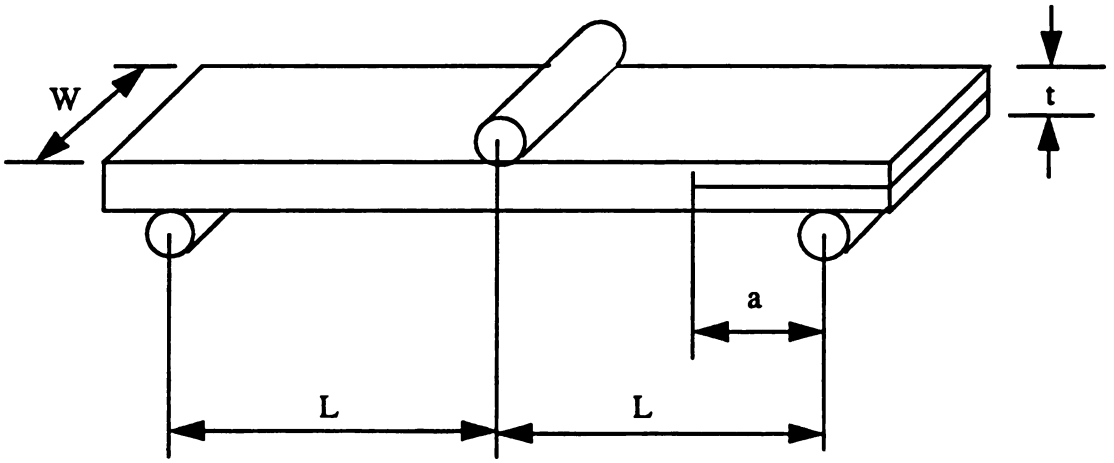

Figure 59. ENF test, loading pins and specimen geometry.

consolidation temperature. The mold with the prepreg tapes was placed between the platens with a K-type thermocouple inserted 1 mm away from the mold face. The millivoltage output of the thermocouple (1 mV/°C) was fed to a chart recorder to monitor the temperature of the part. Ceramic fiber insulation was placed flush on all the four sides of the mold. The platens were then lowered to contact the mold at a consolidation pressure based on the fiber-matrix volume fraction calculated earlier. The temperature of the platens was maintained at the set point for 30 minutes. This includes the initial period of approximately 10 minutes during which the faces of the mold get heated to the set point temperature. After 30 minutes, the heater was shut off and the mold cooled at an approximate rate of 10-15 °C/min with the help of cooling water for 15 minutes to ambient temperature. The consolidation pressure was maintained throughout the duration of the experiment to prevent void formation due to shrinkage. Two of these consolidated parts were placed in the mold with a 75 micron Teflon® film 1 inch from either end as crack initiators for the end-notched flexure test and the consolidation procedure repeated.

The resulting part was cut using a water-cooled diamond saw into specimens for the Mode II fracture toughness (end-notched flexure or ENF) test. Approximately 1/8" was cut from around the part to eliminate edge effects. Figure 59 shows the specimen geometry and the location of the loading pins for the test. The specimens were tested to failure in an Universal Testing Machine (screw-driven, 4480 N load cell, crosshead displacement rate 0.3 mm/min). Load and displacement below the center loading pin were monitored for each specimen. The critical strain energy release rate for mode II failure was calculated from the equation [79] -

$$G_{IIc} = \frac{9\, P_c\, C\, a^2}{2W(2L^3 + 3a^{3)}} \qquad [44]$$

where

P_c = Critical load, N

C = Compliance, calculated from the load-displacement curve by linear regression, mm/N

a = Crack length, mm

W = Specimen width, mm

L = Span, the length between the center loading pin and the outer pins, mm

G_{IIc} = Mode II fracture energy, kJ/m^2

These specimens were analyzed both for volume fractions of fiber and matrix and for void content with the help of an optical image analysis technique called Optical Numeric Volume Fraction Analysis or ONVFA [80]. Small pieces of the specimens (1 inch x 0.5 inch) were cut and mounted in acrylic holders and polished successively to a final grit of 0.05 microns. A 80 grit belt sander, a Struers Abramin Automated Polisher (240, 320, 1000, 2400 and 4000 grit, 3 minutes each), a LECO GP20 Grinder/Polisher (5 micron, 1 micron Al_2O_3 powder, 5 Minutes each) and a Buehler Vibromet (0.05 micron Al_2O_3 powder, 10-12 hours) were used in the polishing sequence. The specimens were cleaned in an ultrasonic cleaner for a few minutes and then cleaned with ethanol for microscopic observation. 15 images were randomly chosen under the optical microscope and digitized. An Olympus microcope with a video monitor and an Amiga computer was used for the digitization. The digitized images were then analyzed using the ONVFA program. The program performs a fiber count and calculates a fiber volume fraction assuming an average fiber diameter. The program was also used to generate a histogram of grey scales to estimate the void fraction in the composite specimen. Void fractions were reported as a range e.g. 1.2-1.5 to underscore the fact that there was some subjectivity in deciding the number of grey scales which corresponded to voids. For most specimens, the void content was estimated by digitizing all the voids present on

the polished face. This was possible because at low void fractions, the number of frames that need to be digitized is usually quite low (less than 20). The measurement of void fractions greater than 5% was prone to statistical error because it was not possible to digitize all the frames where voids occured due to the random and frequent incidence of voids all across the composite specimen.

Section 5.2 discussed the measurement of relative crystallinity for the neat resin. The same procedure was used to determine the relative crystallinity of the composite specimens. A small piece approximately 10 mg in weight was cut from each composite specimen and placed in the DSC sample pan. The DSC run was then conducted at a ramping rate of 5°C/min from ambient temperature to 200°C. The area under the melting endotherm was corrected for fiber volume fraction and an endothermic heat determined for each sample. The fiber volume fraction used in this calculation was the average value determined by ONVFA.

7.2 Optimum Cycles for Void-Free Consolidation :

A series of consolidation experiments were performed at different consolidation pressures for different fiber-matrix volume fractions. The temperature was maintained at 197-202°C for all but one of the experiments while the time was maintained constant at the consolidation temperature for 20 minutes for all the experiments. The fiber-matrix volume fraction, void fraction and Mode II fracture toughness were measured for each part. The results of the entire investigation are presented in Table XVII.

TABLE XVII. CONSOLIDATION AND ONVFA EXPERIMENTS

No	Pressure (psi)	Temperature (°C)	V_f† (%)	V_v† (%)	G_{IIc} (kJ/m^2)	V_{fc}† (%)
1	440	197-202	69.8 ± 1.7	Voids	0.297	> 70
2	440	197-202	70.7 ± 4.7	4.7-6.1	0.133	75.3
3	440	197-202	68.7 ± 5.5	2.2-3.6	-	71.2
4	440	197-202	62.5 ± 7.4	10.4-13.5	0.007	72.3
5	200	197-202	70.8 ± 4.0	3.4-4.0	0.223	73.8
6	560	197-202	69.9 ± 3.6	5.3-5.6	0.011 ± 0.001	74.1
7	1100	197-202	74.2 ± 1.2	Void-free	-	74.2
8	1100	197-202	73.5 ± 1.1	Void-free	0.128	73.5
9	1060	197-202	74.1 ± 2.7	1.2-1.6	0.171 ± 0.028	75.3
10	1150	197-202	71.2 ± 3.0	5.8-7.1	0.009	76.6
11	440	197-202	58.3 ± 5.7	7.7-9.8	0.008	64.5
12	200	197-202	69.8 ± 3.3	Void-free	0.548	69.8
13	440	197-202	63.5 ± 3.4	0.1	0.657	63.6
14	200	197-202	66.5 ± 2.9	Void-free	0.516	66.5
15	225	197-202	62.4 ± 3.0	0.02	0.505 ± 0.039	62.4
16	440	197-202	70.6 ± 3.0	0.36	0.336 ± 0.036	70.9
17	440	197-202	65.8 ± 3.9	1.7-2.9	-	67.8
18	80	≈ 185	40.0 ± 6.1	Void-free	0.672 ± 0.100	40.0

† V_f = Fiber volume fraction
V_{fc} = Fiber volume fraction if specimen were void-free
V_v = Void fraction

Specimens 1 - 6 showed the presence of voids, indicating that a higher pressure is required for consolidation while specimens 7 and 8 were both void-free and specimen 9 had few voids. A limited amount of bleeding was observed for specimens 7 and 8. All the above-mentioned specimens were in the range of 71-75 % V_{fc} if they are corrected for voids. From these experiments, one can surmise that a pressure of around 1100 psi is needed for optimum consolidation of prepreg tapes with a fiber volume fraction of 71-75 %. This assumes that good intimate impregnation is achieved in the powder prepregging process. If the impregnation is not uniform, then even an optimum pressure results in specimens with voids, especially at fiber volume fractions greater than 75 %. This can be seen in specimens 9 and 10, the latter showing very poor impregnation while the former specimen had a void fraction of 1.6%. At such high fiber volume fractions, it is imperative that the polymer matrix be placed in the final position during prepregging. As the fiber volume fraction increases beyond 75 %, intimate impregnation becomes a key factor in the consolidation process. From this investigation into the powder prepregging of 8 micron carbon fibers with 9 micron average particle size polyamide particles, it is believed that a fiber volume fraction of 75 % in the prepreg tape is the maximum that can be used to make void-free parts reproducibly. It is a matter of conjecture whether the use of smaller particles e.g. 5 micron polyamide particles will enable the manufacture of void-free parts with a volume fraction greater than 75 %. This would depend largely on the uniformity of particle impregnation in the prepregging process.

Bleeding of resin from the part increased with increasing consolidation pressure for constant fiber volume fractions in the prepreg tapes. A significant amount of resin bleeding was observed for specimens 12 and 14 while a limited amount of bleeding was observed for specimens 13, 15, 16 and 17. These experiments indicated that an optimum pressure of around 440 and 225 psi are required for fiber volume fractions of 64-68 % and 60-63 % respectively. Specimen

18 was consolidated at a lower temperature of 185 C and 80 psi to form a void-free part with 40 % V_f which implies that a lower pressure is required at 197-202°C at which all the other experiments were performed.

The above analysis suggests a behavior whereby for a particular V_f, as pressure increases, consolidation improves to an optimum above which bleeding occurs until at very high pressures, the fiber squeezes out along with the resin leaving a damaged specimen. The amount of bleeding is proportional to the difference between the optimum pressure and the applied pressure, the latter being greater than the optimum pressure. If the desired fiber volume fraction in the final part is much lower than that in the prepreg tape, a lower consolidation pressure is required than suggested in the above argument. For instance, a pressure of only 200 psi was required to make a void-free part of 69.8% V_f (specimen 12). It is also apparent that the optimum pressure needed for consolidation increases with increasing fiber volume fraction.

An operating curve for optimum consolidation of powder-impregnated tapes (polyamide-AS4) is shown in Figure 60. The underlying assumptions are that temperature is kept constant at 197-202°C and the duration of the consolidation cycle is 20 minutes. The solid line indicates optimum pressures required to make void-free parts for different fiber-matrix volume fractions in the prepreg tapes. Pressures above this line result in bleeding the degree of which is proportional to the deviation of the actual pressure from the recommended value. Pressures below the solid line will result in the presence of voids in the final part. Bleeding of the resin during consolidation is encouraged to a limited extent for the formation of void-free parts. This is to ensure that voids in resin-deficient regions are filled up by the transverse flow of polymer melt. Figure 61 shows the optical micrographs of two void-free specimens 9 and 15. Regions of hexagonal close packing can be observed in both the specimens.

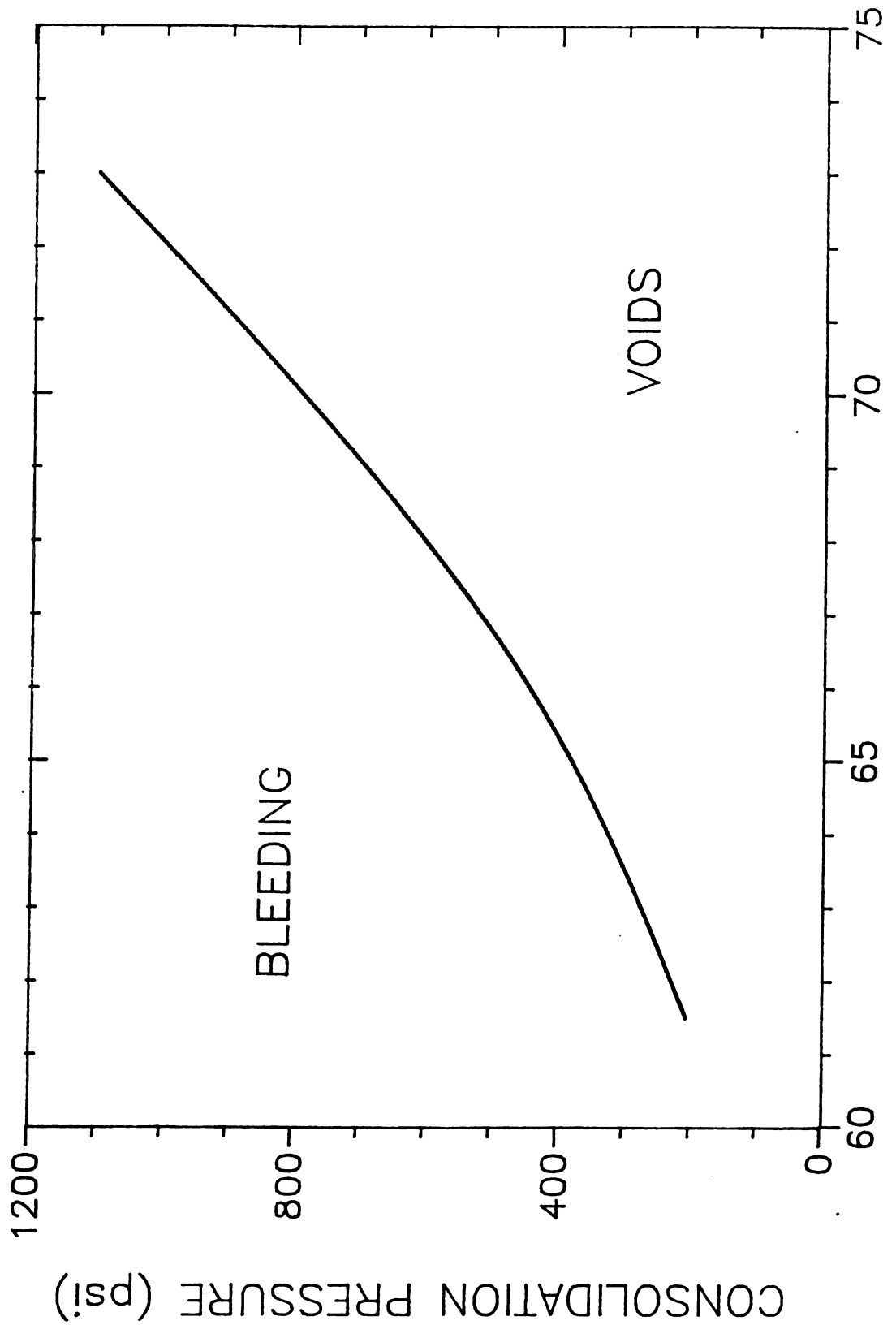

Figure 60. Operating curve for optimum consolidation of polyamide-AS4 composites.

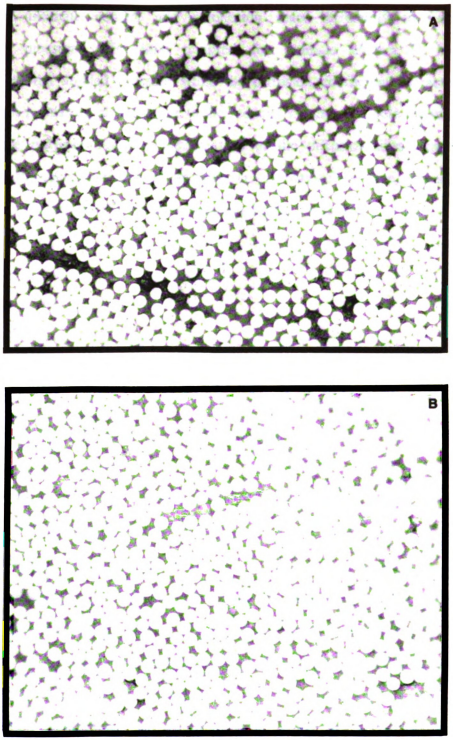

Figure 61. Optical micrographs of polyamide-AS4 composites. (a) specimen 3, and (b) specimen 7.

7.3 Intimate Contact and Autohesion :

In Section 3.2, the theory of consolidation is discussed. The two steps of consolidation, intimate contact and autohesion react differently to increasing consolidation pressure. The time required for intimate contact is inversely proportional to the applied pressure while the diffusion coefficient for autohesion decreases with increasing pressure due to the reduced volume available for segmental motion of the polymer chains. One measure of the diffusion time required for autohesion is the relaxation time of the polymer. A Maxwell relaxation time, λ can be calculated from the rheological measurements by the formula -

$$\lambda = \frac{N_1}{2\,\tau_{12}\,\dot{\gamma}} \qquad [45]$$

where

N_1 = Normal stress, dyne/cm^2

τ_{12} = Shear stress, dyne/cm^2

$\dot{\gamma}$ = Shear rate, sec^{-1}

At a temperature of 187.8°C, N_1 = 58.2 dyne/cm^2,

$\tau_{12} = \dot{\gamma}\,\mu$ = 3.981 x 691 = 2570.9 dyne/cm^2

λ = 0.0027 sec.

The relaxation time for the polyamide is calculated to be less than a millisecond for the entire range of temperatures used for processing in this investigation. In contrast, a processing time of 20 minutes at temperatures above 180°C is used for consolidation of the prepreg tapes into composite parts. In addition, the consolidation experiments follow the trends that would prevail if intimate contact were the only mechanism of adherence i.e. efficiency of consolidation increases with increasing pressure. Hence it can be concluded that intimate contact is the rate-

controlling step in the consolidation process. If autohesion was of greater importance, then it may be advisable to use a two- stage consolidation cycle - a period of high pressure to achieve intimate contact followed by one of lower pressure to facilitate autohesion.

7.4 Crystallinity :

The degree of crystallinity of the matrix affects the mechanical properties of the composite. Lee et al.[54] and Manson et al.[55] noted a decrease in fracture toughness with increasing crystallinity for APC-2 composites. DSC was used to gage the level of crystallinity in this investigation and thereby ensure that it stayed the same for each specimen. DSC runs performed on three composite specimens gave an endothermic heat of 50 ± 8.4 J/gm over a series of 12 runs. The experiments on the neat resin for different cooling cycles showed that the endothermic heat was around 50.8 ± 2.9 J/gm (Section 5.1.2). A comparison of the two indicates that the average level of crystallinity is the same for both the neat resin and the composite specimens. The latter however showed a large standard deviation which is due in part to local variations in volume fraction of matrix (including the presence of voids) in the composite specimens. Average volume fractions measured by image analysis for each specimen were used to compute the endothermic heat absorbed by the matrix.

Within the limits of this experiment, it can be stated that the levels of crystallinity are approximately equal for all the tested specimens. This is not surprising since a cooling rate of around 10-20 °C/min was used for all the consolidation experiments. However, a rigorous technique to measure the exact fiber-matrix volume fraction in the DSC sample is required in order to calculate the relative crystallinity in each specimen with more accuracy than afforded by the above set of experiments.

7.5 Fracture Toughness and Failure Mode :

The fracture toughnesses were measured by the end-notched flexure test. Figure 62 is a plot of G_{IIc} as a function of fiber volume fraction for specimens 9, 15, 16 and 18 each of which were averaged over 3-4 tests. The fracture toughness decreases with increasing fiber volume fraction for void-free or near void-free specimens from a value of 0.672 kJ/m^2 for 40% V_f to 0.171 kJ/m^2 for 74.1% V_f.

A SEM study was undertaken to understand the failure mechanisms for fracture. Specimens 15 and 16 undergo extensive plastic deformation i.e. matrix deformation in the direction of crack propagation. Triangular ribbons of the matrix are pulled at an angle of approximately 45°. This phenomenon occurs because even though the specimen is loaded in shear, there is a tensile stress component at an angle of 45° to the fracture surface [81]. This is shown in Figure 63(a) and (b) which are micrographs of specimen 15. Specimen 9 which is shown in micrographs 63(c) and (d) shows both plastic deformation and the presence of bare fibers. This is understandable since the higher volume fractions confine the matrix to smaller amounts and thinner dimensions. Many regions of hexagonal close packing were noticed under the optical microscope. Hence the toughness of the matrix cannot be achieved to the same extent in the composite. The SEM study indicated that the composite specimens with fiber volume fractions of 60- 65 % which are of interest in the composites industry showed excellent wetting between fiber and matrix. The predominant mode of propagation for fracture is plastic deformation of the matrix at these volume fractions.

Figure 64 shows a plot of Mode II fracture energy as a function of void fraction in the composite for a fiber volume fraction of around 70 %. As can be seen, the fracture energy is maximum for the void-free part and falls with increasing void content. There is a precipitous drop in fracture toughnesses for void fractions greater than 5% as evidenced by Figure 64 and the G_{IIc} values of specimens 4, 6, 10

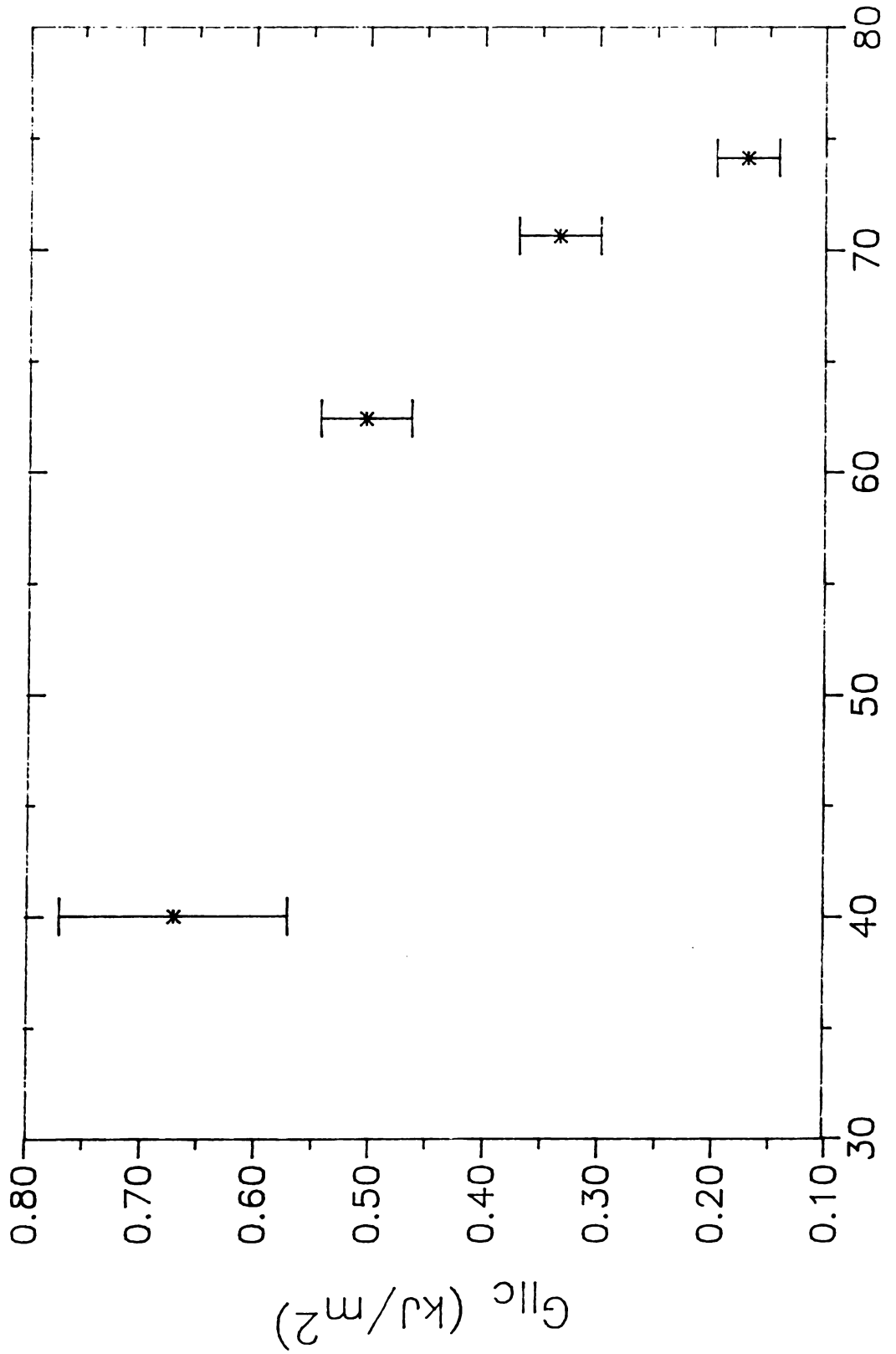

Figure 62. Mode II fracture energy vs fiber volume fraction, polyamide-AS4.

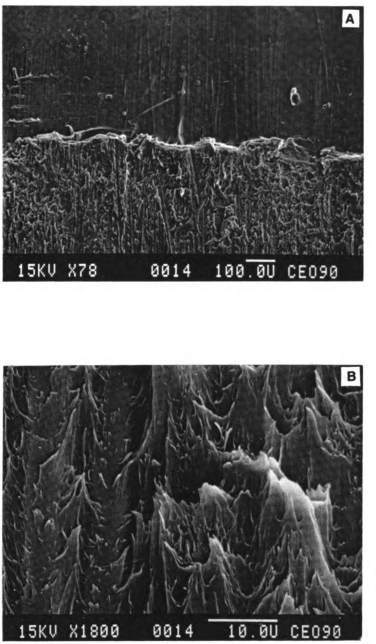

Figure 63. SEM photographs of fractured specimens: (a) and (b) specimen 15.

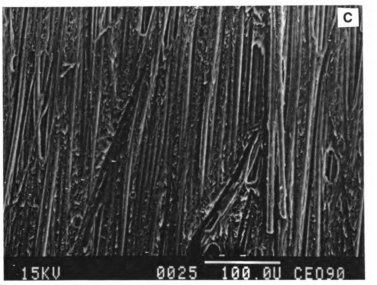

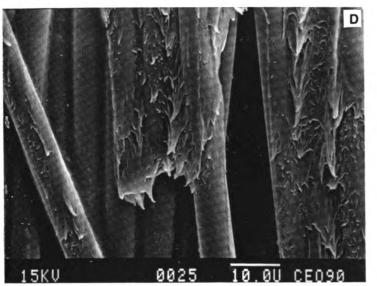

Figure 63. SEM photographs of fractured specimens: (c) and (d) specimen 9.

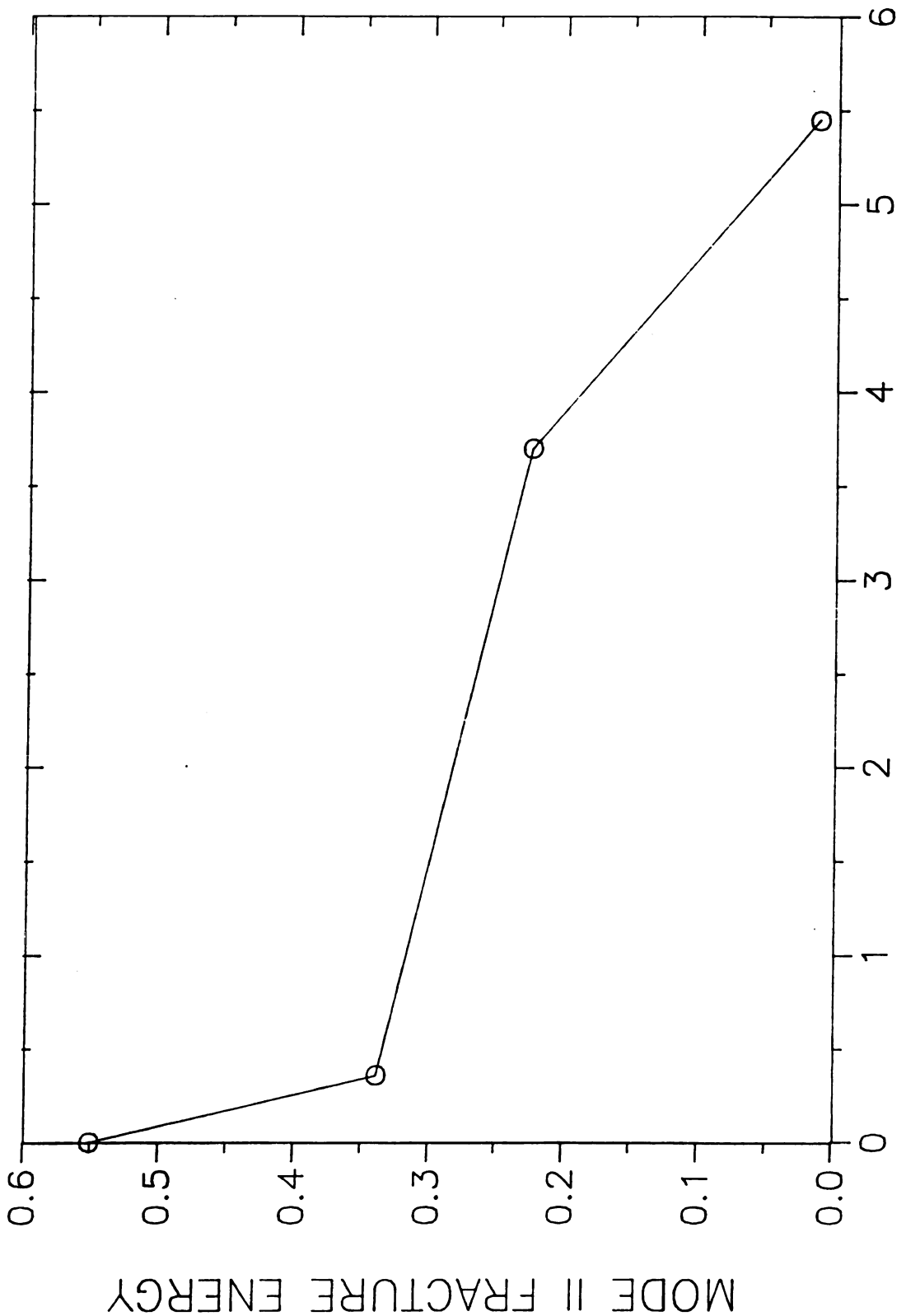

Figure 64. Mode II fracture energy vs void fraction, V_f = 70%.

and 11 listed in Table XVII. It should be noted that there is a statistical error involved in the exact measurement of large void fractions in the composite specimen as pointed out earlier in the experimental section. The correlation between fracture toughness and the void content of the composite as characterized by ONVFA proves that fracture toughness is an effective mechanical test in gaging the quality of the consolidated composite specimen.

7.6 Discussion of Consolidation Experiments :

The consolidation experiments led to the development of an operating curve for the manufacture of void-free composite parts. For a given fiber volume fraction in the prepreg tape, as consolidation pressure increases, void content decreases until an optimum pressure is reached which results in a void-free part. Above this value, resin bleeds out of the part with increasing pressure finally resulting in a damaged specimen as the fibers flow out of the part along with the matrix. The optimum pressure required for consolidation increases with decreasing fiber volume fraction in the composite if temperature and consolidation time are kept constant. The relative crystallinity of each specimen stays approximately constant if the cooling rate during the consolidation cycle is controlled between 10-20°C/min. Consolidation cycles are shown to be simple and require the use of temperatures above the softening or melting point of the polymer, an optimum pressure which depends on volume fraction of fibers in the composite (for a given matrix at constant temperature and contact time) and a contact time which allows for intimate wetting between interfaces and interdiffusion of polymer chains across the interface. Intimate contact is the rate-determining step in the consolidation of polyamide-carbon fiber composites. Image analysis and fracture toughness testing of the specimens were effectively used to gage the efficiency of the consolidation cycle. There is good correlation between the quality of consolidation as characterized by ONVFA (fiber-matrix volume

fraction, void content) and the fracture toughness of the specimen, the latter decreasing with increasing void fraction in the composite part.

Chapter 8

UNIFIED APPROACH

The entire experimental investigation was conducted using polyamide particles and carbon fibers. However, the principles involved in the manufacture of polyamide-carbon fiber composites can be applied to any other fiber-matrix combination. This section lays down general guidelines for the selection of process parameters in order to be able to pre-impregnate any reinforcing fiber with any thermoplastic matrix.

8.1 Fiber Motion :

The fiber motion system may need to be optimized in terms of its PID control parameters to ensure synchronous speeds of the nip rollers. If an alternative system which senses tow tension to control speed of the takeup drum is used, then it has to be calibrated for tow tension as a function of pulling force.

8.2 Spreader :

The frequency at which the reinforcing fibers absorb the most energy and the minimum amplitude at which they respond quickly to instabilities in the system are measured for each type of reinforcing fiber. These parameters can be used for the spreader regardless of the number of fibers/tow if sufficient surface area is available for spreading.

8.3 **Aerosolizer** :

The natural frequency of the system which includes the chamber and the weight of the powder on the lower diaphragm is determined prior to each run. The maximum sound intensity inside the chamber that does not permit sonic agglomeration is determined by a initial series of test runs on the powder being used for prepregging. An operating curve which gives the particle pickup as a function of sound amplitude at the resonant frequency and tow velocity is empirically generated as an aid in setting aerosolizer conditions for each prepregging run.

8.4 **Heater** :

A fundamental study of coalescence times in the heater is the first step in deciding residence times of the impregnated fiber tow in the heater. An operating envelope for the heater should define the maximum possible tow speed for each temperature at which the heater is maintained, up to the matrix degradation temperature. This residence time would ensure that the particles sinter, coalesce and begin to form droplets on the fibers before the prepreg tapes exit the heater. The quality of prepreg tapes during test runs with the predicted residence times would further help in defining the control process. The findings of the coalescence study will also be of value in deciding whether the fiber-matrix interface has to be modified to promote better wetting which is essential in order to make high quality prepreg tapes.

Table XVIII is a summary of the key properties and process parameters for each unit operation in the powder prepregging process. In general, the process in its present configuration can be easily adapted to make prepreg tapes with any fiber-matrix combination. Most of the experiments described above were demonstrated in this investigation and can be performed on other materials without expending a

TABLE XVIII. UNIFIED APPROACH - POWDER-PREPREGGING PROCESS

Unit Operation	Key Properties	Process Parameters
Fiber motion	* Tow weight/length	* Proportional, derivative and integral constants for speed control
Spreader	* Type of fiber	* Natural frequency, * Minimum amplitude
Aerosolizer	* Particle size * Charge-to-mass ratio * Hausner ratio	* System natural frequency * Maximum amplitude * Operating curve for particle pickup vs tow velocity, amplitude
Heater	* Convective heat transfer coefficient * Particle size * Matrix viscosity * Spreading coefficient	* Operating envelope - coalescence times vs heater temperature

significant amount of effort. Key material properties that need to be measured or calculated are particle size, fiber diameter, fiber- particle interactions in terms of electrostatic attraction, matrix viscosity, spreading coefficient of the matrix on the fiber and the convective heat transfer coefficient to the impregnated tow inside the heater. Consolidation of these prepreg tapes to make void-free parts requires the use of heat and pressure in simple processing cycles that can be determined by a set of consolidation experiments to result in an operating curve such as the one developed in this investigation (Figure 60, page 162).

Chapter 9

CONCLUSIONS AND FUTURE WORK

The **conclusions** that can be drawn as a result of this investigation are :

(1) The dry powder prepregging process developed in this investigation is capable of impregnating reinforcing fibers with any desired volume fraction of matrix. It is independent of matrix viscosity, does not use any solvents, relies on the naturally high charge-to-mass ratio for adherence of fine polymer particles to fibers and results in the manufacture of prepreg tapes in which each fiber is intimately wetted by the polymer matrix. The prepreg tapes are almost as flexible as the reinforcing fiber tow with better handling properties. The tapes are also tacky (sticky) because of the roughness induced by the presence of droplets on individual fibers or clusters of fibers and hence do not move relative to one another during the layup procedure prior to consolidation.

(2) The key elements of the process are : (1) The use of fine particles roughly of the order of dimensions of the reinforcing fiber, (2) the aerosolizer which delivers a controlled concentration of fine particles to the fiber tow, (3) the spreader which spreads fiber tows to a width so that individual fibers are exposed, and (4) the heater where the particles coalesce to form droplets on the fibers.

(2a) It is extremely difficult to fluidize cohesive polymer powders less than 30

microns in size. The bed profile for such powders includes a defluidized region near the distributor where cracks/channels form and a bubbling region above where bubbles disrupt crack formation and ensure that the particles remain in a fluidized state. The height of the defluidized region increases as particle size goes down. Good control over fluidization parameters like entrainment rate and bed height is not possible in this particle size regime.

(2b) The aerosolizer which utilizes acoustics to provide a buoyant force to the particles is a stable entrainment system which can provide an aerosol of constant particle concentration for extended periods of time. It operates best at its natural frequency below sound pressure levels at which acoustic agglomeration becomes a problem. Sonic agglomeration increases with decreasing particle size for the same sound intensity levels inside the chamber.

(2c) The spreader which works on the principle of acoustic energy is shown to be a reliable system to spread collimated fiber tows into their individual filaments. It works best at the natural frequency of the reinforcing fibers above a threshold value of sound pressure in the region over the speaker. This threshold value is set by the amplitude of the sound wave metered to the speaker.

(2d) Coalescence of particles on fibers is a sequential process which comprises of heat transfer to the impregnated fiber tow, interparticle sintering, film formation and retraction of the film to form stable droplets on fiber surfaces. Each step has a resistance associated with it and coalescence time is the sum of all the individual times. The material parameters which control each step are the convective heat transfer coefficient (heat transfer), matrix viscosity and particle size (sintering), and the spreading coefficient of the polymer melt on the fiber surface (film and droplet formation).

(3) Simple consolidation cycles can be used to make void-free composite parts from the flexible prepreg tapes manufactured by the process. The requirements for an optimum consolidation cycle are the use of temperatures above the melting or softening point of the polymer, and consolidation pressures at which intimate contact of the polymer interfaces and interdiffusion of polymer chains across these interfaces are both given sufficient time to occur. The first step of intimate contact is the rate-controlling step in the consolidation of polyamide-carbon fiber composites.

The following **recommendations for future work** are made as a result of this investigation -

- The behavior of the aerosolizer can be enhanced with a range of improvements which include an anti-static coating on the chamber walls, a constant feed of particles to the packed bed at the base of the chamber, powder recovery and a deionizer unit online to the Realtime Aerosol Monitor to neutralize charge on the particles.

- Performance can be enhanced by a modification whereby the aerosolizer feeds into an impregnation chamber where the spread fiber tow is impregnated with the entrained particles. Advantages include selective entrainment out of the aerosolizer which would exclude agglomerates and the possibility of ease of operation at constant concentrations by controlling the flow rate of entrained particles into the impregnation chamber.

- A fundamental study should be conducted into the behavior of the aerosolizer. It should take into consideration various factors such as sound attenuation inside the chamber, shear stresses imposed by flow of the entrained particles, particle size, interparticle collisions, acoustic and hydrodynamic forces in

order to predict particle concentration profiles in the chamber. An experimental part i.e. measurement of sound pressures and particle concentrations at various locations inside the chamber should be conducted to verify and iterate on the model proposed by theory.

- The charge-to-mass ratio of the polyamide particles is inherently high so that the particles adhere to the electrically ground carbon fibers without the use of an external charging device. This behavior needs to be understood with the help of a method to measure the triboelectric charge of the powder. Such measurements will aid in the understanding of charge-to-mass ratios essential for the natural adherence of particles to fibers in the process and hence lay down guidelines for prepregging with other fiber-matrix combinations.

- Interparticle forces in fine polymer powders lead to agglomeration of the particles to form clusters. A method to gage the magnitude of interparticle forces will help in understanding the behavior of different polymer powders in the aerosolizer. A powder tester can be used to measure the ratio of the tapped to loosely packed density (Hausner ratio) of a powder.

- The spreader was used to spread unsized carbon fibers. The dynamics of spreading other reinforcements such as glass and kevlar fibers may be different and may require pretreatment to remove sizings and surface finishes. The unit operation of spreading and the absorption of acoustic energy by different fibrous reinforcements at their natural frequencies needs to be explored in a systematic manner.

- The fiber motion system in its present configuration can be improved by installing the second set of nip rollers away from the heater to prevent matrix loss by attrition. An alternative system for fiber motion which may perform

better than the existing system includes the fiber spool to be mounted on air bearings and the tension controlled between the spool and the takeup drum. This system would circumvent the use of nip rollers with synchronous control of motor speeds which is a difficult operation and require only one motor driving the takeup drum.

- The replacement of the heater with a through feed muffle furnace to enable prepregging with high temperature polymers.

- Further work in the coalescence process to study the effect of capillarity between adjacent fibers on flexibility of the prepreg tapes. The relationship between tape width and flexibility also needs to be explored.

- Investigate the effect of consolidation time and temperature on the consolidation process. A complete study into consolidation would attempt to reduce consolidation times for void-free consolidation and thereby reduce labor costs.

- The final issue which needs to be addressed is the question of scale-up of the process to manufacture prepreg tapes at feed rates which would make it competitive with existing processes.

APPENDICES

Appendix A

ENGINEERING DRAWINGS

This appendix contains the engineering drawings of the different equipment designed for the process. They include the following : aerosolizer (figures 1a-d), spreader (figures 2a-b), nip rollers (figures 3a-g), bearing mounts for fiber spool and takeup drum (figures 4a-d), linear motion of takeup drum (figures 5a-k) and consolidation mold (figures 6a-b).

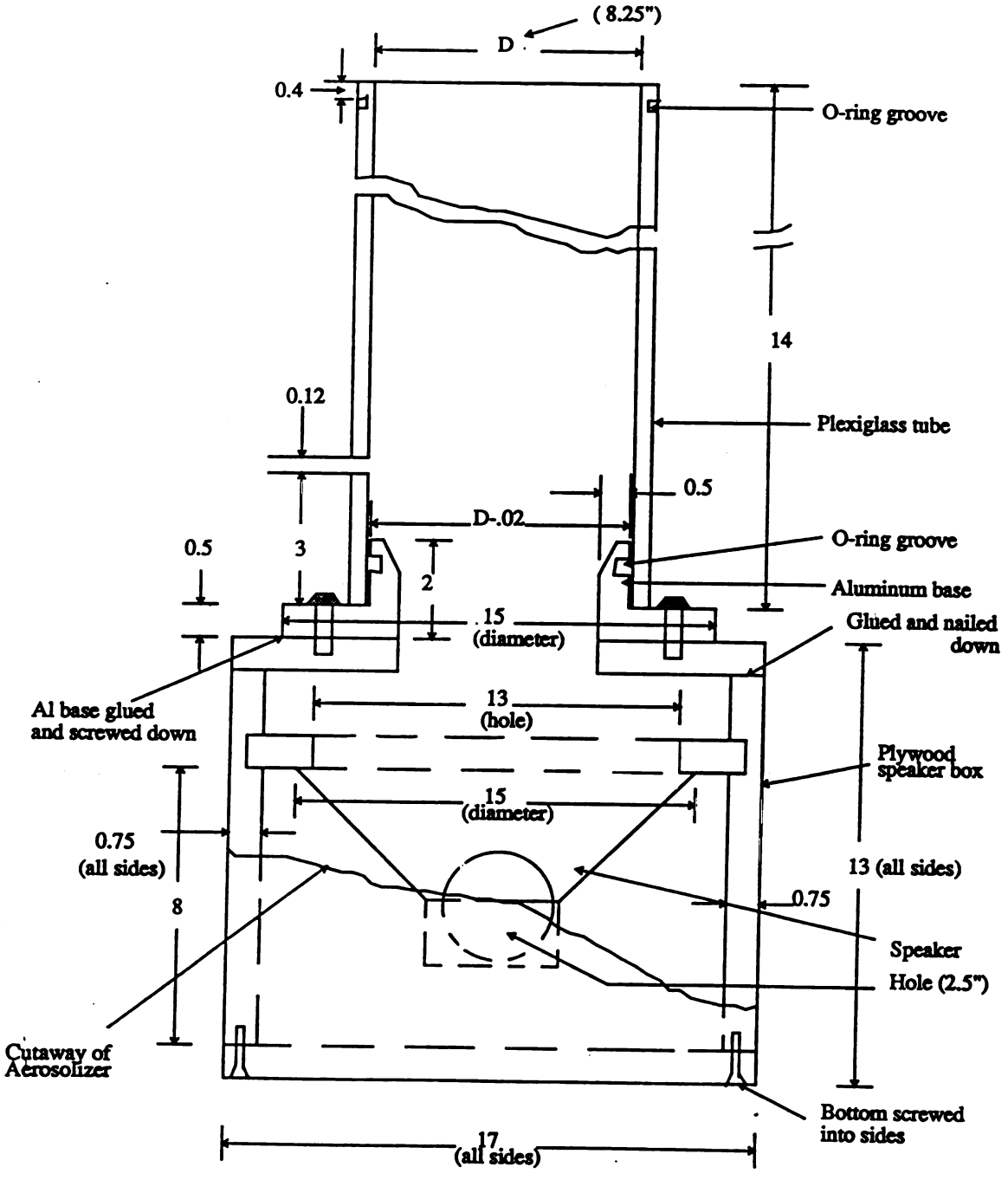

Figure 1a. Aerosolizer (all dimensions in inches).

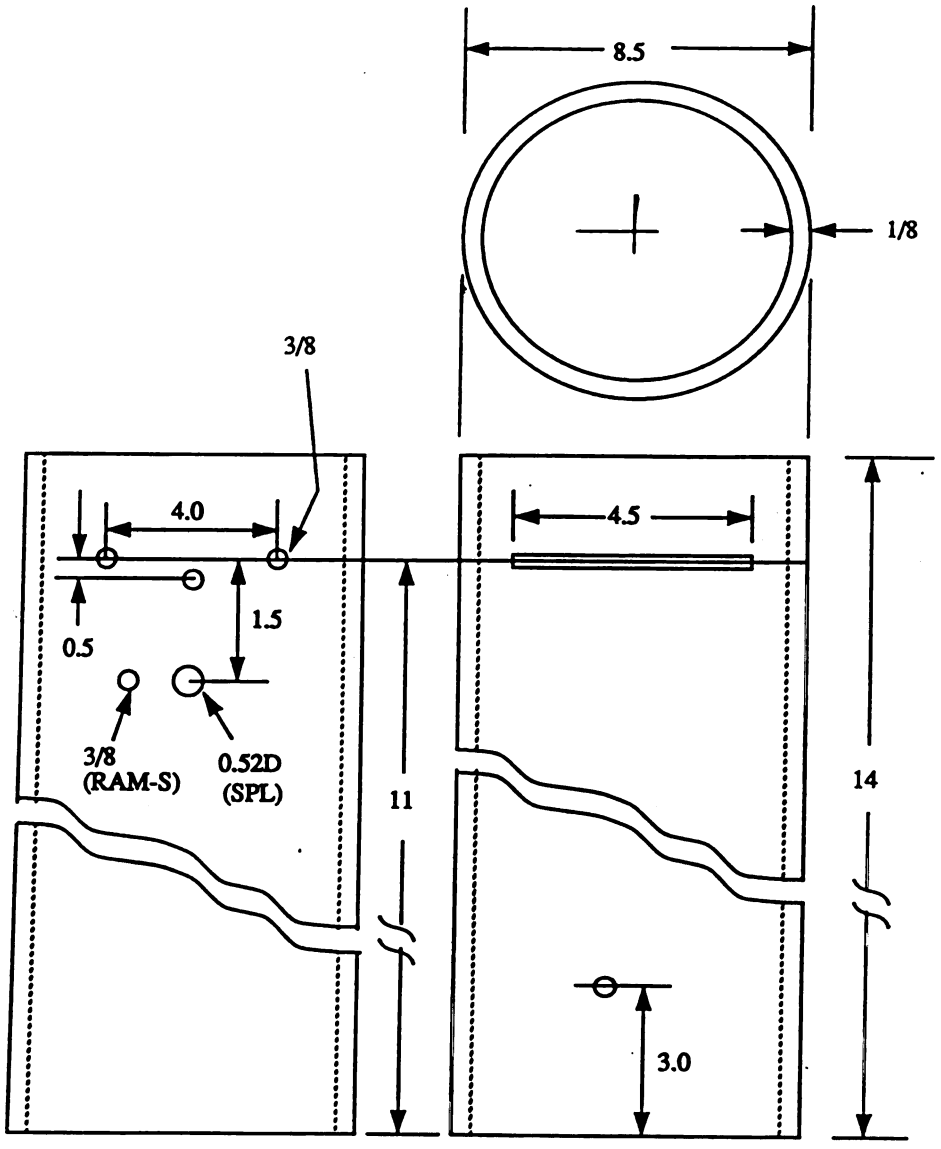

Figure 1b. Plexiglass tube for aerosolizer.

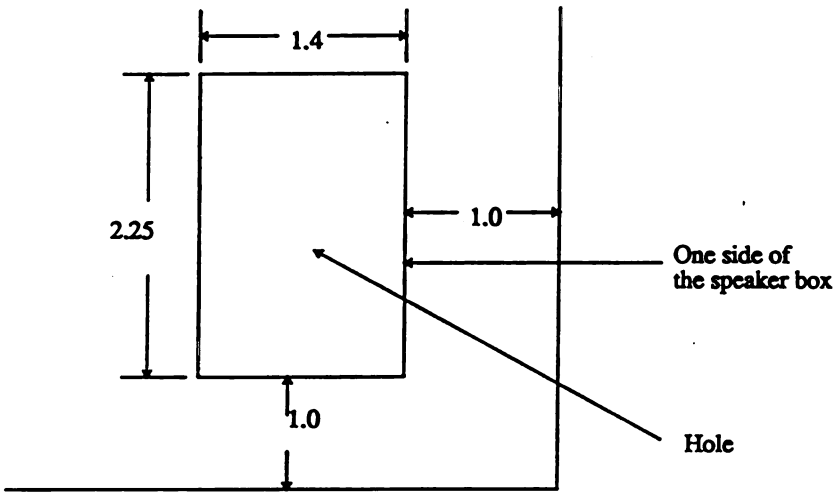

Figure 1c. Switchboard at bottom right hand corner of speaker box.

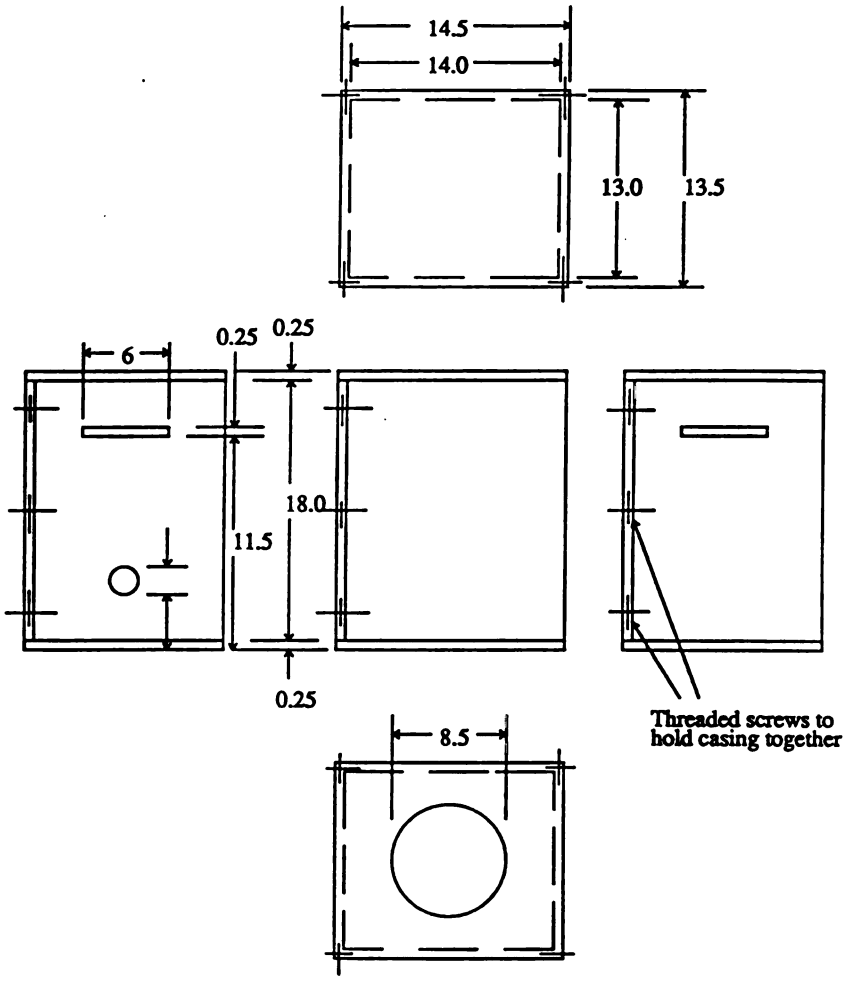

Figure 1d. Plexiglass casing for aerosolizer (encases the plexiglass tube of the aerosolizer and has an exhaust fan with an air filter attached to the backface).

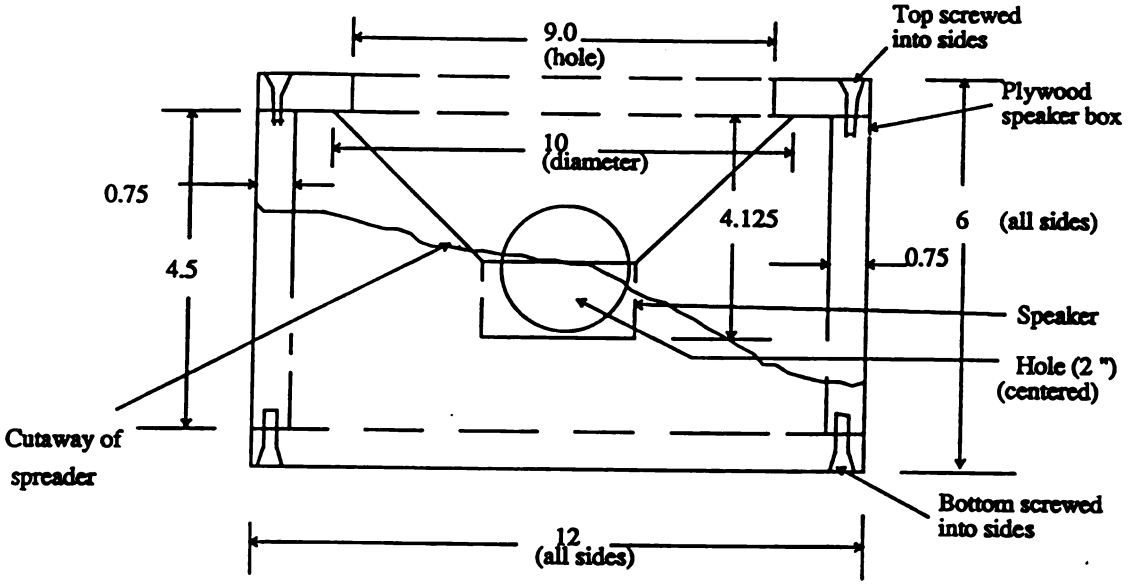

Figure 2a. Spreader.

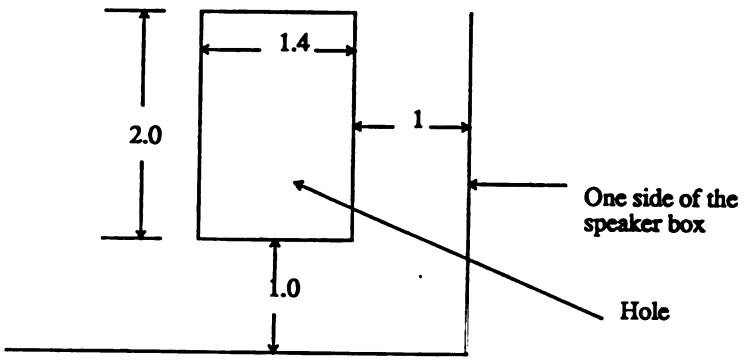

Figure 2b. Switchboard hole for spreader at bottom right hand corner.

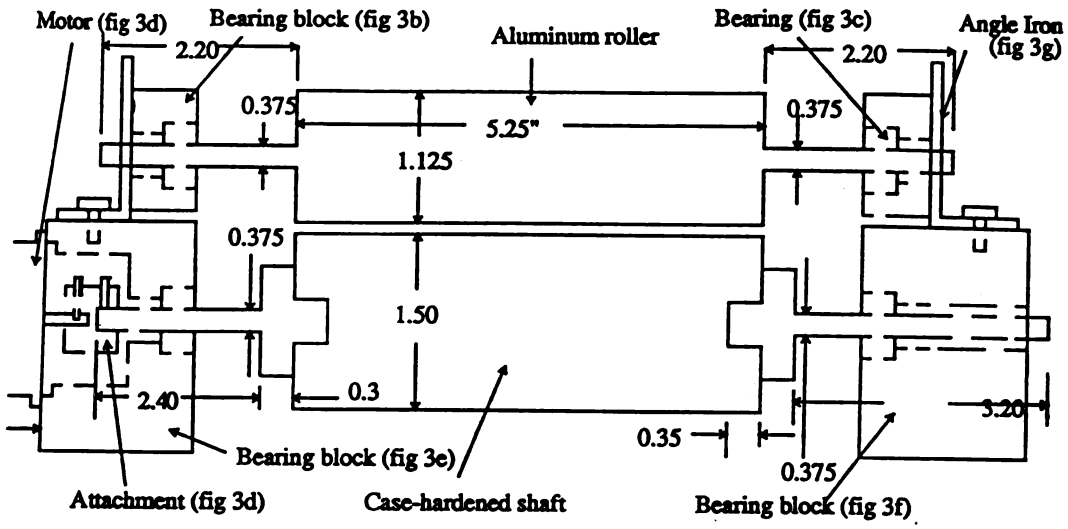

Figure 3a. Motor-driven nip rollers.

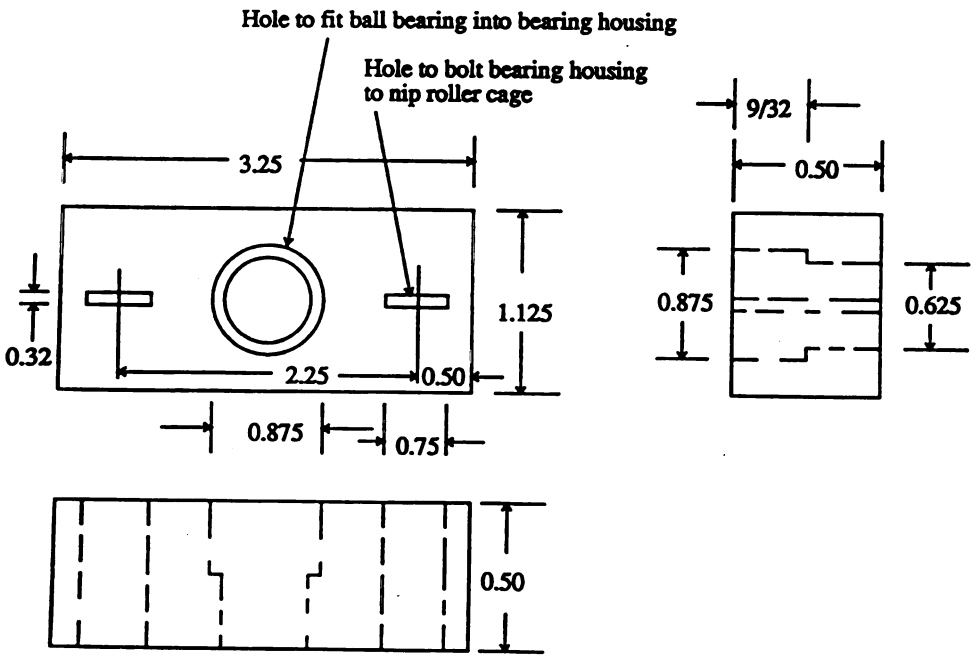

Figure 3b. Bearing housing for the top shaft.

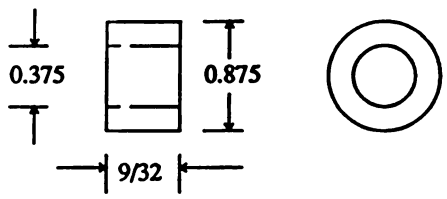

Figure 3c. Dimensions of ball bearing.

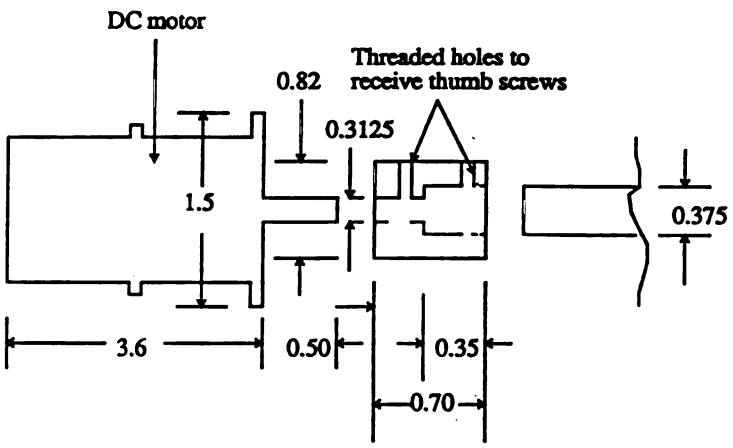

Figure 3d. Attachment of drive motor to drive shaft case-hardened roller.

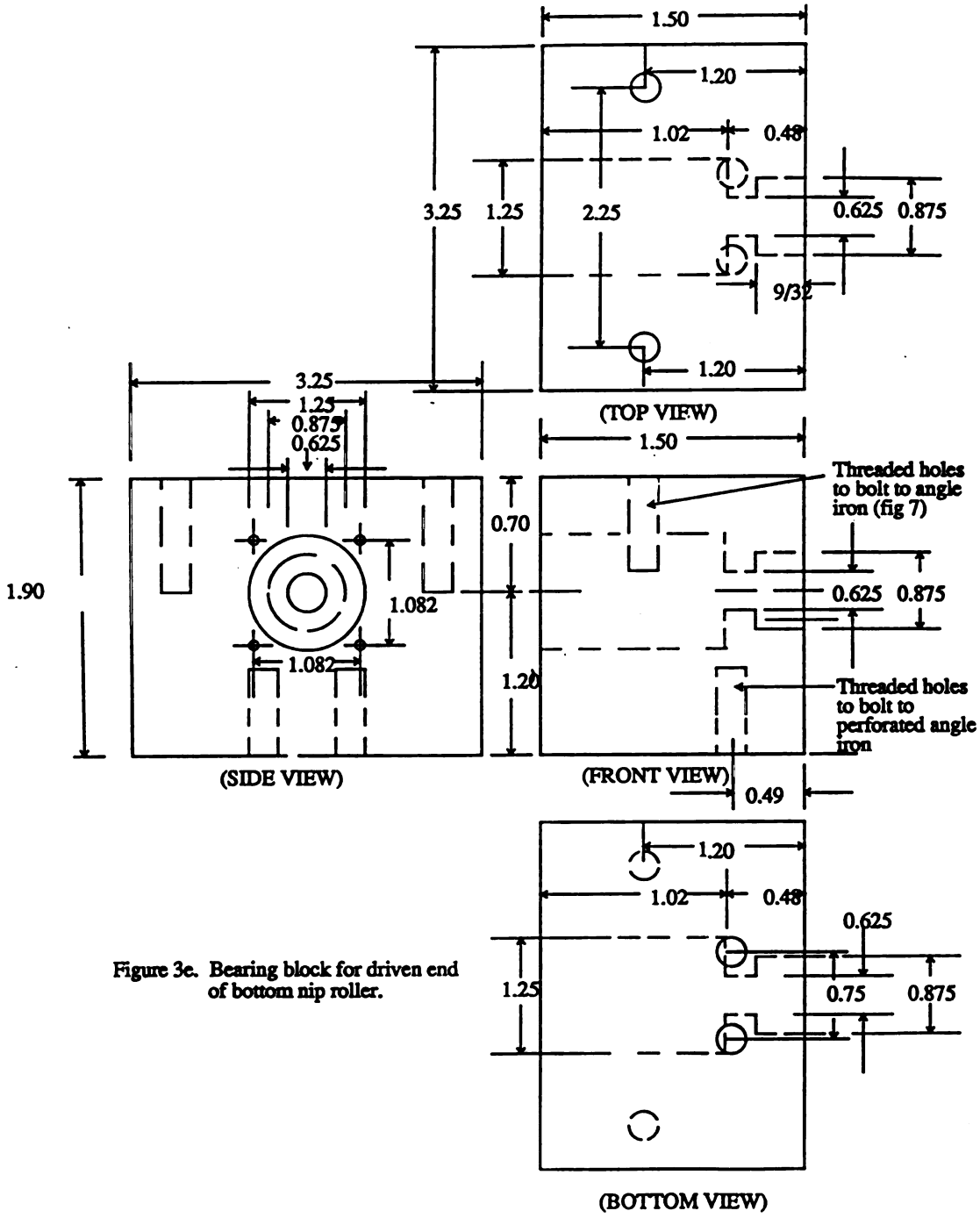

Figure 3e. Bearing block for driven end of bottom nip roller.

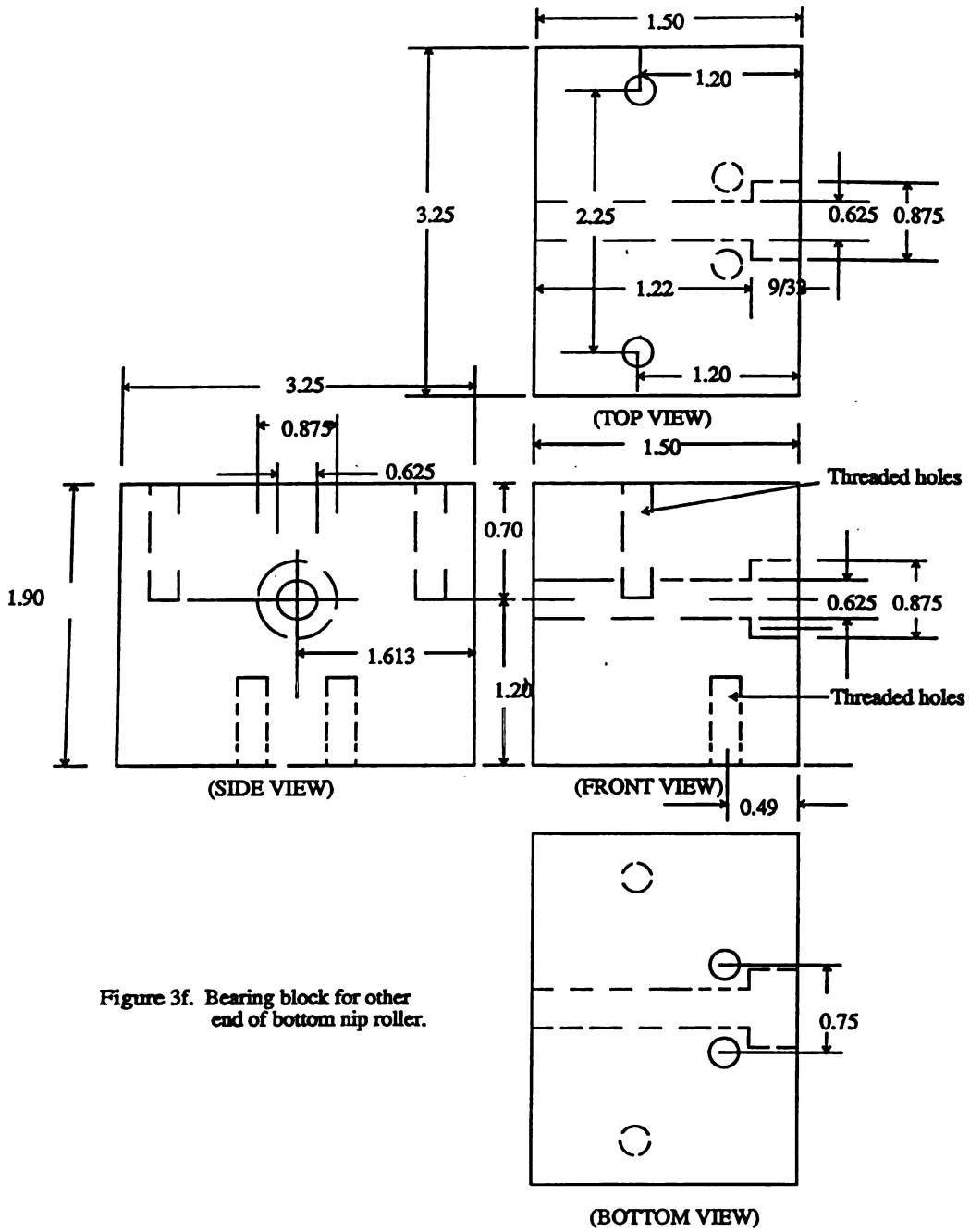

Figure 3f. Bearing block for other end of bottom nip roller.

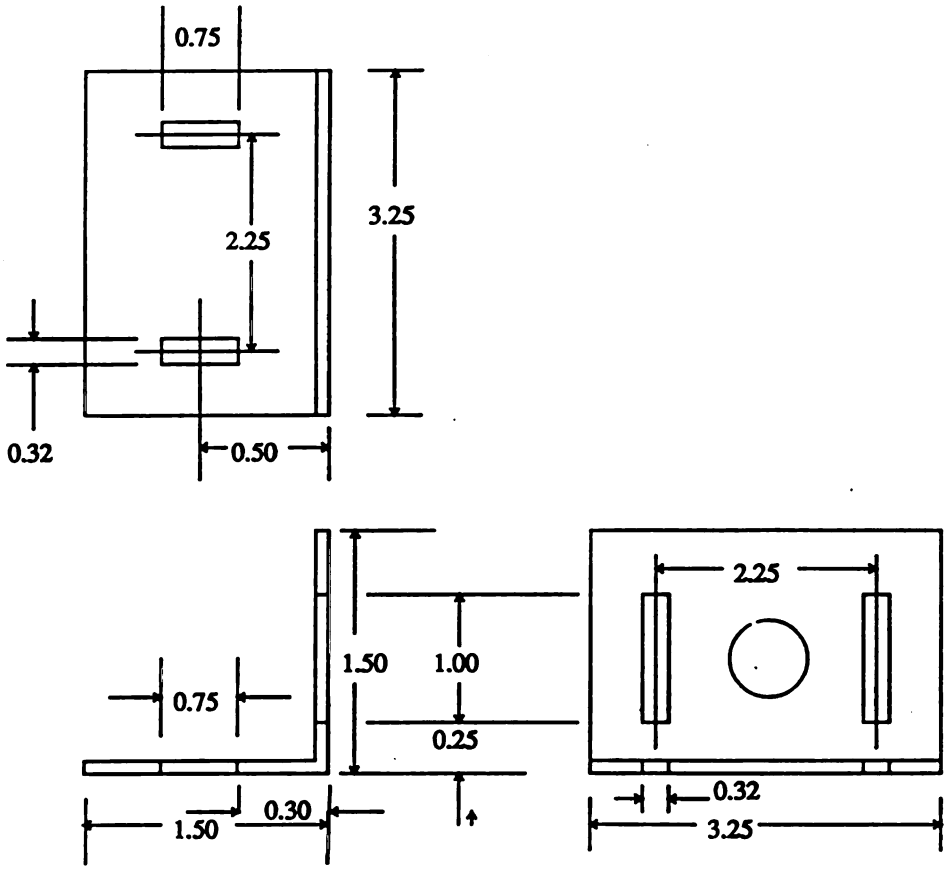

Figure 3g. Angle iron to fasten top bearing blocks to bottom bearing blocks.

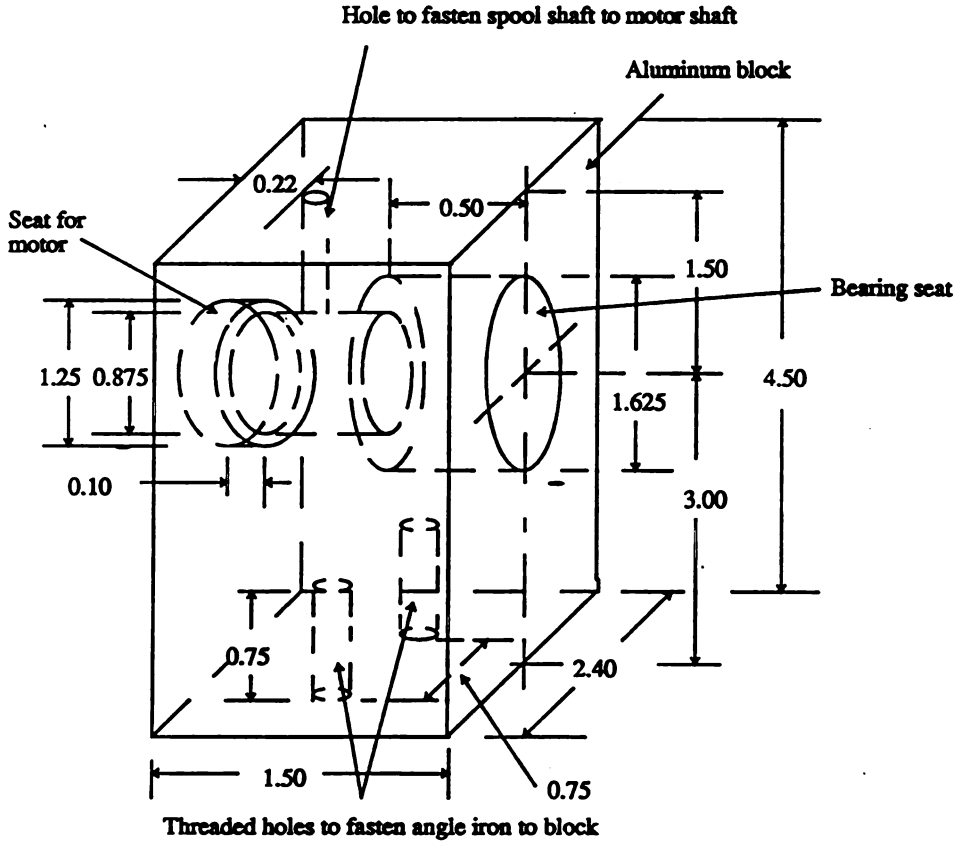

Figure 4a. Bearing block for the driven end of the fiber spool shaft.

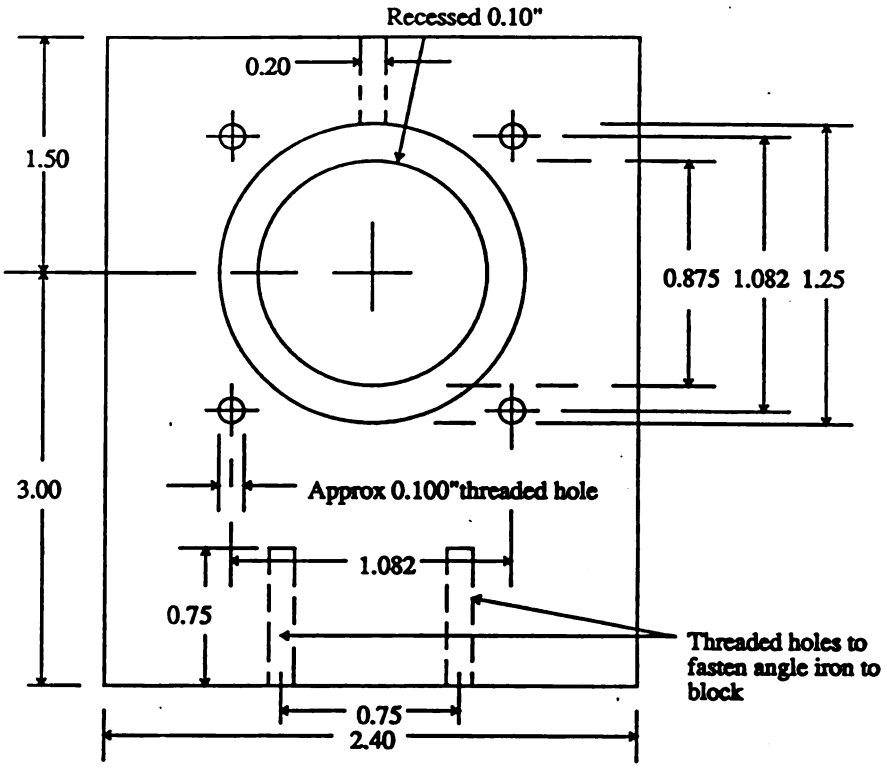

Figure 4b. Backface of bearing block where motor is mounted.

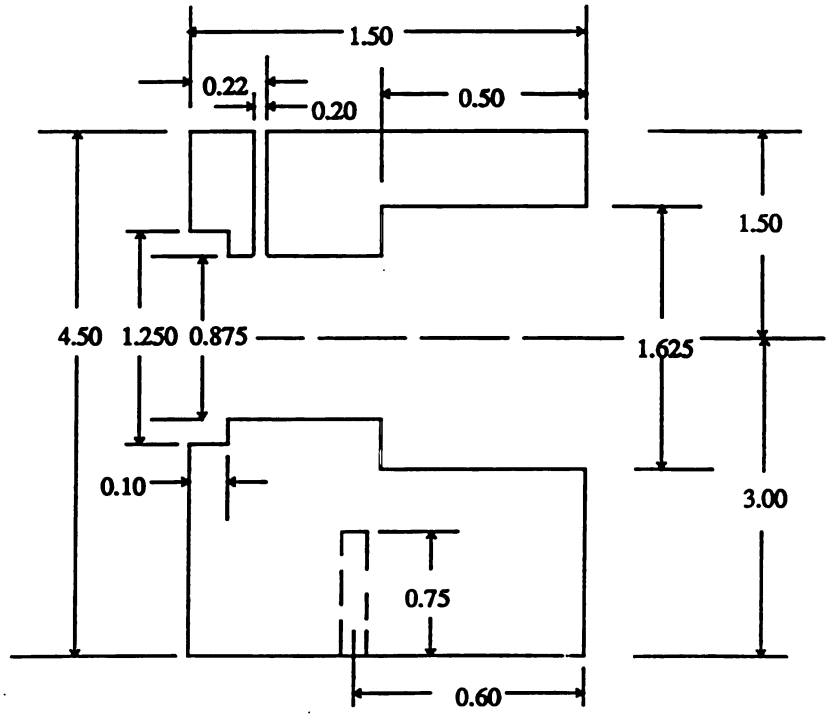

Figure 4c. Cutaway sideview.

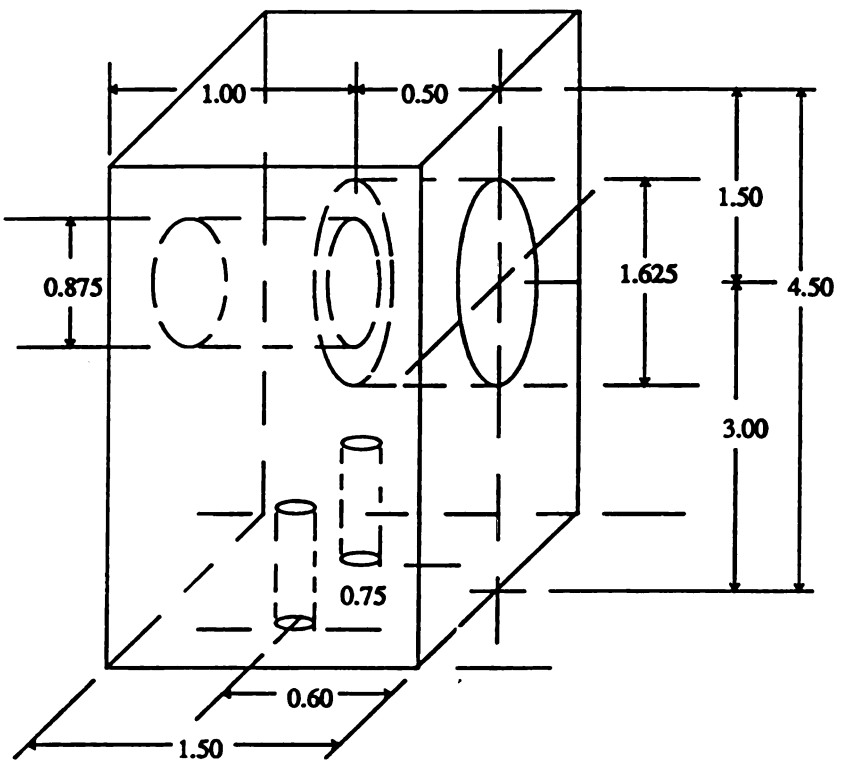

Figure 4d. Bearing block for the other end.
(All dimensions exactly the same as for the first block (figures 4a and 4c) except that there is no recess on the back face and no threaded holes which are present in the first block to mount the motor.)

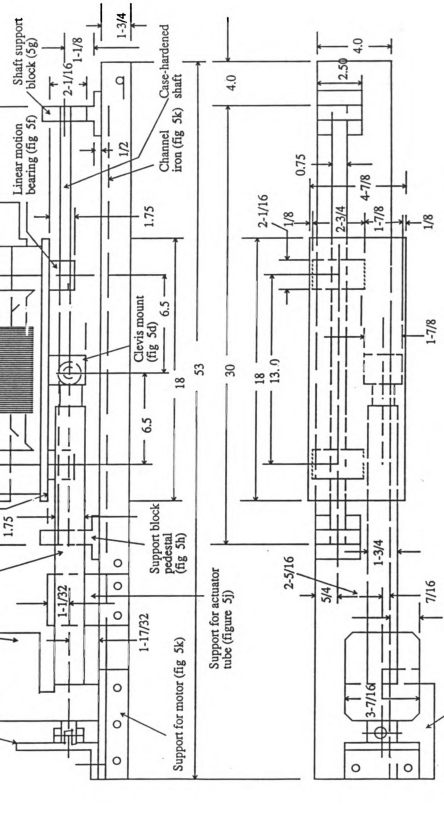

Figure 5a. Linear motion of takeup drum.

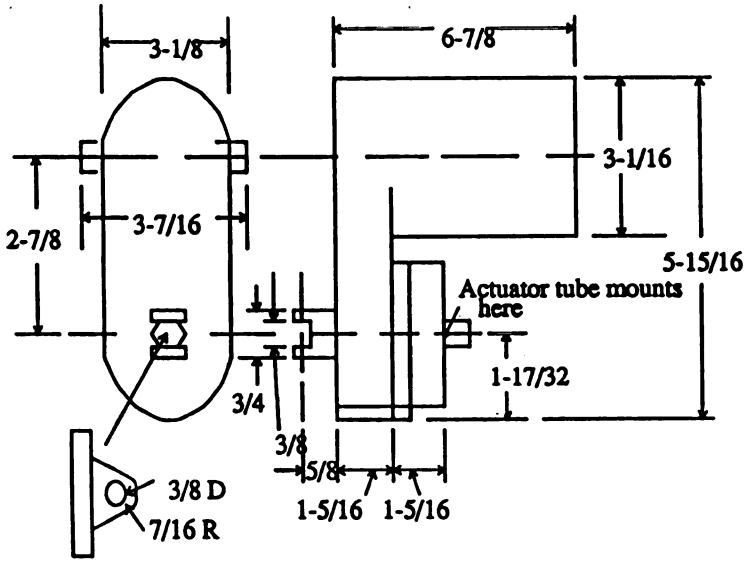

Figure 5b. 90 V DC Drive Dimensions (6.7 lbs)

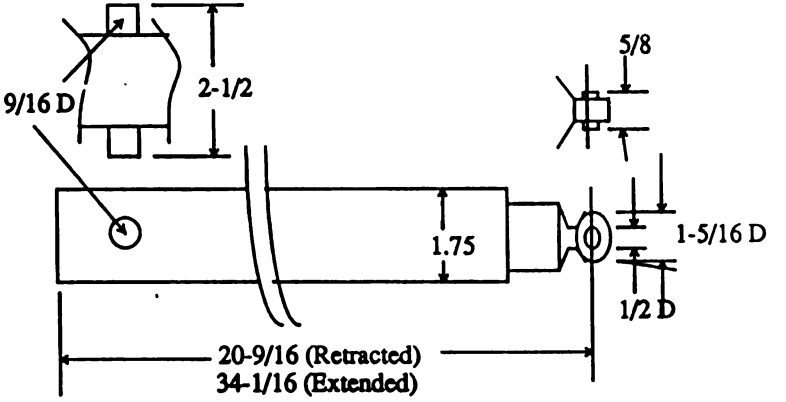

Figure 5c. 6-12 inch Actuator Tube (11.5 lbs)

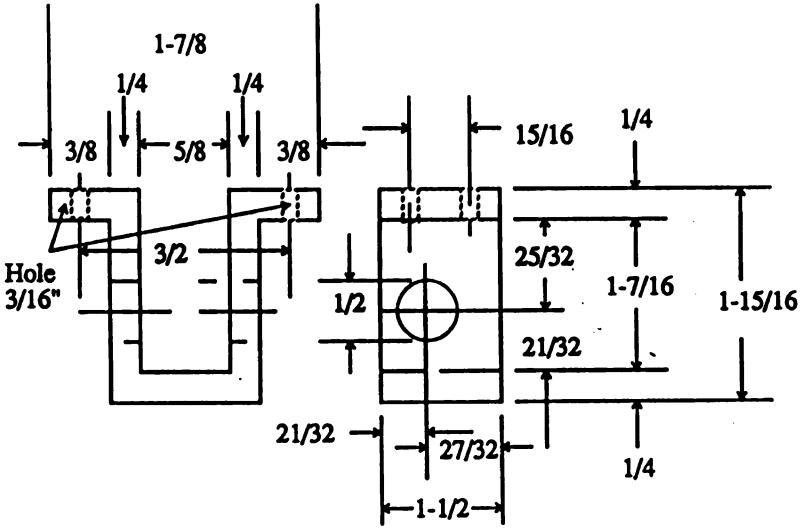

Figure 5d. Clevis mount

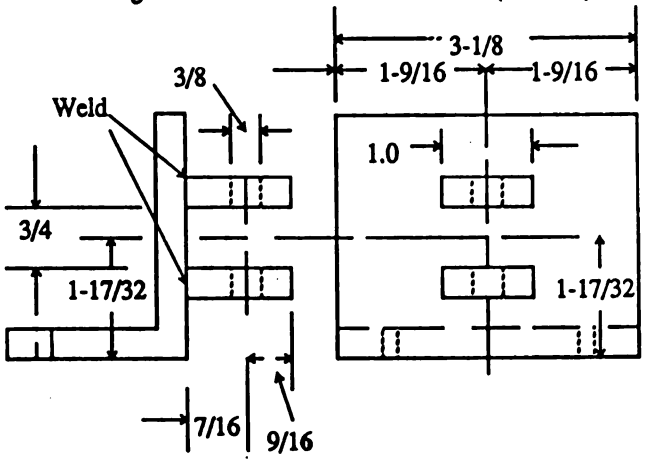

Figure 5e. Angle iron

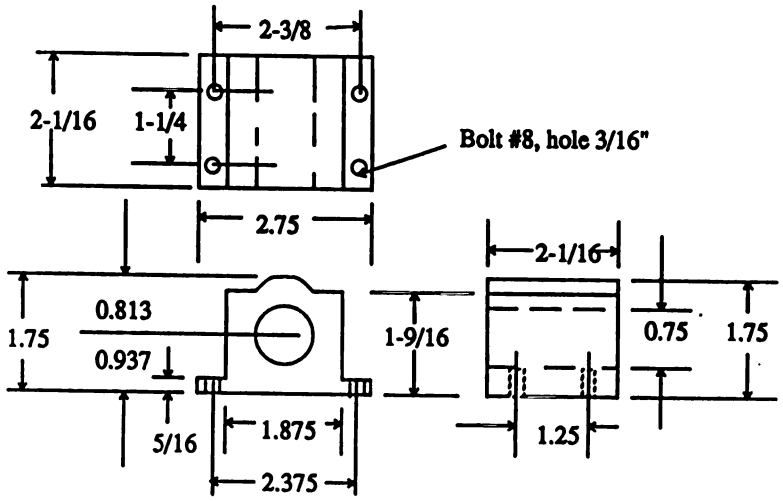

Figure 5f. Thomson Super Ball Bushing Bearing SPB-12

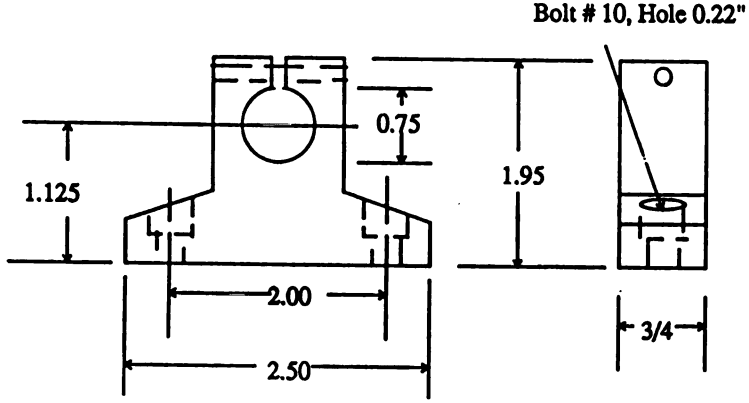

Figure 5g. Thomson Shaft Support Block ASB-12

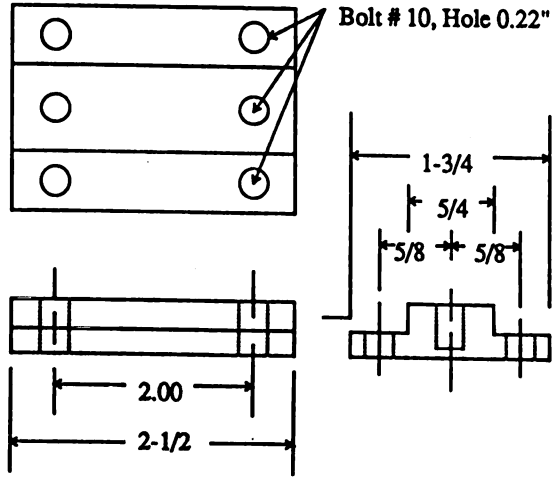

Figure 5h. Support block pedestal

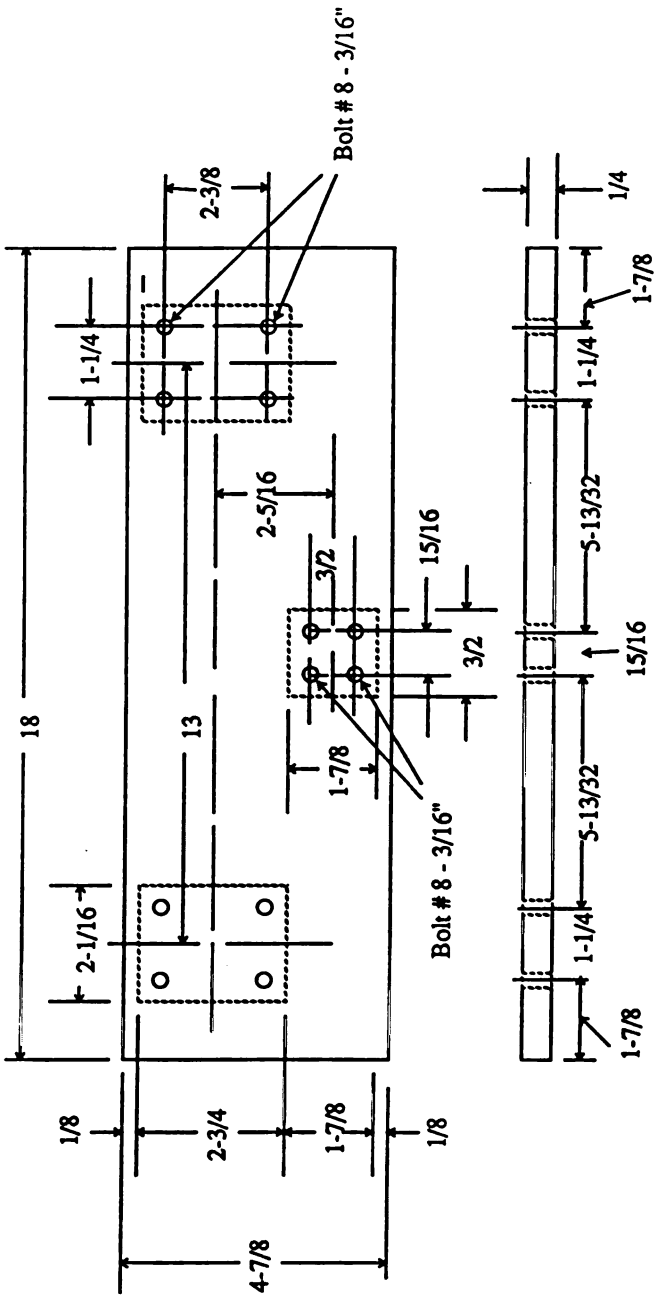

Figure 5i. Tooling plate

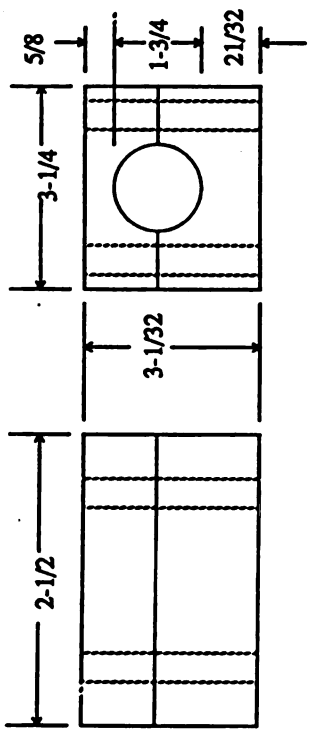

Figure 5j. Support for actuator tube

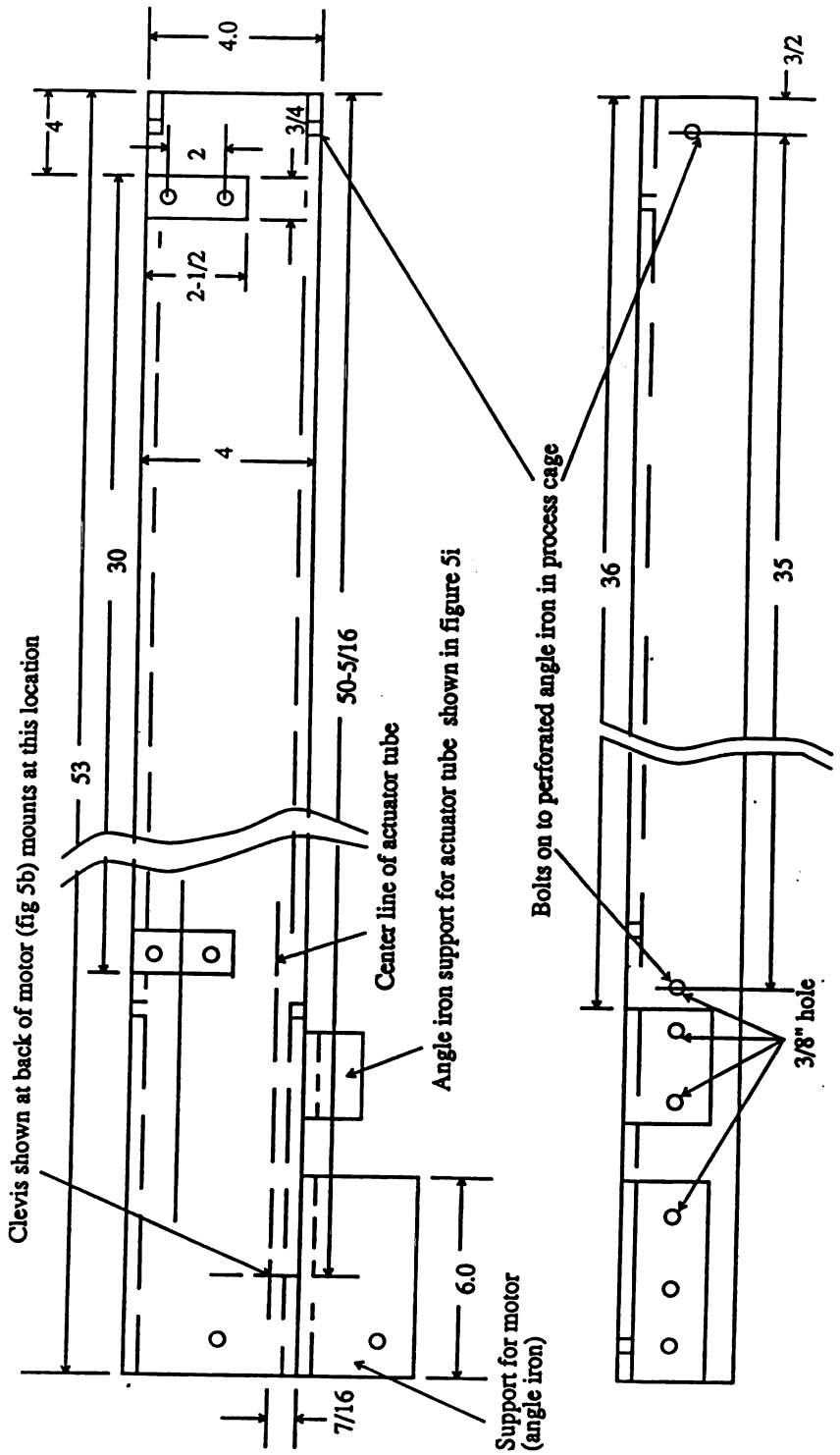

Figure 5k. Channel iron

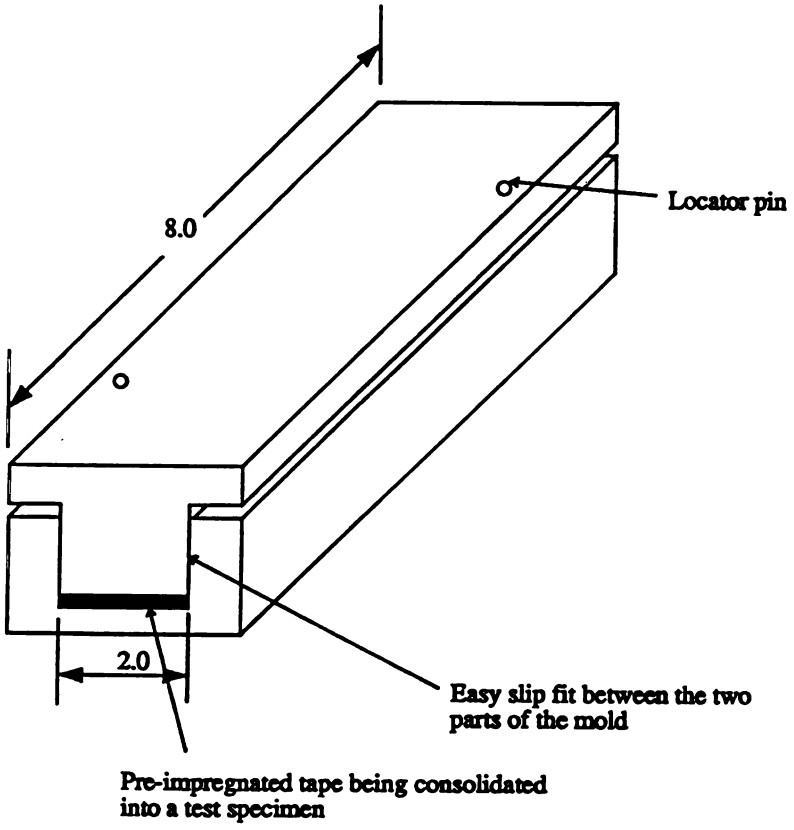

Figure 6a. Consolidation mold (All dimensions in inches).

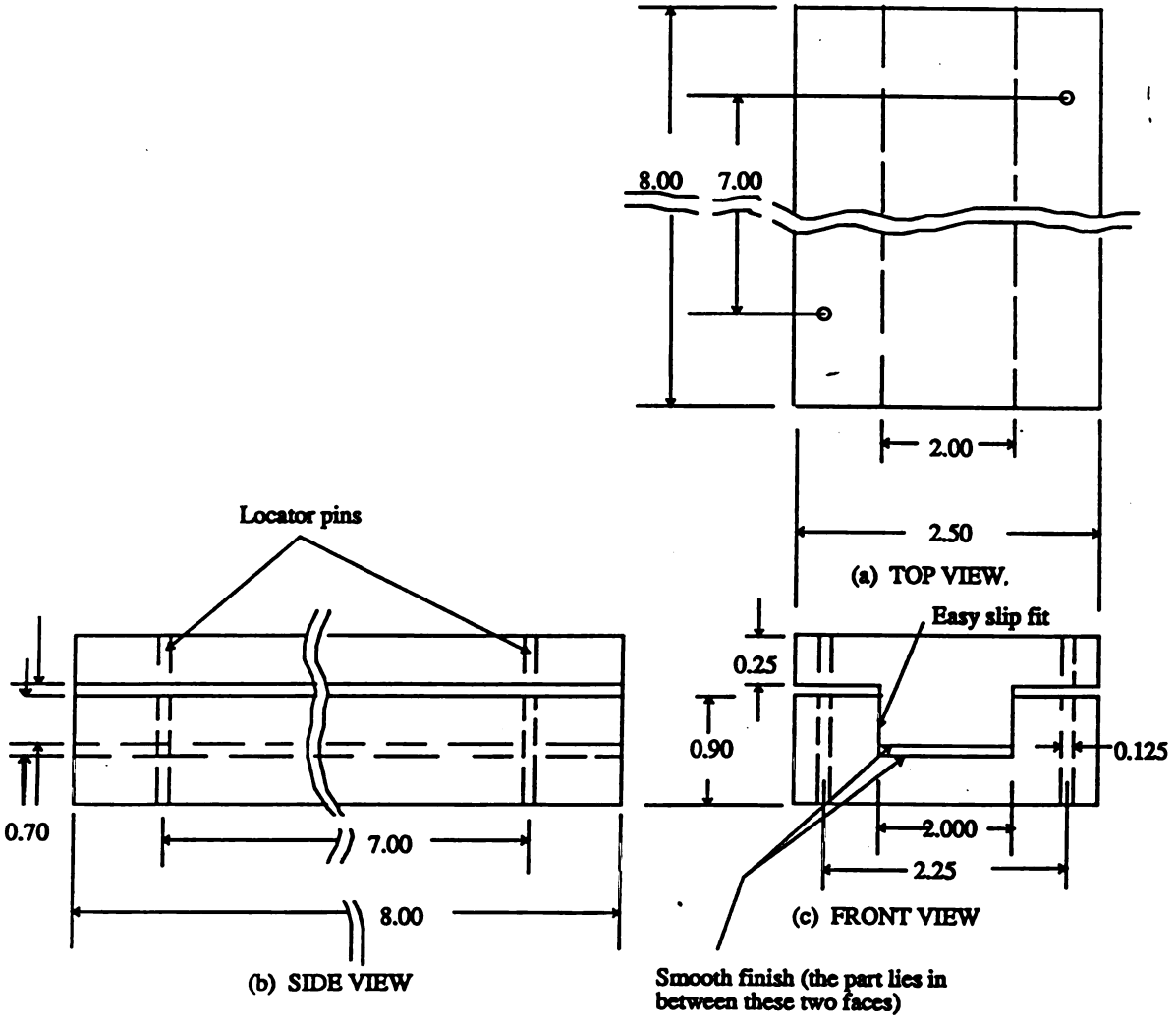

Figure 6b. Consolidation mold (See figure 24).

Appendix B

AUTOMATION

This appendix discusses the automation scheme implemented for the process both in terms of hardware and software. The different inserts include a description of the hardware, the electrical diagrams, the component locations in the Composite Line Controller or CLC, cable descriptions and the two main software programs clc.c and routines.c which control the process.

1. Hardware Description for Composite Line Controller :

The hardware of the Composite Line Controller is composed of several subcircuits: two motor power controllers, two pulse counters, an oven and track controller, two audio volume controllers, a tape height sensor and takeup spool controller, and a variety of interface and power supply components.

Interfacing to the A/D board is largely controlled by a 4-bit data bus and 4- bit address bus. The address bus controls which register (read or write only) is active, and the data bus transfers data. The two buses are implemented using the 8 bit input and 8 bit output ports on the A/D board. A 74LS154 demultiplexer is used to decode the address bus. Each address will be referred to as a register throughout the documentation.

The motor power controllers operate on a pulse-width modulation scheme. The 4 MHZ clock comprised of U30 and XTAL1 is divided by a 12 bit counter to yield a reference clock for the motor power controllers. Each time the 12 bit counter overflows, it pulses the LOAD line on the two motor counters, loading the number stored in the preload registers (4-6,7-9). The motor counters then count up until they carry (at 4096). During this fraction of each cycle, the motor power transistors are enabled. Thus pulse-width modulation control of each motor is obtainable with 12-bit resolution. The two main roller motors are controlled by this scheme; the takeup spool is controlled by a simpler scheme (described later).

In order for the roller motors to run, three other conditions must be met. First, a general motor enable bit (register 10, bit 0) must be set by software. In addition, the MOTORS switch on the front panel must be on. Finally, the software must be periodically polling register 3 (pulse counter 1 TRANSFER; see below). This last condition ensures that the motors stop in the event of software or computer failure.

The pulse counter circuits respond to the optical discs mounted on the two motors. Under normal operation, each counter increments upon receiving a pulse from its sensor. When the clc software wishes to read the value in the counters, it pulses the TRANSFER line (register 3 or 13), enabling a transfer of the count to the holding registers. When the next pulse arrives, the ount is transferred and the number 1 is loaded into the counter. The software is then free to read the count from the holding registers (1 and 2, 11 and 12).

Register 0 is the only other readable register on the board. It holds two status bits from each pulse counter circuit: an overflow bit, which signifies that more than 255 pulses were received without the register being read by software, and a transfer request incomplete bit, set from the time a transfer is requested until it is completed by the reception of a new pulse from the associated optical encoder.

The track controller circuit is relatively simple. Two switches, one at each end of the track's travel, cause a track direction flip-flop to toggle. This drives a direction-reversing relay mounted inside the track speed controller box. The track drive motor is cycled on and off (as per motor speifiations) by a relay driven by bit 2 of register 10. Mounted on the linear rack is a slack takeup spool whose motor is driven by two power transistors and a rheostat. When bit 3 of register 10 is set, the motor runs at a rate determined by its positive supply voltage and the position of the rheostat (mounted on the omposite processing line's frame). When tape slack is sensed between the optical sensor, another transistor is enabled, bypassing the rheostat and operating the takeup motor at a higher rate until the slack is no longer present.

The oven control circuitry is a mix of digital and analog. The differential temperature output from the Omega control box is converted to single-ended by a simple op-amp circuit, and fed into analog input 0. The software then determines when the oven should be cycled on and off, and sets or resets bit 1 of register 10 accordingly. This in turn overides the relay driver in the Omega controller to turn the oven on and off.

Other analog circuitry includes the audio control circuits and SPL and particle concentration circuits. The latter two merely attenuate the SPL and particle concentration inputs from the two meters so that they fall within the 0-5 volt range of the A/D board. The two audio control circuits are identical in design. The two analog outputs of the A/D board are supplied to the Volume pins (1) of the DM205 audio controller chips. The remainder of the support circuitry ensures that the signals pass undistorted (ie without bass or treble boost) through the DM205. An op amp at the output restores the original voltage level of the audio input to compensate for the attenuation of the DM205's.

Four green status lamps are mounted on the front of the controller box. The CABLE lamp is illuminated whenever register 15 is not being read. If the cable is disconnected, the controller defaults to reading register 15 and thus the CABLE lamp would be off. Note that the CABLE lamp being off may be due to other problems (such as software). The PROGRAM lamp is on whenever the clc program is reading register 0. The clc program always returns to reading register 0 after it has accessed any other register; hence if the CABLE lamp is on and the PROGRAM lamp is off, the software has crashed. The LOOP light is illuminated for 200 milliseconds after each time the program reads register 3. This register is one of the pulse counter registers for motor 1. The LOOP light thus indicates that the main control loop in the program is checking the pulse counters periodically. The LOOP light also enables the motors. Whenever the LOOP light is off, motors 1 and 2 are disabled to prevent them from running when they are not being monitored by software.

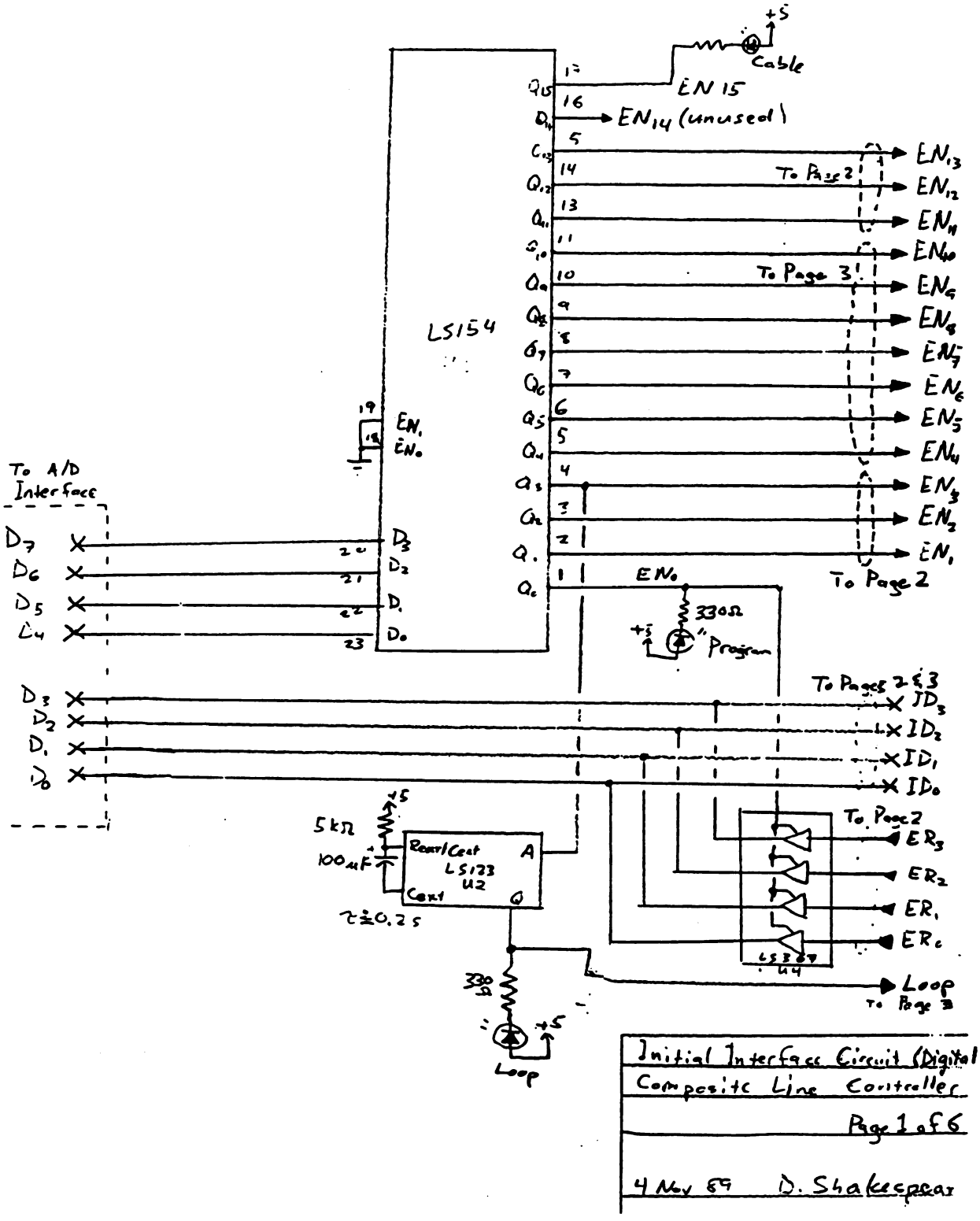
+5
Cable
EN 15
EN14 (unused)
LS154
EN13
EN12
EN11
EN10
EN9
EN8
EN7
EN6
EN5
EN4
EN3
EN2
EN1
To Page 2
To Page 3
To Page 2
EN0
330Ω
"Program"
To A/D Interface
D7
D6
D5
D4
D3
D2
D1
D0
To Pages 2 & 3
ID3
ID2
ID1
ID0
5kΩ
100μF
Reset/Cent
LS123
U2
Cext
A
Q
τ≈0.25
To Page 2
ER3
ER2
ER1
ER0
LS367
U4
330Ω
Loop
To Page 3
Initial Interface Circuit (Digital
Composite Line Controller
Page 1 of 6
4 Nov 89 D. Shakespear

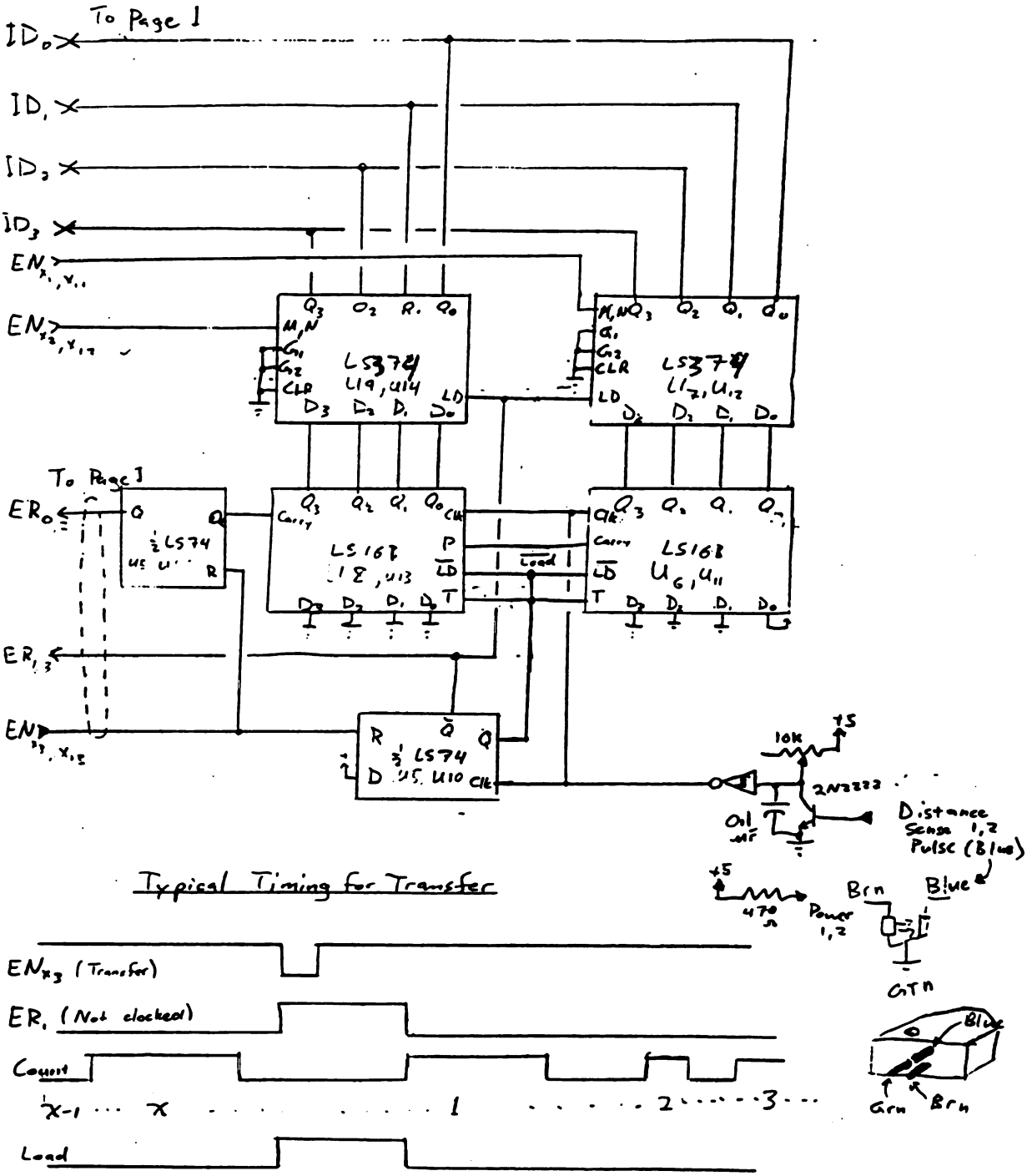

Pulse Counter / Transfer Cct
Composite Line Controller
Page 2056
2 Nov 89 D. Shakespear

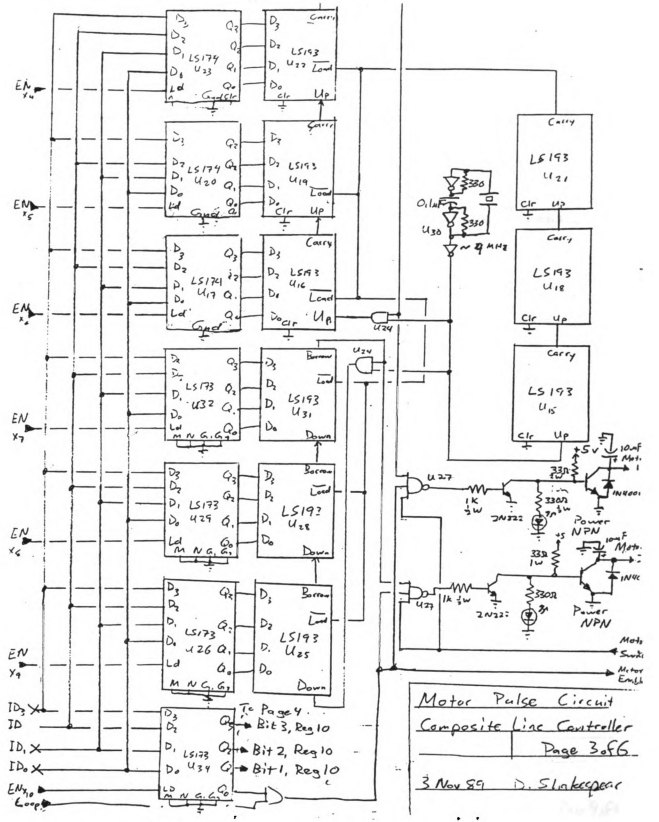
LS174
LS193
Carry
Load
Clr
Up
Down
Gate Clk
To Page 4.
Bit 3, Reg 10
Bit 2, Reg 10
Bit 1, Reg 10
Motor Pulse Circuit
Composite Line Controller
Page 3 of 6
3 Nov 89 D. Slakepear

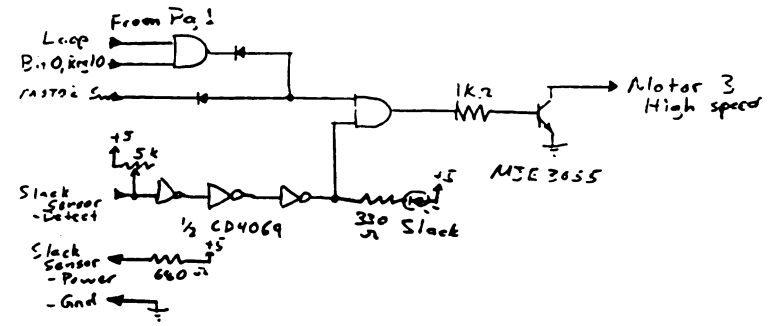

Motor 3 Logic

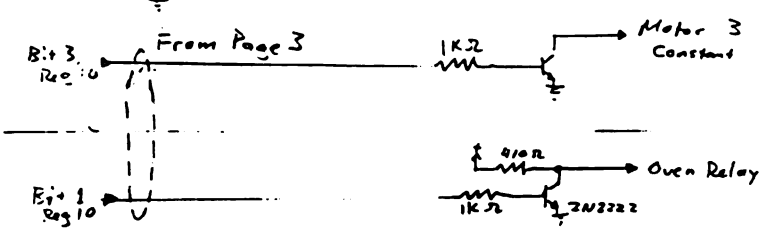

Oven Logic

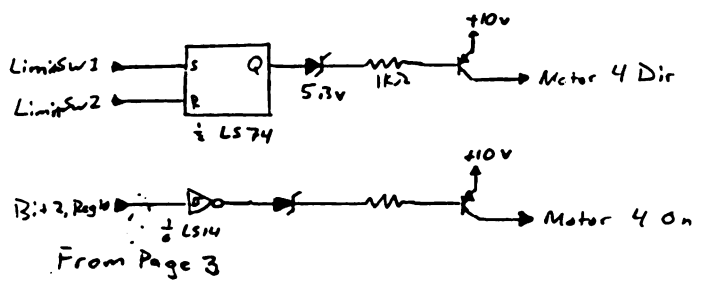

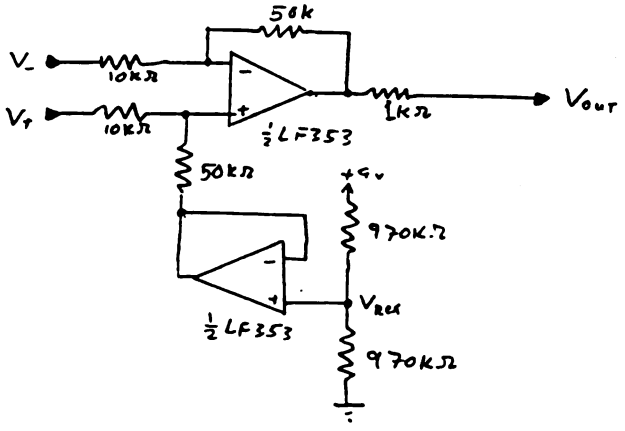

Composite Line Controller	
Temperature (Differential) Box	
8 June 1990	Page 5 of 6
D. Shakespear	ECS

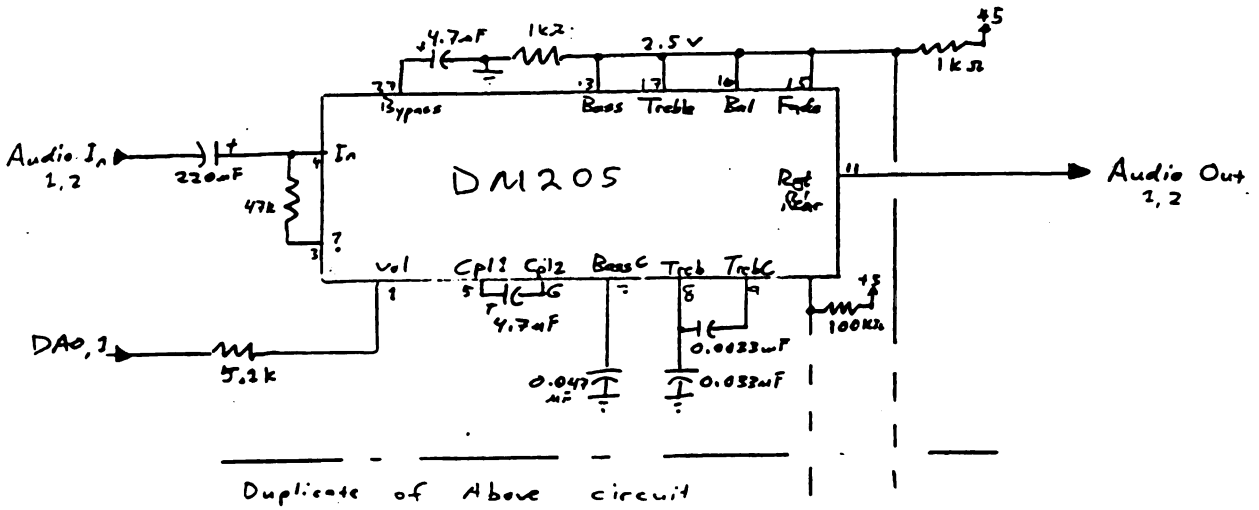

Composite Line Controller
Audio Control Circuit
8 June 1990 | Page 6 of 6
© Shakespeare ECS

COMPOSITE LINE CONTROLLER

Integrated Circuit Component Locations

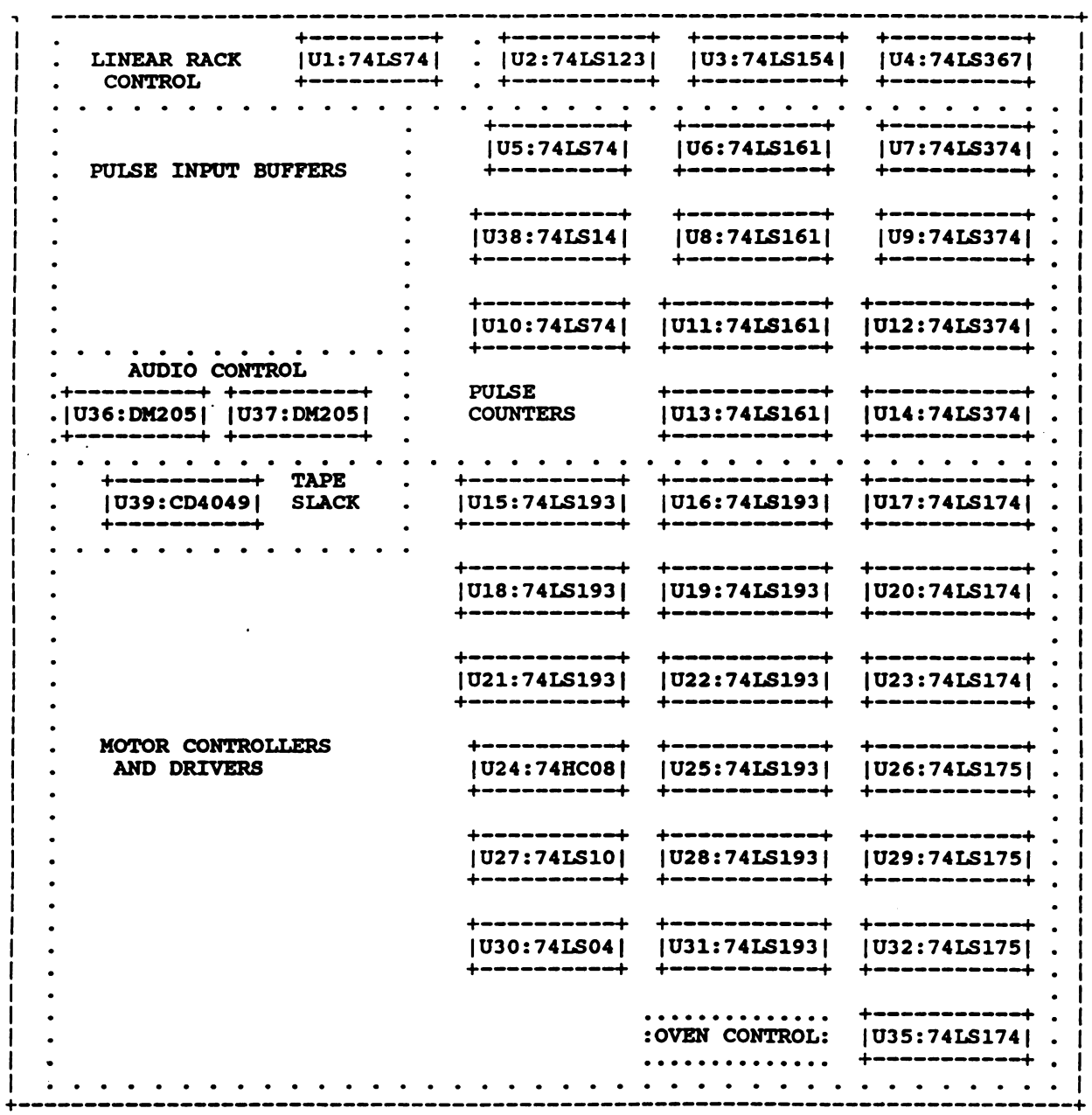

COMPOSITE LINE CONTROLLER

Internal Cables Description

Digital Cable (DB25 Female on Main Board, toward rear)

Pin	Function	Pin	Function
1	ID7	14	Digital Gnd
2	ID6	15	Digital Pwr (10V)
3	ID5	16	Cable Status
4	ID4	17	Program Status
5	ID3-Read	18	Loop Status
6	ID2-Read	19	Slack Status
7	ID1-Read	20	Motor 4 dir
8	ID0-Read	21	Motor 4 on
9	Motor En Sw	22	Motor 1
10	Oven Relay	23	Motor 2
11	Limit Sw1	24	Motor 3 High Speed
12	Limit Sw2	25	Power Gnd
13	Motor 3 Constant		

Analog Cable (DB25 Female on Main Board, center)

Pin	Function	Pin	Function
1	Part. Conc	14	AD2 (Part. Conc.)
2	SPL	15	AD3 (SPL)
3	Oven Temp.	16	AD4 (Oven Temp.)
4	Audio Src. 1	17	AD0 (Audio 1)
5	Audio Amp 1	18	AD1 (Audio 2)
6	Audio Src. 2	19	DA0 (Spkr. 1 Vol.)
7	Audio Amp 2	20	DA1 (Spkr. 2 Vol.)
8	Dist Sns 1 Pwr	21	ID3-Write
9	Dist Sns 1 Pulse	22	ID2-Write
10	Dist Sns 2 Pwr	23	ID1-Write
11	Dist Sns 2 Pulse	24	ID0-Write
12	Height Array Pwr	25	Height Array Pulse
13	Analog Gnd		

COMPOSITE LINE CONTROLLER

External Cables Description

Cable	Conductors	Connectors (Unit:Box)	Length (in)	Cable #
Motor 1	2	- : --	139	
Motor 2	2	- : -|- 8-pin DIN	101	1
Motor 3	2	- : --	125	
Part. Conc.	2+shield	? : 1/8" 3C	105	2
Sound Level	2+shield	1/8" 2C : 1/8" 3C	129	3
Temperature	2+shield	? : 1/8" 3C	114	4
Oven relay	2	1/8" 2C : 1/8" 3C	114	5
Power- low	2	Banana : Banana	89	6
Power- high	2	Banana : Banana	81	7
Audio Src. 1	1+shield	Banana : Phono	70	8
Audio Amp 1	1+shield	1/4" : Phono	80	9
Audio Src. 2	1+shield	Banana : Phono	70	10
Audio Amp 2	1+shield	Phono : Phono	80	11
Dist Sns 1	2+shield	- : 1/8" 3C	<170	12
Dist Sns 2	2+shield	- : 1/8" 3C	<130	13
Height Array	2+shield	- : 5-pin DIN	<105	14
Limit Sw 1	2	- : 1/8" 2C	<100	15
Limit Sw 2	2	- : 1/8" 2C	<120	16
Motor 4 dir	2	? : --	91	
Motor 4 on	2	? : -- |- 5-pin DIN	91	17
Motor 4	(pre-existing wiring)			
Speaker 1	(pre-existing wiring)			
Speaker 2	(pre-existing wiring)			

2. Software Description for Composite Line Controller :

The hardware for the process is controlled by means of two programs, clc.c and routines.c written in C language. The second program routines.c contains a list of subroutines which communicate with the control hardware while the first program clc.c is the main program which acquires data and controls the process.

2.1 *clc.c*:

This program is the main module. It accesses the controller box through routines defined in routines.c. A sectional description follows:

main( )	initialization, main program loop.
run( )	do one run based on current settings. (includes PID speed/slack control)
set_oven( )	cycle the oven based on current and desired temperature.
set_track( )	turn the track on and off at intervals.
batch( )	do several runs based on an input file.
read_input_data( )	read the input file data.
all_done( )	exit the program gracefully.
change( )	change the current settings.
menu( )	display menu and return choice.
tick( )	executed every timer tick (1/18.2)sec.
power( )	raise a number to a power.
keywait( )	wait for a key to be pressed.

2.2 *Routines.c*:

This module contains routines which provide access to the line, and which will not have to be changed unless the hardware scheme of the controller changes. Understanding the logic behind these requires an understanding of the control hardware.

(X = 1 or 2 for motor number or speaker number.)

get_counterX( )	get # of counts from slotted disk X. (0-255)
set_motorX( )	set motor speed X. (0-4095)
get_register( )	get data from a control register. (reg 0-15, data 0-15)
set_register( )	send data to a control register. (reg. 0-15, data 0-15)
set_volumeX( )	set volume of speaker X. (0-4095)
get_conc( )	get particle concentration in chamber. (0-4095)
get_spl( )	get sound pressure level in chamber. (0-4095)
get_temp( )	get temperature in oven. (0-4095)
oven_on( )	turn oven on.
oven_off( )	turn oven off.
motors_on( )	enable all motors.
motors_off( )	disable all motors.
track_on( )	turn track controller on.
track_off( )	turn track controller off.
a2d_init( )	initialize A/D system.
ctrlc( )	handle control-c interrupt.

Program 1 : clc.c

```
/*              Electronic & Computer Services          */
/*              Composite Line Controller Software      */
/*              Frank Palazzolo         6/7/90          */

#include <stdio.h>                              /* Standard Library Modules */
#include <signal.h>                             /* (Described in Microsoft C manual) */
#include <stdlib.h>                             /* Provides support for all string,  */
#include <process.h>                            /*  dos, bios, and graphics functions */
#include <dos.h>
#include <graph.h>
#include <ctype.h>
#include <bios.h>
#include <math.h>

int get_counter1( );                            /* Function Prototypes for routines.c */
int get_counter2( );                            /* (See routines.c for full descriptions */
int set_motor1(int);
int set_motor2(int);
int get_register(int);
void set_register(int, int);
void set_volume1(int);
void set_volume2(int);
int get_conc( );
int get_spl( );
int get_temp( );
a2d_init( );
int ctrlc( );
void oven_on( );
void oven_off( );
void motors_on( );
void motors_off( );
void track_on( );
void track_off( );

/* Function Prototypes for this module */
/* (Descibed in detail at beginning of each routine) */

void interrupt far tick( );
void diag( );
void run( );
void change( );
void batch( );
void alldone( );
char menu( );
void read_input_fields( );
int read_input_data( );
float set_oven( );
void set_track( );
unsigned long power(int, int);
void keywait( );

/* Global Variable Definitions */

unsigned long counts;   /* This is incremented every timer tick (1/18.2 s) */
unsigned long ovencounts;       /* Same as counts, but set to zero by set_oven */
                                                /* twenty_secs*1/18.2 secs. (~20 s) */
unsigned long bigcounts;        /* Incremented every 20 secs by set_oven */
unsigned long twenty_secs;  /* Twenty secs of timer ticks */
unsigned long oven_on_width;    /* Oven on pulse width (0 to twenty_secs) */
```

```
void (interrupt far *oldvector)( );      /* Space to save old jump vector */
int int_flag;                            /* Set to one every other tick (1/9.1 s) */
struct param {                           /* Current settings structure */
        float   length;                  /* Run Length - Not Used */
        float   linespeed;               /* Line Speed */
        float   pconc;                   /* Particle Concentration - Not Used */
        float   vspr;                    /* Voltage Level for spreading speaker */
        float   vaer;                    /* Voltage Level for Aerosolizer */
        float   temp;                    /* Oven Temperature */
        }
struct param *settings;                         /* Current settings */
FILE   *fpin, *fpout;                           /* File Pointers */
char   *infile = "NONAME.IN";            /* Default file names */
char   *outfile = "NONAME.OUT";
int        lineno;                                      /* Input file line number */
struct dosdate_t currdate;                      /* Date and Time */
struct dostime_t currtime;

/*      Main Program Loop */

main(int argc, char *argv[])
{
        int    i;                                           /* general integer variable */
        char   choice;                                  /* selected menu choice */

        oven_off( );                                        /* Shut off everything */
        motors_off( );
        track_off( );
        twenty_secs = 364;      /* twenty seconds (in timer ticks) */
        oven_on_width = 0;      /* oven off (cooling) */
                /* initialize counters */
        counts = 0;
        bigcounts = 0;
        ovencounts = 0;

        /* Set up I/O file routine according to command line arguements */

        switch (argc) {
                case 3: outfile = argv[2];
                        /* Custom outfile & infile */
                case 2: infile = argv[1];
                        /* Only custom infile */
                        break;
                case 1:
                case 0: break;
                default: printf("Usage: clc (inputfile) (outputfile)\n");
                         printf(" defaults:  NONAME.IN & NONAME.OUT\n");
                         /* Improper number of arg's - exit */
                         exit(0);
        }


/*      Install interrupt handler for Ctrl-C                    */
/*      Program will jump to ctrlc( ) when ctrl-c is hit */

        if (signal(SIGINT,ctrlc) == (int(*)( ))-1) {
                fprintf(stderr,"Couldn't set SIGINT\n");
                abort( );
        }
```

```
float   f,dummy;                /* general purpose float's */
int             loopdone = 0;   /* flag */
unsigned        c;                      /* keyboard char */
float   conc, spl;      /* Current particle conc., spl */
float   speed1, speed2; /* instantaneous motor speeds (cm/sec) */
int             n;                      /* printf every 1/18.2 * 2^n */
int             nfpr;           /* fprintf every 1/18.2 * 2^nfpr */
int             num;            /* number of speeds taken */
float   sum1, sum2;             /* sum of motor speeds */
float   sumsq1, sumsq2; /* sum of motor speeds squared */
float   avg1, avg2;             /* average speeds */
float   std1, std2;             /* standard deviations */
unsigned long pmask, pmatch; /* mask and counts to match for print loop */
unsigned long fmask, fmatch; /* mask and counts to match for fprint loop */

/* Controller variables */

float   U1,U11,U12;     /* u(k), u(k-1), u(k-2) for motor 1 */
float   U2,U21,U22;             /* u(k), u(k-1), u(k-2) for motor 2 */
float   Uset;                   /* Set point for current linespeed (counts/tick) */
float   A1,A2,A3;               /* Coefficients for PID controller */
float   B1,B2,B3;               /* (Same for motor 2) */
float   slack;                  /* cm's of slack */
float   slackadj;               /* Adjustment to Uset for motor 2 (counts) */
float   DM1,DM2;                /* Functions of U to eliminate derivative kick */
float   DELT;                   /* Delta T = 1/9.1 secs */
float   P1,P2;                  /* y(k) for motor 1 & 2 */
float   E1,E2,E3;               /* e(k), e(k-1), e(k-2) for motor 1 */
float   F1,F2,F3;               /* same for motor 2 */
float   K1,TI1,TD1;             /* Gain, Taus for Int. & Diff. - motor 1 */
float   K2,TI2,TD2;             /* Same for Motor 2 */
double  sqrt(double);
float   x;


/*      Speaker coefficients */
/*  After calibration:   */
/*  ln(Voltage) = spr2*f^2 + spr1*f + spr0 */
/*  Where f is the setting value          */

float   spr2 = 0, spr1 = 810, spr0 = 2090;
float   aer2 = 0, aer1 = 810, aer0 = 2090;

/* Printf run stats every ~3.5 seconds */
/* Fprintf run stats every ~28 seconds */

n = 7;
nfpr = 10;
pmask = (unsigned long)(power(2.0,(double)n) - 1.0);
pmatch = pmask - 2;
fmask = (unsigned long)(power(2.0,(double)nfpr) - 1.0);
fmatch = fmask - 4;

/* Print heading */

_clearscreen(_GWINDOW);
printf("Composite Line Controller              Electronic & Computer Services - M.S.U.\n");
printf("-------------------------------------------------------------------------------\n\n");

/* Print current date & time to output file */
```

```
/*      Install interrupt handler for timer ticks              */
/*      Program will jump to tick( ) every 1/18.2 secs.  */

        oldvector = _dos_getvect(8);
        _disable;
        _dos_setvect(8,*tick);
        _enable;

/*      Set default settings */

        settings = malloc(sizeof(struct param));

        settings->length = 300;                 /* cm to run (Not Used) */
        settings->linespeed = 2;                /* cm/sec */
        settings->pconc = 50;                   /* mg/m^3 (Not Used) */
        settings->vspr = 5;                     /* Volts */
        settings->vaer = 5;                     /* Volts */
        settings->temp = 210;                   /* degrees C */

/*      Open files */

        if((fpin = fopen(infile,"r")) == NULL) {
                printf("%s could not be opened for reading.\n",infile);
                alldone( );
        }
        if((fpout = fopen(outfile,"w")) == NULL) {
                printf("%s could not be opened for writing.\n",outfile);
                alldone( );
        }

/*      Menu Loop       */
/*  Based on menu choice - jump to appropriate routine  */

        while (1 == 1) {
                choice = menu( );
                switch(choice) {
                        case '1':       run( );
                                        break;
                        case '2':       batch( );
                                        break;
                        case '3':       change( );
                                        break;
                        case '4':       alldone( );
                                        break;
                }
        }
}

/* run( ) - Do one run with current settings */
/* saving pertinent info to a file.            */
/* This routine uses a PID controller for   */
/* Motor speed control, takes care of slack */
/* control, and calls set_oven & set_track  */

void run( )
{
#define MCONST 14.652   /* conversion from ticks/(1/9.1) sec to cm/sec */
        int             i, v;           /* general purpose int's */
        int             tempset;        /* set point temp (0-4095) */
        int             tempnow;        /* current temp (0-4095) */
```

```
        _dos_getdate(&currdate);
        _dos_gettime(&currtime);
        fprintf(fpout,"\"%s:%d\" \"%2d/%2d/%4d\" \"%2d:%2d:%2d\"\n",infile,lineno,
                        currdate.month,currdate.day,currdate.year,currtime.hour,
                        currtime.minute,currtime.second);

        /* Set oven to initial temp - runs until key is pressed */

        printf("Regulating oven temperature - Please Wait...\n");
        counts = 0;             /* Reset Counters */
        ovencounts = 0;
        loopdone = 0;
        while (loopdone == 0) {
                int_flag = 0;
                while (int_flag == 0);
                int_flag = 0;
                if ((counts & 7) == 7) {
                        /* try about once every half second to update us on temp. stats. */
                        f = set_oven( );
                        _clearscreen(_GWINDOW);
                        printf("Set Oven Temp = %.1fC   Current Temp = %.1fC\n",
                                        settings->temp,f);
                        if (_bios_keybrd(_KEYBRD_READY) != 0) {
                                c = getch( );
                                loopdone = 1;
                                /* If key pressed - oven ready */
                        }
                }
        }

/*      Initialize variables for motor control  */

        K1 = TI1 = TD1 = 1;     /* Default Controller Coefficients */
        K2 = TI2 = TD2 = 1;
        P1 = P2 = 300;          /* Initial output pulse-width */
        DELT = 1/9.1;           /* Delta T, (tau) = 1/9.1 */
        printf("K1?\n");        /* Read in controller coefficients */
        scanf("%f",&K1);
        printf("TI1?\n");
        scanf("%f",&TI1);
        printf("TD1?\n");
        scanf("%f",&TD1);

        printf("K2?\n");
        scanf("%f",&K2);
        printf("TI2?\n");
        scanf("%f",&TI2);
        printf("TD2?\n");
        scanf("%f",&TD2);

/*      Turn on the speakers to their proper volume */

        f = log(settings->vspr);
        v = (int)(spr2*f*f+spr1*f+spr0);
        set_volume1(v);
        f = log(settings->vaer);
        v = (int)(aer2*f*f+aer1*f+aer0);
        set_volume2(v);

/*      set_volume1((int)settings->vspr);
```

```
set_volume2((int)settings->vaer); */

/* Initialize error terms to zero */

E1 = E2 = E3 = 0;
F1 = F2 = F3 = 0;

/* Reset statistics variables */

num = 0;
sum1 = sum2 = 0;
sumsq1 = sumsq2 = 0;

/* Set up PID coefficients */

A1 = K1*(1 + DELT/(TI1*2));
A2 = K1*(-1 + DELT/(TI1*2));
A3 = K1*TD1/DELT;
B1 = K2*(1 + DELT/(TI2*2));
B2 = K2*(-1 + DELT/(TI2*2));
B3 = K2*TD2/DELT;

/* Set slack to zero */

slack = 0;
slackadj = 0;
U11 = U12 = 0;
U21 = U22 = 0;

/* clear counters */

U1 = (float)get_counter1( );
U2 = (float)get_counter2( );

_disable;
ovencounts = 0;         /* Reset counters */
int_flag = 0;
_enable;

/* Clear screen */

_clearscreen(_GWINDOW);

/* Set the linespeed set point */

Uset = settings->linespeed*MCONST;
motors_on( );
loopdone = 0;
while (!loopdone) {
        if (int_flag == 1)
                printf("***** Latency *****\n");
        while (int_flag == 0);  /* Wait for end of time period */

        /* Get current speeds */

        U1 = (float)get_counter1( );
        U2 = (float)get_counter2( );
        int_flag = 0;           /* Reset flag for next cycle */

        /* Check for errors */
```

```
        if (U1 == -1) {
                U1 = 255; /* overflow */
                printf("Error - Box Disconnected or not turned on.\n");
                keywait( );
                loopdone = 1;
        }
        else if (U2 == -1) {
                U2 = 255; /* overflow */
                printf("Error - Box Disconnected or not turned on.\n");
                keywait( );
                loopdone = 1;
        }
        if (U1 == -2) {
                printf("Motor 1 Stalled\n");
                U1 = 0;
        }
        if (U2 == -2) {
                printf("Motor 2 Stalled\n");
                U2 = 0;
        }

        /* Calculate Output */
        /* PID with derivative kick control (DM1, DM2) */
        /*  and bounded by slack control */

        E3 = E2;
        E2 = E1;
        E1 = Uset - U1;
        F3 = F2;
        F2 = F1;
        F1 = Uset - U2;
        DM1 = U1 - 2*U11 + U12;
        DM2 = U2 - 2*U21 + U22;
        P1 = P1 + A1*E1 + A2*E2 - A3*DM1;
        P2 = P2 + B1*F1 + B2*F2 - B3*DM2;

        /* Slack adjustment */

        slack = slack + (U1 - U2)/MCONST;
        if (slack < .5)
                slackadj = -5;
        else if (slack > 2)
                slackadj = +5;
        else
                slackadj = 0;

        /* If slack is too small or too great - exit */

/*      if ((slack < .3) || (slack > 5)) {
                set_motor1(0);
                set_motor2(0);
                oven_off( );
                printf("Slack is %fcm, shutting line off\n",slack);
                keywait( );
                loopdone = 1;
        } */

        /* Bound output */
```

```
if (P1 > 4095) P1 = 4095;
if (P2 > 4095) P2 = 4095;
if (P1 < 0) P1 = 0;
if (P2 < 0) P2 = 0;

/* Time passes... */

U12 = U11;
U11 = U1;
U22 = U21;
U21 = U2;

/* Convert speeds to cm/sec */

speed1 = U1/MCONST;
speed2 = U2/MCONST;

/* Keep Statistics */
/* (Sums and sums of squares) */

num  = num + 1;
sum1 = sum1 + speed1;
sum2 = sum2 + speed2;
sumsq1 = sumsq1 + speed1*speed1;
sumsq2 = sumsq2 + speed2*speed2;

/* Every second or so, update oven & track settings */

if ((counts & 15) == 15) {
        f = set_oven( );
        set_track( );
}

/* Printf every 1/18.2 * 2^n seconds */

if ((counts & pmask) == pmatch) {
        conc = ((float)get_conc( ))/20.48;
        conc = ((float)get_conc( ))/20.48;
        spl = ((float)get_spl( ))/40.96+60.0;
        spl = ((float)get_spl( ))/40.96+60.0;
        printf("%.2f\t%.2f\t%.2f\t%.2f\t%.2f\n",speed1,speed2,f,spl,conc);
}

/* Fprintf every 1/18.2 * 2^nfpr here */

if ((counts & fmask) == fmatch) {
        conc = ((float)get_conc( ))/20.48;
        conc = ((float)get_conc( ))/20.48;
        spl = ((float)get_spl( ))/40.96+60.0;
        spl = ((float)get_spl( ))/40.96+60.0;
        if ((num != 0) && (num != 1)) {
                avg1 = sum1/num;
                avg2 = sum2/num;
                x = (float)((num*sumsq1-sum1*sum1)/(num*(num-1.0)));
                std1 = sqrt((double)x);
                x = (float)((num*sumsq2-sum2*sum2)/(num*(num-1.0)));
                std2 = sqrt((double)x);
        }
        else
                avg1 = avg2 = std1 = std2 = 0;
```

```
                    _dos_gettime(&currtime);
                fprintf(fpout,"\"%2d:%2d:%2d\" %.2f %.3f %.2f %.3f %.2f %.2f %.2f\n"
                        , currtime.hour,currtime.minute,currtime.second,
                            avg1,std1,avg2,std2,f,spl,conc);
                printf("\"%2d:%2d:%2d\" %.2f %.3f %.2f %.3f %.2f %.2f %.2f\n",
                            currtime.hour,currtime.minute,currtime.second
                                ,avg1,std1,avg2,std2,f,spl,conc);
                    num = 0;
                    sum1 = sum2 = 0;
                    sumsq1 = sumsq2 = 0;
                }

                /* Send new motor speeds */

                set_motor1((int)P1);
                set_motor2((int)900);

                /* Exit if key pressed */

                if (_bios_keybrd(_KEYBRD_READY) != 0) {
                        c = getch();
                        loopdone = 1;
                }
        }

        /* Everything off */

        motors_off();
        oven_off();
        track_off();
        set_volume1(0);
        set_volume2(0);
}

/* set_oven resets oven_on_width to a number     */
/* based on the oven temperature & the desired   */
/* oven temperature. In addition, set_oven turns */
/* the oven on or off based on the current time  */
/* in the cycle                                                    */

float set_oven()
{
        int     tempset;                                /* Temp. set point (0-4095) */
        int tempnow;                            /* Current temp (0-4095)    */
        int temptemp;                           /* Temporary temperature    */
        int temperr;                            /* Flag for temperature error */
        int     i;                                              /* general purpose */
        float ovencutoff = 5;           /* regulating window is +-5 degrees */
        float reset = 0;                        /* for fine tuning */
        float conv = 3.482;                     /* conversion from degrees to read value */
        float factor = 1.00888;                 /* correction factor and offset */
        float offset = 0.71447;

        /* Assuming sensor reads 5mV/degree C */

        tempset = (int)(conv*factor*settings->temp+offset);
        tempnow = 0;
        temperr = 0;

        /* Calculate new temperature by sampling */
```

```
        temptemp = get_temp( );
        for (i=0;i(5;i++) {
                temptemp = get_temp( );
                if (temptemp/conv ( 10)
                        temperr = 1;
                tempnow = tempnow + temptemp;
        }
        tempnow = tempnow/5;

        if (temperr)
                printf("Invalid Temperature Reading - Shutting oven off\n");

        /* Set new oven_on_width */

        tempset = tempset + (int)conv*reset;
        if ((tempnow - tempset) ) (int)conv*ovencutoff)
                oven_on_width = 0;
        else if ((tempset - tempnow) ) (int)conv*ovencutoff)
                oven_on_width = twenty_secs - 1;
        else
                oven_on_width = (tempset-tempnow)/(conv*ovencutoff)*twenty_secs/2+twenty_secs/2;

        /* Increment bigcounts every 20 secs */

        if (ovencounts ) twenty_secs) {
                        ovencounts = 0;
                        bigcounts++;
        }

        /* Turn oven on or off accordingly */

        if (temperr)
                oven_off( );
        else if (ovencounts )= oven_on_width)
                oven_off( );
        else
                oven_on( );

        /* Return converted temp */

        return(tempnow/conv);
}

/* set_track( ) turns the track on for 60 secs, then off for 20 */

void set_track( )

{
        if (bigcounts ) 3)
                bigcounts = 0;
        if (bigcounts ) 0)
                track_off( );
        else
                track_on( );

}

/* batch( ) reads in the data from the current input file.       */
/* The first line of the file is assumed to contain the field names. */
```

```
/* All other lines are data, one run's worth per line */

void batch( )
{
        char    c;

        /* Print header */

        _clearscreen(_GWINDOW);
        printf("Composite Line Controller              Electronic & Computer Services - M.S.U.\n");
        printf("-------------------------------------------------------------------------------\n\n");

        lineno = 1;

        /* Get the fields from line 1 */

        while (read_input_data( ) != -1) {
                run( );
                lineno++;
        }
}

/* read_input_data( ) reads directly into the */
/* settings structure                         */

int read_input_data( )

{
        /* Read in the data */
        /* (aborting at EOF) */

        printf("Reading from line #%d of file: %s\n",lineno,infile);
        if (fscanf(fpin,"%f",&(settings->linespeed)) == EOF)
                return(-1);
        if (fscanf(fpin,"%f",&(settings->vspr)) == EOF)
                return(-1);
        if (fscanf(fpin,"%f",&(settings->vaer)) == EOF)
                return(-1);
        if (fscanf(fpin,"%f",&(settings->temp)) == EOF)
                return(-1);
}

/* If you really want to, alldone( ) allows you to exit the program */
/* gracefully.     */

void alldone( )
{
        char    c;

        printf("Are you sure?\n");
        c = (char)getche( );
        if ((c == 'Y') || (c == 'y')) {

                /* Ignore ctrl-c */

                signal(SIGINT,SIG_IGN);

                /* shut everything off */

                motors_off( );
```

```
                oven_off( );
                track_off( );
                set_volume1(0);
                set_volume2(0);

                /* reset timer tick vector */

                _disable;
                _dos_setvect(8,oldvector);
                _enable;

                /* close files and exit */

                fclose(fpin);
                fclose(fpout);
                exit(0);
        }
}

/* Change( ) queries the user for new settings information and sets      */
/*  up the settings structure accordingly.                                */

void change( )

{
        char    c;
        float   response;

        _clearscreen(_GWINDOW);
        printf("Composite Line Controller              Electronic & Computer Services - M.S.U.\n");
        printf("-------------------------------------------------------------------------------\n\n")
        printf("Line Speed is %.1f cm\n",settings->linespeed);
        printf("   New Line Speed (1-10)? \n");
        scanf("%f",&response);
        fflush(stdin);
        if ((response < 1) || (response > 10))
                printf("- Unchanged -\n");
        else
                settings->linespeed = response;
        printf("Voltage Level for spreading speaker is %.1f V\n",settings->vspr);
        printf("   New Level for speaker? \n");
        scanf("%f",&response);
        fflush(stdin);
/*      if ((response < 1) || (response > 100))
                printf("- Unchanged -\n");
        else */
                settings->vspr = response;
        printf("Voltage Level for aerosolizer is %.1f V\n",settings->vaer);
        printf("   New Level for speaker 2? \n");
        scanf("%f",&response);
        fflush(stdin);
/*      if ((response < 1) || (response > 100))
                printf("- Unchanged -\n");
        else */
                settings->vaer = response;
        printf("Oven Temperature is %.1f C\n",settings->temp);
        printf("   New Oven Temp? \n");
        scanf("%f",&response);
        fflush(stdin);
        if ((response < 1) || (response > 500))
```

```
                printf("- Unchanged -\n");
        else
                settings->temp = response;
}

/*      menu( ) - Display Menu & return response */

char    menu( )
{
        _clearscreen( _GWINDOW);
        printf("Composite Line Controller              Electronic & Computer Services - M.S.U.\n");
        printf("-------------------------------------------------------------------------------\n\n")
        printf("                  1 - Run line from with current settings\n\n");
        printf("                  2 - Run line from batch file\n\n");
        printf("                  3 - Change current settings\n\n");
        printf("                  4 - Exit to DOS\n\n");
        fflush(stdin);
        return((char)getch( ));
}

/*      Interrupt Handler for Timer  */
/*  (executed every 1/18.2 secs) */

void interrupt far tick( )

{
        /* Increment the two counters */

        counts++;
        ovencounts++;

        /* Every other time set int_flag */

        if ((counts & 0x01) == 1)
                int_flag = 1;

        /* Go about normal business */

        _chain_intr(oldvector);
}

/* power( ) returns x^y */

unsigned long power(int x, int y) {

        unsigned long z;
        int     i;

        z = (unsigned long)x;
        for(i=1;i<y;i++)
                z = z*(unsigned long)x;
        return(z);
}

/* keywait( ) - Prompt and wait for a key to be pressed */

void keywait( ) {

                char    c;
```

```
        fflush(stdin);
        printf("- Hit any key to continue -\n");
        scanf("%c",&c);
}
```

Program 2 : Routines.c

```
/*          Electronic & Computer Services          */
/*          Composite Line Controller Software      */
/*          Frank Palazzolo        6/7/90           */

/* DT2811 Board Register Definitions */

#define     BASEADDR        0x0218          /* Base Address for DT2811          */
#define     ADCSR           BASEADDR+0      /* A/D Control/Status          (R/W) */
#define     ADGCR           BASEADDR+1      /* A/D Gain/Channel            (R/W) */
#define     AD_DA0          BASEADDR+2      /* A/D and DAC0 Data Word      (R/W) */
#define     DA1             BASEADDR+4      /* DAC1 Data Word               (W)  */
#define     DIO             BASEADDR+6      /* DIO Port 0 / DIO Port 1     (R/W) */
#define     TMRCTR          BASEADDR+7      /* Timer / Counter             (R/W) */

#include <stdio.h>          /* Necessary libraries */
#include <signal.h>
#include <stdlib.h>
#include <process.h>
#include <dos.h>

unsigned long counts;
void (interrupt far *oldvector)();
void interrupt far tick();

int reg10stat = 2;                  /* Global variable - status of register 10 */

/* For more information about these routines - see the A/D board guide, */
/* and the specifications for the composite line controller box.        */

int get_counter1()

/* Routine to get number of counts from motor 1 */

{
     int    temp1, notimeout;
     unsigned long  temp;

     temp1 = get_register(0);
     if ((temp1 & 1) == 1) {
        get_register(3);
        return(-1);
     }
     get_register(3);
     temp = counts;
     notimeout = 1;
     while ((((temp1 = get_register(0)) & 2) == 2) && notimeout)
        if (counts > (temp+1)) notimeout = 0;
     if (notimeout == 0)
        return(-2);
     else
        return(get_register(2)*16+get_register(1));
}

int get_counter2()

/* Routine to get number of counts from motor 2 */

{
```

```
      int     temp1, notimeout;
      unsigned long   temp;

      temp1 = get_register(0);
      if ((temp1 & 4) == 4) {
         get_register(13);
         return(-1);
      }
      get_register(13);
      temp = counts;
      notimeout = 1;
      while ((((temp1 = get_register(0)) & 8) == 8) && notimeout)
         if (counts > (temp+1)) notimeout = 0;
      if (notimeout == 0)
         return(-2);
      else
         return(get_register(12)*16+get_register(11));
}

int set_motor1(int value)

/* Routine to set speed for motor 1 */

{
      value = 4095 - value;
      set_register(6,value & 0x0F);
      set_register(5,(value & 0x0F0) >> 4);
      set_register(4,(value & 0x0F00) >> 8);
}

int set_motor2(int value)

/* Routine to set speed for motor 2 */

{
      value = 4095 - value;
      set_register(9,value & 0x0F);
      set_register(8,(value & 0x0F0) >> 4);
      set_register(7,(value & 0x0F00) >> 8);
}


int get_register(int reg_number)

/* Routine to read from register on controller board */

{
      int temp;

      outp(DIO,reg_number*16);
      temp = (0x0f & inp(DIO));
      outp(DIO,0);
      return(temp);
}

set_register(int reg_number, int value)

/* Routine to write to register on controller board */
```

```
{
      outp(DIO,reg_number*16+value);
      outp(DIO,value);
}

set_volume1(int value)

/* Routine to set the volume level of speaker 1 */

{
      outpw(AD_DA0,value);
}

set_volume2(int value)

/* Routine to set the volume level of speaker 2 */

{
      outpw(DA1,value);
}

int get_conc( )

/* Routine to get particle concentration level */

{
      a2d_init( );
      outp(ADCSR,0);
      outp(ADGCR,0);
      while(inp(ADCSR)&128 == 0);
      return(inpw(AD_DA0));
}

int get_spl( )

/* Routine to get sound pressure level (speaker 2) */

{
      a2d_init( );
      outp(ADCSR,0);
      outp(ADGCR,1);
      while(inp(ADCSR)&128 == 0);
      return(inpw(AD_DA0));
}

int get_temp( )

/* Routine to get oven temperature level */

{
      a2d_init( );
      outp(ADCSR,0);
      outp(ADGCR,2);
      while(inp(ADCSR)&128 == 0);
      return(inpw(AD_DA0));
}

void oven_on( )
```

```
{
      reg10stat = reg10stat & 0xFD;
      set_register(10,reg10stat);
}

void oven_off()

{
      reg10stat = reg10stat | 0x02;
      set_register(10,reg10stat);
}

void motors_on()

{
      reg10stat = reg10stat | 0x01;
      set_register(10,reg10stat);
}

void motors_off()

{
      reg10stat = reg10stat & 0xFE;
      set_register(10,reg10stat);
}

void track_on()

{
      reg10stat = reg10stat | 0x04;
      set_register(10,reg10stat);
}

void track_off()

{
      reg10stat = reg10stat & 0xFB;
      set_register(10,reg10stat);
}

a2d_init()

/* Routine to initialize A to D system */

{
      int     i,dummy;

      outp(ADCSR,0);
      for(i=0;i(1000;i++);
      dummy = inpw(AD_DA0);
}

int ctrlc()

/* Routine to Handle Ctrl-C Interrupt */

{

      char    c;
```

```
        /* disable Ctrl-C */

        signal(SIGINT,SIG_IGN);

        motors_off( );
        oven_off( );
        track_off( );
        set_volume1(0);
        set_volume2(0);

        printf("Are you sure you want to quit?\n");
        c = (char)getche( );
        if ((c == 'y') || (c == 'Y')) {

        /* roset timer vector */

                _disable;
                _dos_setvect(8,oldvector);
                _enable;
                exit(0);

        }
        else {
                motors_on( );

                /* set ctrl-c vector back to this routine */

                signal(SIGINT, ctrlc);
        }
}
```

Appendix C

CONTACT ANGLE PROGRAM

This appendix lists the finite difference program written to solve for the contact angle that a polymer matrix makes with a cylindrical fiber. A sample output from a simulation is also enclosed.

Program Algorithm

The algorithm of the finite difference program consists of the following steps :

(1) Read data from a user file in the following sequence - fiber diameter (DIAMETER) , predicted contact angle (THETA), maximum number of iterations (NMAX) and tolerance (TOL) used in subroutine FALSI, ratio of excess pressure to polymer surface tension (DPYLV), the minimum (DPYLVI) and maximum (DPYLVM) values of this ratio (which are related to droplet size) and the step size (DPSTEP) and the regression coefficients (B0, B1, B2 and B3) that are used to fit the experimental data for the fiber-matrix system.

(2) For each droplet size dictated by the value of DPYLV, start with an initial guess for Y(I), solve the finite difference equation given in the subroutine FDROP by means of a root-finding algorithm FALSI for the actual value of Y(I).

(3) Continue this procedure for each Y(I) till the droplet profile is complete for the contact angle THETA and the drop size dictated by DPYLV.

(4) Compare the predicted values of drop median radius for a given drop lengthwith that measured by experiment. Calculate a residual sum of squares for that particular value of THETA for a range of droplet sizes with uniform steps from the minimum to the maximum droplet size.

The residual sums of squares that results from each contact angle simulation are then compared to arrive at the contact angle which best describes the experimental data.

```
C                    CONTACT ANGLE PROGRAM
C
C   This program calculates the contact angle that a liquid makes with a
C   cylindrical fiber.  It uses finite differences (backward difference)
C   and a root-finding algorithm (Regula-Falsi) to solve the ordinary
C   non-linear differential equation.  The drop profile is solved for
C   the wide range of droplet sizes by varying the excess pressure
C   inside the drop.
C
C
C   Variables used:
C
C       A, B      = INITIAL GUESSES FOR Y THAT ARE FED AS ARGUMENTS IN THE
C                   FALSI SUBROUTINE
C       B0,B1,B2,B3  = REGRESSION COEFFICIENTS FOR THE LINE THAT FITS THE
C                      DROPLET EXPERIMENTAL DATA IN THE FORM :
C                       K = B0 + B1*L + B2*L**2 + B3*L**3
C       DIAMETER = DIAMETER OF THE FIBER
C       DPYLV    = EXCESS PRESSURE / LIQUID SURFACE TENSION
C       DPYLVI   = INITIAL VALUE OF DPYLV
C       DPYLVM   = FINAL VALUE OF DPYLV
C       DPSTEP   = STEP SIZE FOR DPYLV
C       DX       = STEP SIZE USED IN THE FINITE DIFFERENCE ALGORITHM
C       F        = DUMMY EXTERNAL FUNCTION USED IN THE SUBROUTINE FALSI
C       I        = COUNTER USED IN MAIN PROGRAM
C       N        = ITERATION COUNTER USED IN SUBROUTINE FALSI
C       NMAX     = MAXIMUM NUMBER OF ITERATIONS USED IN SUBROUTINE FALSI
C       RL       = L, GIVEN BY 2*DROPLET LENGTH/DIAMETER
C       RK       = K, GIVEN BY 2*DROP MEDIAN RADIUS/DIAMETER
C       RKEXPT   = K, MEASURED BY EXPERIMENT
C       SUMSQ    = SUM OF SQUARES OF THE ERROR I.E. DIFFERENCE BETWEEN
C                  RK AND RKEXPT
C       TOL      = TOLERANCE USED IN SUBROUTINE FALSI
C       X0       = FINAL VALUE FOR Y CALCULATED BY SUBROUTINE FALSI
C       X        = AXIAL DISTANCE ALONG THE FIBER, X = 0.0 AT THE
C                  BEGINNING OF THE DROP
C       Y        = RADIAL DISTANCE OF THE DROP FROM THE FIBER AXIS
C
C
C   Characterization of variables :
C
        IMPLICIT REAL*8 (A-H,O-Z)
        DIMENSION Y(1000)
        CHARACTER*20 DIN
        INTEGER I,NMAX,IC
        COMMON DX,DPYLV,Y,IC
        EXTERNAL FDROP
C
C
C   Enter input and output file names :
C   (The program is set up so that it interactively prompts the user
C   for input and output filenames each time it is run).
C
        PRINT *, 'ENTER THE OUTPUT FILE NAME'
        READ (*,100),DIN
        OPEN (UNIT=10, NAME=DIN,STATUS='NEW')
        PRINT *,'ENTER THE INPUT FILE NAME'
        READ (*,100), DIN
        OPEN (UNIT=14,NAME=DIN,STATUS='OLD')
C
C
C   Read the data file entered by the user -
C
        READ (14,*) DIAMETER,THETA,NMAX,TOL,DPYLVI,DPYLVM,DPSTEP,
```

```
      $ B0,B1,B2,B3
C
C   Write the data filename and all the data read from the file into
C   an output file :
C
        WRITE (10,*) '     DATA FILENAME = ', DIN
        WRITE (10,*) ' '
        WRITE (10,*) '  DIAMETER                    = ',DIAMETER
        WRITE (10,*) '  THETA                       = ',THETA
        WRITE (10,*) '  NMAX                        = ',NMAX
        WRITE (10,*) '  TOLERANCE                   = ',TOL
        WRITE (10,*) '  DPYLVI                      = ',DPYLVI
        WRITE (10,*) '  DPYLVM                      = ',DPYLVM
        WRITE (10,*) '  DPSTEP                      = ',DPSTEP
        WRITE (10,*) '  B0                          = ',B0
        WRITE (10,*) '  B1                          = ',B1
        WRITE (10,*) '  B2                          = ',B2
        WRITE (10,*) '  B3                          = ',B3
        WRITE (10,*) '  '
C
C
C   Initialize the error sum of squares :
C
        SUMSQ = 0
C
C
C   The finite difference step used by the program is 1/20 of the
C   fiber diameter :
C
        DX = DIAMETER/20.0
C
C
C   Write headings for the columns in the output file :
C
        WRITE (10,20)
  20    FORMAT (6X,'DPYLV',7X,'l',7X,'k',7X,'L',7X,'K',7X,'K(expt)')
C
C
C   Initiate a do-loop to iterate for each value of DPYLV from the
C   minimum to the maximum value in steps.  This covers the entire
C   range of droplet sizes.
C
        DO 200, DPYLV = DPYLVI,DPYLVM, DPSTEP
C
C
C   For each droplet size (which is dictated by the value of the excess
C   pressure or DPYLV, initialize Y(1) and Y(2), the starting points
C   for the drop profile.
C
        Y(1) = DIAMETER/2.0
        Y(2) = Y(1) + DX*TAN(THETA*3.1415927/180)
        I = 2
C
C
C   If the value of y is greater than or equal to the previous value,
C   then calculate an initial guess for y and feed the initial guesses to
C   the Regula-Falsi subroutine.  If the converse is true, then the
C   droplet profile is complete.
C
  10    IF (Y(I) .GE. Y(I-1))THEN
                I = I+1
                Y(I) = 2*Y(I-1) - Y(I-2)
                A = Y(I)
                B = Y(I-1)
```

```
                IC = I
                CALL FALSI (A,B,FDROP,X0,TOL,NMAX)
                Y(I) = X0
                GOTO 10
        ELSE
                IMAX = I
        ENDIF
C
C
C   Convert the maximum calculated values of x and y for the completed
C   drop profile to dimensionless values.
C
        X = DX*(IMAX - 1)
        RL = 4*X/DIAMETER
        RK = 2*Y(IMAX)/DIAMETER
C
C
C   Compare the predicted drop dimensions with the experimentally
C   measured values by means of residual sum of squares for the
C   entire range of droplet sizes.  Write the calculated values of
C   different parameters in column format.
C
        RKEXPT = - B0 + B1*RL + B2*RL**2 - B3*RL**3
        SUMSQ = SUMSQ + (RK - RKEXPT)**2
        WRITE (10,30) DPYLV,2*X,Y(I),RL,RK,RKEXPT
        TYPE *,RK,RKEXPT,DPYLV
C
C
C   Go back to the beginning of the DO loop to calculate drop dimensions
C   for the next value of excess pressure.
C
  200   CONTINUE
C
C
C   Write the residual sum of squares for the contact angle THETA.
C
        WRITE (10,*) 'ERROR SUM OF SQUARES =  ',SUMSQ
  30    FORMAT (2X,F10.4,2X,F10.4,2X,F10.4,2X,F10.4,2X,F10.4,2X,F10.4)
  100   FORMAT (A)
        END
C
**********************************************************************
C
C
C   Subroutine FALSI is a general subroutine to determine the zero of
C   of a function F(X), the arguments used are as follows :
C
C   A, B    =  The 2 starting values of X
C   F       =  External function of X
C   X0      =  Root of X
C   TOL     =  Tolerance on F
C   NMAX    =  Maximum number of iterations
C
C   The subroutine has a nested loop structure which ultimately yields
C   the root after checking for convergence and tolerance.
C
        SUBROUTINE FALSI (A,B,F,X0,TOL,NMAX)
        IMPLICIT REAL*8 (A-H,O-Z)
        DIMENSION Y(1000)
        INTEGER NMAX,N
        EXTERNAL F
C
        N = 1
C
```

```
C
  20    X0 = (A*F(B) - B*F(A))/(F(B) - F(A))
C
        IF (ABS(F(X0)) .GT. TOL) THEN
                IF (N .LT. NMAX) THEN
                        IF (ABS(F(A)) .LE. ABS(F(B))) THEN
                                B = X0
                        ELSE
                                A = X0
                        ENDIF
                                N = N+1
                        GOTO 20
                ELSE
                        TYPE *, '  THE FUNCTION HAS NO ROOT'
                ENDIF
        ENDIF
        RETURN
        END
C
*****************************************************************
C
C
C   Function FDROP is a real function which calculates the value
C   of the finite difference equation for a specific value of y
C   referred to as A by the FALSI subroutine.  DX, DPYLV, the array
C   of y values before Y(I) i.e. Y(I-1), Y(I-2) etc are all passed
C   on from the main program through the COMMON statement..
C
        REAL FUNCTION FDROP (A)
        IMPLICIT REAL*8 (A-H,O-Z)
        DIMENSION Y(1000)
        INTEGER I,IC
        COMMON DX,DPYLV,Y,IC
C
        I = IC
C
        TERM1 = (A - 2*Y(I-1) + Y(I-2))/(DX**2)
        TERM2 = DPYLV*(1 + (A - Y(I-1))**2/DX**2)**1.5
        TERM3 = (1 + (A-Y(I-1))**2/DX**2)/A
C
        FDROP = TERM1 + TERM2 - TERM3
C
        RETURN
        END
C
C*****************************************************************
```

DATA FILENAME = theta24.dat

DIAMETER = 7.4189999999999999E-04
THETA = 24.00000000000000
NMAX = 200
TOLERANCE = 1.0000000000000000E-05
DPYLVI = 400.0000000000000
DPYLVM = 1800.000000000000
DPSTEP = 100.0000000000000
B0 = 0.5324824000000000
B1 = 0.2425831000000000
B2 = 8.9802280000000000E-03
B3 = 1.3042650000000000E-04

DPYLV	l	k	L	K	K(expt)	
400.0000	0.0120	0.0046	32.4000	12.4361	12.3182	
500.0000	0.0099	0.0036	26.6000	9.7474	9.8195	
600.0000	0.0084	0.0030	22.6000	7.9589	8.0311	
700.0000	0.0073	0.0025	19.6000	6.6854	6.6899	
800.0000	0.0065	0.0021	17.4000	5.7329	5.7202	
900.0000	0.0058	0.0019	15.6000	4.9954	4.9421	
1000.0000	0.0052	0.0016	14.0000	4.4092	4.2659	
1100.0000	0.0047	0.0015	12.8000	3.9317	3.7704	
1200.0000	0.0044	0.0013	11.8000	3.5363	3.3661	
1300.0000	0.0040	0.0012	10.8000	3.2057	2.9706	
1400.0000	0.0037	0.0011	10.0000	2.9246	2.6609	
1500.0000	0.0034	0.0010	9.2000	2.6849	2.3578	
1600.0000	0.0032	0.0009	8.6000	2.4772	2.1350	
1700.0000	0.0030	0.0009	8.0000	2.2976	1.9161	
1800.0000	0.0027	0.0008	7.4000	2.1422	1.7015	

ERROR SUM OF SQUARES = 0.7914268496853361

BIBLIOGRAPHY

BIBLIOGRAPHY

[1] Grayson, M., "Encyclopaedia of Composite Materials and Components", *John Wiley and Sons* 1983.

[2] Hergenrother, P. M., and N. J. Johnston, "Status of High-Temperature Laminating Resins and Adhesives", *Resins for Aerospace*, p3-13, ACS 1979.

[3] Serafini, T. T., "Aerospace Applications for PMR Polyimide Composites", *Fifth ICCM on Composite Materials*, p1007-1023, Metallurgical Soc. Inc. 1985.

[4] O'Connor, J. E., Lou, A. Y., and W. H. Beever, "Polyphenylene Sulfide- A Thermoplastic Matrix for High Performance Composites", *Fifth ICCM on Composite Materials*, p963-970, ibid.

[5] Kitanaka, M. and Kobayashi, H., Norita, T., and Y. Kawatsu, "Damage Tolerance of Thermoplastic/Graphite Fiber Composites" p913-921, *ibid.*

[6] Hartness, T. "Thermoplastic Powder Technology for Advanced Composite Systems", *J. Thermoplastic Composite Materials*, Vol 1, 210-231 (1988).

[7] Taylor, G. J., "Method of Impregnating a Fibrous Textile Material With a Plastic Resin", *U.S. Patent 429105*, Sept 1981.

[8] O'Connor, J. E., "Reinforced Plastic", *U.S. Patent 4680224*, July 1987.

[9] Dyksterhouse, R., and J. A. Dyksterhouse, "Method of Improved Pre-Impregnated Material Comprising a Particulate Thermoplastic Polymer Suitable for Use in the Formation of a Substantially Void-Free Fiber-Reinforced Article", *U.S. Patent Application 114362*, Nov 1987.

[10] Turton, N., and J. McAinsh, "Thermoplastic Compositions", *U.S. Patent 3785916*, 1974.

[11] Moyer, R. L., "Methods of Making Continuous Length Reinforced Plastic Articles", *U.S. Patent 3993726*, Nov 1976.

[12] Cogswell, F. N., Hezzell, D. J., and P. J. Williams, "Fiber-Reinforced Compositions and Methods for Producing Such Compositions", *U.S. Patent 4559262*, Dec 1985.

[13] Chung, T. "Liquid Crystal Polyester-Carbon Fiber Composites", *NASA Contractor Report 172323*, NASA Langley (1986).

[14] Lind, D. J., and V. J. Coffey, *U.K. Patent 1485586*, 1977.

[15] Clemans, S. R., Western, E. D., and A. C. Handermann, "Thermoplastic Hybrid Yarns for High-Performance Composites", *Materials Engineering*, Vol 105, 27-30 (1988).

[16] Price, R. V., "Production of Impregnated Roving", *U.S. Patent 3742106*, June 1973.

[17] Ganga, R. A., "Flexible Composite Material and Process and Apparatus for Producing Same", ATO113 (DPI8176), *U.S. Patent Application*; "Procede de Fabrication d'Objets Composites Obtenus", *FR 2548084-A1*, June 1983.

[18] Muzzy, J. D., "Processing of Advanced Thermoplastic Composites", *ASME Symposium on Manufacturing Science of Composites*, April 1988, p27-39; Muzzy, J. D., Varughese, B., Thammongkol, V., and W. Tincher, "Electrostatic Prepregging of Thermoplastic Matrices", *SAMPE J.*, 25 (5), 15-21 (1989).

[19] Allen, L. E., Edie, D. D., Lickfield, G. C., and J. R. McCollum, "Thermoplastic Coated Carbon Fibers for Textile Preforms", *J. Thermoplastic Composite Materials*, Vol 1, p371-379 (1988).

[20] Baucom, R. M., and J. M. Marchello, "LaRC Dry Powder Towpreg System", *NASA Technical Memorandum 102648*, April 1990.

[21] Baerns, M., "Effect of Interparticle Adhesive Forces on Fluidization of Fine Particles", *Industrial and Engineering Chemistry Fundamentals*, 5 (4), 508-516 (1966).

[22] Bailey, A. G., "Electrostatic Phenomena During Powder Handling", *Powder Technology*, 37, 71-85 (1984).

[23] Masui, N. and Y. Murata, "Method for Measuring the Powder Charge in the Electrostatic Powder-Coating Process", *Rev. Sci. Instrum.*, 53 (4), 532-533 (1982).

[24] Donsi, G., Formisani, B., Valentino, R. and G. Volpicelli, "The Measurement of Characteristic Angles of Powders in the Prediction of Their Behavior in the Gas Fluidized State", *Powder Tech.*, 37, 39-47 (1984).

[25] Geldart, D. and A. C. Y. Wong, "Fluidization of Powders Showing Degrees of Cohesiveness - I. Bed Expansion", *Chem. Engrg. Sci.*, 39 (10), 1481-1488 (1984).

[26] Stern, A. C., Air Pollution, Third Edition, *Academic Press* 1977.

[27] Geldart, D., "Types of Gas Fluidization", *Powder Technology*, 7, 285- 292 (1973).

[28] Geldart, D., and A. C. Y. Wong, "Fluidization of Powders Showing Degrees of Cohesiveness - II. Experiments on Rates of De-Aeration", *Chem. Engr. Sci.*, 40 (4), 653-661 (1985).

[29] Rietema, K., "Powders - What are They?", *Powder Technology*, 37, 5 (1984).

[30] Geldart, D., Harnby, N. and A. C. Y. Wong, "Fluidization of Cohesive Powders", *Powder Technology*, 37, 25-37 (1984).

[31] Dry, R. J., Judd, M. R. and T. Shingles, "Two-Phase Theory and Fine Powders", *Powder Technology*, 34, 213 (1983).

[32] Chaouki, J., Chavarie, C., Klvana, D. and G. Pajonk, "Effect of Interparticle Forces on the Hydrodynamic Behavior of Fluidized Aerogels", *Powder Technology*, 43, 117 (1985).

[33] Frenkel, J., *J. Physics U.S.S.R.*, 9, 385 (1945).

[34] Kuczynski, G.C., Neuville, B. and H.P. Toner, "Study of Sintering of Poly(methyl Methacrylate)" *J. Appl. Poly. Sci.*, vol (14), 2069-2077 (1970).

[35] Rosenzweig, N. and M. Narkis, "Observation and Analysis Technique for Studying Sintering of Polymeric Particles", *J. Appl. Poly. Sci.*, vol 26, 2787-2789 (1981).

[36] Rosenzweig, N. and M. Narkis, "Sintering Rheology of Amorphous Polymers", *Poly. Engr. and Sci.*, vol 21, no 17, 1167-1170 (1981).

[37] Siegmann, A., Raiter, I., Narkis, M. and P. Eyerer, "Effect of Powder Particle Morphology on the Sintering Behavior of Polymers", *J. Materials Science*, vol 21, 1180-1186 (1986).

[38] Carroll, B. J., "Equilibrium Configuration of Liquid Drops on Thin Cylinders Under Forces of Capillarity. A Theory for the Roll-up Process", *Langmuir*, 2, 248-250 (1986).

[39] Kumar, A. and S. Hartland, "Shape of a Drop on a Vertical Fiber", *J. Coll. Int. Sci.*, 124 (1), 67-76 (1988).

[40] Van Oene, H., Chang, Y. F. and S. Newman, "The Rheology of Wetting by Polymer Melts", *J. Adhesion*, vol 1, 54-68 (1969).

[41] Shaw, D. J., Introduction to Colloid and Surface Chemistry, *Butterworths and Co.* 1980.

[42] Brochard, F., "Spreading of Liquid Drops on Thin Cylinders: The Manchon/Droplet Transition", *J. Chem. Phy.*, 84 (8), 4664-4672 (1986).

[43] Quere, D., Di Meglio, J.-M., and F. Brochard, "Making van der Waals Films on Fibers", *Europhysics Letters*, 10 (4), 335-340 (1989).

[44] Carroll, B. J., "The Accurate Measurement of Contact Angle, Phase Contact Areas, Drop Volume and Laplace Excess Pressure in Drop-on-Fiber Systems", *J. Coll. Int. Sci.*, vol 57 (3), 488-495 (1976).

[45] Yamaki, J. and Y. Katayama, "New Method of Determining Contact Angle Between Monofilament and Liquid", *J. Appl. Poly. Sci.*, vol 19, 2897-2909 (1975).

[46] Thomas, G. B., Analytic Geometry, 1972.

[47] McCabe and Smith, Unit Operations of Chemical Engineering, *McGraw- Hill* 1976.

[48] Wool, R. P. and K. M. O'Connor, "A Theory of Crack Healing in Polymers", *J. Appl. Phy.*, 52 (10), 5953-5963 (1981).

[49] Wool, R. P. and K. M. O'Connor, "Time Dependence of Crack Healing", *J. Polymer Science : Polymer Letters Edition*, 20, 7-16 (1982).

[50] Wool, R. P., "Molecular Aspects of Tack", *Rubber Chem. and Technol.*, 57, 307-319 (1983).

[51] Wool, R. P., Yuan, B.-L. and O. J. McGarel, "Welding of Polymer Interfaces", *Polymer Engr. and Sci.*, 29 (19), 1340-1367 (1989).

[52] deGennes, P.-G., "Entangled Polymers", *Physics Today*, 33-39 (1983).

[53] Howes, J. C. and A. C. Loos, "Autohesive Strength Development in Polysulfone Resin and Graphite-Polysulfone Composites", *American Society for Composites*, 110-119, Technomic 1987.

[54] Lee, W. I. and G. S. Springer, "A Model of the Manufacturing Process of Thermoplastic Matrix Composites", *J. Composite Materials*, 21, 1017-1055 (1987).

[55] Manson, J.-A. E. and J. C. Seferis, "Autoclave Processing of PEEK/Carbon Fiber Composites", *J. Thermoplastic Composite Materials*, 2, 34-49 (1989).

[56] Iyer, S. R., and L. T. Drzal, "Behavior of Cohesive Powders in Narrow- Diameter Fluidized Beds", *Powder Technology*, 57 (2), 127-133 (1989).

[57] Iyer, S.R., Drzal, L.T., and Jayaraman, K., "Method For Fiber Coating With Particles", *U. S. Patent Application*, Feb 1990.

[58] Bagnold, R. A., "Experiments on a Gravity-Free Dispersion of Large Solid Spheres in a Newtonian Fluid Under Shear", *Proc. Royal Soc. London*, 225, 49-65 (1954).

[59] Savage, S. B., "Gravity Flow of Cohewionless Granular Materials in Chutes and Channels", *J. Fluid Mech.*, 92 (1), 53-96 (1979).

[60] Johnson, P. C., and R. Jackson, "Frictional-Collisional Constitutive Relations for Granular Materials, With Application to Plane Shearing", *J. Fluid Mech.*, 176, 67-93 (1987).

[61] Fuchs, N., Mechanics of Aerosols, *Pergamon Press* 1964.

[62] Hidy, G. M., Aerosols - An Industrial and Environmental Science, *Academic Press* 1984.

[63] Iyer, S. R., and L. T. Drzal, "Method and System for Spreading a Tow of Fibers", *U. S. Patent Application*, July 1990.

[64] Hall, J. N., "Apparatus for Spreading a Graphite Fiber Tow into a Ribbon of Graphite Filaments", *U. S. Patent 3704485*, 1972.

[65] Seborg, D. E., Edgar, T. F. and D. A. Mellichamp, Process Dynamics and Control, *John Wiley and Sons* 1989.

[66] Rodriguez, F., Principles of Polymer Systems, *McGraw-Hill* 1982.

[67] Image Analysis : Theory and Practice, *Joyce-Loebl Co.*

[68] Beddow, J. K., Particulate Science and Technology, *Chemical Publishing Co* 1980.

[69] Encyclopaedia of Polymer Science and Engineering, Vol 11, p315-381, 2nd Ed., *John Wiley* 1988.

[70] DSC 910 manual, *DuPont Co.*

[71] Encyclopedia of Polymer Science and Engineering, Vol 4, 2nd edition, *John Wiley*, p482-516 (1988).

[72] Wunderlich, B., Macromolecular Physics, Vol 1, *Academic Press* 1973.

[73] Bird, R. B., Hassager, O., and Armstrong, R., Dynamics of Polymeric Liquids, *John Wiley* 1977.

[74] Wu, S., Polymer Interface and Adhesion, *Marcel Dekker* 1982.

[75] Hull, D., An Introduction to Composite Materials, *Cambridge University Press* 1981.

[76] Dry, R. J., Judd, M. R., and T. Shingles, "Bubble Velocities in Fluidized Beds of Fine, Dense Powders", *Powder Technology*, 39, 69-74 (1984).

[77] Kreith, F., Principles of Heat Transfer, *Intext Press* 1973.

[78] Hammer, G. E., and L. T. Drzal, "Graphite Fiber Surface Analysis by X-Ray Photoelectron Spectroscopy and Polar/Dispersive Free Energy Analysis", *Applications of Surface Science*, 4, 340-355 (1980).

[79] Carlsson, L. A., and Pipes, R. B., Experimental Characterization of Advanced Composite Materials, *Prentice Hall* 1987.

[80] Waterbury, M. C., and Drzal, L. T., "Determination of Fiber Volume Fractions by Optical Numeric Volume Fraction Analysis", *J. Reinforced Plastics and Composites*, Vol 8, p627-636 (1989).

[81] Chai, H., "Interlaminar Shear Fracture of Laminated Composites", *International Journal of Fracture*, 43, 117-131 (1990).